Diagenetic processes in reservoir rocks of the North Alpine Foreland Basin (Austria)

Dissertation

zur Erlangung des akademischen Grades eines
Doktors der montanistischen Wissenschaften (Dr. mont.)

vorgelegt von

Marie-Louise Grundtner, MSc.

eingereicht am

Lehrstuhl für Erdölgeologie

Department Angewandte Geowissenschaften und Geophysik

Montanuniversität Leoben

Die vorliegende Dissertationsschrift wurde von
Frau Ass.Prof. Dipl.-Ing. Dr.mont. Doris Groß und
Herrn Univ.-Prof. Mag.rer.nat. Dr.mont. Reinhard Sachsenhofer
(Montanuniversität Leoben) betreut.

Leoben, Dezember 2016

Eidesstattliche Erklärung

Ich versichere an Eides statt, diese Arbeit selbstständig verfasst, andere als die angegebenen Quellen und Hilfsmittel nicht benutzt und mich auch sonst keiner unerlaubten Hilfsmittel bedient habe.

Danksagung

Frau Ass. Prof. Dr. Doris Groß (Montanuniversität Leoben) möchte ich für jede erdenkliche und professionelle Unterstützung und die vielen anregenden Diskussionen danken. Ihr kompetenter Rat und ihre Hilfe trugen maßgeblich zum Gelingen dieser Arbeit bei.

Mein besonderer Dank gilt auch Herrn Prof. Dr. Reinhard F. Sachsenhofer (Montanuniversitaet Leoben). Viel habe ich von seinen umfangreichen Kenntnissen in der Erdölgeologie profitiert, oft in kritisch-konstruktiven Auseinandersetzungen.

Herr Dr. Lorenz Scheucher (Betreuer der RAG) gewährte mir bei der Planung und Durchführung meiner Untersuchungen, ebenfalls bei der Auswahl und Auswertung der Proben sachkundige, erfahrene und wertvolle Unterstützung.

Das Entgegenkommen des FFG-Bridge Projekts 836527 hat mir den großzügigen finanziellen und zeitlichen Rahmen verschafft, diese Studie zu machen.

Für die Bereitstellung des Probenmaterials und die Erlaubnis, meine Forschungsergebnisse zu publizieren, bedanke ich mich speziell bei der Rohoel-Aufsuchungs AG.

Zu großem Dank bin ich dem Team Herrn Dr. Hans Gert Linzer, Herrn DI Alan Reingruber, Frau DI Wilma Troiss und Herrn Dr. Werner Tschelaut verpflichtet. Ihre wertvollen Diskussionsbeiträge sind meiner Dissertation zugutegekommen.

Hilfreiche und fachkundige Beratung gewährten mir Herr Ass. Prof. Dr. Rainhard Gratzer (Montanuniversität Leoben), Frau Prof. Dr. Susanne Gier, Frau Dr. Stefanie Neuhuber und Prof. Dr. Patrick Meister (Universität Wien).

Für die technische Anleitung bei:

- der Dünnschliffpräparation Frau Sabine Feuchter (Montanuniversität Leoben)
- dem Röntgendiffraktometer Herrn Franz Seidl (Montanuniversität Leoben)
- der Mikrosonde Frau Dr. Federica Zaccarini (Montanuniversität Leoben)
- dem Rasterelektronenmikroskop Herrn Peter Onuk, MSc. (Montanuniversität Leoben)
- der Kathodenlumineszenz Herrn Dr. Dieter Mader (Universität Wien)

Meinen Lebenspartner, Dr. Dumitru Sarca, und meinen Eltern, Mag. Ilse Grundtner-Fend und Dr. Franz Grundtner, schufen eine schützende Atmosphäre aus Wohlwollen und Anteilnahme, die zum Gelingen dieser Arbeit beitrug.

Zusammenfassung

Das Hauptziel dieser Studie ist es einen Einblick in Gesteins-Fluid Interaktionen in Kohlenwasserstoff-Speichergesteinen zu erhalten. Die Effekte der Gasbildung auf die Diagenese werden am Beispiel von Speichergesteinshorizonten im nördlichen Vorlandbecken der Alpen untersucht.

Der österreichische Anteil des Vorlandbeckens beinhaltet jurassische bis miozäne Sedimente und zwei Kohlenwasserstoff-Systeme: Unteroligozäne Muttergesteine generierten Öl und thermogenes Gas, das in oberkretazischen und eozänen Speichergesteinen gespeichert ist. Mikrobielles Gas befindet sich innerhalb der oligozänen-miozänen Schichtfolge. Neue geochemische Daten deuten auf eine Mischung von mikrobiellen und thermogenen Kohlenwasserstoffen in allen Horizonten hin.

Für ein besseres Verständnis der Diagenesegeschichte wurden 180 Kernproben (Tiefe: 600 - 2300 m) mittels optischer Licht-, Kathodolumineszenz-, Mikrosonden- und Rasterelektronen-Mikroskopie untersucht. Zusätzlich wurde röntgendiffraktometrisch die Mineralogie qualitativ und semi-quantitativ ausgewertet. Die stabilen Kohlenstoff- und Sauerstoffisotopen-Verhältnisse wurden an karbonatischen Zementen gemessen. Petrophysikalische Daten wurden von RAG zur Verfügung gestellt. Poröse wasser- oder kohlenwasserstoffführende und dichte Sandsteine innerhalb der Reservoirhorizonte wurden untersucht.

Die Speichergesteine des thermogenen Kohlenwasserstoff-Systems sind oberkretazische seichtmarine Subarkosen und eozäne fluviatile bis seichtmarine lithische Arkosen. Diese weisen Zemente auf, die während der Eo-, Meso- und Telogenese gebildet wurden.

Eogenese – Die eogenetischen Prozesse sind von den Ablagerungsbedingungen und dem primären mineralogischen Eintrag beeinflusst. Tonmineralzement bildete sich durch die Zersetzung von Feldspäten und Phyllosilikaten und ist die dominante authigene Phase. Eine Fülle an Glaukonit-Pellets bildete sich in Kreide-Sandsteinen. Mikrobielles Gas (CH_4, CO_2) wurde durch die Metabolisierung von organischer Materie in eingeschalteten Tonen generiert. Das mikrobiell produzierte CO_2 wurde in Karbonatminerale eingebaut. Dieser Zement bildete sich mit säuliger (Cc I), mikritischer (Cc II), blockig/homogener (Cc III) oder poikilitischer (Cc IV) Morphologie aus. Die Karbonatausfällung ging mit der teilweisen Lösung von siliziklastischen Komponenten einher. Die $\delta^{13}C$ Werte der Karbonatzemente (Cc I - Cc III) der porösen Sandsteine sind im Bereich von -6,7 bis +3,3‰ [VPDB] und die $\delta^{18}O$

Werte im Bereich von -10,2 bis -4,3‰, vergleichbar mit Isotopiewerten von marinen Karbonaten. Leichtere $\delta^{18}O$-Verhältnisse der eozänen fluviatilen und tidalen Sandsteine spiegeln das nicht-marine Milieu wider.

Mesogenese – Einige Sandsteinlagen wurden stark mit Karbonat zementiert (Cc III, (Cc IV)). Basierend auf den Isotopenwerten können zwei Typen unterschieden werden: (i) Kalzitzement mit leichtem Kohlenstoff ($\delta^{13}C$: -32,7‰) und geringer Mg-Anreicherung bildete sich während der „fortgeschrittenen“ Sulfatreduktion, (ii) isotopisch schwerer Zement ($\delta^{13}C$: +8,7‰) mit gering erhöhten Fe-Gehalten bildete sich während der Karbonatreduktion.

Telogenese – Durch den Einfluss von meteorischem Wasser kam es in porösen, marinen Sandsteinen zur teilweisen Korrosion von Mineralen (Feldspäte, Karbonate) und zu spätem Kaolinit-Wachstum. Zudem wurde die Isotopie der eogenetischen Karbonatzemente überprägt ($\delta^{18}O$: -23,9 bis -9,4‰).

Die oligozänen-miozänen Sedimente des mikrobiellen Kohlenwasserstoff-Systems wurden im tiefmarinen Bereich abgelagert. Die Porenfüllung der lithischen Arkosen bis Lithareniten setzt sich aus eogenetischen Zementen zusammen (Cc I - Cc III, Dolomit), die sich durch Korrosionsspuren auszeichnet. Ihre Isotopenzusammensetzung ist ähnlich mariner Karbonate ($\delta^{13}C$ +1,1‰, $\delta^{18}O$ -5,3‰). Stark zementierte Zonen (Cc III) bildeten sich entlang des Gas-Wasser-Kontakts während der Telogenese. Zemente dieser Horizonte sind gering abgereichert an ^{18}O ($\delta^{18}O$: -8,0‰).

Abstract

The main goal of the present study is to gain insights into rock-fluid interactions in hydrocarbon reservoir rocks. The effects of gas generation on the diagenesis are studied using the example of reservoir rocks from different stratigraphic horizons in the northern foreland basin of the Alps.

The Austrian part of the foreland basin comprises Jurassic to Miocene sediments and two petroleum systems: Lower Oligocene source rocks generated oil and thermogenic gas, which is trapped in Upper Cretaceous and Eocene reservoir rocks. Microbial gas is present within Oligocene-Miocene strata. New geochemical data suggests a mixture of microbial and thermogenic hydrocarbons in all horizons.

For a better understanding of the diagenetic history, 180 core samples from 600 to 2300 m depth were investigated by optical light-, cathodoluminescence-, microprobe-, and scanning electron microscopy. Further, the mineralogical composition was analysed qualitatively and semi-quantitatively by X-ray diffractometry. Stable isotope ratios of carbon and oxygen were measured on calcitic cements. Petrophysical data were provided by RAG. Porous water- or hydrocarbon-bearing as well as low permeable sandstones within the reservoir horizons were investigated.

The reservoir rocks of the thermogenic petroleum system are Upper Cretaceous shallow marine subarkoses and Eocene fluviatile to shallow marine lithic arkoses. They contain cements, which were formed during eo-, meso- and telogenesis.

Eogenesis – The eogenetic processes were controlled by the depositional environment and primary mineralogical input. Clay mineral cement is the dominant authigenic phase and formed by disintegration of feldspar and phyllosilicate minerals. Abundant glauconite pellets developed within Cretaceous sandstones. Microbial gas (CH_4 and CO_2) was generated by metabolization of organic matter in intercalating shales. The microbial CO_2 was incorporated into carbonate minerals, which formed with columnar (Cc I), microcrystalline (Cc II), blocky/homogenous (Cc III) and later poikilitic (Cc IV) morphology. Carbonate precipitation was accompanied by partial dissolution of siliciclastic components. The $\delta^{13}C$ values of carbonate cements (Cc I - Cc III) range from -6.7 to +3.3‰ [VPDB] and the $\delta^{18}O$ values from -10.2 to -4.3‰ [VPDB], comparable to the isotopic composition of marine carbonates. Lighter $\delta^{18}O$ values of Eocene fluviatile to tidal sandstones reflect the non-marine setting.

Mesogenesis – Some sandstone layers were strongly cemented with carbonate (Cc III, (Cc IV)) during the mesogenetic stage. Based on the isotopic composition, two types can be distinguished: (i) calcite cement with light carbon isotopy (δ^{13}C: -32.7‰) and slight Mg-enrichment formed during "advanced" sulfate reduction, (ii) isotopically heavy cement (δ^{13}C: +8.7‰) with slightly elevated Fe contents formed during carbonate reduction.

Telogenese – An influx of meteoric water caused partial mineral corrosion (feldspar, carbonate) and late kaolinite growth in porous, laterally continuous marine sandstones. Additionally, isotope ratios of eogenetic carbonate cements were overprinted (δ^{18}O: -23.9 to -9.4‰).

The Oligocene-Miocene sediments of the microbial petroleum system were deposited in a deep-marine setting. The pore filling of these lithic arkose to litharenites consists of eogenetic cements, (Cc I - Cc III, dolomite), which show corrosion marks. Their isotopic composition is similar to marine carbonates (δ^{13}C: +1.1, δ^{18}O -5.3‰). Sediments near the gas-water contact in Oligocene-Miocene sediments are often strongly cemented by calcite (Cc III), which precipitated during the telogenetic stage. Cements of these horizons are slightly depleted in ^{18}O (δ^{18}O: -8.0‰).

Table of Contents

1. Introduction

1.1. Introduction to the topic / Study aims

Petroleum is the leading source of energy. Despite of the growth of renewable energy forms, hydrocarbon exploration and production are still of prime importance. The reservoir quality and production behavior is strongly controlled by the depositional environment and diagenetic history of reservoir rocks.

Diagenesis looks at questions like the evolution of reservoir rocks, focusing on the decrease of primary porosity, and the development of secondary porosity. In general, the reservoir geometry and arrangement and the influence of detrital minerals on pore space evolution are well understood (Bjørlykke, 2014). For example, Groß et al. (2015a) showed that diagenetic processes are affected by primary input. However, the rock-fluid interaction in hydrocarbon systems and the influence of gas and oil on the formation of authigenic minerals are still a matter of discussion (e.g. Curtis, 1978; Surdam et al., 1989; Lundegard et al., 1992; Prochnow et al., 2006; Gorenc & Chan, 2015). The impact of fluids, especially of hydrocarbons, on pore space is discussed controversially (Bjørlykke et al., 1989; Van Berk & Schulz, 2015).

A strong relationship between carbonate precipitation and microbial gas generation can be demonstrated (e.g. Hesse & Schacht, 2011). Specific mineral parageneses are used to retrace changes in the hydrogeochemical conditions over time. Thus, the formation and dissolution of mineral phases within reservoir rocks are an important archive for reconstruction of changes in pore fluid composition and pore space development.

In the present study the diagenetic history of reservoir sandstones, filled with microbial and thermogenic hydrocarbons, in the Austrian part of the North Alpine Foreland Basin (NAFB) is investigated. To achieve a better understanding of the relationship between gas generation and carbonate formation, samples from gas-, oil- and water-bearing sandstones were studied and their mineralogy, petrology and diagenetic history were determined.

Oil and gas exploration in the Austrian part of the NAFB, also referred to as the (Alpine) Molasse Basin, commenced in the 1950ies. In 1960 RAG (Rohoel-Aufsuchungs AG) started to focus on gas production. In addition, many oil fields, more than 60 gas fields were discovered and RAG still remains successful in finding new fields (Veron, 2005). Therefore, a large amount of information of the subsurface, based on seismic and well information, exists. This provides an ideal base for research on basin history and hydrocarbon systems.

Within the study area – the Austrian sector of the NAFB - two hydrocarbon systems can be distinguished (e.g. Malzer et al., 1993; Wagner, 1996, 1998; Sachsenhofer & Schulz, 2006; Pytlak et al., 2016; in press):

- Thermogenic hydrocarbon system:
  This system is defined by Lower Oligocene source rocks and Cretaceous and Eocene reservoir rocks.
- Microbial gas system:
  Upper Oligocene and Lower Miocene sediments are both source and reservoir rock for microbial in-situ generated gas.

New geochemical data indicates a mixture of biogenic and thermogenic hydrocarbons in Oligocene-Miocene strata (Reischenbacher & Sachsenhofer, 2011; Pytlak et al., 2016; in press).

The NAFB provides a unique opportunity to study the effects of detrital sediment input, depositional environment, organic matter metabolization (including gas genesis) and hydrocarbon alteration on the diagenetic history. This is also the main aim of the present contribution. Apart from the understanding of fundamental processes, this research should also contribute to a better prediction of the distribution of pore space in the reservoir rocks.

The present study was supported by the FFG Bridge-Project 836527. The influence of gas generation, migration and alteration on reservoir rocks is investigated. The emphasis is to develop a model that explains the presence of authigenic minerals present today by using precipitation and dissolution reactions in relation to gas generation.

1.2. Previous studies of the NAFB

An overview of essential studies on the geology and the petroleum potential of the Austrian part of the NAFB are given below:

Fundamental early studies on geology and petroleum potential of the Austrian part of the NAFB were published by Aberer (1958), Janoschek (1959, 1966), Braumüller (1961) and Kollmann (1977). The main reservoir horizons were described by Wagner (1980) and Malzer (1981), whereas the distribution of the oil- and gas-fields in the study area was characterized by Polesny (1983). Wessely et al. (1981) described the lithostratigraphy of Cretaceous rocks in the easternmost part of the study area (OMV concession area), whereas an overview of the Mesozoic and Paleogene evolution of the NAFB has been provided by Nachtmann & Wagner (1987).

Malzer (1993), Malzer et al. (1993) and Wagner (1996) summarized the knowledge of the geological evolution and the petroleum geology of the Austrian part of the NAFB. Wagner (1998) focused on tectono-stratigraphy and hydrocarbons in the basin and introduced the currently used stratigraphic nomenclature. Malzer et al. (1993) and Wagner (1996, 1998) in addition emphasize the presence of two petroleum system: a thermogenic petroleum system based on Lower Oligocene source rocks with Cenomanian and Eocene reservoir units and a microbial petroleum system in Oligocene-Miocene reservoir rocks. Schmidt & Erdogan (1996) used numeric models to describe hydrocarbon generation beneath the Alps as well as northward migration of oil.

During this time, Nachtmann studied fault-related traps (Nachtmann, 1995a) and described the major Sattledt and Trattnach oil fields (Nachtmann, 1989, 1995b). The Trattnach field was re-evaluated by Groß et al. (2015b). The sedimentological characteristics of the Eocene Lithothamnium Limestone were described by Rasser (2000) and Rasser & Piller (2004).

The structure and kinematics of the complex southern margin of NAFB (Molasse imbricates) were described by Hinsch (2013).

Studies published since 2000 provided valuable new information on the thermogenic and microbial petroleum systems:

Thermogenic petroleum system - Depositional environment and source rock potential of Lower Oligocene source rocks (Schöneck Formation, Dynow Formation, Eggerding Formation), considered the main source for thermogenic hydrocarbons, were studied by Schulz et al. (2002, 2004), Schulz (2003), Sachsenhofer & Schulz (2006) and Sachsenhofer et al. (2010). Gratzer et al. (2011) and Bechtel et al. (2013) investigated facies and maturity of oil samples using biomarker and isotope parameters and established oil-oil and oil-source rock correlations. Hydrocarbon alteration (asphaltene precipitation, biodegradation) has been described by Sachsenhofer et al. (2006) and Gratzer et al. (2011). Gusterhuber et al. (2012) quantified the Miocene-Pliocene uplift of the Austrian part of the NAFB. This information was integrated into numeric models of hydrocarbon generation and migration (Gusterhuber et al., 2013; 2014). Pytlak et al. (2016) studied the molecular and isotopic composition of gas and proved the presence of mixed thermogenic and microbial gas.

Microbial petroleum system - Based on 3D seismic data, new insights into the Oligocene-Miocene sedimentary evolution and the architecture of Oligocene-Miocene reservoir rocks for microbial gas were gained in the 2000s. The deep-marine Puchkirchen channel (as part of the Puchkirchen Group) was first recognized by Linzer (2001, 2002, 2009) and De Ruig (2003) and later described by Hubbard et al. (2005, 2008), Hubbard (2006), De Ruig & Hubbard (2006), Lonergan & Derksen (2007), Stright & Bernhard (2007), Hinsch et al. (2007), Hinsch (2008), Covault et al. (2009), and Masalimova et al. (2015). Süss et al. (2008) established a sequence stratigraphic model for the Puchkirchen trough. The sedimentation of the Burdigalian Hall Formation was described by Strauss (2008), Borowski (2006) and Grunert et al. (2012). Grunert et al. (2015) provided a new stratigraphic model for Oligocene-Miocene succession (Puchkirchen Group, Hall Formation).

Microbial gas generation in the Upper Puchkirchen Formation was described by Schulz et al. (2009). They investigated potential source rocks (organic matter-rich mudstones; see also Belaed, 2007) and reservoir rocks (turbiditic sandstones). Schulz & Van Berk (2009) retraced gas generation and the filling history of the Atzbach-Schwanenstadt field by applying hydrogeochemical modelling techniques. Pytlak et al. (in press) investigated gas samples from Oligocene-Miocene reservoirs and verified the mixing of microbial gas with upward migrated thermogenic hydrocarbons (see also Reischenbacher & Sachsenhofer, 2011).

Studies on diagenesis - Several diagenetic studies on rocks in the Austrian part of the NAFB have carried out:

- Investigations of the diagenetic evolution of pelitic rocks with an Eocene to Miocene age were carried out by Gier (1999, 2000) and Gier et al. (1998). Amongst others, they examined clay mineralogy and organic diagenetic processes in the Schöneck Formation.
- Bottig (2008) and Bottig et al. (2016) studied the influence of gas storage on the growth of clay minerals in sandstones of the Puchkirchen Group at the southern slope (Haidach field).
- A sediment petrological and diagenesis study was conducted by Scheucher et al. (2012) using samples with a Rupelian age from three wells.
- Facies and diagenesis of Cenomanian sandstones were investigated by Schnitzer (Schnitzer et al., 2012; Schnitzer, 2013) and by Samsu (Samsu, 2015).
- Early results of the present project were published by Groß et al. (2015a) who investigated the effect of pore filling on porosity and permeability of reservoir sandstones from different stratigraphic units.

1.3. Diagenesis

The term "diagenesis" is defined as the sum of all physical, chemical and biological processes, which influence each other and transform loose sediment into consolidated rock (e.g. Füchtbauer, 1988; Einsele, 2000; Bahlburg & Breitkreuz, 2004; Flügel, 2010; Ulmer-Scholle et al., 2014). Thereby the primary sedimentary characteristics, such as mineral composition, texture, porosity and permeability, are modified (Tucker, 1985). It comprises the time interval of the final sedimentary deposition to the onset of metamorphism (e.g. Füchtbauer, 1988).

The boundaries of weathering/diagenesis and diagenesis/metamorphism are obliterated and cannot always be discriminated easily (Füchtbauer, 1988; Ali et al., 2010). Weathering is defined as mechanical, chemical and biological treatment of the rock and diagenesis as rock lithification (e.g. Einsele, 2000; Selley, 2000; Bahlburg & Breitkreuz, 2004; Flügel, 2010). The demarcation is dependent on the availability of solvents. Metamorphism is reached at temperatures above 150 - 200°C (Tucker, 1985) or 250 - 300°C (Nichols, 2009). The relationship of depth and temperature is illustrated in Fig. 1. Considering normal geothermal gradients, diagenesis ends and metamorphosis starts in a depth of approximately 5000 m at 250 - 300°C (Nichols, 2009).

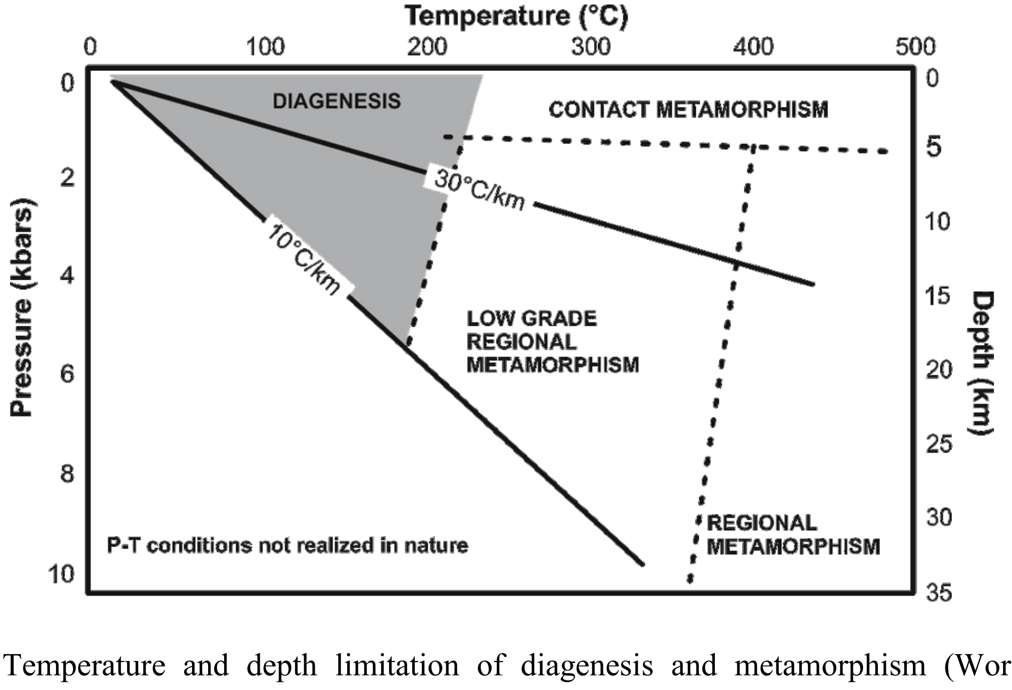

Fig. 1 Temperature and depth limitation of diagenesis and metamorphism (Worden & Burley, 2003).

In general, lithification is a result of compaction and cementation (Bahlburg & Breitkreuz, 2004). The succession of the trend of consolidation of the sediment is shown in Fig. 2:

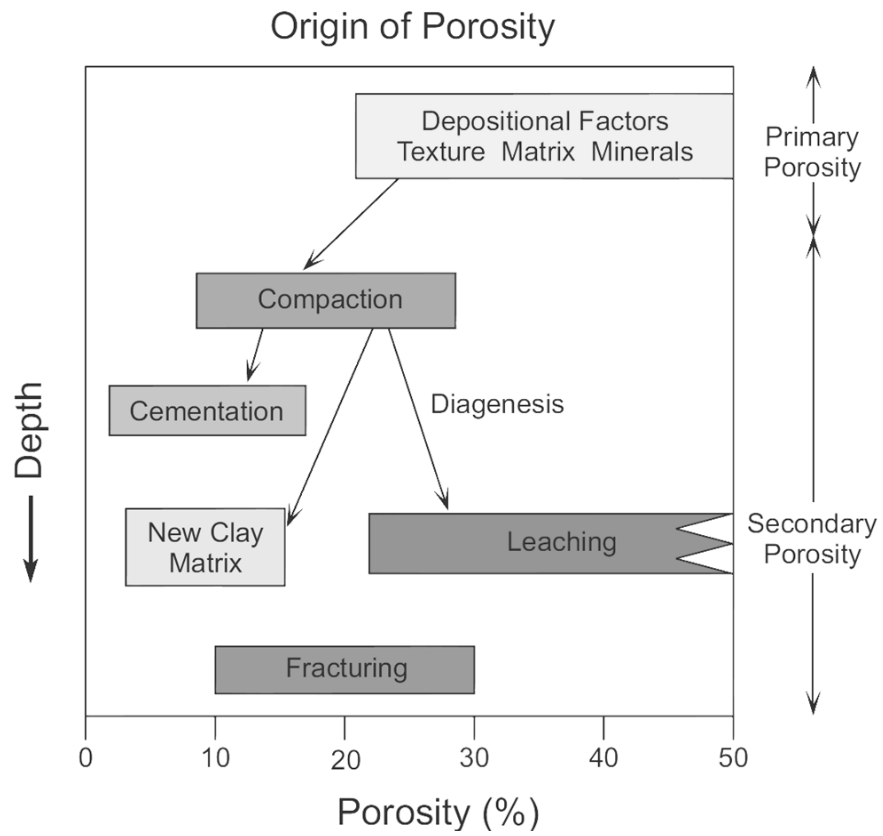

Fig. 2 General processes of the sediment right after deposition leading to consolidation (Slatt, 2006).

The reservoir quality is controlled by facies and diagenesis. Factors, which influence the initial situation, are grain size, sorting, depositional structures and stratigraphic anisotropy and lithological intercalation (Brenner et al., 1991). Based on the initial conditions, factors, which affect reservoir quality during burial, are temperature, pressure and fluid chemistry (Selley, 2000; Worden & Burley, 2003; Flügel, 2010).

There are some factors which impede further mineral formation and thus porosity decrease, such as eogenetic overgrowths on mineral surfaces (Ulmer-Scholle et al., 2014). In addition, diagenesis is also affected by the (partial) dissolution of minerals and the generation of secondary porosity.

An overview of secondary porosity phenomena is exemplified in Fig. 3 after Füchtbauer (1988):

a: Cement relicts
b: Oversized pores
c: Feldspar dissolution
d: Corroded grains
e: Fractured grains

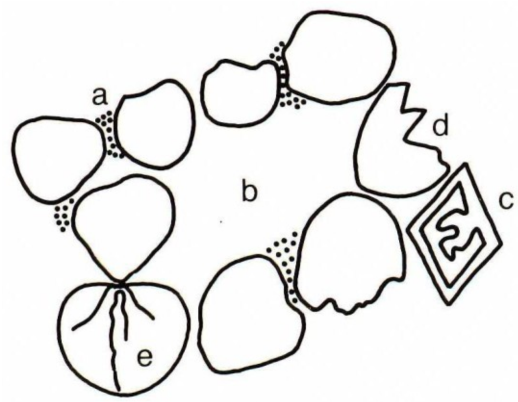

Fig. 3 Types of secondary porosity (Füchtbauer, 1988).

1.3.1. Controlling factors for diagenesis

Diagenesis includes a wide range in (re-)actions of chemical, physical, biological processes and everything else within these processes. Consequently, diagenesis is controlled by an immense number of factors. Here, the most prominent controlling factors are discussed after Brenner et al. (1991) and Worden & Burley (2003):

The fluid chemistry is influenced by the dissolution and precipitation of minerals, which cause a change in the hydrogeochemical equilibrium. Vice versa, disequilibrium is visible by mineral solution and formation. Further, the fluid transport of solutes is dependent on the permeability.

Primary control

External factors, involving the hinterland, climate, depositional environment and transport distance, control the mineralogical composition and grain size. This primary sedimentary input is decisive for the subsequent processes (Fralick & Barrett, 1995; Brenner et al., 1991).

In addition, the geometry of the deposited sediment body and in this way also the type of the neighboring rock, and the contact to it, is also important in relation to the fluid communication (Brenner et al., 1991).

The control of facies for the subsequent diagenetic relations on authigenic clay mineral formation and thus on reservoir quality is illustrated after Worden & Morad (2003) in Fig. 4.

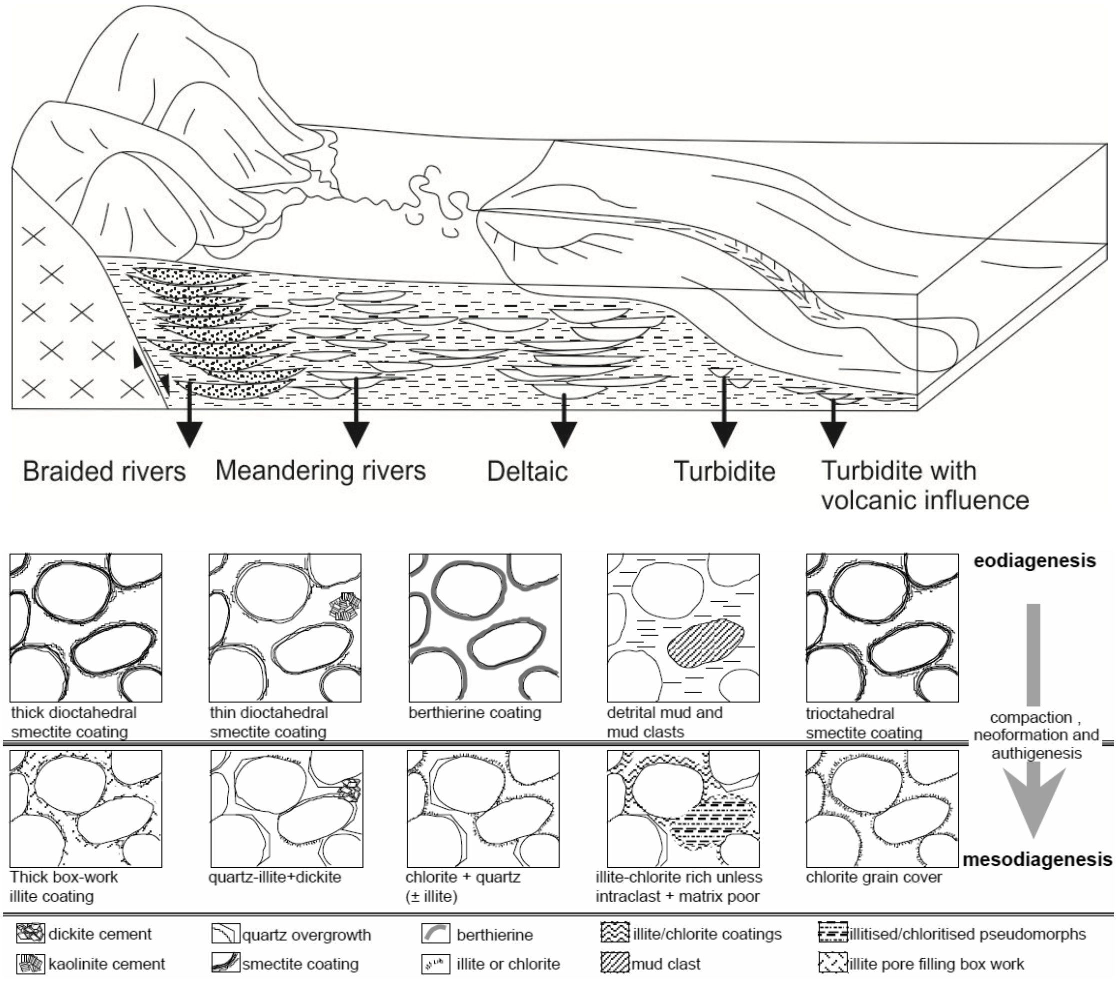

Fig. 4 The relationship of facies and authigenic mineral growth during eogenesis and mesogenesis (Worden & Morad, 2003).

Secondary control

After deposition of the sediment, diagenetic processes are controlled by fluid flow, chemical composition of the fluid and of the minerals, temperature and pressure during burial (e.g. Einsele, 2000; Worden & Burley, 2003; Ali et al., 2010; Flügel, 2010). Further, the retention time plays a significant role in the controlling factors of diagenesis. Also, the availability of reactants, thermodynamic stability of mineral phases and saturation level of the pore fluids are important for the rate of diagenetic processes (MacInnis & Brantley, 1992; Flügel, 2010). The presence of water is essential for diagenetic reactions. Water acts as medium for mass transport and enables mass transfer even in the deeper parts of burial (Ali et al., 2010). Fig. 5 shows different diagenetic pore water types.

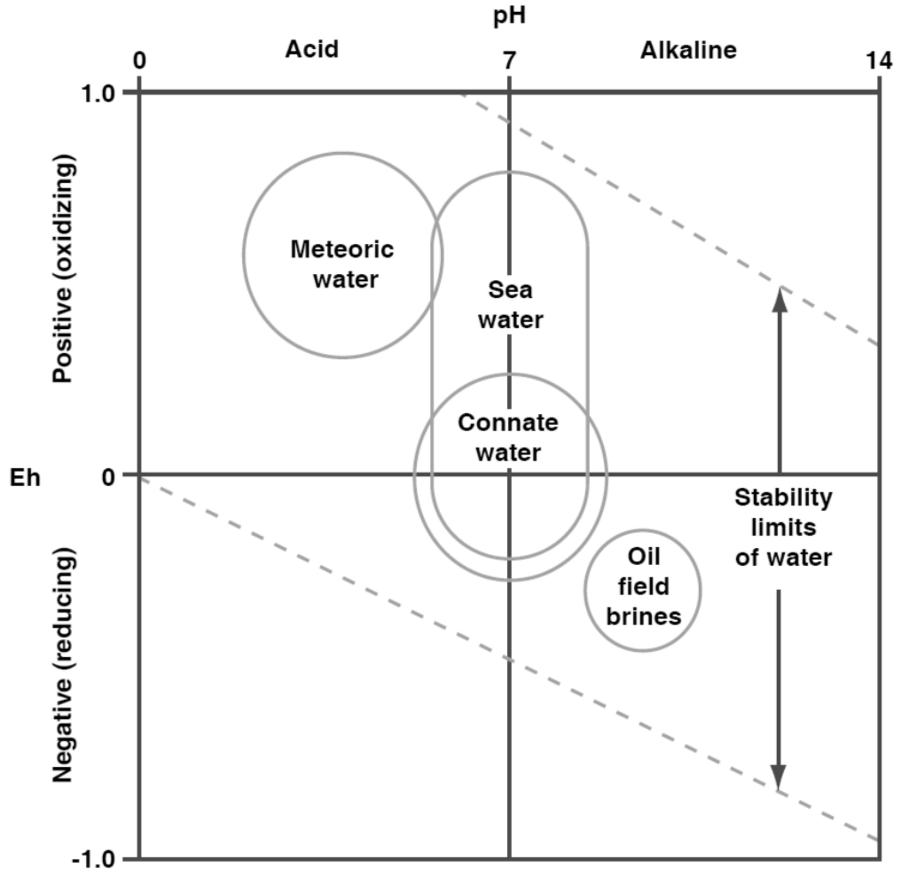

Fig. 5 Diagenetic pore water types plotted in Eh-pH diagram (Selley, 2000).

Besides of water, gas and oil may be present as pore fluids as well. Compared to the water-bearing horizons, diagenetic reactions are slowed downed considerably in zones filled with hydrocarbons (Hesse, 1986). The formation of faults and thus improvement of directional permeability along conductive zones facilitates fluid flow and exchange between systems. Also basin movement (e.g. uplift) causes fluid drive. In this context, the formation, migration and emplacement of hydrocarbons play an important role in diagenetic evolution in matters of reaction rates. It is also necessary to differentiate if diagenesis happens in an open or closed system.

Temperature and pressure increase with depth and thus influence fluid chemistry as well. This is evident in the formation of characteristic minerals. Although they show a general trend with depth, an exact relation with a specific depth stage depends on the basin type and its geothermal gradient (Hesse & Schacht, 2011). Pressure in the diagenetic realm, comprises lithostatic and fluid pressure (Worden & Burley, 2003). Temperature is controlled by the geothermal gradient of the basin. Temperature and pressure are also essential for the maturation of source rocks.

1.3.2. Subdivision of diagenesis

The sequence of diagenetic processes with time is subdivided into distinct regimes, depending on their stage of burial. These stages are differentiated by changes in the diagenetic setting, such as temperature, pressure and fluid chemistry visible in mineral precipitation and dissolution (Choquette & Pray, 1970; Ulmer-Scholle et al., 2014):

Eogenesis

Eogenesis comprises diagenetic processes which happen right after deposition (syn-, postdepositional) of the sediment. This first phase is strongly influenced by the depositional environment, like content of detrital mineral input. These processes are affected by changes in acidity and redox conditions, besides, also by temperature, pressure and hydrochemistry (Worden & Burley, 2003). A high amount of solvents is available, because the sediment is rich in primary meteoric or sea water. This is a prominent support for ion delivery and removal.

Mesogenesis

The transition of eogenesis to mesogenesis is indistinct, because of interdependent processes. The mesogenesis is uncoupled from the primary meteoric fluid system (Worden & Burley, 2003). In general, this stage is characterized by porosity destruction and restricted water supply, and therefore the source of new solvents for geochemical exchange is limited (Einsele, 2000). In addition, the formation water is hydrochemically modified and has a higher mineralization in comparison to the original water (Worden & Burley, 2003).

Telogenesis

Telogenesis describes diagenetic processes during the uplift of the sediment package (Worden & Burley, 2003; Ulmer-Scholle et al., 2014). This uplift movement facilitates a newly influence to the hydrogeochemical system of meteoric water from the surface (Worden & Burley, 2003). Accordingly, disequilibrium is generated, which may result in mineral precipitation and dissolution. Obviously, this stage may be absent, since uplift does not happen in every basin.

1.3.3. Stages of bacterial oxidation of organic matter during diagenesis

After sedimentation, organic substances get reduced by bacterial activity (Schulz et al., 2009; Hesse & Schacht, 2011). Organisms use them for energy generation. Thereby, degradation of organic chemical compounds follows the pathway after Gibbs free energy (ΔG°) which is available for organisms (Froelich et al., 1979). This metabolic process proceeds throughout the diagenesis. Especially, the eogenesis is affected. Caused by the degradation of organic matter, pH and Eh conditions of the pore water are modified. The significance of organic matter metabolization for authigenic mineral formation is discussed by Schulz et al. (2009) and Schulz & Van Berk (2009).

In general, six possible stages are described for bacterial organic matter oxidation. They are differentiated by their oxidizing agents, which ideally succeed one other at a temporal distance. This could be also used as equivalent for depth zonation (Hesse & Schacht, 2011). The reactions of the pathway stages of organic matter oxidation are described by Froelich et al. (1979). The processes and products in sediments of organic matter metabolization are summarized in Fig. 6.

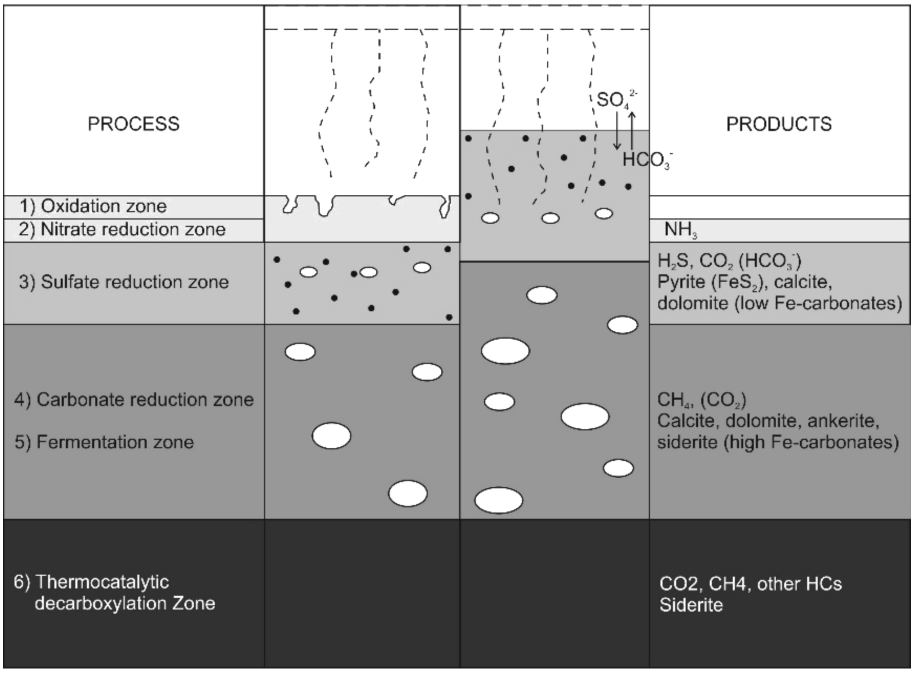

Fig. 6 Six stages of eogenetic organic matter oxidation, characterized by their processes and products for intermediate sedimentation in a ventilated basin (left) and for high sedimentation rate in a stagnant basin (right) (modified after Claypool & Kaplan, 1974; Bjørlykke, 1983; Hesse, 1986; Curtis, 1977; Einsele, 2000; Hesse et al., 2004).

Oxidation Zone

The uppermost part of the sediment column is characterized by aerobic bacterial activity. These organisms degrade organic matter with the help of O_2. Aerobic bacteria are not the only contributors towards degradation, but the most effective ones, because the rate of substance exchange is reliant on the surface area of bacteria. After the consumption of oxygen, facultative aerobe bacteria take over. These microorganisms live in oxygen and in oxygen-poor settings (Hesse & Schacht, 2011).

The chemical reactions are very complex and not all of these processes at this zone can be recorded. Therefore, a simplified reaction is given in Eq. (1) (Froelich et al., 1979):

$$Oxidation\ by\ freely\ dissolved\ O_2\ (aerobic\ respiration)$$

$$(CH_2O)_{106}(NH_3)_{16}(H_3PO_4) + 138\ O_2 \rightarrow 106\ CO_2 + 16\ HNO_3 + H_3PO_4 + 122\ H_2O \tag{1}$$

The equation is simplified to an overall reaction in Eq. (2), whereas CH_2O stands for the sum of the chemical composition of organic substances (Pettijohn et al., 1987; Hesse & Schacht, 2011):

$$CH_2O + O_2 \rightarrow CO_2 + H_2O \tag{2}$$

The thickness of the oxidation zone depends on the oxygen concentration. In a stagnant basin this zone is missing. In contrast, it can reach a thickness of some 100 m in a pelagic setting (Hesse & Schacht, 2011).

Nitrate reduction Zone

When the oxygen concentration $[O_2]$ is < 0.5 ml O_2/l H_2O, the nitrate-reduction zone takes over (Devol, 1978). This zone is also named as the zone of suboxic diagenesis, indicating that bacterial processes take place in a predominant dysaerobic regime at this zone (Hesse & Schacht, 2011). The drop of the abundance of benthonic microorganism goes hand in hand with this change (Rhoads & Morse, 1971). First, the concentration of ammonia is increased by the aerobic respiration and decreased in the nitrate reduction zone after Eq. (3) and Eq. (4) (Froelich et al., 1979):

Nitrate reduction

$$(CH_2O)_{106}\,(NH_3)_{16}\,(H_3PO_4) + 94.4\,HNO_3 \rightarrow 106\,CO_2 + 55.2\,N_2 + H_3PO_4 + 177.2\,H_2O \tag{3}$$

$$\begin{aligned}(CH_2O)_{106}\,(NH_3)_{16}\,(H_3PO_4) &+ 84.8\,HNO_3 \\ &\rightarrow 106\,CO_2 + 42.4\,N_2 + 16\,NH_3 + H_3PO_4 + 148.4\,H_2O\end{aligned} \tag{4}$$

The nitrate reduction is accompanied with manganese and adjacent iron reduction. The electrochemical potential moves from positive to negative and enables the solution of Mn- and Fe-oxides and hydroxides by reduction. In that way, electron acceptors are formed to support nitrate oxidation (Froelich et al., 1979). Furthermore, alkaline conditions are induced, because of H^+ depletion (Hesse & Schacht, 2011).

The reaction pathways for these two transition metals are given in Eq. (5) for Mn^{2+} and Eq. (6) for Fe^{2+} (Froelich et al., 1979):

Manganese reduction

$$\begin{aligned}(CH_2O)_{106}\,(NH_3)_{16}\,(H_3PO_4) &+ 236\,MnO_2 + 472\,H^+ \\ &\rightarrow 236\,Mn^{2+} + 106CO_2 + 8N_2 + H_3PO_4 + 366\,H_2O\end{aligned} \tag{5}$$

Iron reduction

$$\begin{aligned}(CH_2O)_{106}\,(NH_3)_{16}\,(H_3PO_4) &+ 212\,Fe_2O_3\ (or\ 424\,FeOOH) + 848\,H^+ \\ &\rightarrow 424\,Fe^+ + 106\,CO_2 + 16\,NH_3 + H_3PO_4 + 530\,H_2O\ (or\ 742\,H_2O)\end{aligned} \tag{6}$$

Sulfate reduction Zone

After a further decrease in oxygen concentration, sulfate reduction commences in the sediment column below the nitrate reduction zone. Only a few types of bacteria can survive under these conditions, where toxic H_2S and HS^- are formed (Hesse & Schacht, 2011). The reaction of sulfate reduction after Froelich et al. (1979) is given in Eq. (7):

Sulfate reduction

$$\begin{aligned}(CH_2O)_{106}\,(NH_3)_{16}\,(H_3PO_4) &+ 53\,(SO_4)^{2-} \\ &\rightarrow 106\,CO_2 + 16\,NH_3 + 53\,S^{2-} + H_3PO_4 + 106\,H_2O\end{aligned} \tag{7}$$

The simplified equation for sulfate reduction is given with Eq. (8) (Pettijohn et al., 1987; Hesse & Schacht, 2011):

$$2\,CH_2O\ +\ SO_4{}^{2-}\ \rightarrow\ S^{2-} + 2\,H^{+} + 2\,HOC_3{}^{-} \tag{8}$$

Sulfate reduction is accompanied with Fe(III) oxides and hydroxides reduction. Fe(II) becomes free and undergoes chemical bonding with sulfides. Thus, ferrous sulfide (FeS) forms, which recrystallizes into pyrite (FeS_2) later (Einsele, 2000; Hesse & Schacht, 2011).

Compared to the general thickness of oxidation and nitrate-reduction zone, the sulfate-reduction zone is considerably thicker, as illustrated in Fig. 6.

Carbonate reduction Zone

When the concentration of oxygen is almost zero, the diagenetic setting passes over in the carbonate reducing and methane generating zone. As other reactants are depleted, carbon (C^{4+}) itself serves as substrate for further reduction for energy extraction. Carbonate species get produced during oxidation to sulfate reduction and provide new substance for reduction via oxidation. The equation of carbonate reduction is given in Eq. (9) (Froelich et al., 1979):

$$Carbonate\ reduction$$

$$(CH_2O)_{106}(NH_3)_{16}(H_3PO_4) \rightarrow\ 53\,CO_2 + 53\,CH_4\ +\ 16\,NH_3\ +\ H_3PO_4 \tag{9}$$

During this zone methane and carbon dioxide are produced (Eq. 9). Simultaneously, carbon dioxide gets reduced by methanogenic bacteria (Eq. 10):

$$8H + CO_2 \rightarrow CH_4 + 2H_2O \tag{10}$$

The temperature range of methane generating bacteria spans from 0 - 75°C (Zeikus & Wolfe, 1972). This does not mean, that a single strain of bacteria is active in the entire interval. Moreover, there is a complex interplay of different bacteria types, which are restricted to a certain temperature zone of some degrees only (Hesse & Schacht, 2011).

Fermentation Zone

The fermentation zone is characterized by the presence of fermentative bacteria. In this zone, the O_2 of the organic substances is used to reduce organic matter. According to Hesse & Schacht (2011), the fermentation zone belongs to the biogeochemical regime of the carbonate reduction zone, but follows below. Here, methane and carbon dioxide are also produced.

Thermocatalytic decarboxylation Zone (abiogenic)

Thermocatalytic decarboxylation is a process of abiogenic organic matter degradation. In this diagenetic zone organic compounds, like methane, carbon dioxide and other hydrocarbons, are produced. This zone is formed during telogenesis (Einsele, 2000).

At a temperature boundary of 75° to maximal 100°C the survival habit of bacteria is reached. Above these temperatures, only some types of bacteria exist. The inorganic oxidation of organic substances comprises reactions such as the decarboxylation of organic acids (Hesse & Schacht, 2011). The thermocatalysis ceases, when all organic substances for further reactions are exhausted (Einsele, 2000).

1.3.4. Implication of diagenetic zones on pore water chemistry

The above described diagenetic succession of biochemical zones can be traced by the evolution of mineral precipitation and dissolution in pore water. The concentration of compounds in the water is controlled by these processes. Their change with depth is shown in Fig. 7.

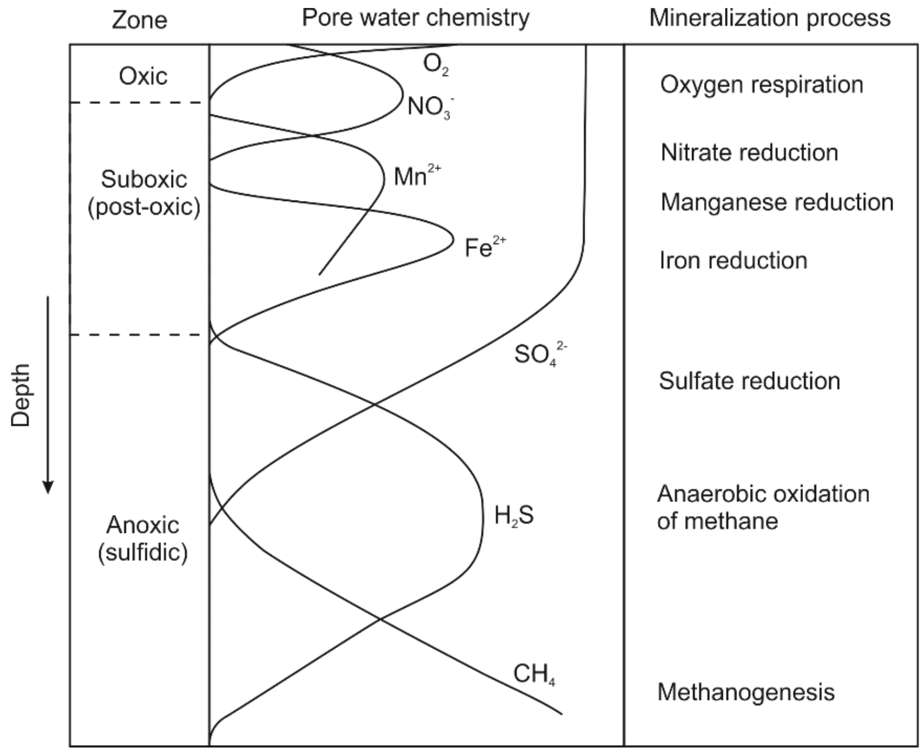

Fig. 7 Hydrochemical pore water evolution of the concentration of water components with depth correlated to the diagenetic zones in marine sediments (modified after Froelich et al., 1979; Berner, 1981; Jørgensen & Kasten, 2006).

The oxic zone is controlled by oxygen respiration. Consequently, the oxygen concentration decreases significantly. When oxygen is totally consumed, the setting gets suboxic and nitrate and manganese reduction take over. The concentration of iron decreases later in the deeper parts of the suboxic area. The considerable decrease in sulfate, dissolved in pore water, notifies the onset of the anoxic state. Within this zone hydrogen sulfide is produced. Below the sulfate reducing zone, methane is produced via carbonate reduction (Hesse & Schacht, 2011).

1.3.5. Implication of diagenetic zones on isotope fractionation

Within a sediment, different carbonate phases form at different stages of biochemical diagenesis and thus at different formation conditions. Stable isotope analysis can be used to identify the environment under which the mineral formed. For this study, authigenic carbonates are the key component to deduce the diagenetic succession of biochemical zonation. Thereby the carbon (C) and oxygen (O) isotopic composition of carbonates within the investigated sandstones are measured.

Three stable oxygen isotopes are present (^{16}O, ^{17}O, ^{18}O), but ^{17}O is negligible because of its low occurrence. The oxygen isotope ratio is given in the $\delta^{18}O$ ($^{16}O/^{18}O$) notation (Eq. 11):

$$\delta\ [‰\,] = \left[\frac{\left(\frac{^{18}O}{^{16}O}\right)_{sample}}{\left(\frac{^{18}O}{^{16}O}\right)_{standard}} - 1 \right] \times 10^3 \tag{11}$$

Carbon has two stable isotopes (^{12}C, ^{13}C). Their ratio is expressed as $\delta^{13}C = {}^{12}C/^{13}C$ (Eq. 12; Friedman & O´Neil, 1977; Stosch, 1999):

$$\delta\ [‰\,] = \left[\frac{\left(\frac{^{13}C}{^{12}C}\right)_{sample}}{\left(\frac{^{13}C}{^{12}C}\right)_{standard}} - 1 \right] \times 10^3 \tag{12}$$

In most cases, the initial conditions of diagenesis are those of sea water, which is therefore set as an initial reference point. For oxygen isotopes the “standard mean ocean water” (VSMOW; the “V” stands for Vienna) or the “Pee Dee Belemnite” (VPDB) serve as standard material. For carbon isotopes the VPDB is used as standard material (Stosch, 1999). These standard materials have formed at sea water conditions and are considered as reference points. Therefore, both the $\delta^{13}C$ and the $\delta^{18}O$ of a carbonate formed under marine condition is 0‰ [VPDB]. According to Dimitrakopoulus & Muehlenbachs (1987) $\delta^{13}C$ and $\delta^{18}O$ of marine carbonates range from -5 to +4‰ and from -5 to +3‰ [VPDB], respectively.

The initial isotope pool (e.g. sea water) is affected by diagenetic processes (Fig. 8). The dissolved carbonate species in the pore fluids (e.g. HCO_3^-) get fractioned by e.g. precipitation, dissolution, modification of mineral composition (recrystallization, metabolization) and mixing with other pools (e.g. meteoric influx). In general, $\delta^{13}C$ is comparatively stable during diagenetic processes, whereas $\delta^{18}O$ is more sensitive to exchange reactions (Aharon, 2000).

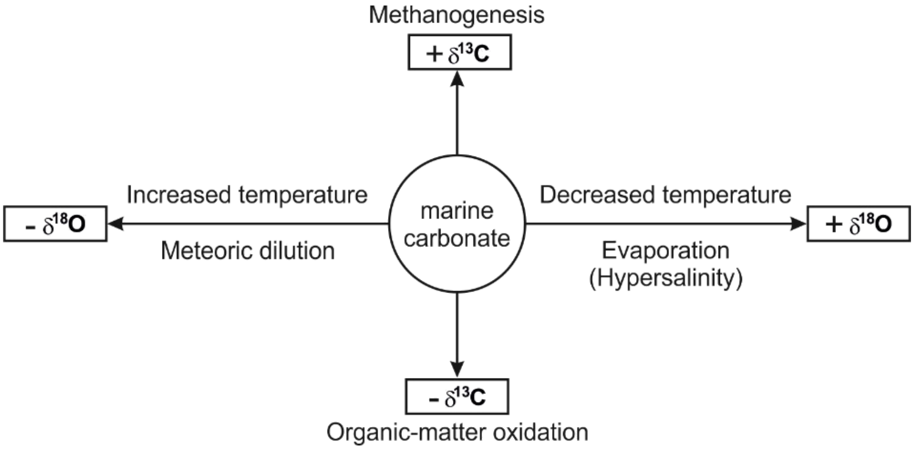

Fig. 8 Trends of stable carbon and oxygen isotopy affected by different diagenetic processes (modified after Allan & Wiggins, 1993)

Stable carbon isotopy - $\delta^{13}C$ of carbonate minerals may be strongly influenced by the incorporation of organic matter derived carbon. The initial $\delta^{13}C$ of HCO_3^- is modified by microbial metabolization of organic matter (Fig. 9; Hesse & Schacht, 2011):

- Bacterial oxidation has a low impact on the isotope fractionation.
- Sulfate reduction results in a progressive depletion of ^{13}C. $\delta^{13}C$ around -25‰ [VPDB] indicate advanced sulfate reduction.
- Methanogenesis (carbonate reduction and fermentation) is characterized by an increase in ^{13}C of HCO_3^-. This increase is explained by the intensified methane (and carbon dioxide) production, which causes strong isotope fractionation. Thereby, CO_2 enriched in ^{12}C is converted preferably into methane (Rosenfeld & Silverman, 1959), whereas the remaining CO_2 is enriched in ^{13}C resulting in positive $\delta^{13}C$ (+15 to +25‰) of HCO_3^- (Rayleigh distillation) (Curtis et al., 1972).

Stable oxygen isotopy - $\delta^{18}O$ of carbonate cements is affected by the isotopic composition of pore water. If the initial conditions are known (e.g. sea water composition), $\delta^{18}O$ ratios can be used to deduce changes in the formation water. The determining factors are the precipitation temperature and the isotopic composition of the formation water, which is strongly dependent on salinity variations (Friedman & O´Neil, 1977; Irwin et al., 1977).

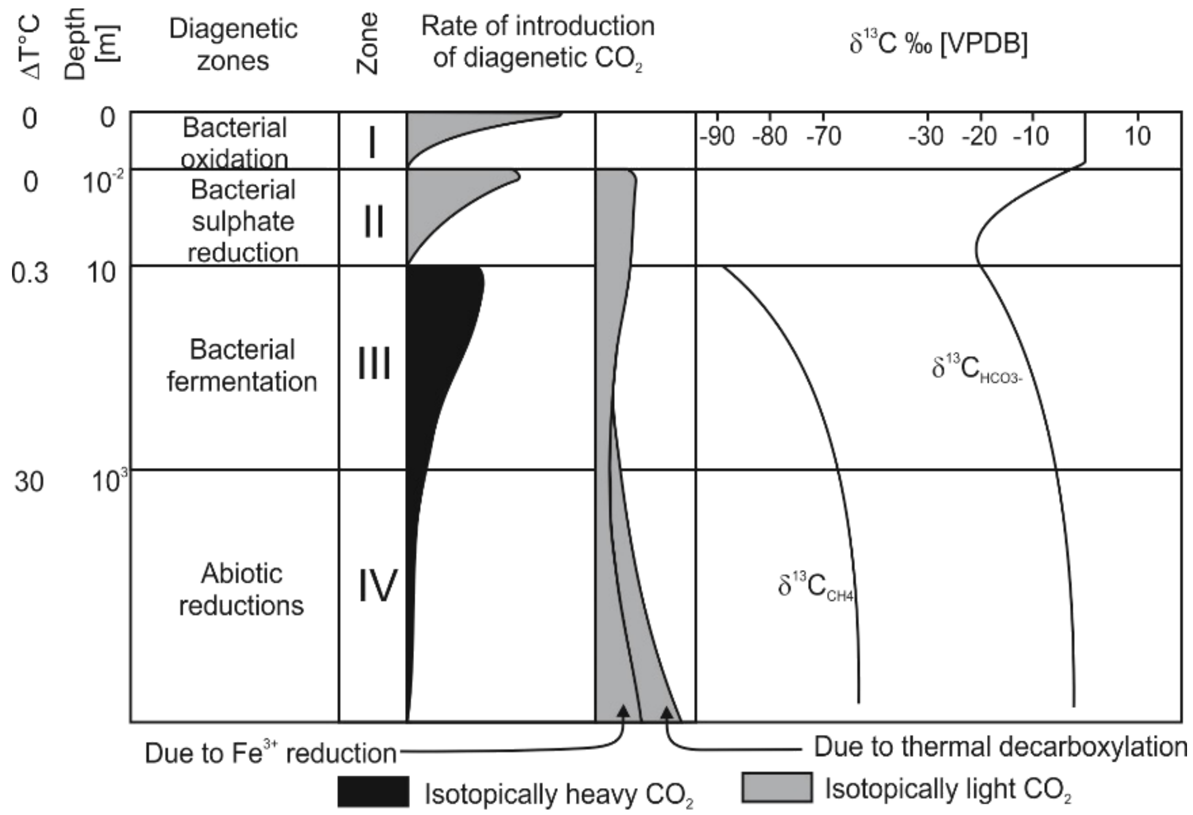

Fig. 9 Carbon isotope profile of dissolved carbonate in correlation to the introduced diagenetic CO_2, showing characteristic trends for the diagenetic stages during burial (modified after Irwin et al., 1977; Claypool & Kaplan, 1974; Gautier & Claypool, 1984; Zymela, 1996).

1.4. Gas generation

Generally, natural gas maybe composed of methane, ethane, propane, butane, pentane, and higher hydrocarbons. The $\delta^{13}C_{CH4}$ ratio distinguishes if the gas formed by microbial or thermogenic processes. The δD_{CH4} ratio of thermogenic gas provides information about the thermal maturity, whereas the δD_{CH4} ratio of microbial gas on the formation process, like CO_2 reduction and fermentation (Whiticar et al., 1986; Whiticar, 1993, 1999). The designation "wetness" respectively "dryness" is a classification of gas depending on the quantity of liquid vapor the gas is saturated with (Selley, 2000). The dryness of a gas is calculated as the ratio of methane over ethane and propane ($\frac{CH_4}{(C_2H_5+C_3H_6)}$). C- and H-isotopes from methane are useful tools to deduce the formation process. Gases can be discriminated after their formation mechanisms into three types:

- **Primary microbial gas** is produced via bacterial degradation of organic matter in sediments. It has typically light $\delta^{13}C_{CH4}$ (< -50‰ VPDB), light $\delta^{13}C_{CO2}$ (-15.8 - +2‰ VPDB) and light δD_{CH4} (Stahl, 1975; Coleman, 1976; Schoell, 1977). Based on the high concentration of methane ($\frac{CH_4}{(C_2H_5+C_3H_6)}$> 1000), the microbial gas is characterized as dry.
- **Secondary microbial gas** is produced by anoxic bacterial degradation of preexisting hydrocarbons. The $\delta^{13}C_{CH4}$ ranges from -55 to -35‰ VPDB and $\delta^{13}C_{CO2}$ exceeds +2‰ VPDB (Jones et al., 2008; Milkov, 2011). This gas, mainly associated with biodegraded oil, is also often dry (dryness: > 50).
- **Thermogenic gas** is produced by thermogenic decomposition of kerogen or oil. It is characterized by heavy δC_{CH4} (> -45‰ VPDB) and δD_{CH4} (-275 to -100‰; Stahl, 1975; Coleman, 1976; Schoell, 1977; Bernard et al., 1978; Whiticar, 1999). Depending on maturity of the source material, gas dryness varies between <10 (low maturity) and >1000 (overmature).

1.5. Rock-fluid interactions

Degradation reactions during organic matter decomposition affect the composition of the organic fraction itself and also change pH and Eh conditions in pore waters that may trigger dissolution of primary minerals and precipitation of cements. Such a mineral stability diagram is shown in Fig. 10.

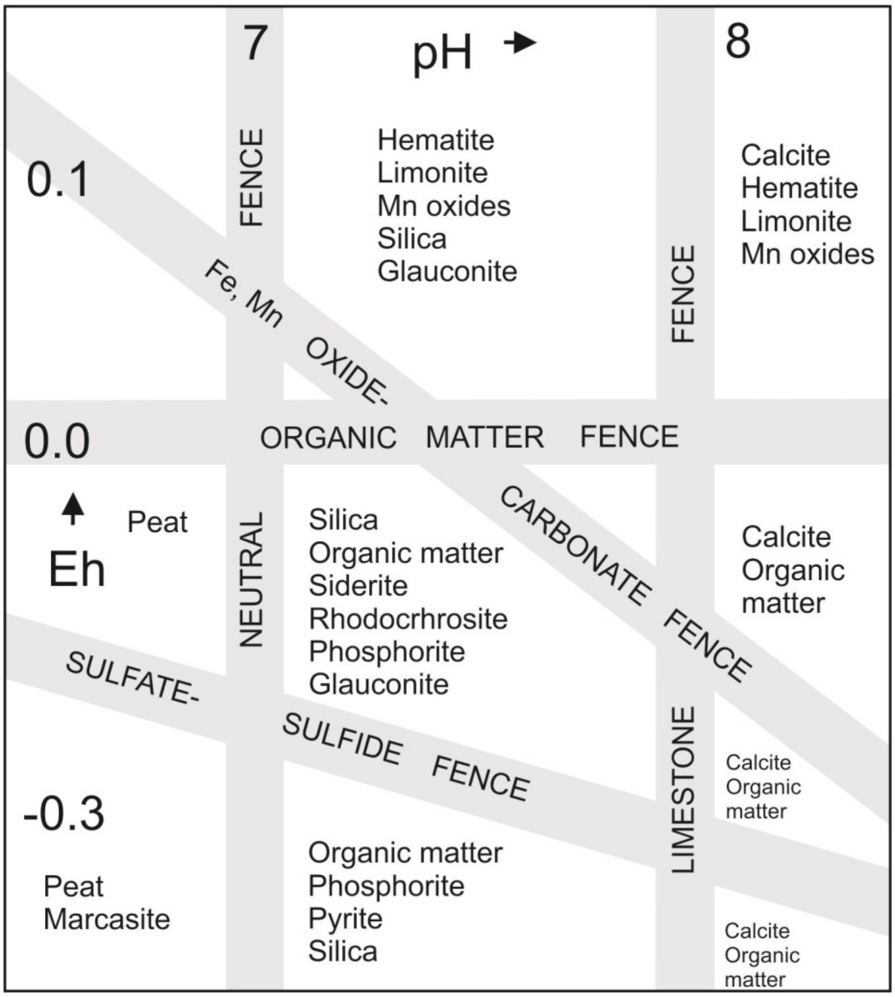

Fig. 10 Mineral stability diagram in Eh-pH stability fences (Krumbein & Garrels, 1952).

The organic substance is also a source of ions, mainly carbon (C) that becomes available for the reactions. Organic matter degradation may follow two extreme endmembers and any combination of them (i) organic matter $C^{(0)}H_2O$ degrades in anoxic conditions into $C^{(IV-)}H_4$ and thus results in a consumption of H^+ (increase in pH) and (ii) when free oxygen or oxidizing agents such as iron or manganese oxides are present $C^{(0)}H_2O$ reacts to $C^{(IV+)}O_2$. This results in the release of $4H^+$ per mole CH_2O and thus in a pH decrease.

Free $CO_{2(aq)}$ in pore waters containing Ca^{2+} triggers carbonate precipitation in alkaline conditions (Schulz et al., 2009; Schulz & Van Berk, 2009). Thus, microbial gas production alters the carbonate solubility product indirectly via pH change and may result in either precipitation or dissolution of carbonate cement within the pore space. These reactions have a strong impact on reservoir quality and are an important record for factors controlling reservoir parameters and their changes over time.

pH has a great effect on the stability of silica and calcite, whereas Eh changes have no impact on these mineral phases. With increasing pH, the solubility of silica increases and that of calcite decreases. A decrease of pH has the opposite effect (Blatt, 1980) (Fig. 11).

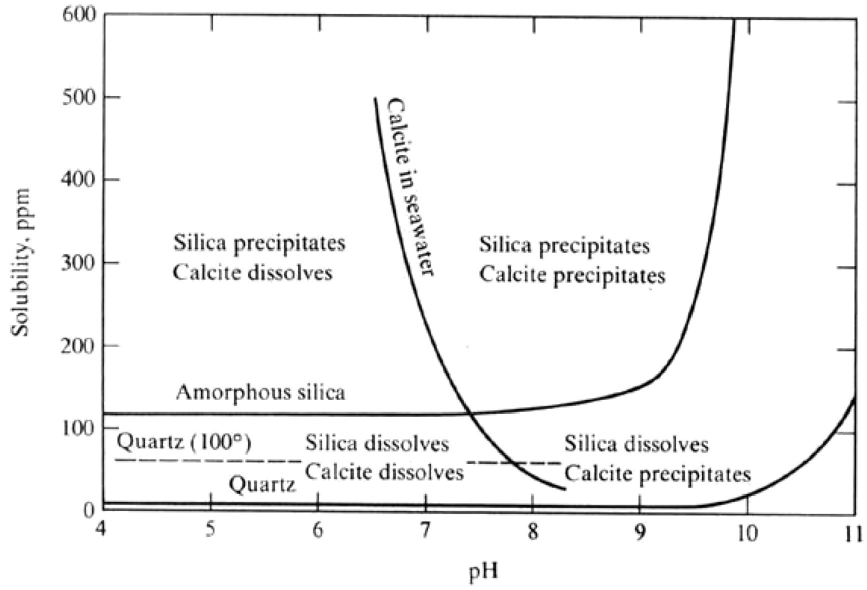

Fig. 11 Calcite and silica solubility in relation to pH (Blatt, 1980; in Selley, 2000).

Important insights into the relation of hydrocarbon generation and their alteration products are provided by $\delta^{13}C$ of authigenic carbonate minerals. The C-isotopy is subject to the diagenetic carbon cycle and depends on the carbon source (Friedman & O´Neil, 1977; Curtis, 1978). Thereby, the organic source is modified by different processes during biochemical zonation, involving microbial oxidation, microbial sulfate and carbonate reduction, and abiogenic thermally-induced decarboxylation (Irwin et al., 1977; Irwin & Hurst, 1983). As a result of these processes microbial gas (CH_4 and CO_2) is produced.

2. North Alpine Foreland Basin (NAFB)

2.1. Geological setting

The NAFB, extending from Geneva (Switzerland) to Vienna (Austria), comprises shallow to deep marine sediments of Eocene to Miocene age, which overlie crystalline basement and Mesozoic sediments of a passive continental margin. The NAFB was formed as a result of the middle Paleogene collision between the European plate represented by the Bohemian Massif in the north and the Eastern Alps in the south (Röder & Bachmann, 1996; Sissingh, 1997; Wagner, 1996, 1998) (Fig. 12).

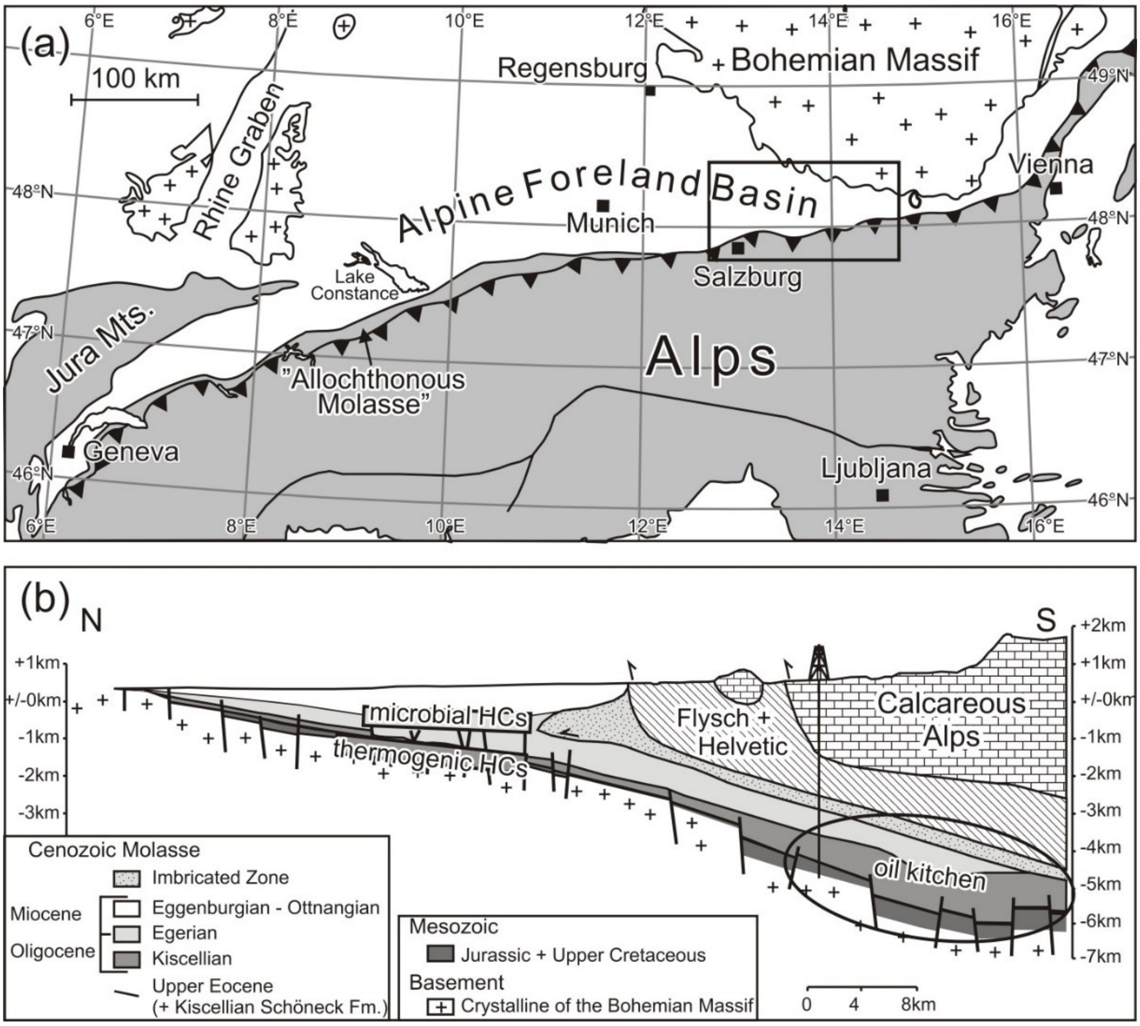

Fig. 12 a) Geological setting of the NAFB. The study area in its Austrian part is marked by a black rectangle. b) N-S trending cross section through the NAFB with its two hydrocarbon systems (HCs: hydrocarbons) (after Sachsenhofer & Schulz, 2006).

2.2. Stratigraphy

The crystalline rocks of the Bohemian Massif, representing the basement of the NAFB, is overlain by sediments deposited during three evolutionary stages (Wagner, 1996; Veron, 2005; Fig. 13): (i) Synrift stage with Permo-Carboniferous graben sediments, (ii) epicontinental and passive margin stage with mixed carbonate-siliciclastic deposits at the Mesozoic shelf (Sissingh, 1997; Wagner, 1996), (iii) foredeep stage, which began in the Late Eocene (e.g. Bachmann et al., 1987) and ended in the Late Miocene. Since Early Oligocene time, the NAFB belonged to the Central and Western Paratethys (Senes & Marinescu, 1974).

2.2.1. Permo-Carboniferous

Tectonic movements during a Permo-Carboniferous synrift phase enabled the formation of small elongated depressions. These graben structures follow ENE-WSW and WNW-ESE directed Variscian fault system. The sedimentary successions include terrestrial sandstones, shales and coal layers. In the study area, these sediments are present only locally beneath the Mesozoic and Cenozoic sediments (Malzer et al., 1993; Wagner, 1998).

2.2.2. Jurassic

Deposition of Mesozoic sediments commenced in the Middle Jurassic with the accumulation of coal-bearing siliciclastic sediments in a fluviatile environment. These sediments grade upwards into shallow marine sandstones and carbonates (Malzer et al., 1993).

During Late Jurassic time a transgression resulted in the formation of a thick carbonate platform (Brix & Schulz, 1993), which was partly eroded and karstified as a consequence of an Early Cretaceous regression (Nachtmann & Wagner, 1987; Wagner, 1980, 1998).

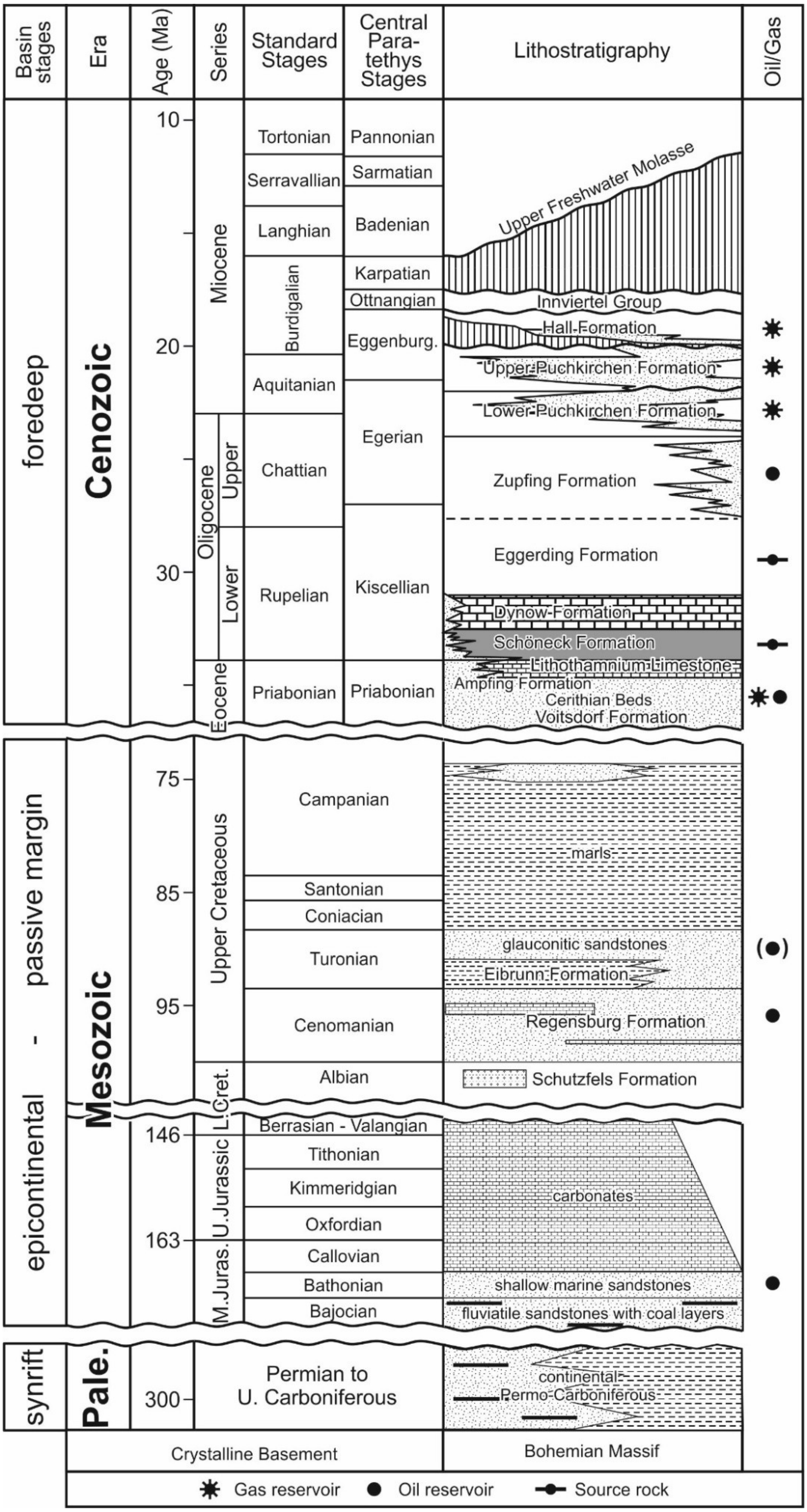

Fig. 13 Lithostratigraphy of the NAFB with the main source rocks and reservoir rocks (modified after Malzer, 1993; Wagner, 1998, Grunert et al., 2015 and Groß, 2015a).

2.2.3. Cretaceous

During Early Cretaceous (Albian?) time, fractures of the karstified and tectonically stressed Jurassic carbonates were filled with fluviatile sandstones and clays (Schutzfels Formation; Nachtmann, 1995b; Niebuhr et al., 2009) (Nachtmann & Wagner, 1987; Nachtmann, 1995b).

The following Late Cretaceous transgression resulted in deposition of siliciclastic rocks with a Cenomanian to Campanian age. Near their base, the Cretaceous succession includes Cenomanian shallow-marine glauconitic sandstones (Regensburg Formation; Niebuhr et al., 2007), which form an important reservoir horizon and, therefore, are described in some detail:

The Regensburg Formation starts with a conglomerate and grades into strongly bioturbated or fine laminated sandstones (Nachtmann, 1995b), which have been interpreted as storm deposits beneath the wave base by Polesny (1983). Based on well log facies, the Regensburg Formation in the study area has been subdivided from bottom to top into CE3, CE2 and CE1 (Nachtmann, 1995b). Niebuhr et al. (2009) subdivided the Regensburg Formation into the Saal Member and the overlying Bad Abbach Member. Groß et al. (2015b) tentatively correlated the Saal Member with CE3 and CE2 and the Bad Abbach Member with CE1. The Bad Abbach Member includes carbonate layers reflecting progressive transgression and a red “marker bed” near its base (Nachtmann, 1995b). The Regensburg Formation is overlain by pelitic rocks of the Eibrunn Formation.

Finally, the Cretaceous cycle ended due to the uplift of the European plate.

2.2.4. Eocene

The actual Molasse sedimentation commenced in the Late Eocene (Priabonian) as a consequence of Paleogene overthrusting of Alpine nappes on the European plate. The facies distribution during the latest Eocene (after Wagner, 1998) is shown in Fig. 14.

The Upper Eocene sedimentary succession, up to 120 m thick, starts with terrestrial sediments of the Voitsdorf Formation (former Limnic Series; Wagner, 1998) with varicolored mudstones, bright-grey fluvial sandstones and thin coal seams. They are overlain by brackish Cerithian Beds, which are characterized by fossil-rich dark-grey clay and sandstone bodies, interpreted as tidal channel fills (Wagner, 1980, 1998). They are followed by shallow marine, often bioturbated, sandstones of the Ampfing Formation (former Sandsteinstufe; Wagner, 1998). In the western part of the study area a red algal reef (Lithothamnium Limestone) developed, containing carbonates and their debris (Wagner, 1998; Rasser & Piller, 2004). Open marine nummulitic sandstone, Discocyclina Marl and Globigerinia Limestone deposited in the deep south-western part complete the Eocene sedimentary succession. A northeastward-directed transgression caused a shift of Eocene facies zones towards east-northeast (Malzer et. al., 1993; Wagner, 1998; Rasser & Piller, 2004).

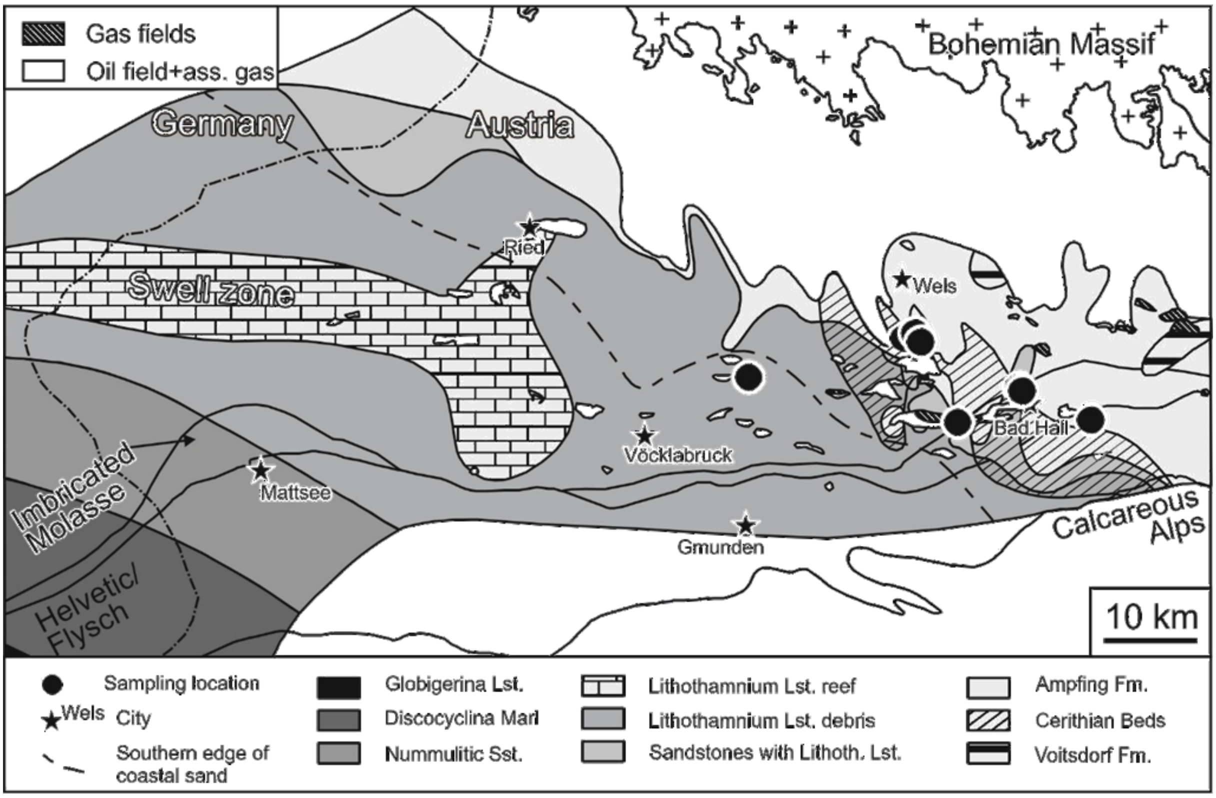

Fig. 14 Upper Eocene facies distribution of the NAFB during deposition of the Upper Lithothamnium Limestone (after Wagner, 1980) and the location of oil and gas fields with Eocene reservoir rocks and sampled wells.

2.2.5. Oligocene

As a consequence of rapid subsidence, the Priabonian shallow marine facies, inclusive the carbonate platform in the western part of the study area, drowned in early Oligocene time (Bachmann et al., 1987). Deep marine pelitic sediments accumulated in the NAFB. The Schöneck Formation (former Fish Shale) was deposited in a reduced and stagnant setting. The sediment succession is characterized by two organic matter rich marlstones units at the bottom and an organic matter rich shale unit at the top (Schulz et al., 2002). As a result of fresh water inflow and reduced salinity during early Rupelian times, the sediments of the Dynow Formation (former Bright Marlstone), rich in calcareous nanoplankton, developed (Schulz et al., 2004, 2005). The Dynow Formation is overlain by the Eggerding Formation (former Banded Marl). Sediments of this horizon are dark grey laminated marls, which indicate enrichment in organic matter, alternating with white layers (Malzer et al., 1993; Schulz, 2003; Sachsenhofer et al., 2010).

In early Chattian time, the Paratethys developed into an open marine setting. Consequently, turbidite and hemipelagic sediments were deposited (Zupfing Formation; formerly Rupelian Marl), still in an oxygen depleted setting. The sediment material was transported from the north. By comparison to the underlying horizon, an increase in carbonate content is evident (Sachsenhofer et al., 2010). The top of the Zupfing Formation is strongly eroded by the Puchkirchen channel (Malzer et al., 1993; Wagner, 1998).

2.2.6. Oligocene-Miocene

Deep marine conditions prevailed in the eastern part of the NAFB ("Puchkirchen Trough") until the Early Miocene. Since late Chattian time, detritus from the Bavarian Shelf and the Alpine Hinterland was transported into the Puchkirchen Trough, where a deep-water channel system, with eastward directed flow, formed parallel to the Alpine thrust front (Linzer et al., 2002; Hubbard et al., 2005; De Ruig & Hubbard, 2006) (Fig. 15). The channel was filled during Late Oligocene and Early Miocene times by sediments, up to 2000 m thick. Water depth estimates range between 1000 and 1500 m (Rögl et al., 1979; Robinson & Zimmer, 1989; Malzer et al. 1993; Wagner, 1996) and bottom water temperatures were probably about 4°C (Schulz et al., 2009).

The continuing northward movement of the Alpine nappes caused overthrusting of the southern part of the NAFB. Cenozoic sediments were incorporated into the Alpine wedge and the Imbricated Molasse was formed (Kuhlemann & Kempf, 2002). Contemporaneously, coarse grained debris was transported from the tectonically active Alpine margin into the steep southern slope (Linzer et al., 2002).

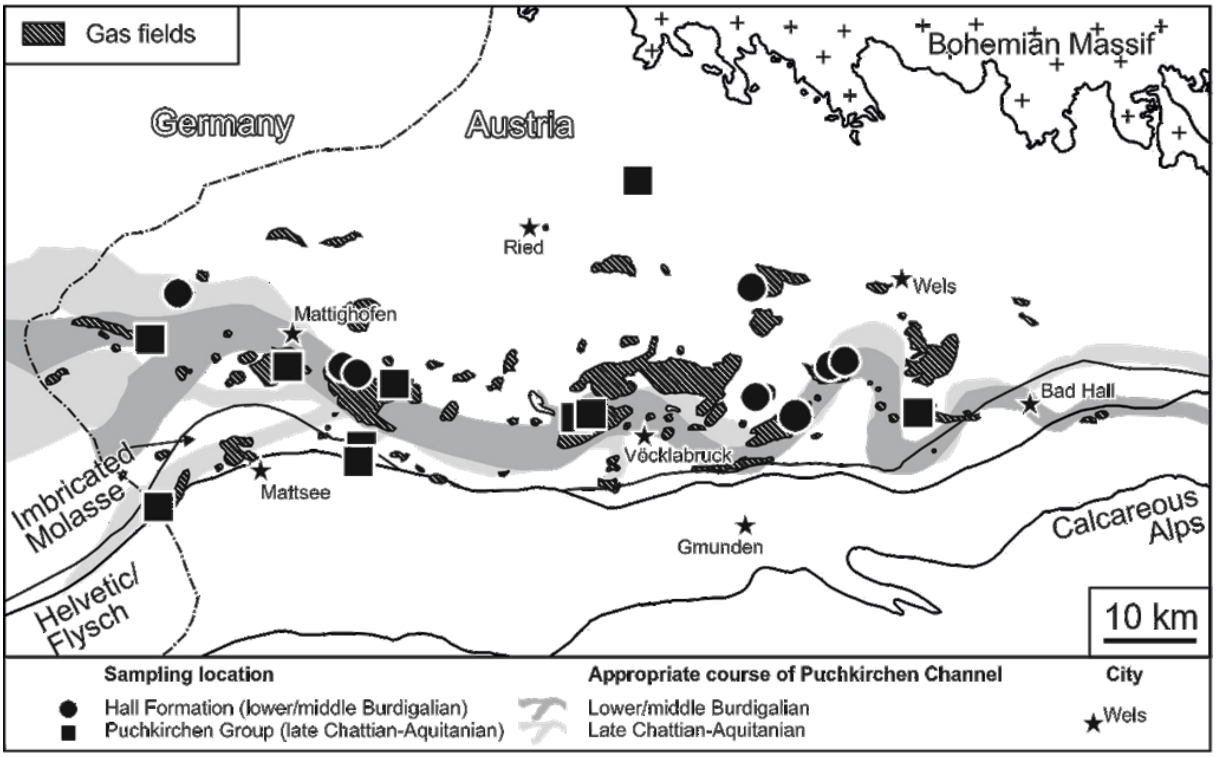

Fig. 15 Oligocene-Miocene facies distribution of the NAFB (after Wagner, 1998 and Kröll et al., 2005) and the location of Oligocene-Miocene gas fields and sampled wells.

The Chattian to Burdigalian sediments of the Puchkirchen Trough are subdivided into the Puchkirchen Group at the base and the overlying Hall Formation. The Puchkirchen Group consists of the Lower and Upper Puchkirchen formations (Grunert et al., 2015). The Lower Puchkirchen Formation can be subdivided into a Sand-Gravel Group and under- and overlying shale units. The Upper Puchkirchen Formation can be divided into four horizons (A4 to A1; bottom to top) (Aberer, 1958). Both formations are characterized by alternations of sandstones and conglomerates with calcareous shales (De Ruig, 2003).

The Hall Formation is separated by an unconformity from the Upper Puchkirchen Formation (Wagner, 1998). The facies of the Hall Formation reflects an Early Miocene shallowing of the depositional environment (Malzer et al., 1993; Sissingh, 1997). Deposition started in early Burdigalian time, due to a renewed transgression of the Paratethys (Sissingh, 1997). Based on biostratigraphy, the Hall Formation is subdivided into three parts (Rögl et al., 1979; Cicha et al. 1998; Wagner, 1998; Grunert et al., 2012): The deep marine basal Hall Formation represents the continuation of the deep marine Puchkirchen channel (Hall channel sensu Grunert et al., 2013). The lower Hall Formation represents a deep marine to shallow marine transition facies (Grosos, 2010), while the unconformably overlying upper Hall Formation is formed by deltaic deposits. The development of a prograding delta announces the following shallowing upward succession (Zweigel, 1998; Borowski, 2006; Hinsch, 2008; Grunert et al., 2012).

During the late Early Miocene, marine conditions persisted and continuous material transport infilled the Hall trough (Grunert et al., 2010, 2013) and the shallow-marine Innviertel Group was deposited. Thereby a transition from a fully marine to a fluviatile/brackish facies is obvious (Grunert et al., 2012). The Innviertel Group is separated by a Late Burdigalian to Langhian/Serravallian unconformity from overlying freshwater sediments (Wagner 1998). Sediments of the Upper Freshwater Molasse were deposited after a westward tilting of the NAFB (Gusterhuber et al., 2012). Typically, the freshwater sediments are composed of fluviatile gravel and sand with some coaly layers (Malzer et al., 1993; Wagner, 1998).

The Molasse stage ended in Tortonian time (ca. 8 Ma) due to uplift and the upper parts of the Freshwater Molasse were deeply eroded (Gusterhuber et al., 2012). These Molasse sediments are overlain by Quaternary deposits.

2.3. Hydrocarbon Systems

Oil and gas fields in the Austrian part of the NAFB are illustrated in Fig. 16.

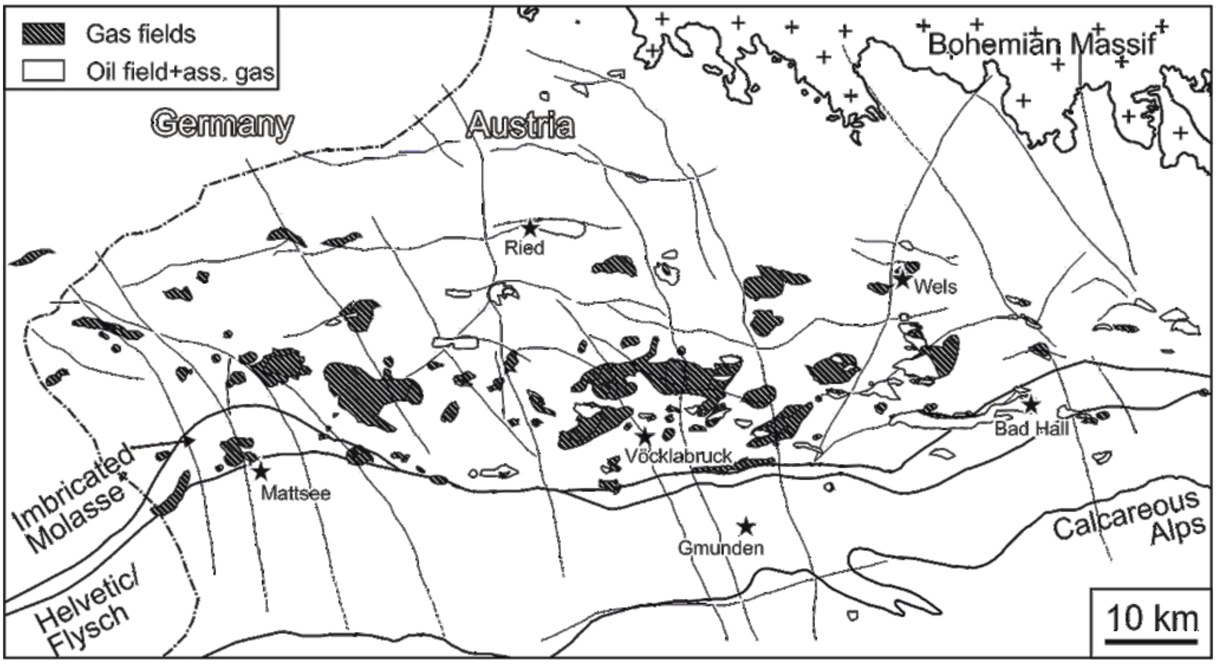

Fig. 16 Distribution of oil and gas fields in the Austrian part of the Alpine Foreland Basin.

Within the Austrian sector of the NAFB a thermogenic and microbial hydrocarbon system can be distinguished:

2.3.1. Thermogenic Petroleum System

The thermogenic system is defined by Lower Oligocene source rocks (Schulz et al. 2002; Sachsenhofer & Schulz, 2006; Sachsenhofer et al. 2010):

Schöneck Formation

Schöneck Formation is considered as the main source rock in the thermogenic system of the NAFB (Bachmann et al., 1987; Schulz et al., 2002). This horizon reaches a thickness up to 20 m and can be subdivided into a marly lower part (units A/B) and into a shaly upper part (unit C). The lower marly part has a mean TOC of 2.3% and a HI of 500 mg HC/gTOC. By comparison, the upper shaly part has a mean TOC of 5.0% and a HI of 600 mg HC/gTOC (Schulz et al., 2002).

Dynow Formation

The marlstones of the Dynow Formation, up to 15 m thick, reveal a lower source rock potential. At the base of this horizon the sediments have a comparably low TOC (0.5 - 3%) content, which increases upwards (Sachsenhofer & Schulz, 2006; Schulz et al., 2004).

Eggerding Formation

The Eggerding Formation, up to 50 m thick, can be qualified as a source rock because of high TOC content (max.: 5%; Schmidt & Erdogan, 1996; Sachsenhofer & Schulz, 2006). The HI reaches a maximum of 600 mg HC/gTOC (Sachsenhofer et al., 2010).

Hydrocarbon generation started in Miocene times, when the Alpine nappes overthrusted the southern NAFB and ended about 5 Ma ago due to uplift and cooling (Gusterhuber et al., 2013, 2014). The oil window is entered at a depth of about 4 to 6 km below sea level.

The expelled gas and oil migrated laterally northwards into Mesozoic and Cenozoic reservoir rocks (Schmidt & Erdogan, 1996; Bechtel et al., 2013):

Jurassic and Upper Cretaceous

Middle Jurassic basal sandstones, about 10 m thick, may host minor amounts of hydrocarbons (Malzer et al., 1993).

Significant hydrocarbon accumulations occur in Cenomanian sediments of the autochthonous Mesozoic cover on top of the Bohemian Massif. These Upper Cretaceous reservoir rocks are up to 60 m thick and have porosities up to 17% and permeabilities ranging from several tens of mD to 400 mD (Malzer et al., 1993).

Upper Eocene

Eocene fluviatile (Voitsdorf Formation), tidal (Cerithian Beds) and shallow marine deposits (Ampfing Formation, Lithothamnium Limestone) are the most important reservoir rocks for the thermogenic hydrocarbon system. The Eocene sediments reach a thickness of up to 30 m with varying, but generally good reservoir quality in average. Shallow marine sandstones of the Ampfing Formation are the best reservoir sandstones and show porosity values between 15 and 25% and permeabilities from several mD to 2000 mD (Wagner, 1980).

With the exception of shallow biodegraded oil, the API gravity typically varies between 30 and 35, classifying the oil as light (Gratzer et al., 2011). Pytlak et al. (2016) show that the thermogenic gas is often mixed with primary or secondary microbial gas (Fig. 17).

2.3.2. Microbial Petroleum System

Oligocene and Miocene strata (Puchkirchen Group and Hall Formation), up to 3250 m thick (Grunert et al., 2015), are source rocks and reservoirs for in-situ formed microbial gas (Malzer et al., 1993; Wagner, 1996; Schulz et al., 2009; Schulz & Van Berk, 2009).

Organic matter rich shale layers, intercalating with potential reservoir sandstones, are considered as source and seal rocks. TOC contents of the fine-grained rocks are typically around 0.7%, but reach 3.4% in the uppermost part of the Upper Puchkirchen Formation ("A1 fish shale"). The immature organic matter is dominated by kerogen type III-II (Belaed, 2007). Gas was produced from organic matter by microbial metabolization (Schulz et al., 2009; Schulz & Van Berk, 2009).

Turbiditic sandstones and sandy conglomerates of the Puchkirchen Group and the Hall Formation provide the main reservoirs (De Ruig & Hubbard, 2006; Hubbard et al., 2009). Reservoir sandstones have porosity values of about 20% and permeabilities in the order of 10s to 100s of mD (Malzer et al., 1993; Groß et al, 2015a).

Reischenbacher & Sachsenhofer (2011) and Pytlak et al. (in press) showed that, although separated by several hundred meters of rocks, microbial gas is mixed with small amounts of thermogenic wet gas (Fig. 18). Upward migration of thermogenic hydrocarbons into Oligocene-Miocene horizons probably occurred along faults and via diffusion.

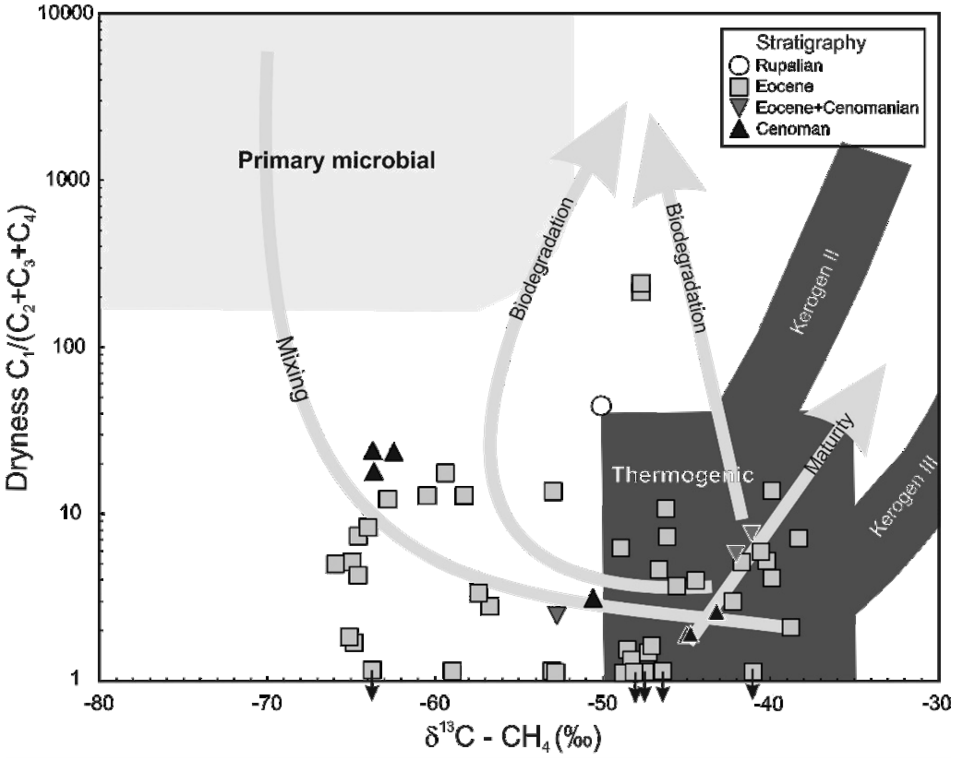

Fig. 17 Origin and alteration trends from oil associated gas of the thermogenic hydrocarbon system, sampled from fields all over the Austrian NAFB (Pytlak et al. 2016; modified after Bernard et al., 1976; Jones et al., 2008; Milkov, 2011).

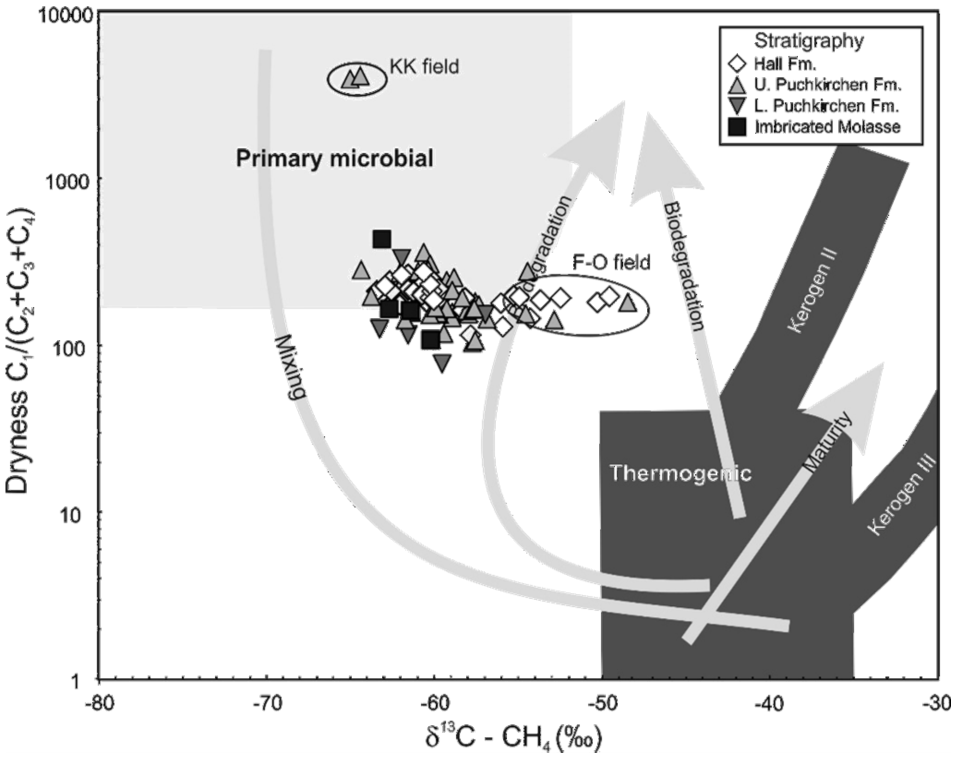

Fig. 18 Origin and alteration trends from oil associated gas of the microbial hydrocarbon system, sampled from fields all over of the Austrian NAFB. Mixing trend with depth is determined by results of mud gas measurements from well penetrating Imbricated Molasse (Pytlak et al. 2016; modified after Bernard et al., 1978).

3. Material and Methods

3.1. Samples

Samples were taken in the core shed of RAG (Pettenbach). Typically cores are 10 to 19 m long and core recovery is about 95%. Sampling of sandstones concentrated on core sections near the oil-water and gas-water contacts to compare characteristics of rocks with different fluid content. Wherever possible, samples have been taken across fluid contacts in order to minimize the effect of primary sediment petrological variations, controlled by the depositional environment.

For the present study reservoir rocks from the (i) microbial system represented by Oligocene-Miocene sandstones and from the (ii) thermogenic system represented by Eocene and Cenomanian sediments, were investigated. The location of sampled wells is shown in Fig. 19.

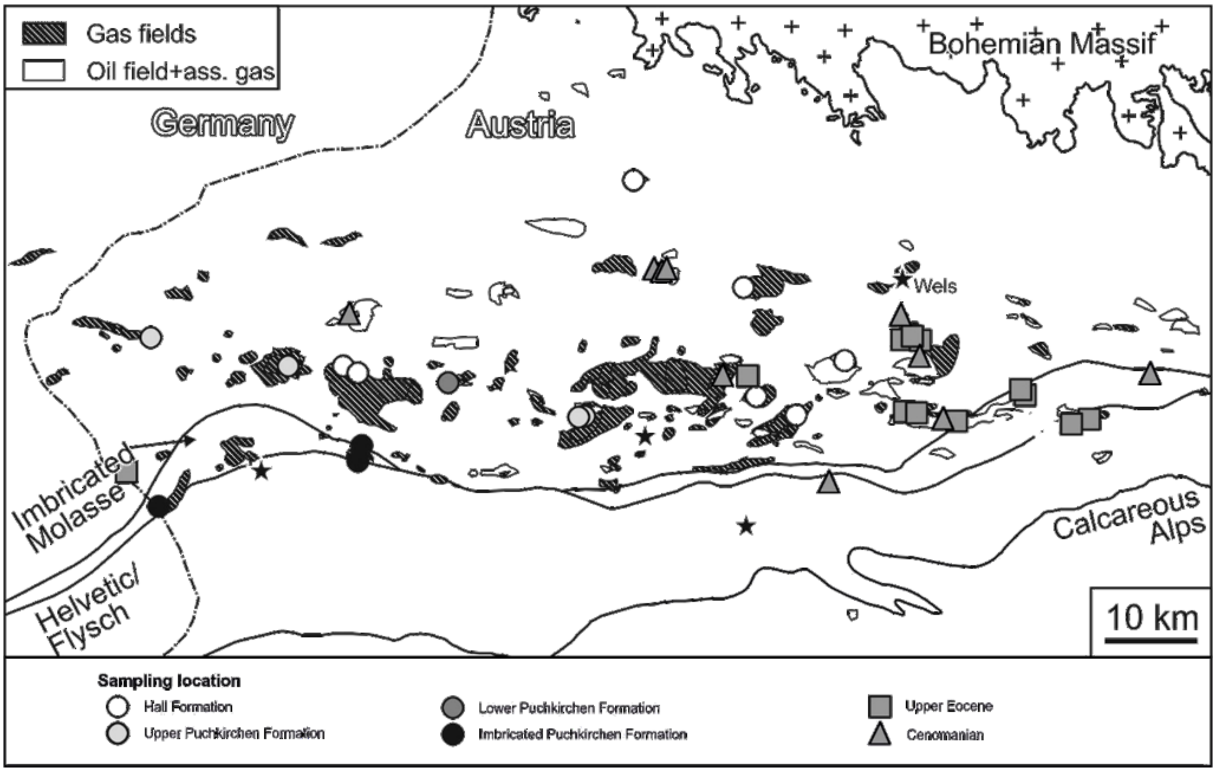

Fig. 19 Location of gas fields and sampled wells in the Austrian part of the NAFB. The age of sampled reservoir rocks is indicated by different labels.

Oligocene-Miocene reservoir rocks

More than 110 Oligocene to Miocene sandstone samples from water- and gas-bearing sections near the gas-water contact (GWC) have been investigated. Cores represent sediments from the Puchkirchen Group and Hall Formation deposited along the Puchkirchen/Hall channel, but also at the northern and southern slope of the Puchkirchen/Hall trough. In average six samples per core were taken. The samples cover a depth range of 1000 to 2000 m below ground level.

- Water-and gas-bearing section, GWC:
    - Two wells from Hall Formation,
    - Seven wells from Upper Puchkirchen Formation
    - One well from Lower Puchkirchen Formation.
- Only gas-bearing section:
    - Five wells from Hall Formation,
- Only water-bearing section:
    - One well from Hall Formation.

Upper Eocene reservoir rocks

A total of 40 core samples from Eocene reservoir units have been selected for the present study. In average, three samples per sandstone layer were taken. Following samples, at depths ranging from 1500 to 2000 m below ground level, were taken:

- Gas cap, oil- and water-bearing zone, OWC, GWC:
    - Six wells from Ampfing Formation
    - Two wells from Cerithian Beds
    - One well from Voitsdorf Formation
- Strongly cemented sections (OWC?):
    - Two wells from Ampfing Formation
    - One well from Cerithian Beds
    - One well from Voitsdorf Formation

Upper Cretaceous reservoir rocks

149 sandstone samples were selected from Cenomanian units to characterize cement phases. These samples were taken by Schnitzer within a former project between RAG and Montanuniversitaet Leoben (PEPE; Petroleum Engineering Program of Excellence). The depositional environment, diagenesis and reservoir properties of these sandstones were investigated by Schnitzer (Schnitzer, 2013; Schnitzer et al., 2012) and the pore properties by Samsu (Samsu, 2015). The first study of Schnitzer was performed within the PEPE project. The second study (Samsu, 2015) is part of the present research, supported by the FFG Bridge-Project. Upper Cretaceous samples are integrated into this study and the results presented in chapter “4.3. Upper Cretaceous”, to give a complete picture of the influence of fluids on all reservoir sections in the NAFB. Further they are interpreted together with the reservoir sections of Eocene and Oligocene-Miocene age. The implication of different pore fillings on the reservoir parameters in Cenomanian sediments is described in Groß et al. (2015b) and their results are used for this study as well.

3.2. Methods

3.2.1. Core Gamma Ray (CGR)

The core gamma ray is a tool to measure the total and spectral gamma radiation of the core in situ. The gamma ray represents the natural radiation of the rock. The total gamma ray summarizes all energies emitted from the formation on a single count rate. The spectral gamma ray separates the radioactive elements into the isotopes of potassium, thorium and uranium (Doveton, 1994). In general, this method is used to differentiate between sandy and clayey horizons. Clay has higher potassium content and thus a higher radioactivity. Material, enriched in organic matter, displays a higher uranium signal compared to the non-enriched material (Nichols, 2009). The thorium content gives information about the presence of clay minerals and heavy minerals in the sediment. Gamma spectrometric investigations of Cenomanian green sandstones by Rech (2011) reveal that the conventional usage of potassium and thorium content as grain size indicator (clay minerals) has to be treated with caution. The gamma log of glauconite-rich (K) sandstones and heavy mineral-rich (Th) mica-sandstone appear to be shaly, due to the fact that these elements would lead to a wrong presumption of the grain size otherwise. Thereby, the high potassium content is associated with high glauconite content within the sandstones.

A hand-held gamma ray spectrometer (Gamma Surveyor from GF Instruments) was used to record the natural radiation of the core in the core shed during lithological documentation. It is a multi-channel gamma-ray spectrometer and measures both, the total and the spectral gamma ray of the rocks. Measurements were performed along the whole core length. In each 1-m-long core box measurements were carried out at cm 25 and at cm 75, resulting in measurement spacing of 0.5 m. The recording time was two or three minutes.

The total gamma log from the core boxes was correlated to the lithologic core descriptions. In order to enable the investigation of rock-fluid interactions in zones with different pore fluids, lithologic profiles and CGR from investigated cores were correlated with wireline gamma-ray logs (GR), provided by RAG. Based on similarities, the exact position of the cores within the borehole could be determined by log to core shift. Resistivity logs (RES; also provided by RAG) were used to determine the exact position of the hydrocarbon- (oil, gas) and water-bearing sections, and in particular of the OWC and GWC locations.

3.2.2. Thin section microscopy

Thin section microscopy is the most effective and conservative method to characterize sandstones petrographically (Tucker, 1996).

The thin sections were prepared from core samples and embedded in blue-colored epoxy resin for porosity evaluation. Partly, thin sections were stained with Alizarin Red (Alizarin S) to differentiate between dolomite and calcite (Tucker, 1996). Using an optical light microscope Leica DM 4500P, the mineralogy of the grains was identified. Also sediment texture, involving grain size, sorting, roundness and sphericity, and pore filling type (matrix/cement and cement type) have been determined. For taking microscope photos, a Leica DFC 420 camera was used. A quantitative evaluation of the mineralogical composition was done by point counting on 300 points per thin section applying the point counting system PETROG™ and the PetrogLigte™ Software. All presented mineral percentages are given in vol.%, based on the average from point counting and semi-quantitative XRD analysis.

3.2.3. Cathodoluminescence (CL)

Cathodoluminescence microscopy is applied to discriminate different carbonate cement types and to identify the hinterland of a certain environment of detrital grains (Tucker, 1996).

With this technique, the irradiance of electrons on the minerals of the thin section causes luminescence of specific minerals. Based on the luminescence color and intensity of the particular material, conclusions can be made about its chemical composition: Carbonate is characterized by orange, red to brown luminescence color, whereby coloring is induced by Mn^{2+} and Fe^{2+} contents. Mn^{2+} causes a yellow to red color. Replacement of Mn^{2+} by Mg^{2+} provokes red coloring (Sommer, 1972). In general, Mg-poor calcite is yellow, Mg-rich calcite orange to red. Dolomite is typically brick-red. Increasing Fe^{2+} content in the carbonate dims the luminescence (Amieux, 1982). The Mn^{2+} content of the cement is often used to deduce the formation conditions as oxic, suboxic and anoxic (Tucker, 1996). Quartz usually has no luminescence and appears black. Violette color and brown color of quartz indicates magmatic and metamorphic origin (Zinkernagel, 1978; Matter & Ramseyer, 1985). K-feldspar exhibits blue and plagioclase green luminescence (Marshall, 1988).

Samples with strong carbonate cementation were polished and vapor coated with carbon (graphite), to improve the electrical conductivity. The thin sections were analyzed on a Lumic HC5-LM microscope with an acceleration voltage set at about 14 kV and a beam current of ca. 2 mA. In addition, a CITL (Cambridge Image Technology Ltd.) 8200mk3 cold cathode with 16 to 19 kV and 0.2 mA was used for these investigations also.

3.2.4. X-Ray diffractometry (XRD)

Semi-quantitative and qualitative mineralogical composition of bulk rock samples was determined by X-ray diffraction analysis, in addition to conventional microscopy and point counting. This method is used especially for fine grained sediments, when the grain size is too small for sufficient mineral identification under optical light microscopy (Tucker, 1996).

XRD analysis is based on characteristic diffraction patterns of the X-rays, which have been emitted from an X-ray tube and deflected at the mineral surface. The diffraction pattern gives information about the crystal structure (Nichols, 2009). It is characteristic for each mineral and thus minerals can be identified easily.

In addition, semi-quantitative information about the mineral content is also possible by XRD analysis, but has to be handled with caution because minerals of different crystal systems show different reflection behavior (Tucker, 1996). The intensity of a mineral is proportional to its concentration. The peak height or area of the main reflector expresses the intensity. A percentage amount of the minerals is assessable via height and area relationships (Tucker, 1996).

A Philips PW 1830/40 diffractometer with a CuKα-radiation (35 kV, 35 mA, step size 0.08°, 1 s per step) were used for XRD analysis of Oligocene-Miocene and Cenomanian samples and a Panalytical X`Pert diffractometer with a CuKα-radiation (35 kV, 35 mA, step size 0.0167°, 20 s per step) for Eocene samples. The measurement device was changed due to equipment failure. The angle range reaches at both from 2° to 67° 2θ.

For XRD, bulk rock samples were analyzed. The rock samples were crushed and grinded manually in an agate mill to a fine powder (5 - 10 µm). The manual procedure clearly decreases the breakdown of rather instable crystal lattices. Only texture free specimen slides were used, because the study focuses on the carbonate cement types and because of the general low content of clay minerals. Oligocene-Miocene and Cenomanian samples were analyzed with an object plate. For this preparation, the powder was filled into the aluminum sample holder at the side to receive a statistical mineral grain distribution. Eocene sandstones were measured with an aluminum ring, where the pulverized samples are pressed into the hollow mold from the back. This method also enables a statistically dispersal of the minerals.

The minerals have been identified by the characteristic peaks by means of the JCPDS table (1974), Brindley (1980) and Moore & Reynolds (1997). The semi-quantitative evaluation was done by the software of ADM-V7, RMS Kempten and the method of Schultz (1964).

3.2.5. Scanning Electron Microscopy (SEM)

Scanning electron microscopy (SEM) is a tool to illustrate the mineral morphology, growth and mineral relationships at a 20 to 100,000 times magnification. This method is a key for the reconstruction of diagenetic parasequences, because mineral grains, pore space and their filling are identified in-situ (Tucker, 1996). With this technique, clay mineral morphologies are visualized and thus clay minerals can be distinguished. Moreover, it is possible to detect different generations of mineral overgrowths.

The sample surface is scanned by an electron beam in a raster. The electrons are sent from an electron gun and impinge at the surface. There, they interact with the atoms of the sample and get reflected. The intensity of the re-emitted rays is dependent on the distance to the detector. Hence, the relief of the surface can be reproduced. Thereby, the structures are transformed into a grayscale picture, which imitates topography by light and dark areas (Tucker, 1996; Nichols, 2009).

In addition to the grayscale topography images, an energy dispersive X-ray (EDX) spectrometry (EDS) is used for elemental analysis of minerals. An electron or X-ray beam is blasted on a selected area on the sample surface. It impacts on the crystal surface, whereupon an element-specific X-ray is emitted. They are collected and displayed in a spectrum, which presents the energy of the reflected rays. The mineral can be identified, based on peaks corresponding to particular elements. Restrictions of EDX spectrometry include that elements lighter than the element Na cannot be identified. Furthermore, the rock sample should not contain any fluids in order to allow the generation of a sufficient vacuum.

Investigations were carried out on a Zeiss Evo MA 15 with an Inca Dry Cool EDX spectrometer and a high vacuum system at 10 mm working distance to investigate the texture of rock samples and of single minerals. The acceleration voltage amounted 15 or 20 kV and the beam current 10 nA.

Rock specimen with particular high and low porosities were selected for this analysis. The rock samples were freshly broken and trimmed to a size of ca. 1x1 cm with flat nose pliers. Then they were stuck on a sample holder with a double-faced adhesive tape. When fixing, care was taken to provide an even surface for a better and constant beam intrusion. The carbon coating enables the conduction of the electron beam to the sample. Afterwards the samples were placed on the holder of the vacuum chamber for the analysis.

3.2.6. Electron microprobe (EMP)

Electron microprobe analysis is a nondestructive method to analyze the chemical composition of the surface in µm scale (Tucker, 1996). It is commonly used for mineral identification and measurement of elemental concentration in a mineral as addition to conventional optical light microscopy.

The back scatter electron (BSE) method uses re-emitted electrons, produced by an electron beam, focused on a selected area before. The electrons impinge on the surface and are scattered back in all directions. The electrons are collected by the BSE detector. A grayscale image section of the thin section is created, based on the number of reflected electrons. The number of free electrons is dependent on the average of the atomic number of the mineral phase (the higher the atomic number, the more electrons are backscattered). The shades of grey give information about the atomic number (Tucker, 1996).

The operation mode of element identification is similar to SEM energy dispersive X-ray spectrometry (EDX, respectively EDS). Here, also an electron beam is focused on a selected area on the thin section and an elemental specific spectrum is emitted. The mineral phase can be read from the elemental composition of the spectrum. Limitations of EDX spectrometry disable the detection of elements lighter than Na.

In addition, the distribution of chosen elements was analyzed on selected areas. This was done via wavelength dispersive X-ray (WDX) spectrometry (WDS). In contrast to EDX, elements are deduced from the spectrum which differentiates the elemental composition by their wave length, and not from their intensities. In small steps the whole selected area is scanned by this method automatically.

A Superprobe JEOL JXA 8200 electron microprobe was used to analyze chemical composition and to identify mineral phases via BSE and EDX spectra. Additionally, Na, Mg, Al, Si, K, Mn and Fe contents were mapped on selected areas by WDX.

Selected thin sections, samples with strong carbonate cementation and Cenomanian and Eocene sandstones samples with high clay mineral content, have been polished to enable a clear impact of the beam on the surface. In addition, they have been vapor coated with carbon (graphite) to enable the electrical conductivity of the sample. Afterwards, they were put in the sample holder of the vacuum chamber together with mineral specific standards for analysis.

3.2.7. Stable isotope analysis

The stable isotope analysis is a method which measures the isotopic composition of a specific element, in order to evidence formation conditions. Stable isotopes do not disintegrate spontaneously, thus no age dating is possible. The most common representatives are the elements H, C, N and O, which are presented as ratios to the standard (Tucker, 1996). In this study the stable isotopes of carbon and oxygen were measured, mainly on carbonate cements. Oxygen is used as a petrogenetic indicator, from which formation temperature can be derived. Carbon provides information about the carbon source (Friedman & O´Neil, 1977; Stosch, 1999).

The relative ratio of the isotopes is measured with a mass spectrometer (MS) by means of the atom mass. The sample is measured as gas, which gets heated and ionized in the cathode. The ionized phase is accelerated by an electrical field and deviated by a magnet. The deviation results into a partitioning according to their mass-to-charge ratio. This means that the smaller the mass or the bigger the charge, the stronger the ion beam is detracted from the flat trajectory. The separated ions impact on the deflector and discharge electrically, which is measured and displayed as a mass spectrum. This mass spectrum gives the relationship of the ^{12}C and ^{13}C by difference in peak size (Tucker, 1996; Stosch, 1999).

The measured $\delta^{13}C$ ($^{12}C/^{13}C$) and $\delta^{18}O$ ($^{16}O/^{18}O$) values of the samples are set in relation to the standard material. The isotopic composition of the measured carbonates is expressed with δ [‰] (Stosch, 1999).

With a microdrill, fine powder has been gouged out from the hand specimen in order to excavate only the carbonate cement. The carbonate material may comprise different generations of authigenic carbonates, involving calcite (Cc I to Cc IV), dolomite, small amounts of ankerite and siderite and very rare detrital carbonate lithic fragments. A distinction of the isotopic composition of the particular carbonate types and generations was not possible, based on the measuring technique.

The necessary amount of sample powder is reliant on the carbonate content, which was estimated from the semi-quantitative XRD analysis. According to this, a rock composed of 100% carbonate requires a sample quantity of 0.2 mg. Rock samples with a lower carbonate content need correspondingly more mass, in the same carbonate content-mass ratio.

The powdered samples were treated with 100% H_3PO_4 at 70°C in an online system (Gasbench II with carbonate option) and the released CO_2 was analyzed by a ThermoFisher DELTA V isotope ratio mass spectrometer.

The measured values were normalized to the VPDB (Vienna-Pee Dee Belemnite) standard for both $\delta^{13}C$ and $\delta^{18}O$. The data have a standard deviation of 0.8% for $\delta^{13}C$ and 0.1% for $\delta^{18}O$.

3.2.8. X-ray tomography

The radiology is a non-destructive method to illustrate open space between the grains. It is used to visualize the porosity or fracture distribution in a hand specimen with resolution in microscale (Landis & Keane, 2010).

The adsorption of X-rays is indicative for the permeability for the rock. Thus higher adsorption values are achieved in tight sections of the sample, whereas higher porosity and permeability enables a transmissivity of the emitted X-rays.

Within the frame of the present study, a single sample, characterized by strong cementation, has been analyzed using a X-ray rock tomography scanner Universal HD 400 by DI DI Sabine Schatzmann at Clausthal University of Technology, Institute of Petroleum Engineering.

3.2.9. Petrophysical data

Porosity and permeability data from investigated cores, measured shortly after core recovery, were provided by RAG. Petrophysical parameters have been measured on core plugs. The site of the core plugs is clearly visible in the cores (holes). This enabled an efficient correlation of petrophysical data with the newly taken samples.

4. Results and Discussion

4.1. Oligocene-Miocene

4.1.1. Sedimentary petrology

Puchkirchen Group

Sandstones from the Puchkirchen Group are medium-grained with local thin conglomerate beds and show a bright grey color. Single sandstone horizons are homogenous, about 2 m thick and separated by cm-thick dark brown-grey silty calcareous shales. An overview of core boxes from different positions in the basin is presented in Fig. 20.

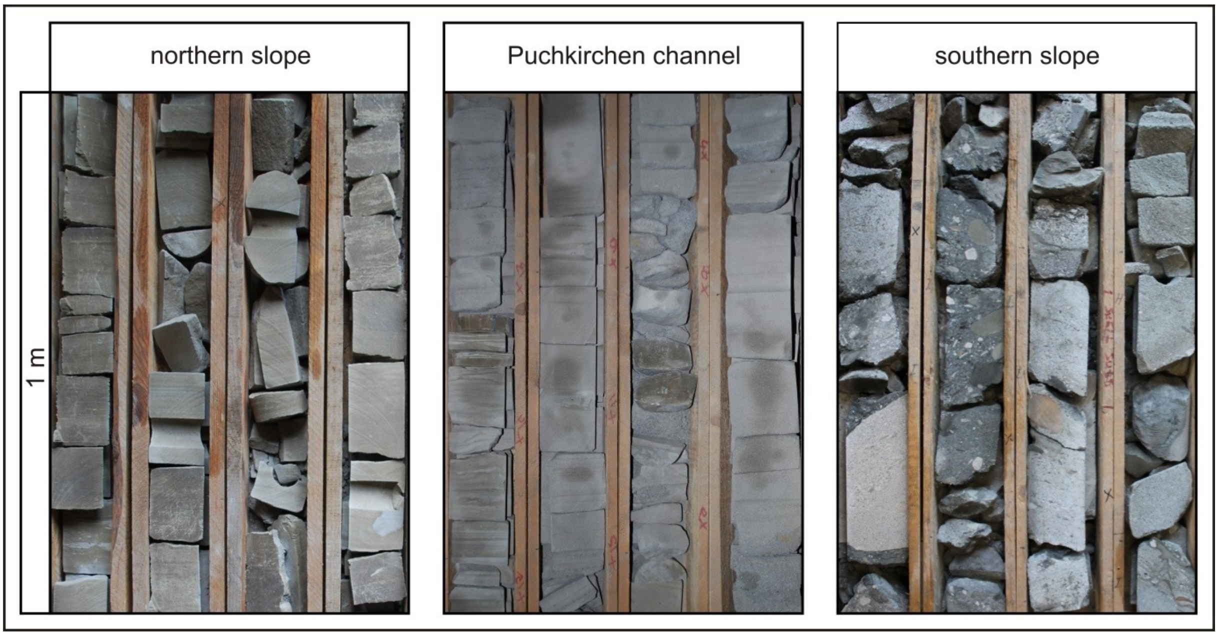

Fig. 20 Overview of core boxes from investigated cores with Hall Formation from the northern slope (ca. 760 m below ground level), and Upper Puchkirchen Formation from the Puchkirchen channel (ca. 1290 m) and the southern slope (ca. 1690 m).

Representative lithological profiles from cores of the Upper Puchkirchen Formation together with mineralogy, porosity and isotopic composition of the particular sections (water-, transition and gas-zone) are shown in Fig. 21a. The relationship between mineralogy and porosity is summarized in ternary diagrams of Fig. 22. In the western part of the basin grain size of the conglomerates can reach up to 5 cm. Lithoclasts comprise of well-rounded metamorphites and minor carbonates. Besides also mud clasts are present.

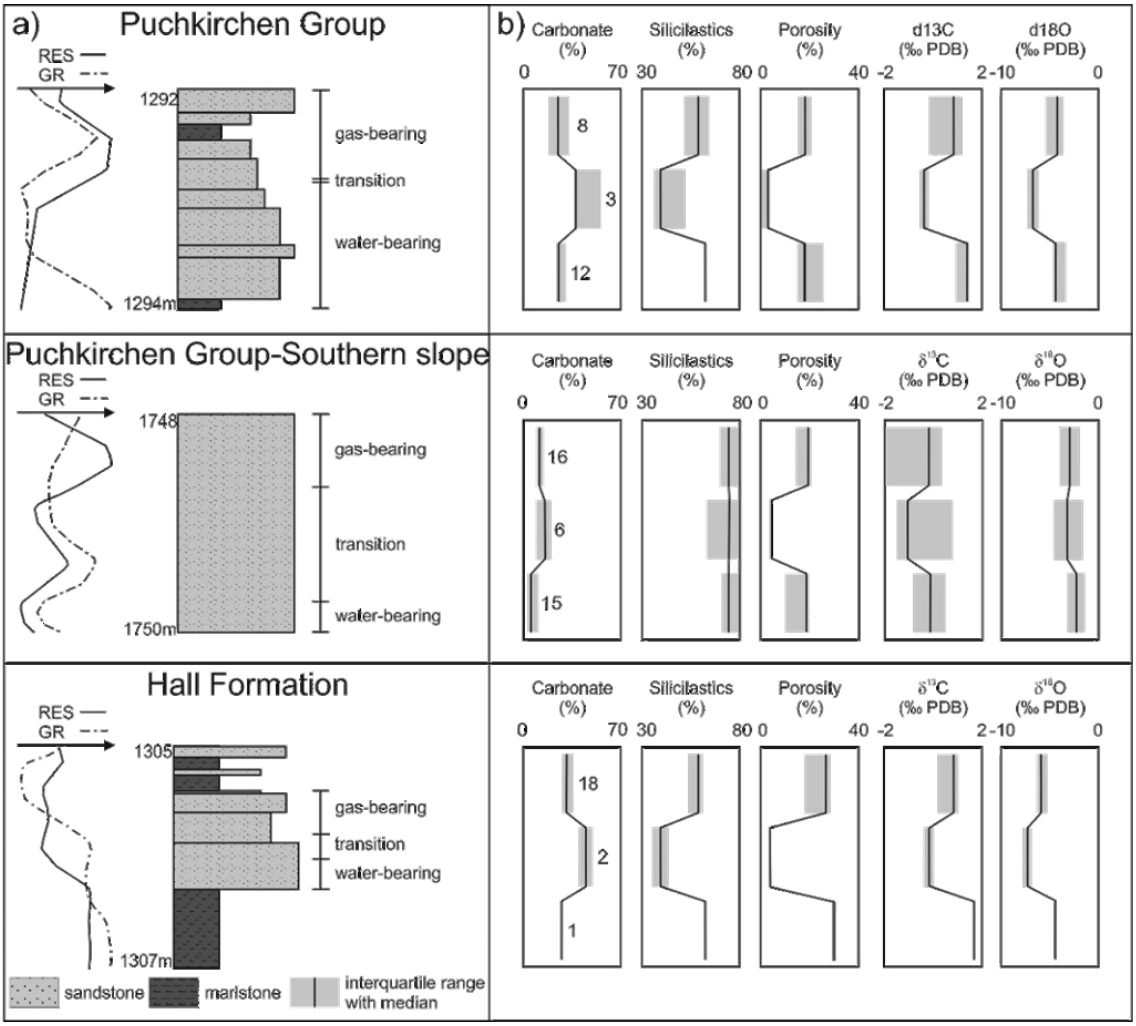

Fig. 21 a) Representative lithological profiles of the stratigraphic units (GR: gamma ray log; Res: resistivity log). b) Mineralogy, porosity and isotopic composition of the different units. Interquartile range (grey area) and median (black line) were calculated after Tukey (1977). The amount of samples from the particular horizons is given to the right of the boxes.

Sediments along the Chattian-Aquitanian Puchkirchen channel system are mostly feldspatic litharenites with high quartz content (up to 31%), feldspar content up to 8% and lithic fragments (schist, gneiss and rare sandstone remnants; 13%). In general carbonate content is about 23% and porosity is on average 24% (Figs. 22). Both, mono- and polycrystalline quartz grains are common. K-feldspar and plagioclase have been identified by XRD and microprobe analysis, where K-feldspar may reach up to 5%, and albite up to 3%. Low amounts of glauconite, chlorite, muscovite, iron oxides (e.g. goethite, hematite) and fossil remains (foraminifera, mollusk fragments) are detrital components. The fossils are reworked, partly disintegrated and recrystallized. Grains are angular to subangular (0.3) and show a subprismoidal sphericity of 0.5 (after Flügel, 1978). Sandstone samples are grain supported and moderate to well sorted.

In comparison, sandstones of the southern slope are significantly coarser grained and contain up to dm-sized clay and Lithothamnium Limestone clasts (Figs. 21a). The sandstones are composed of about 22% quartz, 6% feldspar (4% K-feldspar and 2% plagioclase) and 40% lithic fragments. They comprise a comparatively lower amount of carbonate minerals (8%) and are poorly sorted. Porosity is high with around 24%. In summary, the sediments can be classified as litharenites to feldspatic litharenites (Figs. 22a). In comparison to the channel deposits, fossils are more frequent and comprise fragments of foraminifera, bivalves, bryozoan and echinodermata.

Sediments of the northern slope contain 32% quartz, 12% feldspar (7% K-feldspar and 5% plagioclase) and 2% lithic components. They consist of fine-grained (to medium-grained) sandstones and are well sorted. Carbonate content is high (49%). Due to cementation porosity is low (<5%) (Figs. 22b).

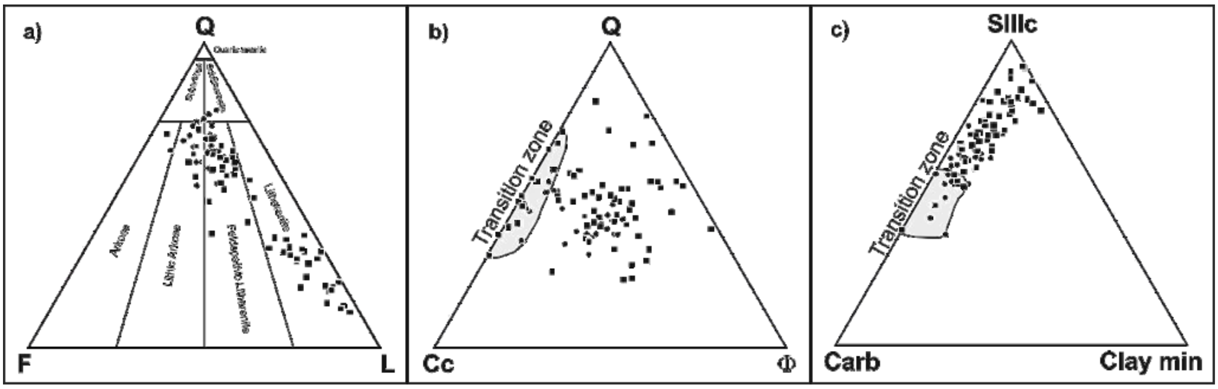

Fig. 22 a) Sandstone classification after Folk (1974), b) relationship between calcite (Cc), quartz (Q) and porosity (Φ) percentage and c) carbonate (Carb), siliciclastic (Silic) and clay minerals (Clay min) percentage for samples of Puchkirchen Group (rectangle) and Hall Formation (points).

Basal Hall Formation

Sandstones in the basal Hall Formation are similar to those in the Puchkirchen Group. They are bright grey sandstones intercalated with brown silty calcareous shales but their lithology is more homogenous than that of the sandstones from the Puchkirchen Group. A representative lithological profile from a core of the basal Hall Formation is shown in Fig. 21a. The thickness of sandstone layers in the Upper Austrian NAFB varies, but their mineralogical composition is similar. Sandstone horizons in the middle part of the basin are about 0.8 m thick, thicknesses in wells of the eastern part of the basin reach 3.5 m. Sandstones are medium-grained and show a good to moderate sorting. They are feldspatic litharenites to lithic arkoses with 33% quartz, 8% of feldspar (6% K-feldspar and 2% plagioclase) and 8% of lithic fragments on average (Fig. 22a). The mean carbonate content is 28% and porosity averages 22% (Figs. 22). Accessory fossil remains are also present and show reworking.

Sandstones of the northern part of the basin show a fining upward trend and are well to very well sorted. The mean mineralogical composition is 33% quartz, 9% feldspar (6% K-feldspar and 3% plagioclase) and 9% lithic fragments. Furthermore, they exhibit higher carbonate content (31%) and lower porosity (19%) than those from the basin axis (Fig. 22, 23). Reworked foraminifera are abundant within these sediments.

XRD analysis

Oligocene-Miocene samples of the NAFB are differentiated into three geographic settings:

- **Puchkirchen channel (channel belt)**

X-ray diffraction patterns from each zone, representative for channel sediments within the Upper Puchkirchen and Hall formations, are shown in Fig. 23.

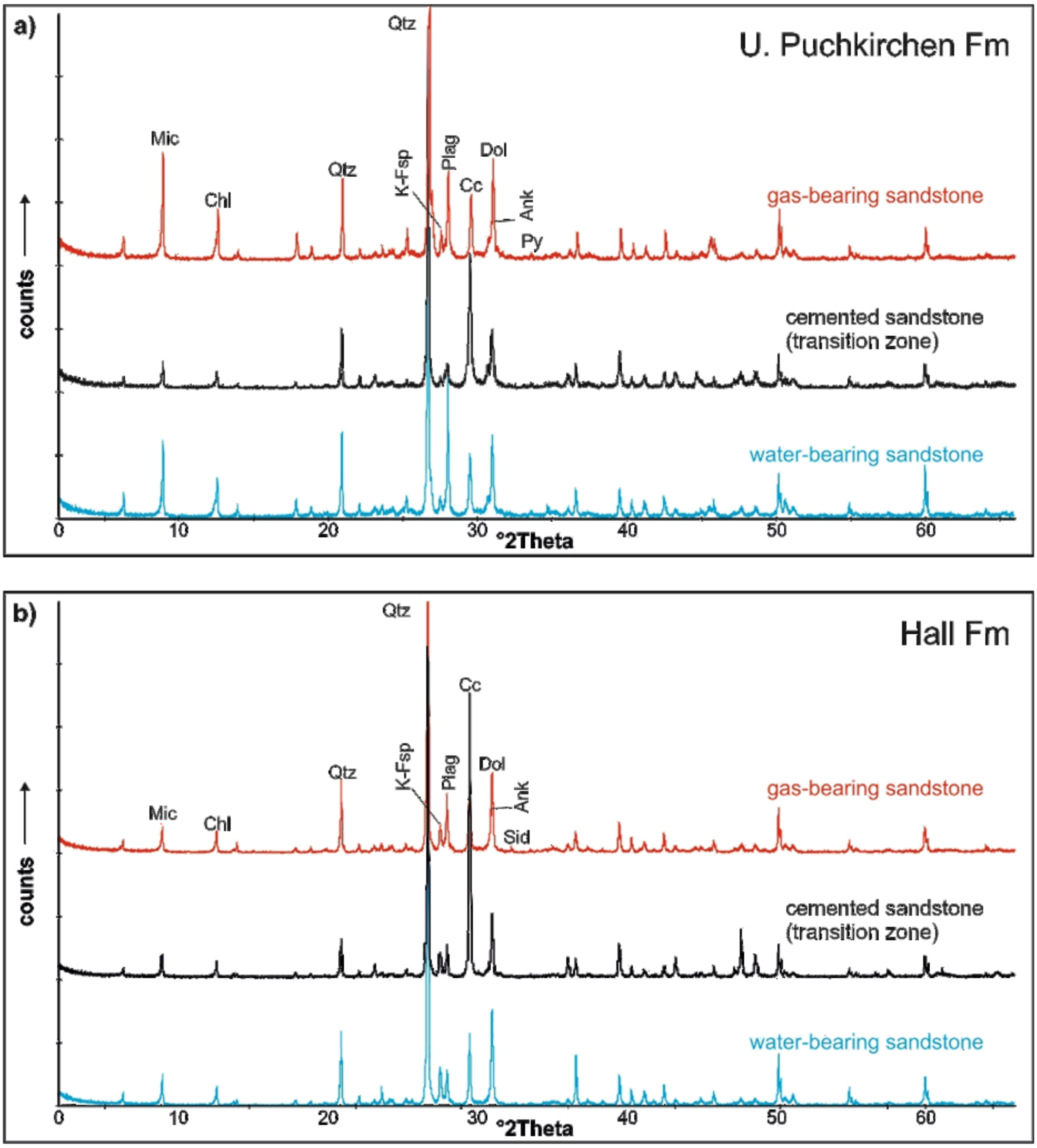

Fig. 23 Representative X-ray diffraction patterns of a water-bearing sandstone, a cemented sandstone from the transition zone and a gas-bearing sandstone from a) Upper Puchkirchen Formation and b) Hall Formation along the Puchkirchen channel (Mic=mica, Chl=chlorite, Qtz=quartz, K-Fsp=K-feldspar, Plag=plagioclase, Cc=calcite, Dol=dolomite, Ank=ankerite, Sid=siderite, Py=pyrite).

- **Northern slope of the NAFB**

X-ray diffraction patterns of representative samples of the northern slope of the NAFB are shown in Fig. 24. It comprises gas-bearing sandstone from the Upper Puchkirchen Formation, and sediments from the water-bearing and transition zone of Hall Formation.

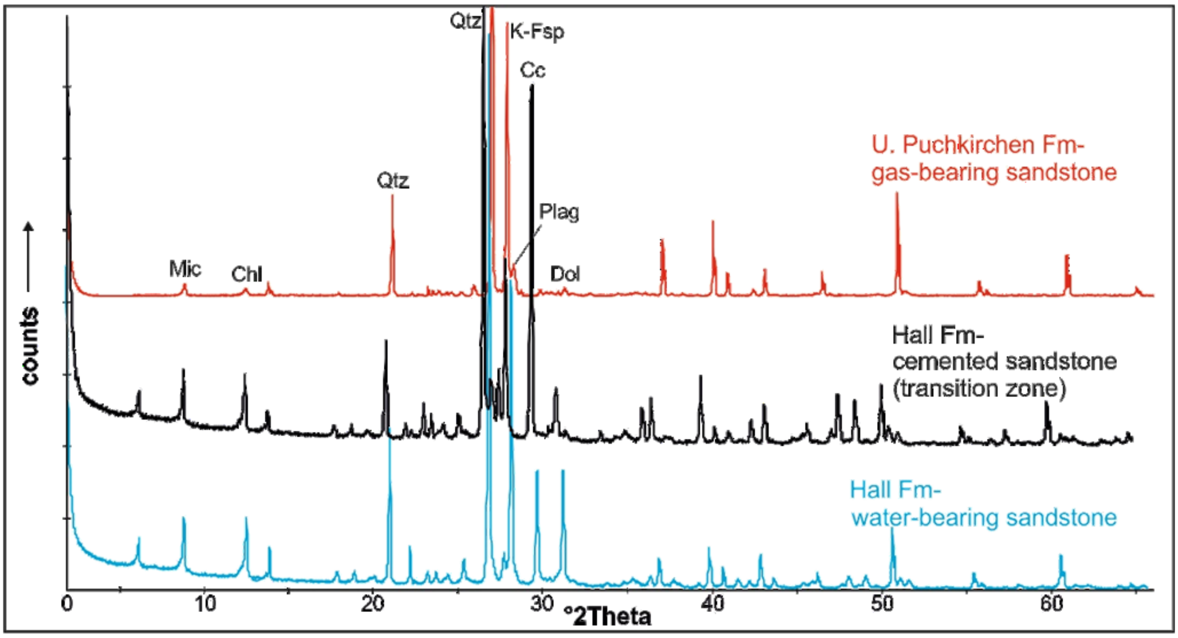

Fig. 24 Representative X-ray diffraction patterns of a water-bearing sandstone, a cemented sandstone from the transition zone and a gas-bearing sandstone from Upper Puchkirchen Formation (red, gas-bearing sandstone) and Hall Formation (black and blue, cemented and water-bearing sandstone) at the northern slope (Mic=mica, Chl=chlorite, Qtz=quartz, K-Fsp=K-feldspar, Plag=plagioclase, Cc=calcite, Dol=dolomite).

- **Sothern slope of the NAFB**

X-ray diffraction patterns representative for samples from the southern slope of the NAFB are given in Fig. 25. They belong to the Upper Puchkirchen Formation and comprise zones with different fluid content.

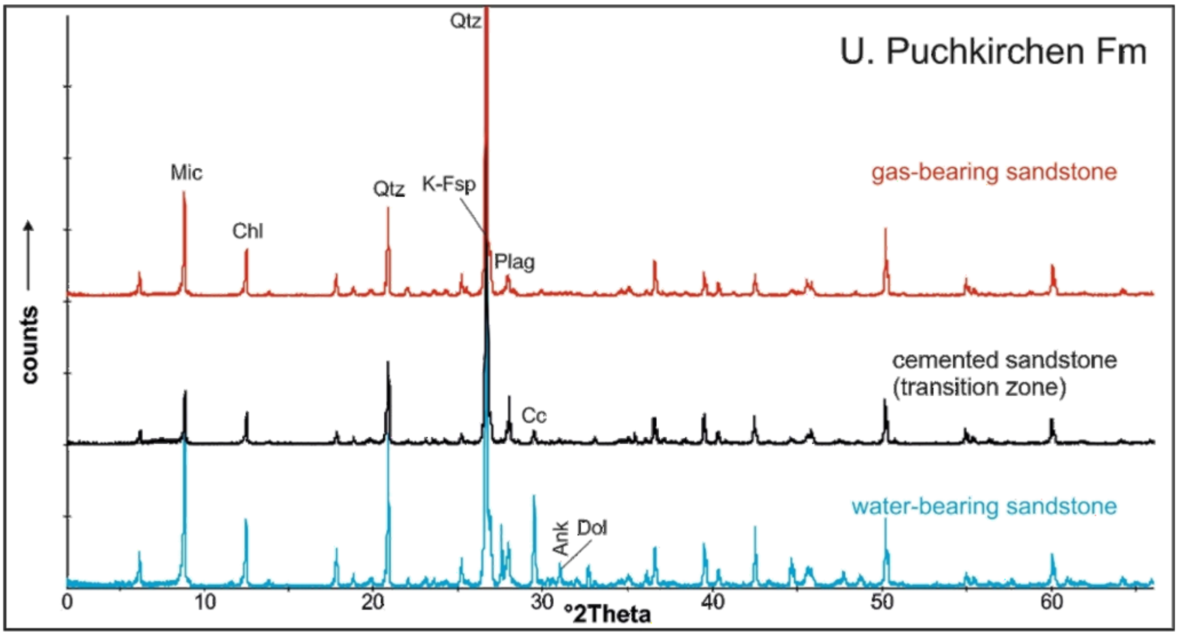

Fig. 25 Representative X-ray diffraction patterns of a water-bearing sandstone, a cemented sandstone from the transition zone and a gas-bearing sandstone from Upper Puchkirchen Formation at the southern slope (Mic=mica, Chl=chlorite, Qtz=quartz, K-Fsp=K-feldspar, Plag=plagioclase, Cc=calcite, Ank=ankerite, Dol=dolomite).

Based on the sedimentpetrographic investigations the mineralogy and porosity of all Oligocene-Miocene samples are summarized in Fig. 26. They were differentiated according to their stratigraphic age and geographic situation within the NAFB. Furthermore, the depth range of the samples below subsurface are indicated.

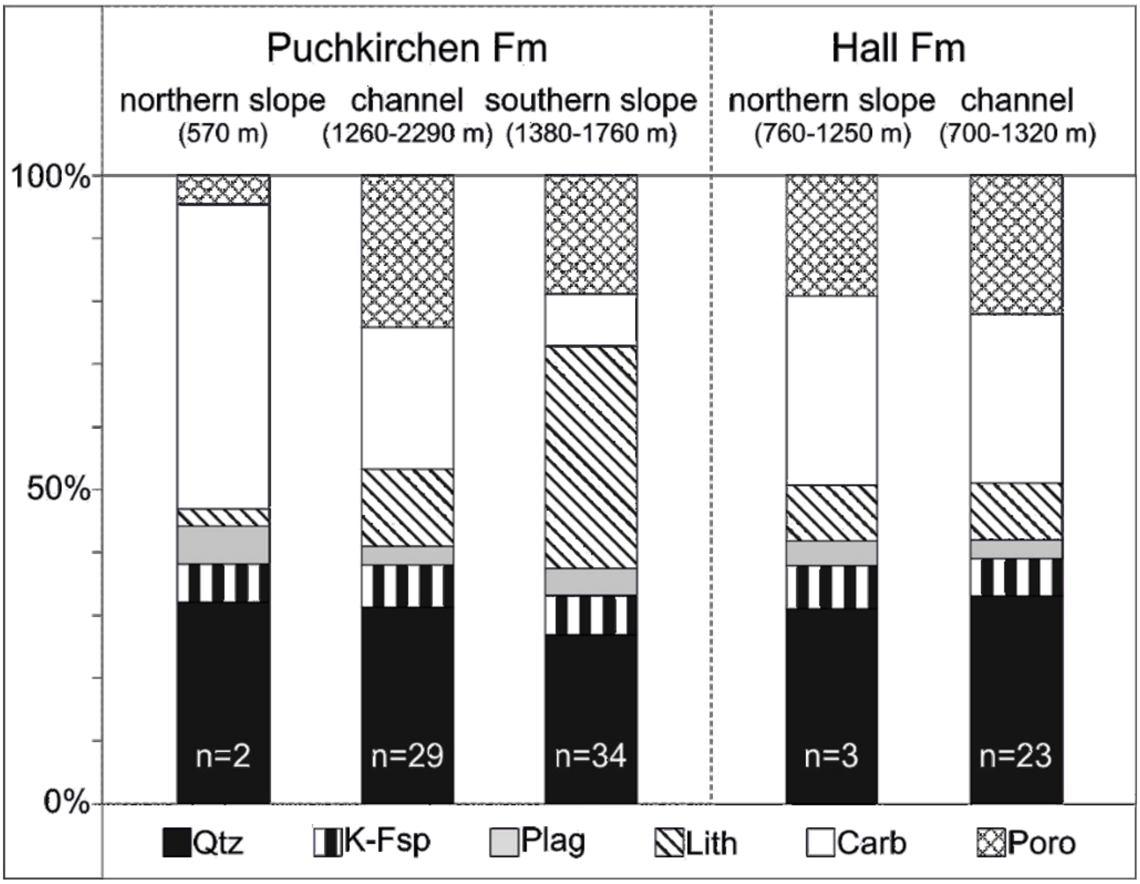

Fig. 26 Mineralogical composition and porosity (%) determined by point counting and semi-quantitative XRD analysis of samples from Puchkirchen Group and Hall Formation from different parts of the basin. (Qtz=quartz, K-Fsp=K-feldspar, Plag=plagioclase, Lith=Lithic fragments, Carb=carbonate, Poro=porosity; n=number of samples).

4.1.2. Diagenetic features

Transition zone

The transition zone can be defined as an approximately 10 cm thick tight zone at the GWC. The transition zone itself displays consistently homogenous properties. The difference of this zone in comparison to water- and gas-bearing zones is visible in Figs. 22-26.

The investigated samples from the transition zone originate from a depth of 1250 - 2290 m below ground level.

a. Thin section microscopy

Mineralogically, the tight zone is characterized by (i) a significant reduction in siliciclastics (from 63% to 32%) and (ii) a concomitant increase in carbonate cement minerals. Clay minerals occur in small amounts (<2%). Under the microscope accessory minerals (e.g. detrital carbonate grains, glauconite, and muscovite) and fossil remnants are visible.

The amount of authigenic carbonate minerals (>38%) is high in sandstones of this zone (Figs. 27a,b). Calcite is the main cement phase (25%) followed by dolomite (10%). Ankerite and siderite are present only in trace amounts (~1%). Three separate calcite cement generations enclosing detrital grains are visible (nomenclature of cement morphology sensu Flügel, 2010) (Figs. 27c,d):

- Calcite I (Cc I): very rare columnar calcite, as rim around grains
  Comm. This calcite type was observed only within the strongly cemented sandstones of the transition zone.
- Calcite II (Cc II): microcrystalline (micritic) calcite
- Calcite III (Cc III): blocky/homogenous calcite, surrounding Cc I and Cc II

The strong cementation results in a decrease in porosity and permeability along the GWC and is accompanied by an enhanced dissolution of siliciclastic grains. The partial corrosion of detrital grains effects minerals such as quartz, feldspar and glauconite (Figs. 27e,f). In addition, replacement of grains by carbonate minerals is also evident (Figs. 27g,h).

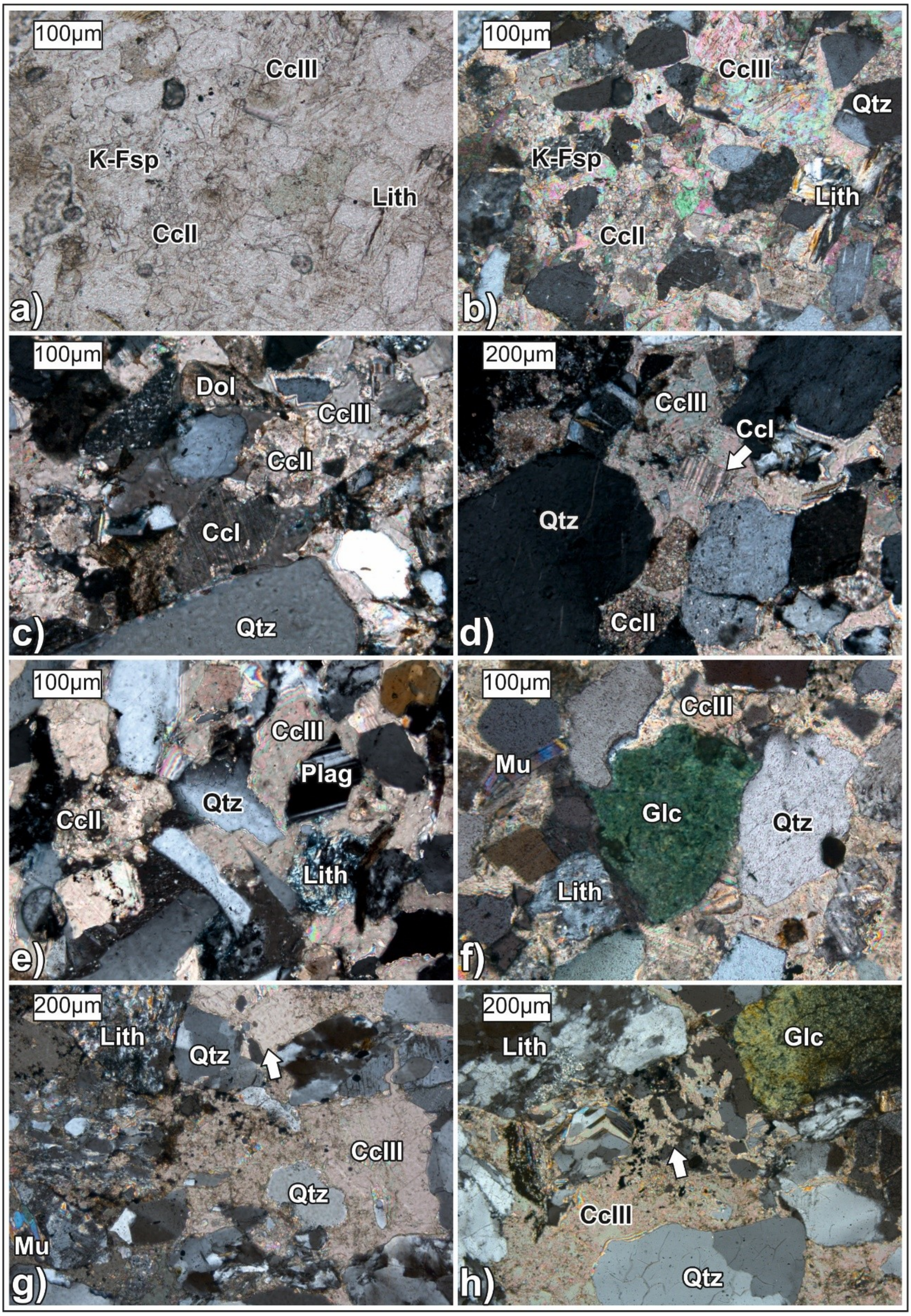

Fig. 27 Thin section photographs of cemented Oligocene-Miocene sandstones: a,b) overview of the texture in plane- and cross-polarized light; c,d) three carbonate cement generations (Cc I-Cc III); corrosion marks of the margin of e) quartz and f) glauconite detrital grains; g,h) partial replacement of detrital polycrystalline quartz by carbonate cement.

b. Cathodoluminescence microscopy

CL-microscopy indicates heterogeneities of the different calcite cement types (Figs. 28a,b). Calcite I has a bright orange color. Calcites II and III show a brownish-orange luminescence. Microcrystalline cements (Cc II) and dolomite exhibit higher color intensities than Cc III. Besides, a foraminifer appears within the cement.

The older carbonate generations (Cc I and Cc II) are present between grains (Figs. 28a-h). Fossils, represented by a shell (Fig. 28c) and a foraminifer (Fig. 28d), become visible under cathodoluminescence stimulation and have similar bright orange color like Cc II.

K-feldspar and plagioclase grains are visible in Figs. 28b,d,e,f,g. Both reveal partial corrosion marks at the contact to the carbonate cement. The partial replacement of a quartz grain by bright orange Cc II is evident in Figs. 28c,h.

The blocky morphology of Cc III is also visible with a dark-orange color in the cathodoluminescence images (Figs. 28b,c). Cc III encases the grains, and authigenic Cc I, Cc II and dolomite particles (Figs. 28b,c,f,g). In addition, Cc II exhibits corroded rims (Figs. 28f,g) at contact to Cc III.

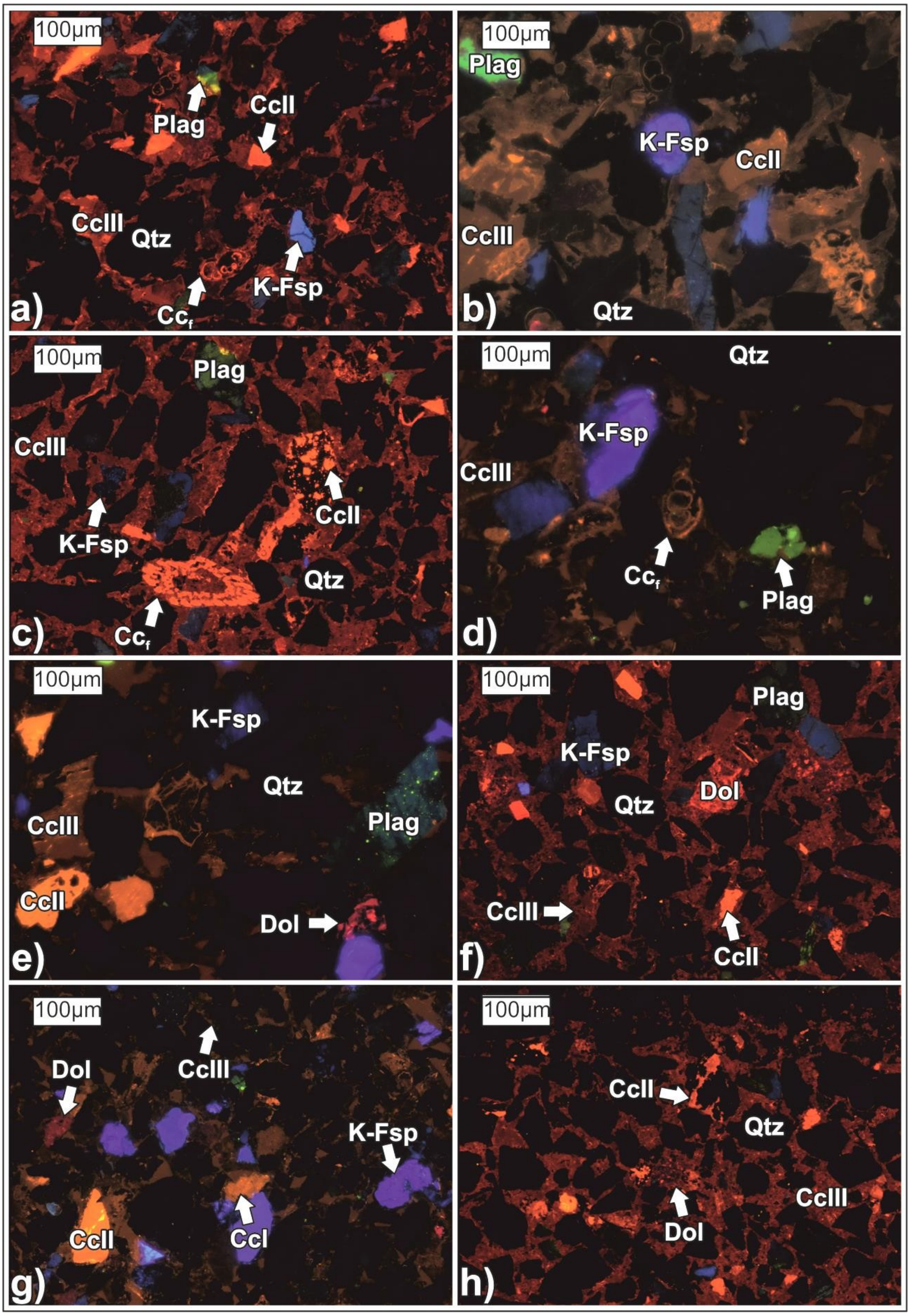

Fig. 28 Cathodoluminescence images of cemented Oligocene-Miocene sandstones: a,b) different calcite cement types show different orange CL-colors, whereas Cc III is the main pore filling cement phase; c,d) Fossils (shell, foraminifer); e.-g) K-feldspar and plagioclase grains with corrosion marks; g,h) replacement of quartz grain by Cc II.

c. Electron microprobe microscopy

Results of microprobe analysis of the samples from the transition zone are presented in Fig. 29. An overview of the texture is presented in Fig. 29a. Thereby it is evident that the sediment is completely cemented by carbonate.

In Figs. 29a,b the carbonate generations Cc II and Cc III, as well as the primary components (quartz, feldspar and lithic fragments), are presented. Locally, feldspar grains have overgrowths with same chemical composition. The darker color of the rim in Fig. 29c suggests a higher proportion of heavy (Si, Al), and lower proportion of lighter (K) elements. A detail of the carbonate types between grains is shown in Fig. 29d, where the presence of calcite, dolomite and siderite is evident.

Note also the presence of corrosion marks on quartz grains and that dolomite rhombs are frequently zoned (Fig. 29d). Further the different feldspars K-feldspar, albite and anorthite are present, but the last two occur only in small quantities (Fig. 29e).

In Figs. 29f,g the mineral replacement of detrital particles (e.g. quartz) by the surrounding carbonate cement Cc III is visible. Calcareous fossils (e.g. shell) and framboidal pyrites are also encased by Cc III (Figs. 29e,g). The paragenetic relationship of the carbonate types is evident in Figs. 29f,h, where dolomite, ankerite and calcite Cc II are encased by Cc III. Cc III is the main carbonate cement phase in the transition zone and consists of pure Ca-carbonate (Figs. 29a-h).

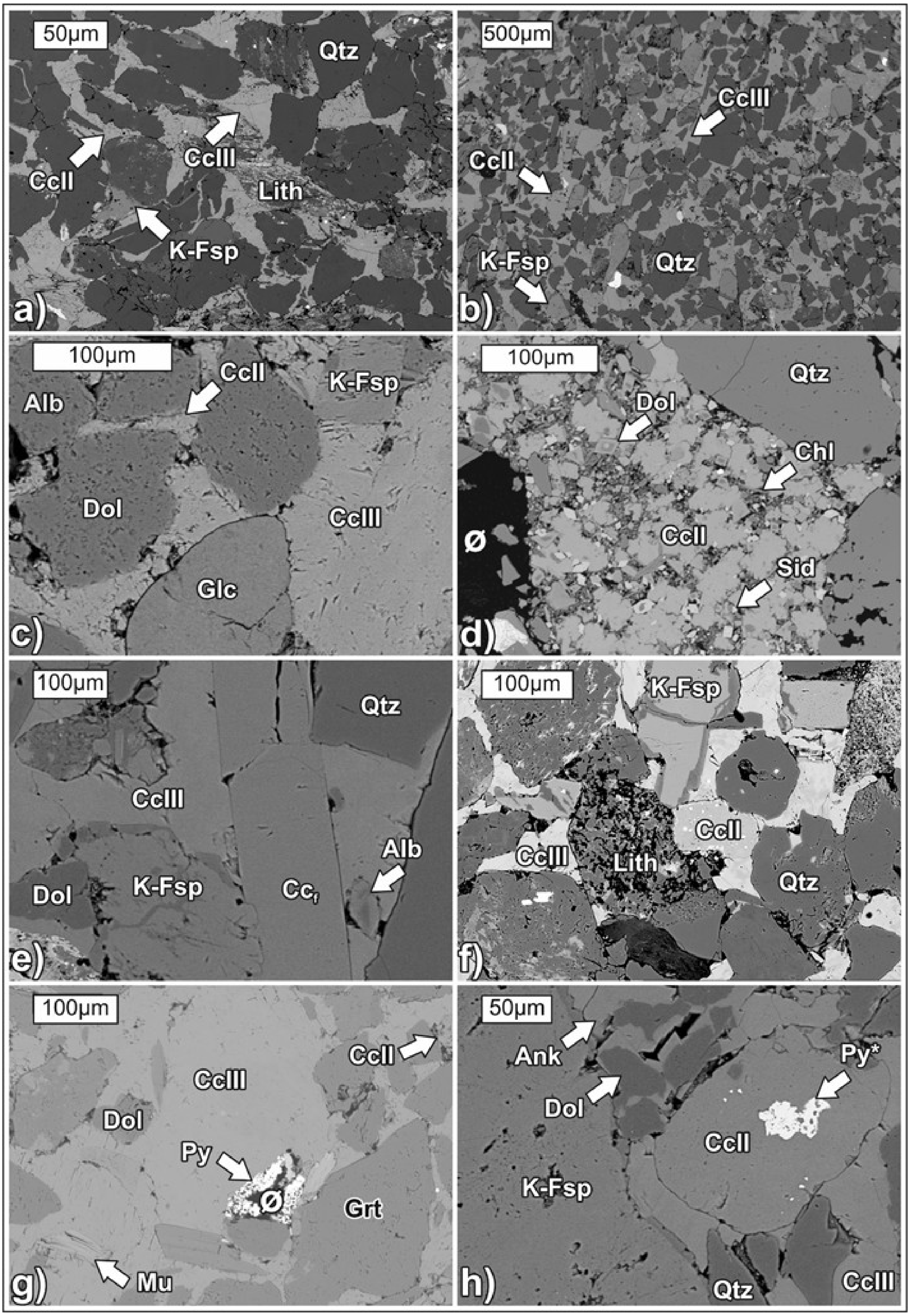

Fig. 29 BSE-images of cemented Oligocene-Miocene sandstones: a,b) carbonate generations Cc II and Cc III; c) different carbonate minerals at interstices; d) Feldspar types; e,f) replacement of siliciclastic grains by Cc III; g) Cc II, dolomite and ankerite encased by Cc III; h) Cc III is the dominant cement type.

WDX maps of three samples are shown in Figs. 30, 31 and provide information on geochemical composition of detrital grains and authigenic cements. The paragenetic relationship of the minerals is apparent based on the element distribution. The elements Ca, Mg, Mn and Fe were selected for illustrating the composition of the carbonate phases; Si, Al, K and Na to differentiate feldspar and clay mineral types, and quartz.

The presence of dolomite (Ca, Mg), siderite (Fe) and ankerite (Ca, Mg, Fe, Mn) is evident. The carbonate types calcite (Ca) and dolomite predominate (Fig. 30). Please note the zonation of the dolomite rhombs in Fig. 31a. Especially, along margins, the calcite is slightly enriched in Mg and Fe (Fig. 31a). In the upper part of Fig. 31b the interstices filling between two detrital grains, both lithic fragments (Si, Al, K, Na, Mg, Fe), is visible. The cement in this area comprises in different carbonate types, indicated by the abundance of the elements Ca, Mg and Fe. Thus, the presence of calcite (Ca), dolomite (Ca, Mg), and siderite (Fe) is evident. As it is visible from the Ca-map, the carbonates in the interstice appear in particles.

Besides quartz (Si), other grains are represented by feldspar and lithic fragments. All silicate grains display corroded margins at contact with carbonate (Figs. 30, 31). The feldspars K-feldspar (Si, Al, K) and albite (Si, Al, Na) are predominant (Fig. 30). Also lithic fragments show some Ca-spots, which might be a sign of incipient replacement by calcite (Fig. 31b).

Cc III is the main carbonate cement phase in the transition zone and consists of pure Ca-carbonate (Figs. 30, 31). Along the margin of the detrital particle in Fig. 31b on the left side a seam forms, which is slightly enriched in Mg and Fe. It resembles to the mineral phases in the interstice in Fig. 31a. Indeed, it was established by microscopy, that this Ca-carbonate is the dominating pervasive cement within this sample.

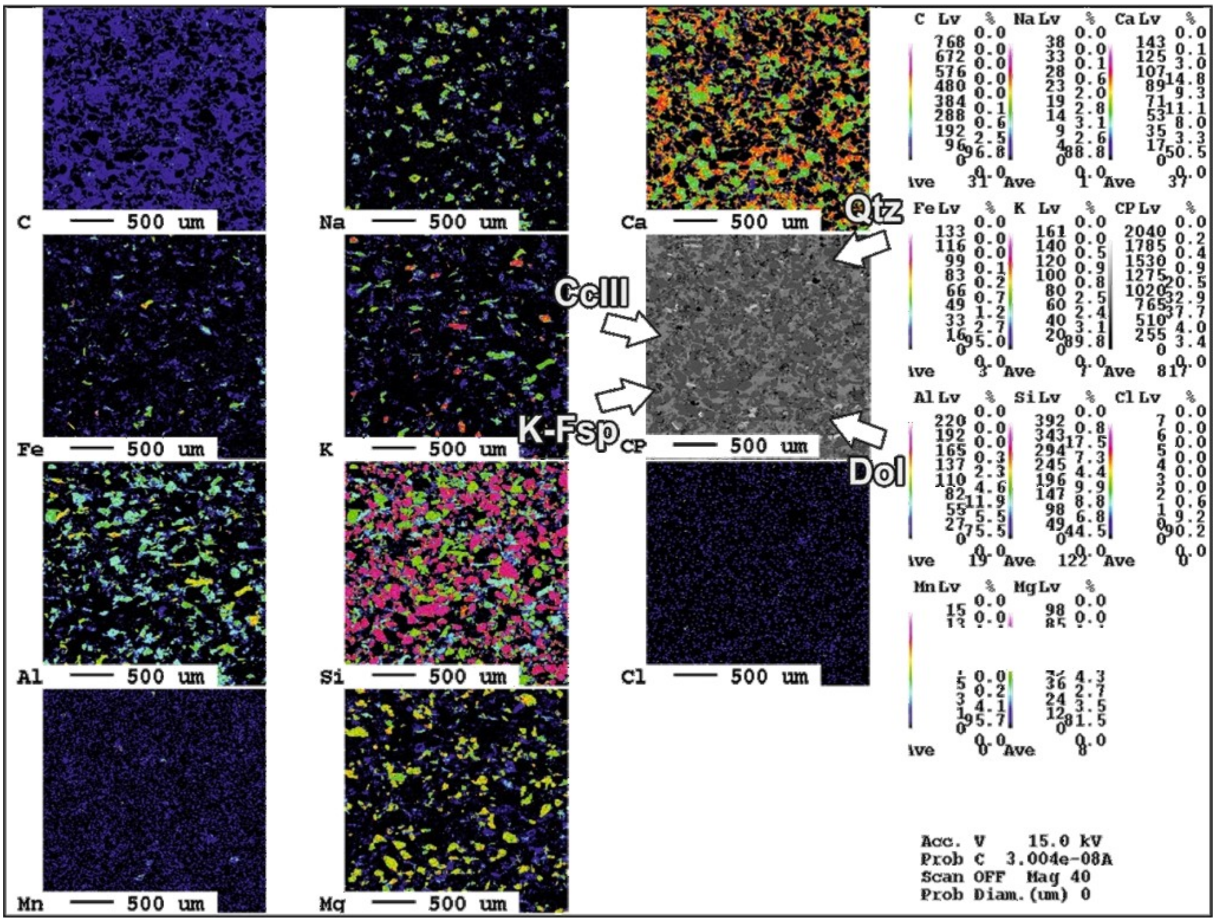

Fig. 30 Wave length dispersive (WDX) element maps of cemented Oligocene-Miocene sandstone in transition zone (CP=BSE image).

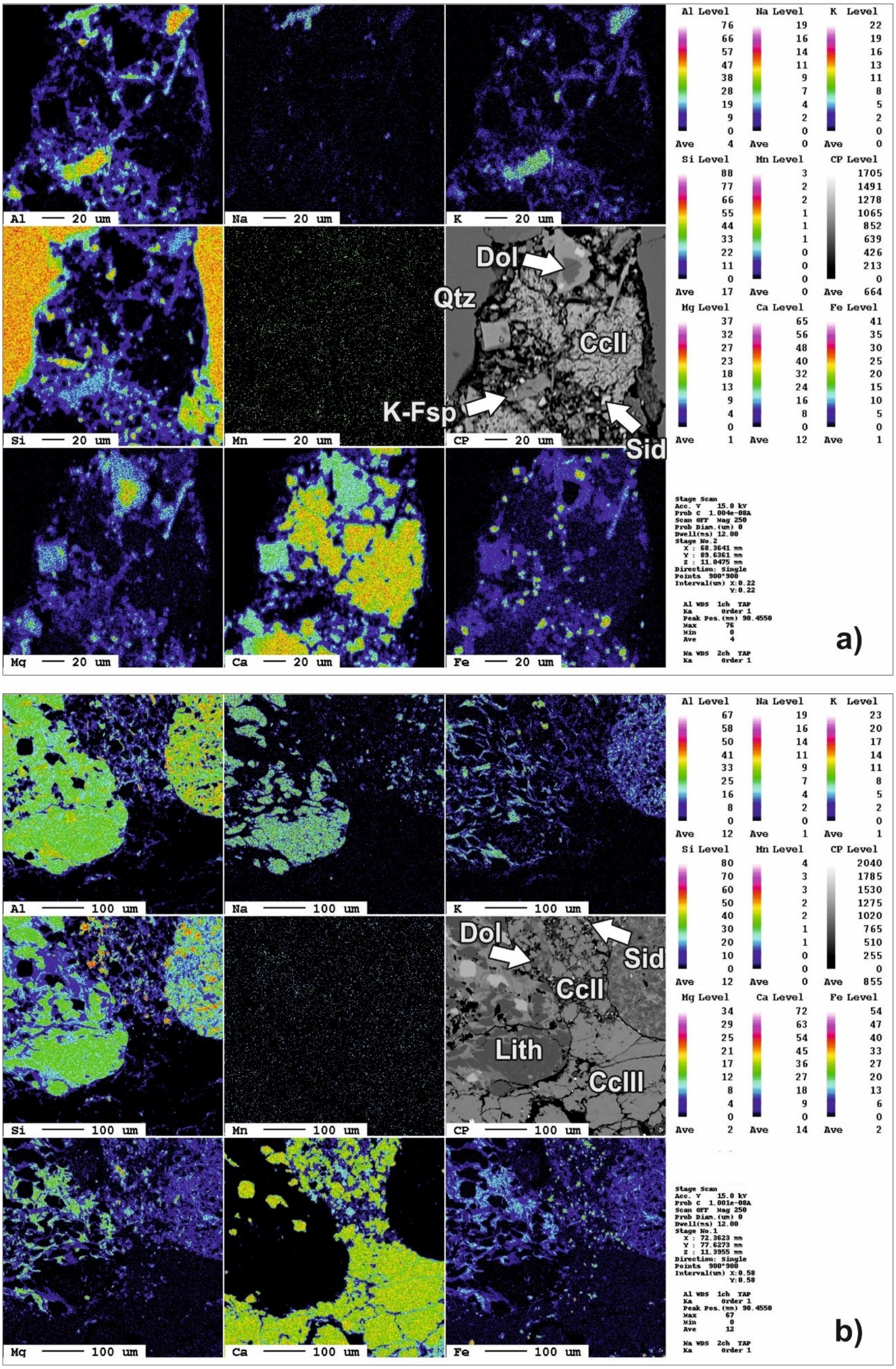

Fig. 31 Wave length dispersive (WDX) element maps of cemented Oligocene-Miocene sandstones in transition zone of a) Hall and b) Upper Puchkirchen Formation (CP=BSE image).

d. Scanning Electron Microscopy

SEM-pictures provide information on the morphology and growth pattern of minerals and their spatial relationship (Fig. 32). Fig. 32a offers an overview of the texture of the cemented samples from the transition zone.

Detrital grains, like the dominating mineral phase quartz are embedded in calcite cement (Fig. 32b). Quartz grains have a rough surface.

A close up view of a calcite crystal is shown in Fig. 32c. Here, the blocky formation of this carbonate is visible. Dolomite forms as rhombohedral minerals (Fig. 32d).

The eogenetic carbonate minerals calcite Cc II and dolomite display some corrosion marks, but the paragenetic relationship of them is not discernible (Fig. 32d,e). The corrosion marks of dolomite rhombs are remarkable (Fig. 32c,d).

Note that the grains are covered by carbonate and only their relief of them is visible (Figs. 32a,c). In detail, the relationship of the grains is portrayed by Fig. 32b. It is clear, that the grains are encased and the pores are filled by carbonate, which shows different states of mineral firmness. Cc II is located between grains, whereas Cc III seems to cover the detrital grains and Cc II, as it is also visible in Fig. 32a. The structure of calcite Cc III is evident from Figs. 32e,f. It shows a lamellar structure within the former open pores. Furthermore, the fine crystal growth of calcite is shown in Figs. 32g,h. In Fig. 32f a single columnar calcite crystal is present. It is embedded in a fine grained carbonate cement (Cc III).

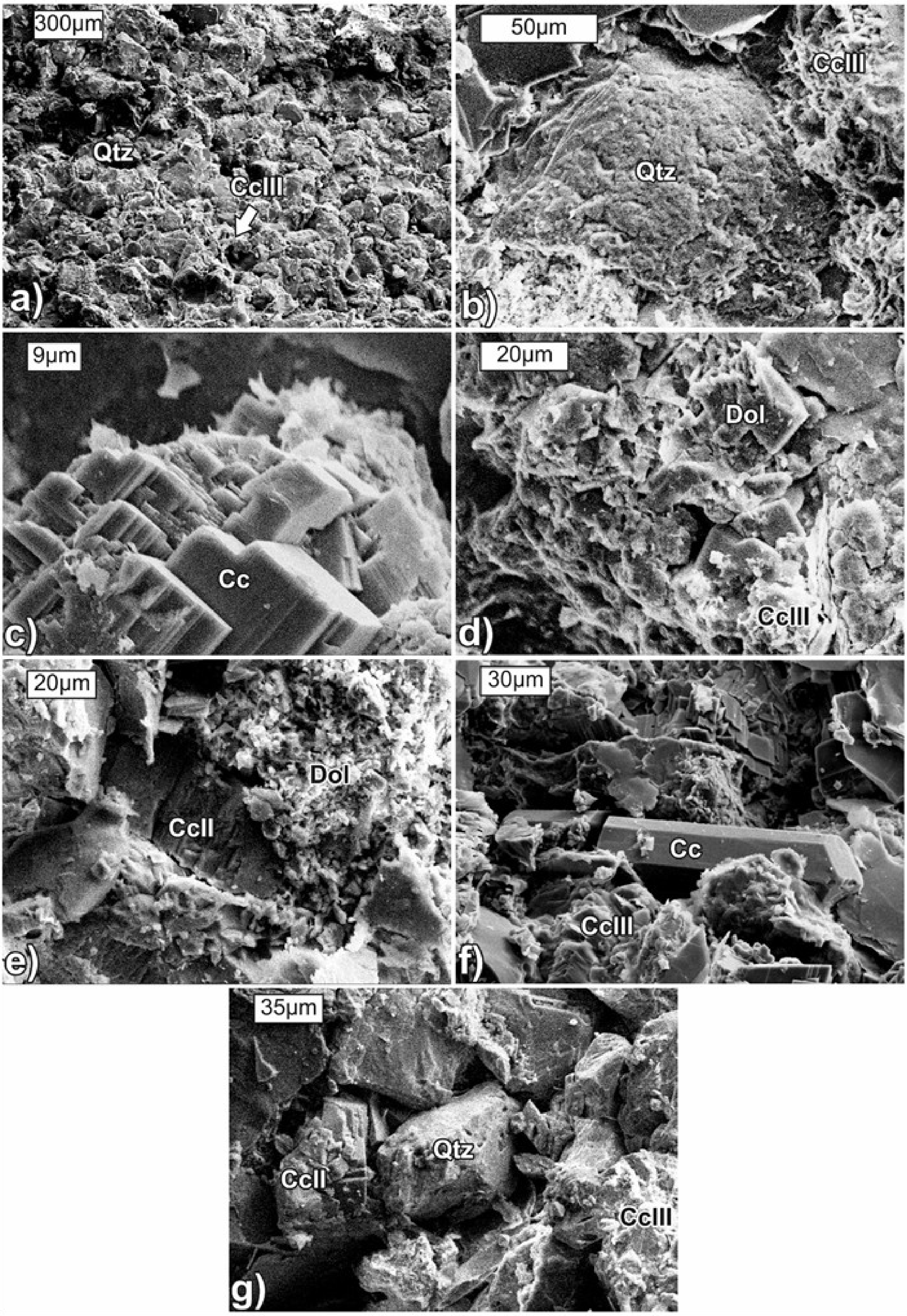

Fig. 32 SEM-images of cemented Oligocene-Miocene sandstones: a) overview of the texture of the transition zone; b) quartz grain surrounded by calcite cement (Cc III); c) calcite crystal; d,e) carbonate types calcite (Cc II and Cc III) and dolomite; f) calcite crystal surrounded by Cc III; g) calcite (Cc II and Cc III) appears as pore filling between grains.

Water-bearing zone

The investigated samples from the water-bearing zone originate from a depth of 1250 - 2290 m below ground level.

Semi-quantitative and qualitative analysis of the mineral phases in water-bearing sandstones, from all investigated samples, are shown in Figs. 22-26. The amount of authigenic carbonate minerals is about 15% consisting mainly of calcite (Cc II and Cc III; 7%) and dolomite (4%), whereas ankerite and siderite are present in traces (each ~1%). The average of quartz is 24%, of feldspar is 7% and of lithic fragments (24%). Clay minerals (6%) and mica (5%) are of minor importance. Glauconite, pyrite, detrital carbonate grains and fossils occur as accessories. Sandstones of the water-bearing horizon have a mean porosity of 19%, which was measured in the lab.

a. Thin section microscopy

The texture is loosely grain supported, partly cement-supported in these sandstones. Relative high porosity values are a result of interparticle porosity (Figs. 33a,b). At the partial dissolved carbonate relicts some intraparticle porosity occurs.

Similar to the sandstones from the transition zone, two carbonate generations (Cc II, Cc III) are evident (Fig. 33c). Carbonate cement displays a microcrystalline (Cc II) and a blocky/homogenous (Cc III) morphology. But in contrast to the transition zone Cc II dominates. Some microfossils are preserved. Fossils (e.g. foraminifera) are comparably well preserved and little compacted. Occasionally they are filled with pyrite or with carbonate cement (Cc II and Cc III) (Fig. 33d).

Different types of secondary porosity after Füchtbauer (1988) are present, such as oversized pores (see also Fig. 3e) and pores resulting from leaching and mineral replacement (Figs. 33c,f,g). Carbonate cements show distinct dissolution features (Fig. 33h). Hence, only remnants of carbonate cement are present.

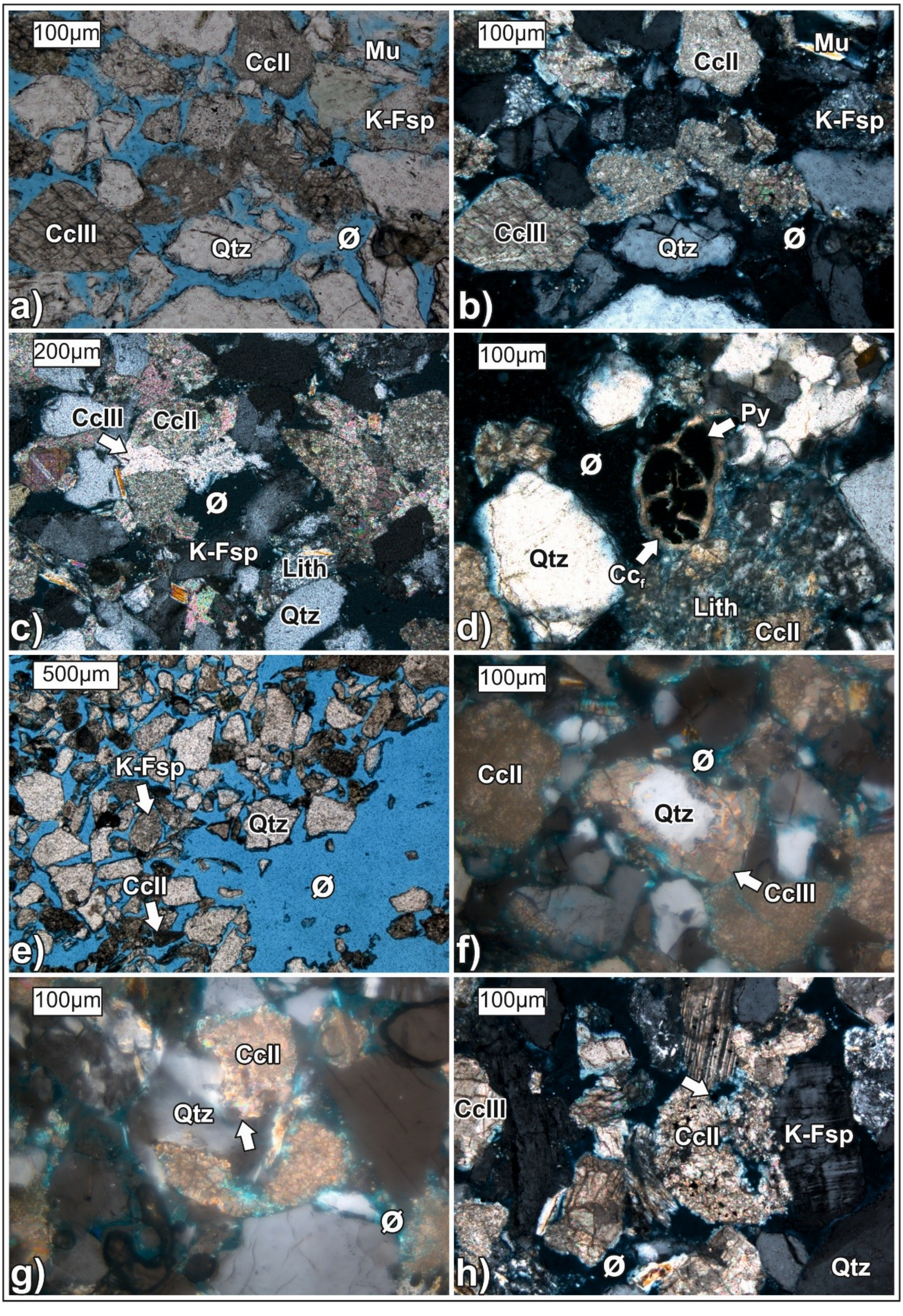

Fig. 33 Thin section photographs of Oligocene-Miocene water-bearing sandstones: a,b) overview of the texture in plane- and cross-polarized light; c) paragenetic relationship of Cc II and Cc III. Cc III shows etched marks generating secondary porosity; d) foraminifera filled with framboidal pyrite; e) oversized pores appear in loose texture; f,g) corrosion marks at the margin of quartz grains; h) partial dissolution of Cc II increases porosity

b. Electron microprobe microscopy

Electron microscope images in Fig. 34 provide information on chemical composition of grains in water-bearing sandstones. A broad view of the particles is shown in Fig. 34a. In comparison to the transition zone, increased porosity is apparent.

From Fig. 34b it is visible, that quartz, lithic fragments, feldspar and calcite are the main mineral phases. Different feldspars, including K-feldspar (Si, Al, K) and albite (Si, Al, Na) are present (Fig. 35), whereat K-feldspar prevails. Calcite (Ca) is the dominant pore filling type. K-feldspar overgrowths occur around feldspar grains and as healings of fissures in feldspars (Fig. 34c). Chemical differences of detrital and authigenic phases were measured with the microprobe. Measurements show a depletion of K^+ in the authigenic phase in comparison to the detrital feldspar. The increase of Fe, Mg, (and Mn) elements indicates, that besides dolomite (Ca, Mg), also siderite (Fe) and ankerite (Ca, Fe, Mg) occur in low amounts. Further, the presence of the chlorite is evident, which is encased by the Cc II (Fig. 34d).

Partial dissolution and replacement of detrital quartz grains by carbonate cement is apparent in Figs. 34d,e. Besides, K-feldspar shows dark grey rims, which are depleted in K content.

Carbonates cements occur as relicts and consist mainly of calcite (Ca). Relictic carbonate cement is present between detrital grains in Figs. 34a-f. Oversized pores are evident as well.

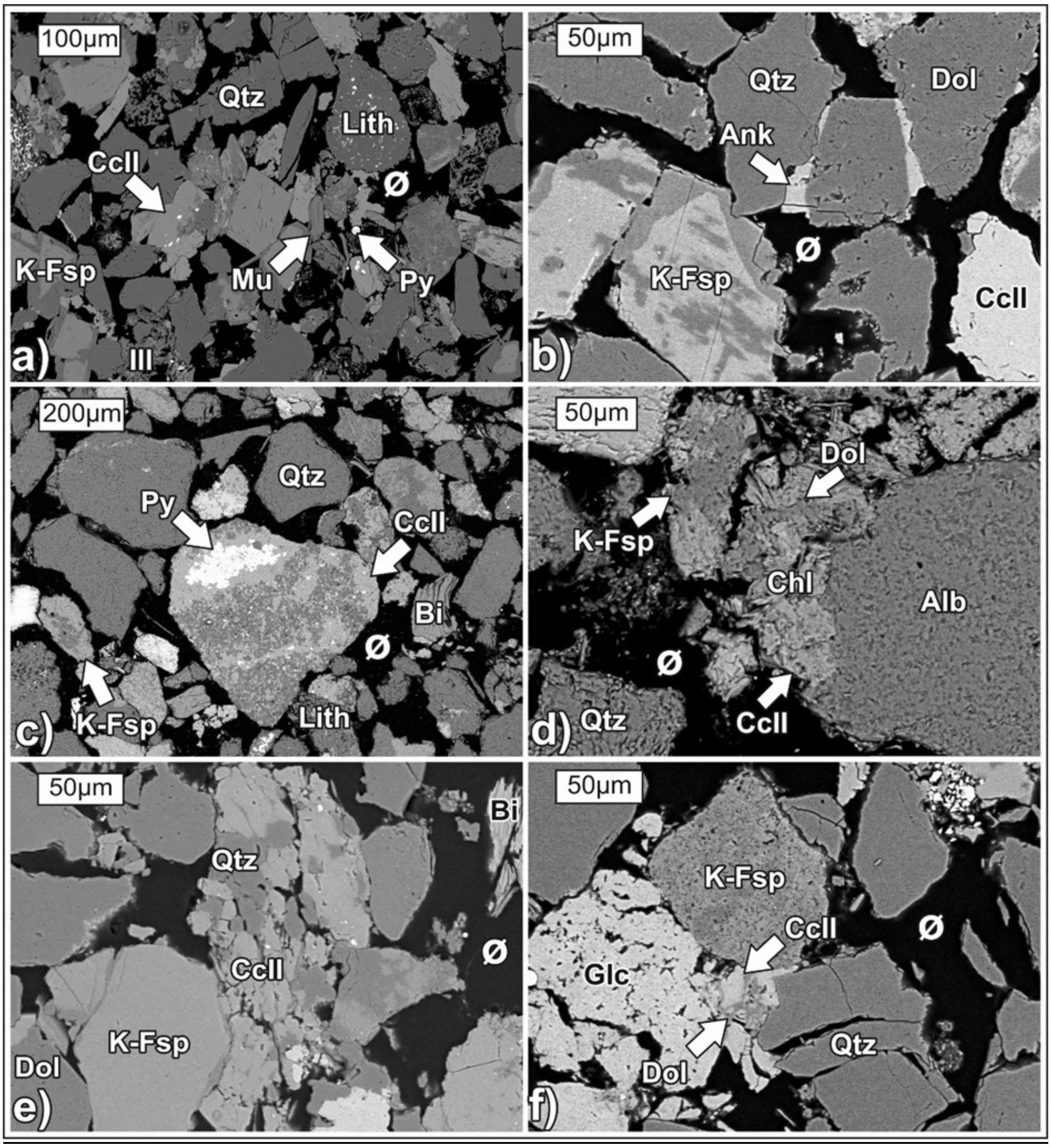

Fig. 34 BSE-images of water-bearing Oligocene-Miocene sandstones: a) overview of the texture with relictic carbonate cement as pore filling; b) main mineral composition of these sandstones; in the centre partial replacement of quartz grain by carbonate; c) strongly corroded calcite at the margin of a feldspar grain; dolomite is also present and surrounded by this relictic cement; d) Cc II encases quartz grains and replaces it partially, the calcite itself displays also a fragmented character; c) relictic carbonate is present between siliciclastic grains, which is represented by calcite and dolomite; f) the relictic appearance of carbonates (Cc II and dolomite) is evident, further quartz shows distinct corrosion marks as well.

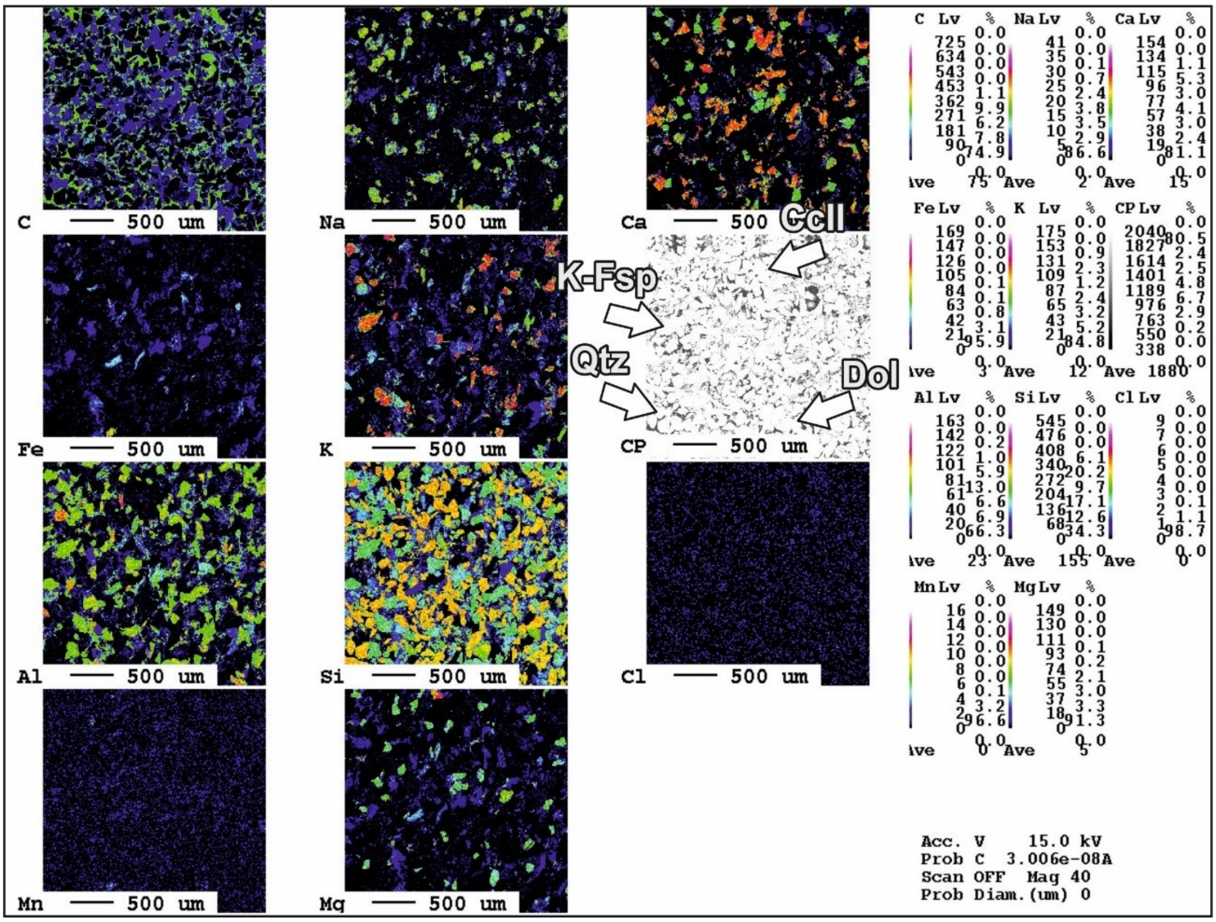

Fig. 35 Wave length dispersive (WDX) element maps of an Oligocene-Miocene sandstone in the water-bearing zone (CP=BSE image).

c. Scanning Electron Microscopy

To illustrate the mineral morphology, growth and relationship of the grains, selected samples from the water-bearing horizon were investigated with SEM.

An overview of the texture is presented in Figs. 36a,b, thereby quartz and calcite particles are visible. Mica, mainly muscovite, is characteristic for the mineralogical composition of these Oligocene-Miocene samples. Muscovite flakes seem to be pinched and deformed between grains, indicating light to medium compaction (Figs. 36c,d). In comparison to the pictures from the transition horizon, the single grains are more clearly visible and not covered with carbonate. Moreover, feldspar is covered with some isochemical overgrowth (Fig. 36b). Between these particles framboidal pyrite formed (Fig. 36b). Pyrite occurs as framboids (Fig. 36e) and as polyhedral crystals (Fig. 36f).

In Fig. 36g, smectite, locally with a webby morphology, covers a K-feldspar grain, which shows a relative well preserved habitus. On the right side of this image chlorite platelets are visible, also in the interstices between grains.

The high-resolution picture of Fig. 36h shows calcite cement with a rough surface.

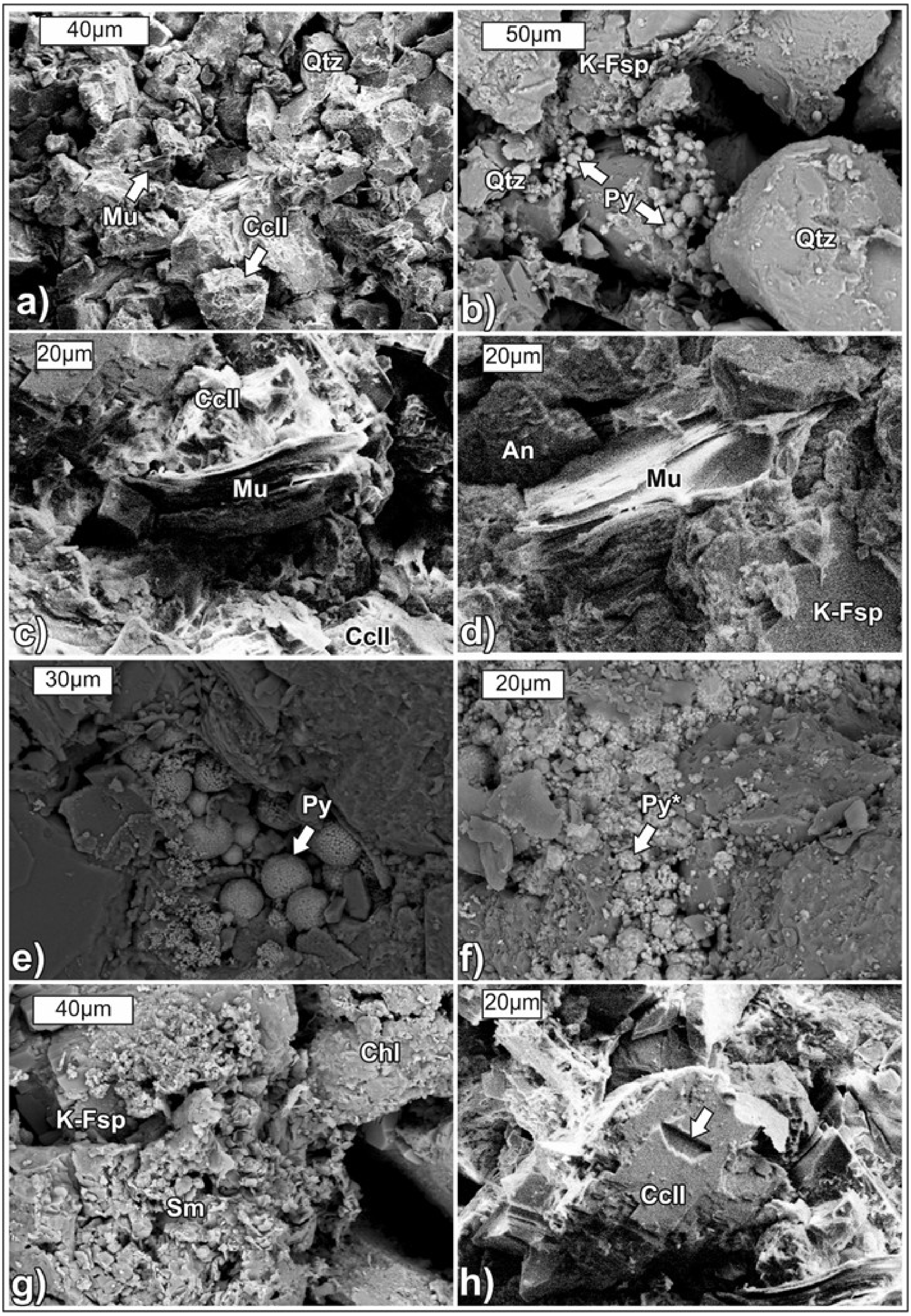

Fig. 36 SEM-images of water-bearing Oligocene-Miocene sandstones: a) overview of the texture of the higher permeable zones; b) pore space distribution and its filling with pyrite; c,d) muscovite flakes wedged between grains; e) framboidal pyrite and f) polyhedral pyrite; g) pore space distribution and its filling with pyrite and smectite; h) calcite component with rough surface.

Gas-bearing zone

The investigated samples from the gas-bearing zone originate from a depth of 570 - 2230 m below ground level.

Gas-bearing sandstones are often characterized by a loose and crumbly consistency, so that only fist-sized chunks of these reservoir rocks are left in the core boxes. Nevertheless, the amount of authigenic carbonate minerals is high (19%) within all investigated gas-bearing samples of the NAFB. Calcite cement (10%) has a microcrystalline (Cc II) as well as a blocky morphology (Cc III). Moreover, dolomite is present with 7%, and ankerite and siderite in traces with 1% each. Siliciclastic grains account for 47%, whereof quartz constitutes 26%, feldspar 6% and lithic fragments 15%. Clay minerals (6%) and mica (5%) are rare and the porosity, measured in the lab, is about 23%. Accessory minerals consist of glauconite, pyrite, detrital carbonate grains and fossils. The qualitative and semi-quantitative analysis of the mineral content of gas-bearing sediments is indicated in Figs. 22-26.

a. Thin section microscopy

Microscopically, sandstones of the gas-bearing zone are similar to those of the water-bearing zone (Figs. 37a,b).

In addition to the main components, quartz and feldspar (K-feldspar), also detrital glauconite pellets occur in these gas-bearing sediments (Figs. 37a,b). The preservation of shells during compaction is good. Occasionally, space between the separated chambers of the fossil is filled with carbonate cement (Fig. 37c). The early carbonate generations of microcrystalline Cc II and blocky/homogenous Cc III are present as well (Fig. 37d). The amount of the microcrystalline cement exceeds that than of the blocky/homogenous one.

K-feldspar is replaced by carbonate. K-feldspar grains have etched margins at contact to microcrystalline Cc II (Figs. 37e,f) locally. Similarly, quartz exhibits strongly etched and wavy margins next to Cc II (Fig. 37g).

Oversized pores (Füchtbauer, 1988) occur locally (e.g. Fig. 37h). The fragmented appearance of the two cement types Cc II and Cc III is recognizable. Both are relicted and poorly preserved, which generates secondary porosity (Fig. 37d-f). Furthermore, replacement of a quartz grain by carbonate (Cc III) is evident (Fig. 37g).

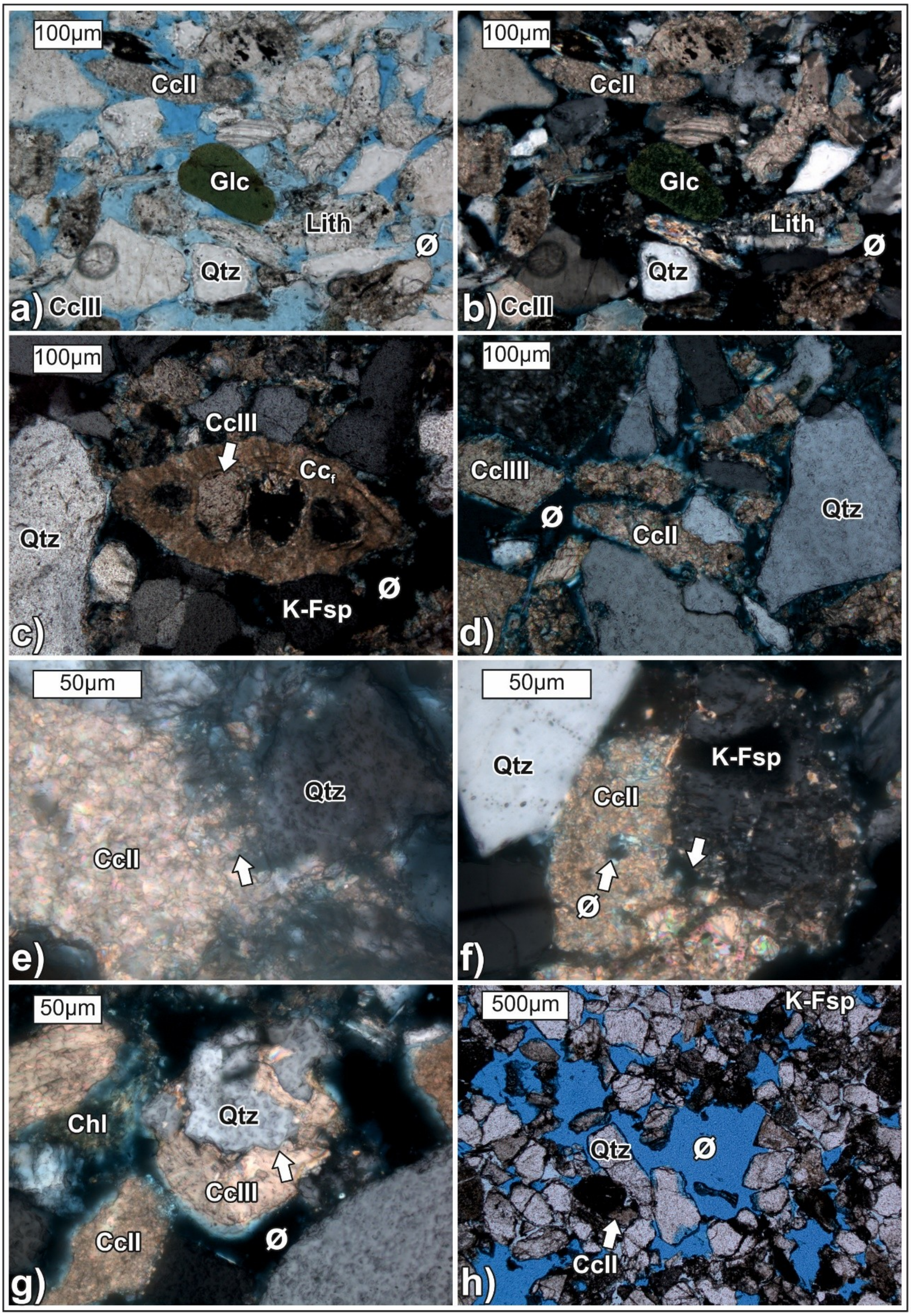

Fig. 37 Thin section photographs of gas-bearing Oligocene-Miocene sandstones: a,b) overview of the texture in plane- and cross-polarized light; c) preserved foraminifera filled with carbonate cement; d) carbonate generations Cc II and Cc III exhibit relictic character; e,f) corrosion marks of the margin of quartz and feldspar grains at contact to Cc II; g) partial replacement of a detrital quartz grain by Cc III; h); h) oversized pores appear in loose texture.

b. Electron microprobe microscopy

Microprobe analysis confirms that quartz (Si) and feldspar are the main detrital grains.

Besides, also some lithic fragments were identified (Fig. 38a). The presence of K-feldspar (Si, Al, K), albite (Si, Al, Na) and few anorthite (Si, Al, Ca) are apparent (Figs. 39). Some chlorite and pyrite assemblages are encased by microcrystalline Cc II (Fig. 38b). Calcite (Ca) and dolomite (Ca, Mg) minerals are the dominant carbonate phases (Fig. 39). Furthermore, they show slight enhanced contents in Mg and Fe.

The carbonate cement replaces partly disintegrated quartz grains, (Figs. 38c,d). Besides, albite also shows disintegration (Figs. 38e,f). In Fig. 38e the grain is partly surrounded by chlorite minerals and, in addition, K-feldspar and albite grains are enclosed by a clay mineral of albite composition.

A high secondary porosity of these sandstones is apparent (Fig. 38a). It is clearly visible that the carbonate phases are leached (Figs. 38b,g,h, 39). Dolomite is incorporated into the calcite cement and even this Mg-bearing carbonate demonstrates corrosion (Fig. 38g). By the dissolution of carbonate, the secondary porosity is increased.

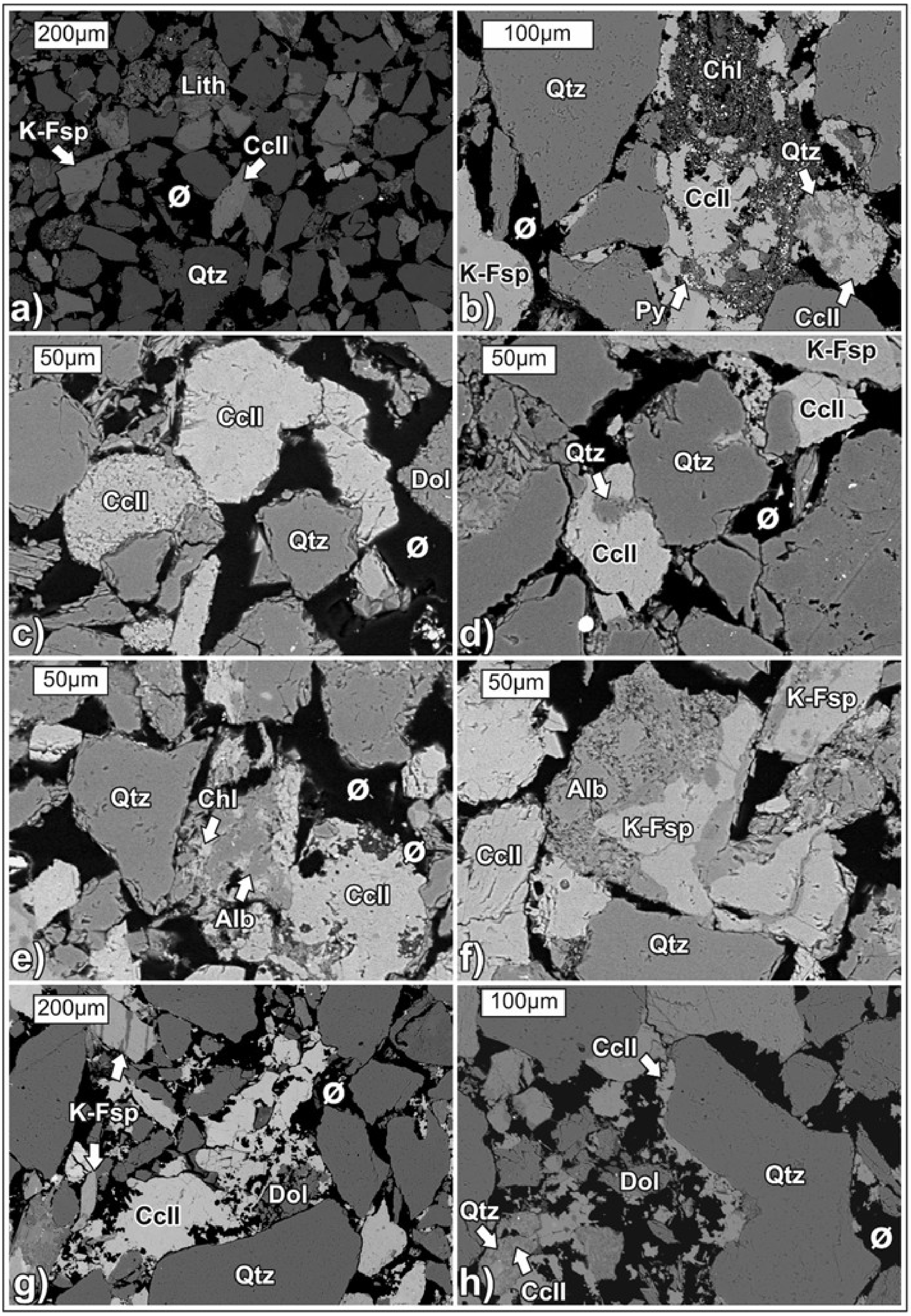

Fig. 38 BSE-images of gas-bearing Oligocene-Miocene sandstones: a) overview of the texture with relictic carbonate cement as pore filling; b) chlorite and pyrite minerals surrounded by Cc II, partial replacement of quartz by Cc II; c,d) replacement of quartz by Cc III; e,f) disintegrating albite minerals, Cc II with corrosion marks; g) dolomite surrounded by relictic Cc II,.

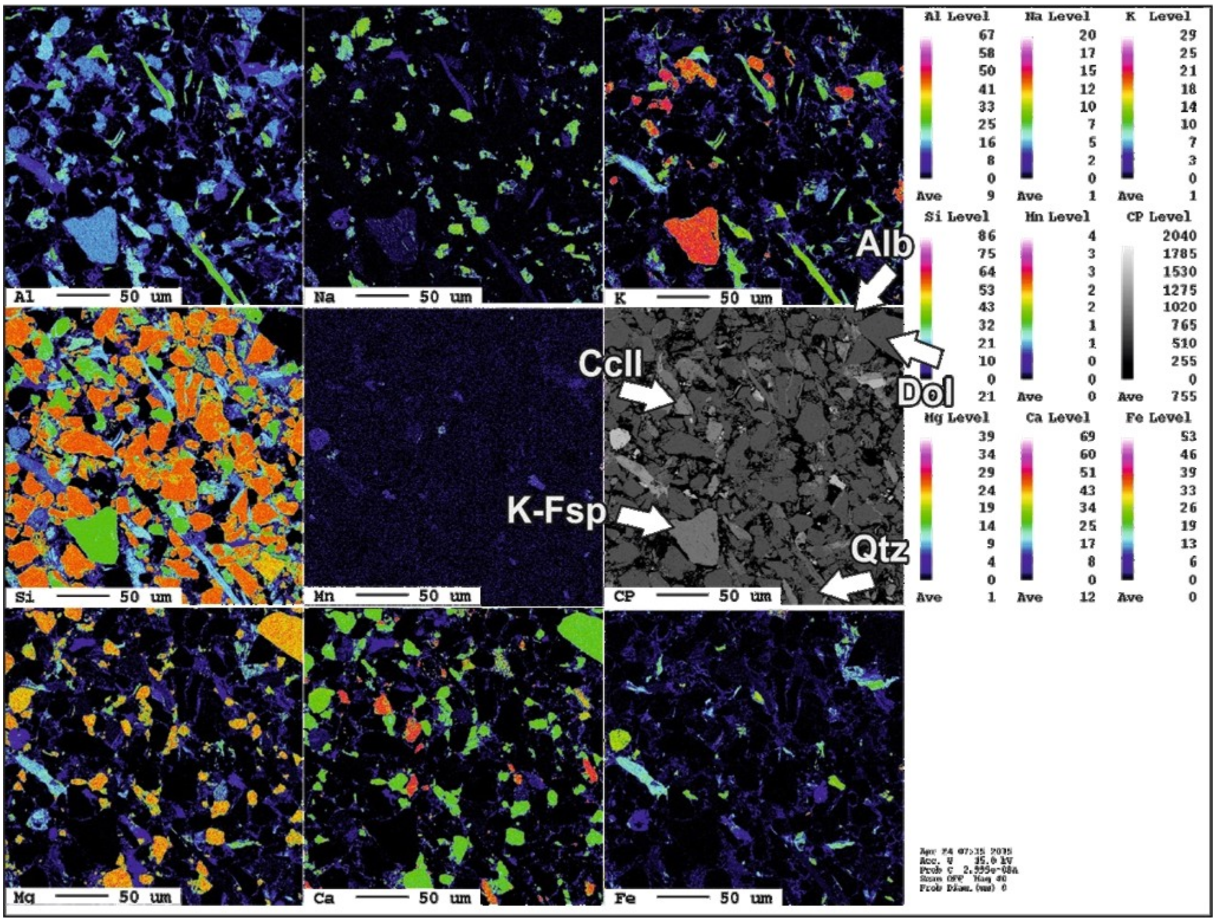

Fig. 39 Wave length dispersive (WDX) element maps of an Oligocene-Miocene sandstone in the gas-bearing zone (CP=BSE image).

c. Scanning Electron Microscopy

The morphology and arrangement of mineral grains in gas-bearing sandstones is shown in Fig. 40.

Beside quartz also detrital K-feldspars are present (Fig. 40a,b). Between these grains, muscovite flakes are wedged and pyrite framboids are located between the grains. Quartz grains prevail, whereas some carbonate (calcite) is present as cover (Fig. 40a,c). The morphology of carbonate minerals is evident in Figs. 40d,e. Calcite and dolomite are present as filling between the detrital siliciclastics (Fig. 40f). Dolomite and siderite rhombs grow into the open pores (Figs. 40d,e). A close-up view of a contact zone of grains exhibits a growth of a dolomite rhomb and chlorite between the detrital grains. In addition, chlorite and illite appears as pore filling between detrital quartz and feldspar grains (Figs. 40).

Differences in stability of mineral types are visible in Fig. 40f,h: Calcite, anorthite and K-feldspar grains show etching marks, whereas anorthite is strongly degraded. Dissolved carbonate minerals are apparent. Calcite looks disintegrated and encases a dolomite rhomb. The calcite is a remnant of a former more pervasive calcite cement (Fig. 40g).

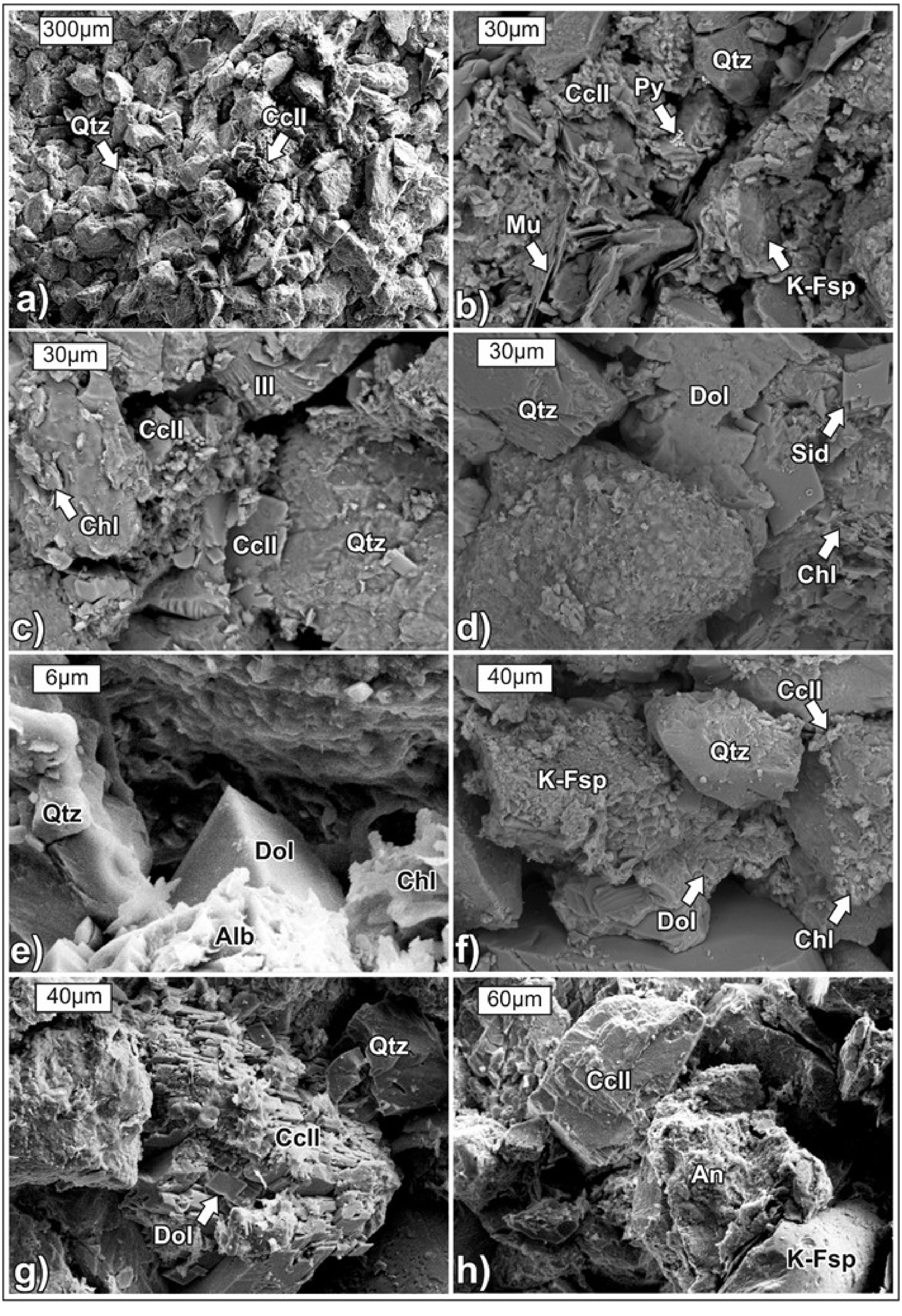

Fig. 40 SEM-images of gas-bearing Oligocene-Miocene sandstones: a) overview of the texture of the higher permeable zones; b,c) pore space distribution and its filling with chlorite and carbonates, mica sheets are intercalated and framboidal pyrite is present; d) dolomite and siderite rhombs with chlorite; e) close-up of space between grains, filled with dolomite rhomb and chlorite; g) dissolved calcite cement (Cc II) encases dolomite rhomb; h) different states of calcite and feldspar (anorthite, K-feldspar).

4.1.3. Adsorption patterns

In order to achieve a higher resolution view of the transition zone between the water- and gas-bearing sandstones, an intensively cemented rock sample from the GWC was selected for radiography and adsorption analysis in borehole P28 (see Fig. 20).

Fig. 41a shows a photograph of the quartered core, 22.5 cm long. The water-bearing zone is situated at the bottom of this rock piece. A mm-thin lamination of bright- and dark-grey layers is visible within the porous water-bearing zone. This section is followed by the transition zone, which is bright grey and more homogenous. The upper part represents the gas-bearing horizon and is similar to the water-bearing zone.

In Fig. 41b the digital radiography (CT-scan) of this hand specimen is shown. The characteristics of the section, like lamination, were correlated to the core photograph (Fig. 41a). The transition zone is characterized by dark colors resulting from the strong absorption of the emitted X-rays.

The adsorption of the rays is quantified (Fig. 41b): The measured adsorption is indicative for the permeability of these zones. A low adsorption coefficient (~37,000) is characteristic for the water- and gas-bearing horizons and increases towards the transient zone, which is characterized by values about 46,000. Within the transition zone the values are largely uniform. While at the water-transition zone passage the adsorption values increase gradually, a thin zone with an abrupt decline in values is visible across the transition-gas passage.

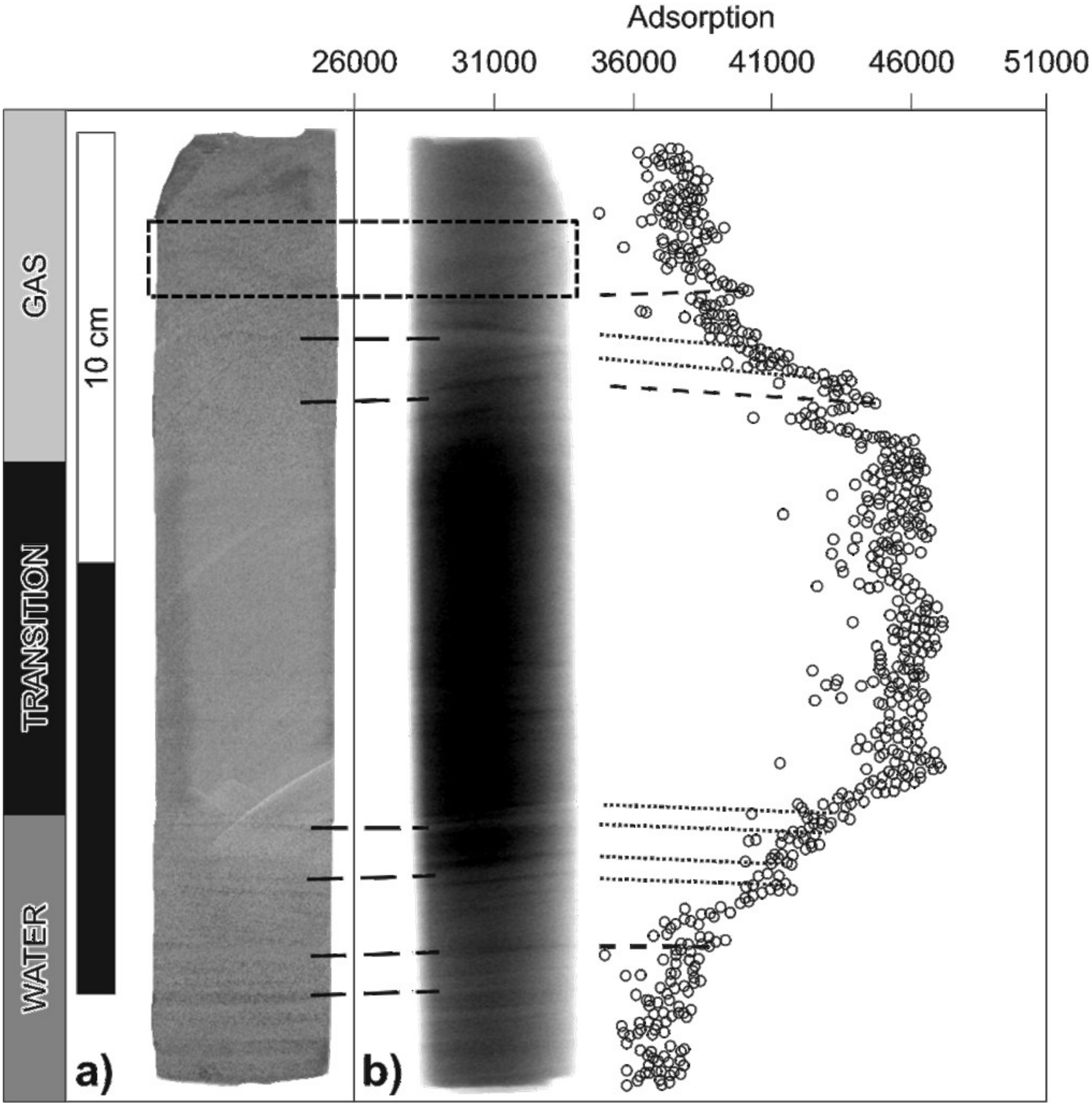

Fig. 41 a) Photographic illustration of the core piece at the GWC; b) CT-scan, digital radiography correlated with absorption curve.

4.1.4. Effect on pore space quality

The effects of authigenic mineral growth on pore space quality are presented in Figs. 42 to 47. Petrophysical data from sampled sandstones was provided by RAG. Please note, that not for all studied samples permeability values exist.

Porosity versus permeability

The porosity and permeability values are plotted against each other and separated according to the stratigraphic age in Fig. 42. Note that the permeability values are available for samples from the Upper Puchkirchen and the Hall Formation, but not for investigated samples from the Lower Puchkirchen Formation.

Porosity in samples from the Hall Formation ranges between 3% and 30%. The mean porosity of a sample from this stratigraphic horizon is 22%. Permeability values vary between 0 and 1330 mD, with a mean of 440 mD. Sandstones from Upper Puchkirchen Formation exhibit similar porosity (3 - 26%; mean 15%) and permeabilities (0 - 4440 mD; mean 870 mD) ranges. The porosity of the Lower Puchkirchen Formation samples is in average 11% (3 - 26%), permeability data from this horizon is not available. It is visible that, both age groups (Puchkirchen Group and Hall Formation) feature similar characteristics. There is a positive correlation between porosity and permeability.

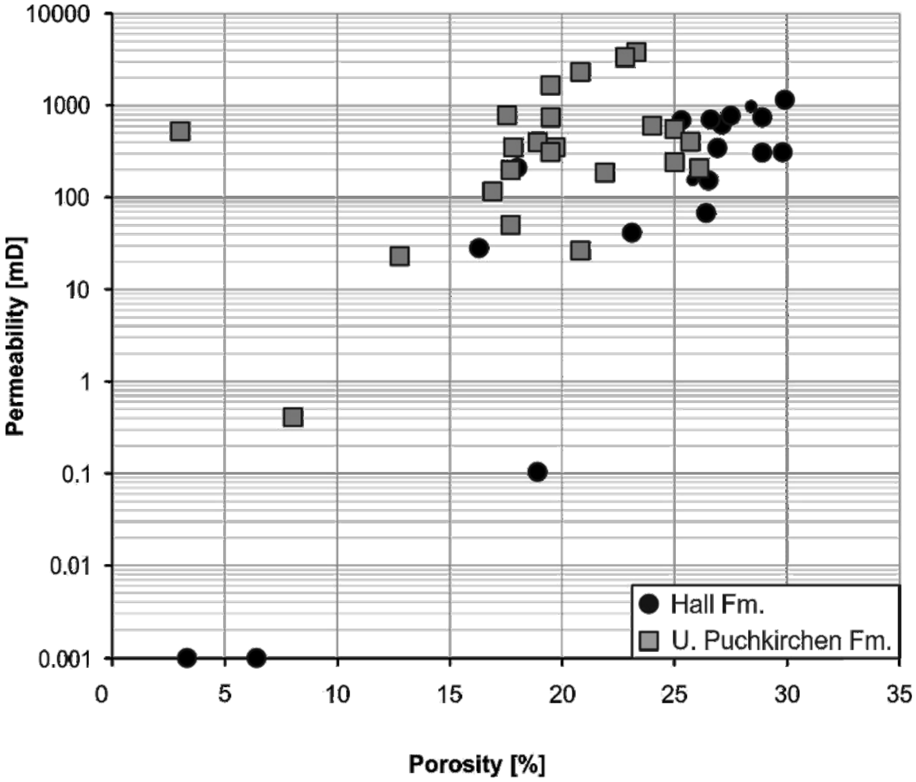

Fig. 42 Semilog plot of permeability versus porosity from samples, grouped by age.

The influence of the paleo-geographic position of the samples is visible from Fig. 43. They were subdivided into northern and southern slope and axial Puchkirchen channel; the stratigraphy was disregarded in this case.

From the northern slope no permeability data exist. The porosity of these samples ranges from 3 to 30%, with a mean of 15%.

The main reservoir rocks along the axial Puchkirchen channel have porosity values ranging from 3 to 30%(mean: 23%) and permeability values from 0 to 1330 mD (mean: 620 mD).

Sandstones which are located at the overbank wedge of the axial Puchkirchen channel have comparable porosity values (16 – 26%; mean 24%), whereas permeability is lowered (0 – 80 mD; mean 220 mD).

Samples from the southern slope show porosities from 8 to 23% (mean: 15%), and permeabilities from 0 to 4440 mD (mean: 1240 mD).

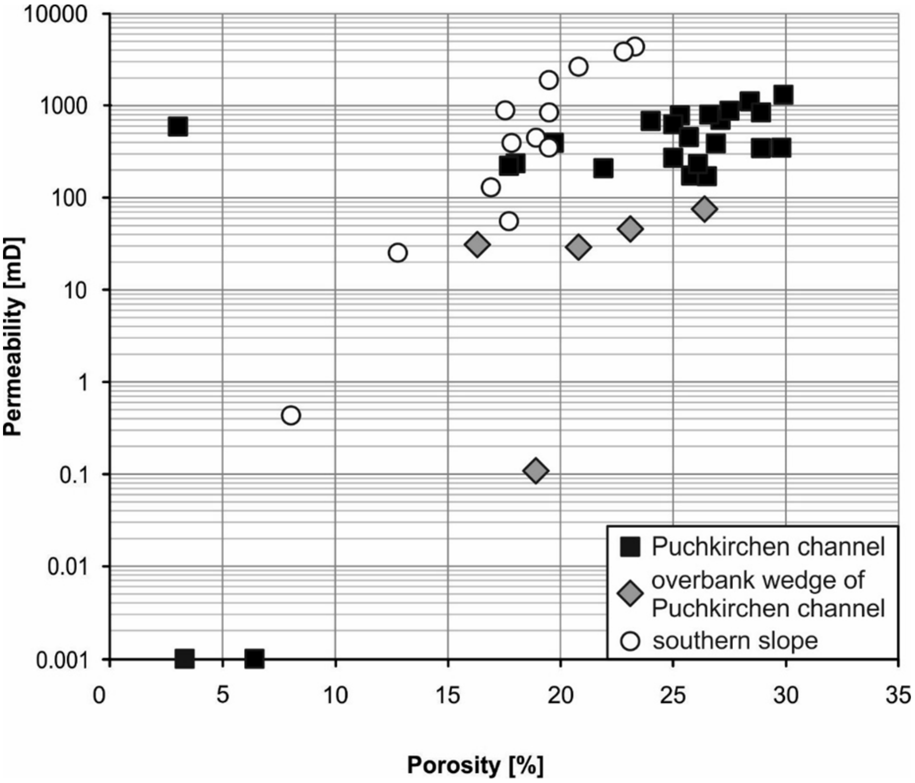

Fig. 43 Semilog plot of permeability versus porosity from samples, differentiated according to their paleo-geographic position in the NAFB.

In Fig. 44 the porosity and permeability values are differentiated according to the pore fluid (water, gas, transition zone).

Gas-bearing samples have porosities ranging from 16 to 30% and permeabilities from 0 to 1120 mD. The mean values for porosity and permeability are 23% and 420 mD, respectively.

Samples from the transition zone show a porosity and permeability range from 3 to 23% and from 0 to 4440 mD permeability, respectively. A mean porosity of 7% and a mean of permeability of 1110 mD are determined. Samples situated along the axial Puchkirchen channel exhibit porosities and permeabilities between 3 and 6% (mean 4%) and 0 and 600 mD (mean 200 mD), respectively. Cemented sediments of the transition zone reveal comparably low porosity values; the two samples with higher porosity values are from the southern slope.

Water-bearing sandstones have porosities from 18 to 30% and permeabilities from 210 to 3910 mD. In average they exhibit a porosity of 19% and a permeability of 840 mD. Values of water- and gas-bearing sandstones are in the same range. Some gas-bearing samples from the southern slope plot also into the low permeability area.

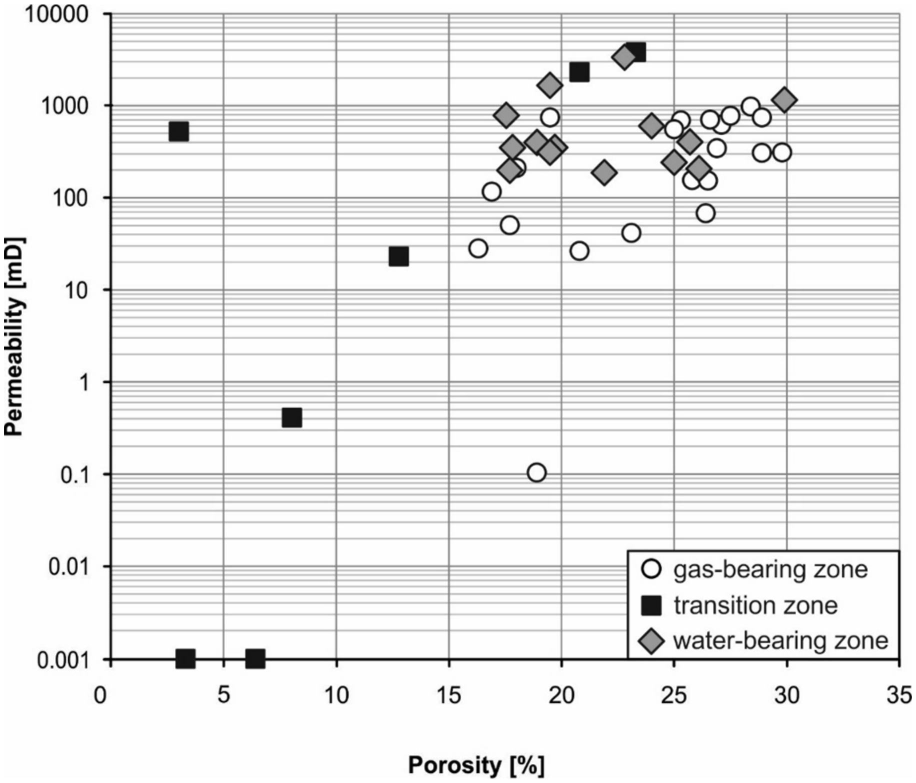

Fig. 44 Semilog plot of permeability versus porosity from samples, differentiated according to their fluid content (water/gas/transition).

Influence of carbonate cementation on pore space quality

The effect of carbonate cementation on the pore space quality is shown in Figs. 45 and 47. The prevailing pore filling carbonate is plotted against the reservoir parameters porosity and permeability in order to identify the influence of the pore space contents (water/gas/cement). For these graphs, the mineral amount (%) was calculated using the mean values of semi-quantitative XRD-analysis and point counting.

In Fig. 45 the calcite content is plotted versus porosity: Porosity values in water- and gas-bearing sediments range from 7 to 30% (mean 22%). The porosity values are independent of the calcite content of the samples (1 - 42%; mean 12%).

It is visible that samples from the transition zone reveal the lowest porosity values (1 - 23%; mean 6%). They comprise calcite minerals ranging from 1 to 42% (mean 18%). The rectangles with high porosities (8 - 23%; mean 10%) are derived from sandstones of the southern slope. These samples from the southern slope have calcite contents ranging from 21 to 13% (mean 15%).

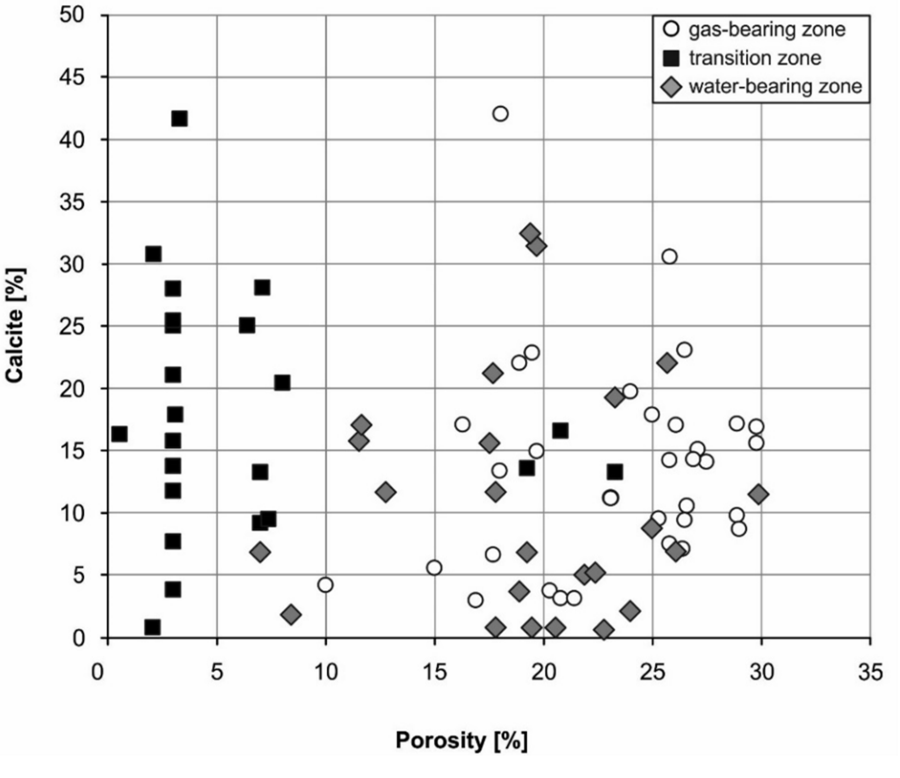

Fig. 45 Plot of calcite content (based on whole rock) versus porosity, differentiated according to their fluid content (water/gas/transition).

Although the individual values do not show a clear correlation in Fig. 45, after the interpolation of these values a reciprocity is clearly evident (Fig. 46). The Pearson correlation of 84 samples with a significance of 0.05, which means that 95% of all values, provides a bivariate correlation for calcite and porosity.

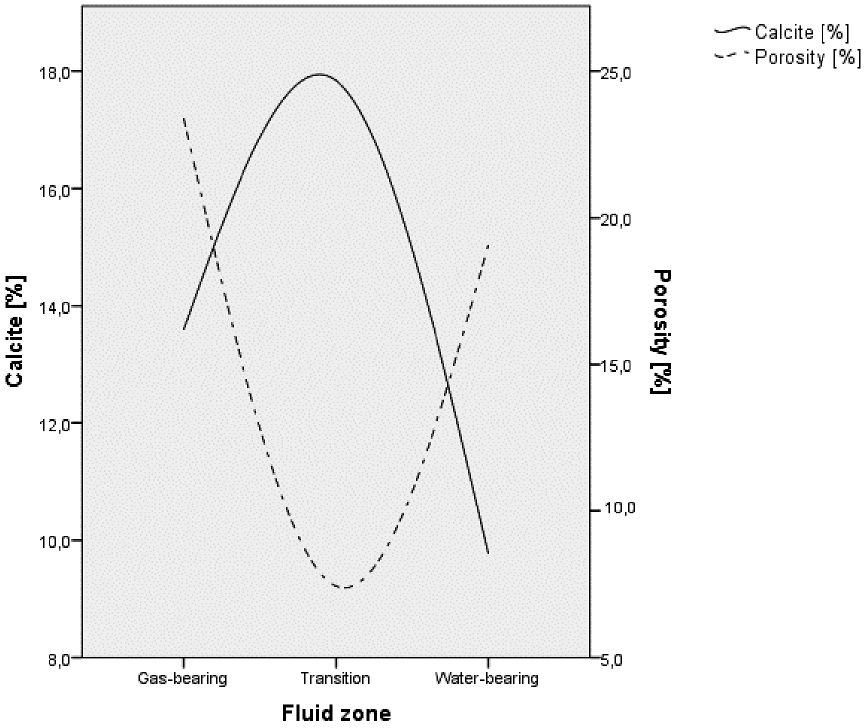

Fig. 46 Interpolation of all calcite and porosity values in the appropriate group (fluid zone: water/gas/transition) in spline lines (values are located logarithmically).

Analog to Fig. 45, the calcite content was plotted versus permeability in Fig. 47:

In Fig. 47, samples with high permeability values (< 3910 mD) have a comparably low calcite content (< 32%), which is characteristic for the water- and gas-bearing sandstones and those from the transition zone of the southern slope.

The cemented samples from the transition zone of the axial Puchkirchen channel depict values of 0 mD and an amount of calcite of 22% in average (25 - 42%).

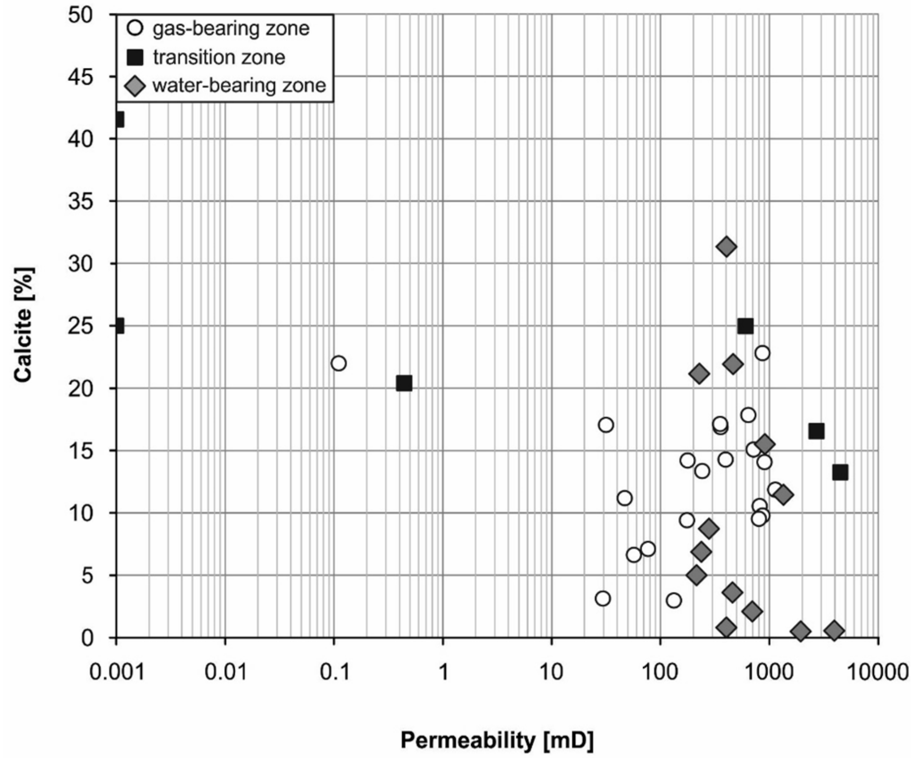

Fig. 47 Semilog plot of calcite content (based on whole rock) versus permeability, according to their fluid content (water/gas/transition).

4.1.5. Isotopic composition

Measurements of $\delta^{13}C$ and $\delta^{18}O$ of the carbonate cements can help to infer reactions during cement precipitation. The isotopic fractionation in comparison to the initial isotope ratios of primary marine carbonate may identify diagenetic pathways. Isotope ratios were grouped according to their stratigraphic position and the fluid zone (water/gas/transition zone) (Fig. 48). A mixture of different carbonate generations, such as eogenetic calcite, dolomite and lower amount of ankerite and siderite, and some detrital lithic carbonate was analyzed. Samples of the transition zone contain almost up to 40% calcite (Cc III). In spite of this mixture, the isotope data provides an important tool to assess effects of diagenetic processes on the stable isotope trends.

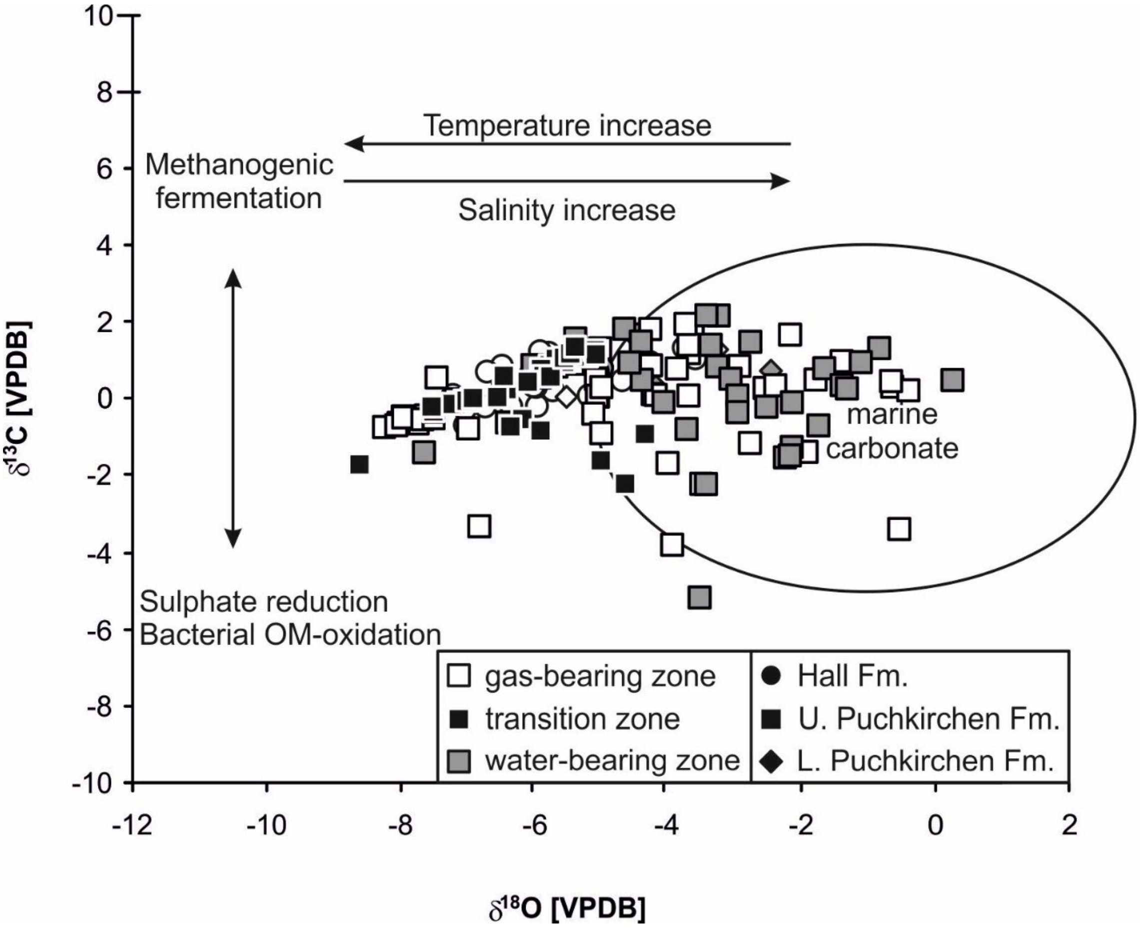

Fig. 48 Carbon and oxygen isotopic composition of bulk carbonate cements from investigated sandstones. Effects of diagenetic processes on stable isotope trends are given after Allan & Wiggins (1993). In comparison, marine carbonates vary in their $\delta^{13}C$ from +4 to -5‰ and $\delta^{18}O$ from -5 to +3‰ (Dimitrakopoulus & Muehlenbachs, 1987) (OM=organic matter).

Water-bearing zone

The $\delta^{13}C$ for sediments of the Puchkirchen Group vary between -2.2 and +2.2‰, $\delta^{18}O$ varies between -5.4 and +0.2‰. $\delta^{13}C$ for carbonate cements of the Hall Formation amount from +0.7 to +1.7‰, the $\delta^{18}O$ ranges from -5.0 to -4.5‰.

Gas-bearing zone

Isotopic ratios of cements of the Puchkirchen Group ranges from -3.8 to +2.0‰ for $\delta^{13}C$ and from -7.5 to -0.4‰ for $\delta^{18}O$. Isotopic composition of samples from Hall Formation are similar ($\delta^{13}C$: -0.7 to +1.3‰; $\delta^{18}O$: -7.2 to -3.6‰).

Transition zone

$\delta^{13}C$ for carbonate cements of the Puchkirchen Group vary from -2.2 to +1.4‰. $\delta^{18}O$ range from -8.6 to -4.4‰. Carbonates of the transition zone from the Hall Formation range in their isotopy between -0.4 to +0.6‰ for $\delta^{13}C$ and -7.7 to -5.7‰ for $\delta^{18}O$.

These values show a slight but significant negative shift in the transition zone comparison to the fluid-bearing horizons for both isotope ratios. This corresponds to a relative increase in light isotope (^{16}O or ^{12}C) in this zone.

Most of the cements from the gas and water filled zones have values, like those which are found in marine carbonates. In contrast, all but two samples from the transition zone (Puchkirchen and Hall formations) are more negative than the stable oxygen isotope ratio of sea water. At the transition zone, the blocky/homogenous calcites cement (Cc III) that fills large parts of the pore space.

The GWC of one well with Puchkirchen Group was examined in detail and its isotopic trend is shown in Fig. 49a. The values show a slight but significant negative shift in the transition zone in comparison to the fluid-bearing horizons for both isotopic ratios. This corresponds to a relative increase in light isotopes (^{16}O or ^{12}C) in this zone.

Isotopic data from one well with the Hall Formation shows a similar shift at the transition zone as in the Puchkirchen Group (Fig. 49b) even though only those data points are available.

At both locations for both isotope ratios the maximum decrease is 2‰.

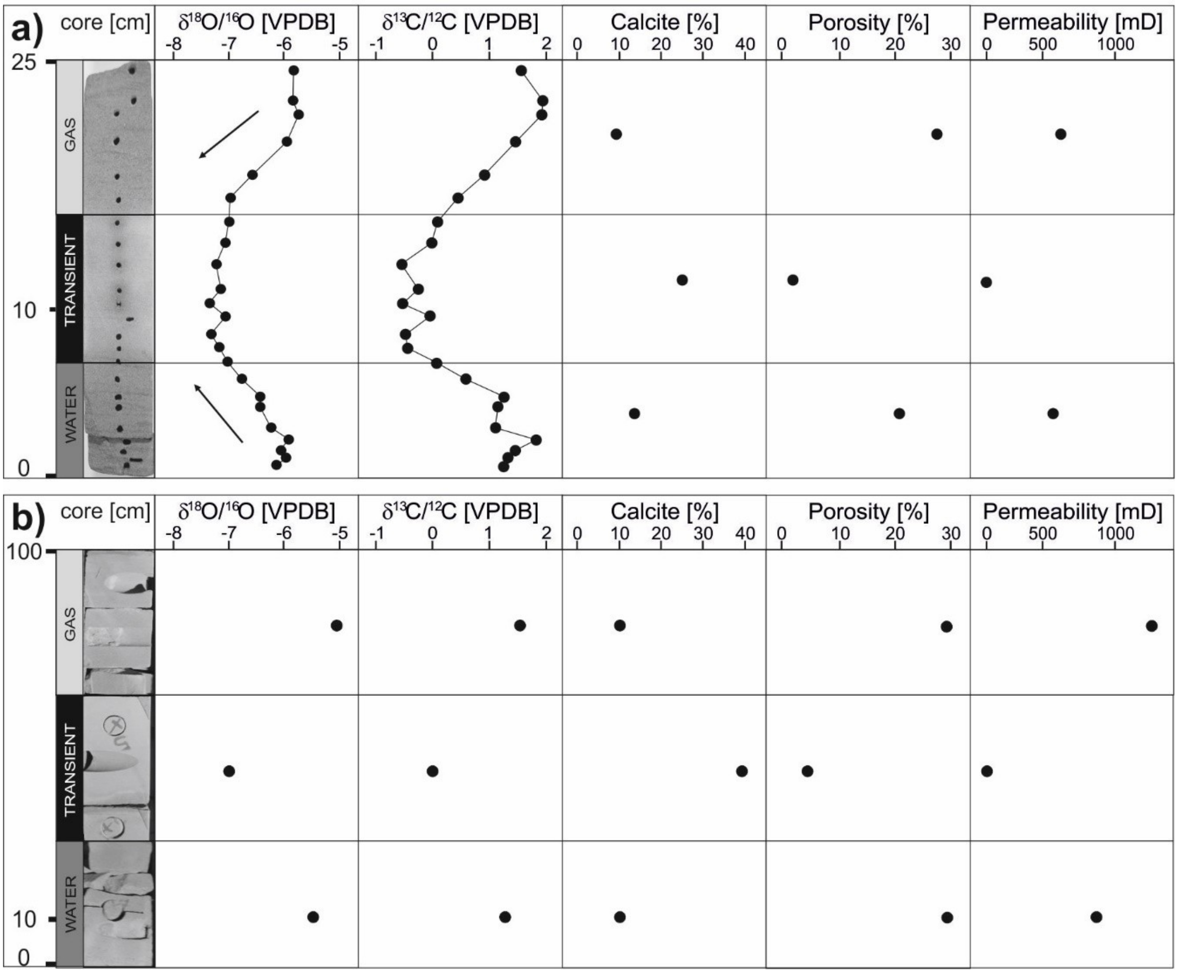

Fig. 49 Cores of sandstone near the GWC of Oligocene-Miocene in age, correlated to δ^{18}O and δ^{13}C, calcite content, porosity and permeability.

4.1.6. Discussion

Influence of depositional environment on sedimentary petrology

Sedimentologic investigations indicate that Oligocene-Miocene reservoir rocks can be differentiated into three depositional settings: northern slope, channel belt and southern slope (Fig. 26). Their reservoir quality is primarily controlled by the position along the Puchkirchen channel and their relative distance to the channel. Investigated sandstones, which were deposited along the Puchkirchen channel, are sedimentologically similar. Sandstones deposited along the Puchkirchen channel have high porosities (up to 30%), whereas sandstones deposited outside the channel belt have low porosities (5 - 28%). Sediments in the vicinity of the Alps are poorly sorted and contain up to dm-sized clay and Lithothamnium Limestone clasts. These sediments are compositionally immature and show primary porosities between 8% and 23%.

Glauconite grains occur in all paleo-geographic settings and have a granular shape and were transported from a shallow marine environment. Hence, glauconite is not considered as a depositional (suboxic shelf) environment indicator.

Paragenetic relationships (microfacies)

Silicate minerals - Partial feldspar dissolution and replacement by clay minerals is evident. In all reservoir units feldspar and, to some extent, quartz show dissolution features. Hydrogeochemical modeling of siliciclastic reservoir rocks published by Van Berk et al. (2009) showed that anorthite dissolves first and K-feldspar last. Disintegration of silicate minerals and, besides also the alteration of mica, release Si^{4+}, minor K^+ and Al^{3+}. The Si^{4+} and K^+ solution precipitated locally also as K-feldspar overgrowths around, or as healings of fissures of, feldspar grains (e.g. Figs. 29f, 34b,f). These rims are depleted in K^+ compared to the grains. Pure quartz (Si^{4+}) overgrowths were not observed within these samples. Also authigenic clay minerals, most prominent illite, formed as overgrowths on detrital grains or locally as alteration product in-situ. The disintegration of albite minerals supplies Na for smectite growth. Further, chlorite developed due to the corrosion of Fe- and Mg-rich lithic fragments and glauconite.

Carbonate minerals - Early calcite (Cc I; e.g. Fig. 27c,d) grew columnar on the grain surfaces and correspondingly porosity decreased. The microcrystalline cement (Cc II) extensively replaced the early columnar cement. Due to these early cementation phases the relative loose sediment got consolidated preventing subsequent compaction. Consequently, the rocks show point to planar grain contacts (e.g. Figs. 27, 33, 37) in spite of considerable present-day burial depth (~1800 m). Carbonate generation was accompanied by partial disintegration of siliciclastic minerals.

Extensive eogenetic carbonate precipitation at a great extent impeded silicate cementation and compaction. At larger distance to carbonate sources, like fossils or detrital limestone, the magnitude of carbonate cementation decreases.

Diagenetic processes

Diagenetic reactions largely depend on the availability of terminal electron acceptors during the degradation of organic matter and on diffusion/dispersion processes (e.g. permeability and hydrological gradients) in the reservoir. Eogenetic reactions consume organic matter and result in the release of protons. Clayey marls have a primarily higher content of organic matter compared to sandstones. Therefore, the redox sequence during organic matter degradation evolved in this fine grained material compared to the coarser grained sediments, significantly. Bacterial metabolism within the clay marls undergoes - depending on the availability of terminal electron acceptors - all steps from oxidations up to methanogenesis. All these reactions release CO_2 that can dissolve in the pore fluid and then react with divalent cations such as Ca^{2+} in the pore waters and thus may be a source of carbonate minerals.

Based on the observed diagenetic features, the following post-depositional processes can be interpreted (Fig. 50):

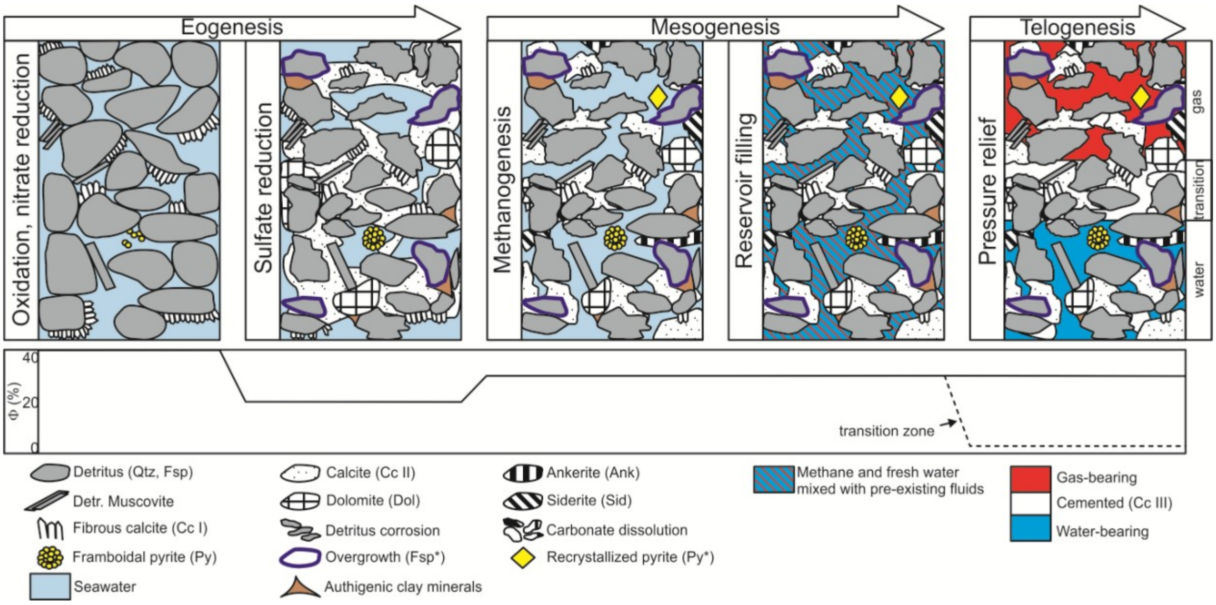

Fig. 50 Diagenetic history in Oligocene-Miocene reservoir sandstones.

a. Eogenesis

Primary porosity and permeability values right after deposition depend on the facies zones of the different sites, which were discussed above. Schulz & Van Berk (2009) assume a primary porosity of about 40% for these sediments. Synsedimentary oxidation and later nitrate reduction initiated a reduced setting (Froelich et al., 1979; Einsele, 2000; Schulz et al., 2009).

After nitrate and oxygen are consumed, sulfate reduction commenced in marine environments. A trace of this metabolic process is recorded in the presence of pyrite framboids (Hudson, 1982; Morse & Wang, 1997; Wilkin & Barnes, 1997; Schoonen, 2004; Maclean et al., 2008). Depending on the presence of other terminal electron acceptors (TEA) this process may start already in the water column, if the bottom water is sulfidic or if there are reducing microzones such as decaying organic matter in tests of organisms, e.g. as foraminifera. Pyrite formation can be either (i) a fast process where free H_2S diffuses upward and reacts with Fe^{2+} released during iron oxide reductions or (ii) can be slow and may form via polysulphides that need in sum a four electron transfer (Rickard et al, 1995; Rickard, 1997). Typically, framboidal pyrite forms by the first process in fine-grained rocks, however it may form also in sandstones (e.g. Kraishan, 1997; Weibel & Friis, 2004). At the study site, framboidal pyrite (e.g. Fig. 36e) only occurs in traces of a few percent (1-2% of whole rock).

As sulfate is a main component in seawater, low amounts of authigenic pyrite within the Upper Puchkirchen Formation have been used as an indicator for minor sulfate reduction by Schulz et al. (2009). These authors suggest an insufficient exchange with sulfate-bearing sea water that indicates deposition in a closed system without exchange to the overlying sulfate-rich water column. An alternative explanation offered in this study is that pyrite formation follows the fast pathway where it is not governed by the presence of sulfate but limited by the presence and complete uptake of ferrous iron.

All available Fe is incorporated fast in pyrite. Therefore, non-Fe-bearing carbonates, including microcrystalline cement (Cc II) and a low amount of dolomite, formed along grains. Nonetheless the carbonate phases are enriched in Mg and Mn suggesting a suboxic setting (Einsele, 2000). For the dissolution of quartz, Kashik (1965) and Friedman & Sanders (1978) expect a pH >9.

b. Mesogenesis

Fe-bearing carbonate minerals (ankerite, siderite) precipitated after the relatively short time span of sulfate reduction (Schulz et al., 2009), which is characterized by non-Fe-bearing carbonate minerals (calcite, dolomite) (e.g. Figs. 29d,h). The incorporation of Fe in carbonate minerals can only occur in reduced (ferrous) form and indicates the primary presence of free Fe^{2+} in the pore waters. Once the zone of methanogenesis is reached where hydrogen sulfide is no longer produced, no pyrite will precipitate in the presence of iron (Einsele, 2000). Iron incorporated into the carbonates might for this reason be from a different (e.g. hydrothermal) source because the zone of iron oxide reduction lies before (above) the zone of methanogenesis. An alternative explanation for the presence of ferrous iron in methanogenetic pore waters might be a discrete area of higher Eh where bacterial iron oxide reduction is still ongoing and in this way delivers ferrous iron to anoxic pore waters. The microfacies and thin section evaluation does not provide evidence for either scenario so both ideas remain speculation.

The production of CO_2 during methanogenesis is likely to drop the pH, which causes rather carbonate (dolomite) dissolution than precipitation (Rodriguez et al., 2000; Meister et al., 2011). Thereby the pre-existing carbonate cements were partly dissolved in this zone under high pCO_2 conditions and reprecipitated as Fe-bearing carbonates (Rodriguez et al., 2000). Wallmann et al. (2008) and Meister et al. (2011) speculated that the alkalinity is less controlled by carbonate dissolution than by corrosion of feldspar, quartz and other silicate minerals. The alteration of siliciclastics is more efficient to buffer the pH by neutralizing the acidification by CO_2 production. Alternatively, a high alkalinity can be also induced by carbonate dissolution or by an increase in pH during enhanced anaerobic methane oxidation (AMO) (Meister et al., 2011).

In the study area, primary microbial gas was generated in calcareous shales intercalated between sandstone horizons (Schulz & Van Berk, 2009). Claypool & Threlkeld (1983) and Kastner et al. (1990) stated that decomposition of organic matter by microorganisms releases CH_4 and CO_2. Based on a paleo-water depth of about 1200 m and a bottom-water temperature of 4°C, Schulz et al. (2009) postulated that gas hydrates were stable during deposition of the Puchkirchen Group. At low temperature and high pressure conditions these gas phases are rapidly incorporated into gas hydrates (Whiticar, 1999; Hesse, 2003; Schulz et al. 2009), which in addition to CH_4 and CO_2 may contain H_2S and N_2 as guest molecules in low amounts (Swart et al., 2000). Circone et al. (2003), Doose et al. (2007) and Mazurenko et al. (2009) noted that gas hydrates comprise predominantly CH_4 (90 -99%). The stability field of gas hydrates is dependent on the predominating geothermal gradient and increases with increasing pressure (Hesse, 2003). The reservoir filling with microbial gas might be related to the dissolution of these gas hydrates. This process is announced by glauconite alteration (Fu, 2015), which was observed in the investigated samples for some of these pellets. Gas hydrate disintegration occurred at the base of the hydrate-stability zone at approximately 400 - 450 mbsf (meters below sea floor) (Rodriguez et al., 2000; Hesse, 2003). During decomposition, fresh water and microbial CH_4 were released to the system and mixed with the pre-existing fluids (Schulz et al., 2009; Schulz & Van Berk, 2009). This dilution is considered to be an indicator for gas hydrate decomposition as it provides H_2O (Hesse, 2003). Hydrogeochemical modeling of one gas field in the NAFB (Atzbach-Schwanenstadt, Upper Puchkirchen Formation) supports the formation and decomposition of gas hydrates and the release of microbial gas (Schulz & Van Berk, 2009). Commonly salinity increases with progressive burial. In a closed system, as in the studied sediments, diffusion is the only pathway to exchange ions following a concentration gradient (Bjørlykke et al., 1989). In the investigated sections, cations and anions were clearly affected by diagenetic processes, but salinity did not overall increase (Andrews et al., 1987). In fact, water salinities in the investigated gas fields of the Puchkirchen Group (cCl^-: 0.22 mol/kgw; 7,908 mg/kgw) and the Hall Formation (cCl^-: 0.29 mol/kgw; 10,1133 mg/kgw) are only about half of observed concentrations in present-day sea water (cCl-: 0.57 mol/kgw; 20,055 mg/kgw; Nordstrom et al., 1979). Thus, a dilution of Oligocene-Miocene formation waters is apparent.

c. Late diagenesis

During late diagenesis, a strongly cemented and low permeable zone between the gas- and water-bearing horizons formed (Figs. 21, 27). Strong carbonate cemented zones were observed near OWCs (oil-water contacts) by Walderhaug & Bjørkum (1998), with 10 to 100 cm thickness and varying lateral extent. Carbonate precipitation along OWCs in the Siri Oil Field (North Sea) was hydrogeochemical modeled by Fu (2014). There, the strong cementation was constrained by external chalk water inflow due to seismic pumping. Hence, these observations prove cementation after reservoir filling and represent the last authigenic mineral formation. According to Bjørkum & Walderhaug (1990), zones with extensive cementation are restricted to layers with abundant calcareous fossils or detrital carbonate. Based on petrographic data, such a relation can be excluded for the studied succession. Siliciclastic components within the carbonate cemented transition zone “float” within the cement Cc III. This suggests that carbonate precipitation was accompanied by advanced partial dissolution of silicates and further supports alkaline conditions.

The position of a low permeable zone near GWC may have a significant influence on hydrocarbon production. Within one investigated core a second low permeable horizon was observed within the gas-bearing zone. This horizon was neither mineralogically nor isotopically as prominent as the underlying transition zone at the actual GWC. Nonetheless, this phenomenon might be interpreted to reflect a downward movement of the GWC. The less distinct characteristics (mineralogy, isotopy) of the low permeable zone above the main GWC might be due to the short time span, caused by a short retention time of this “paleo-GWC”. The typical sedimentological characteristics (e.g. increased carbonate and decreased siliciclastic content, low permeability) of the GWC are more pronounced at the present-day position at investigated sandstones. This is probably due to the fact that, the total retention time of the contact zone of water and gas lasted longer and, additionally, therefore the availability of possible reactants was present longer as well (Fu, 2014).

A downward migrating GWC is expected during reservoir filling, concomitant pressure increase and tectonic movements. Hydrocarbon production can be excluded, because this process initiates an upward movement.

d. Stable isotopic composition

Carbonates, formed by biogenic processes in the water column in equilibrium with ocean water, have a range of +4 to -5‰ for $\delta^{13}C$ and -5 to +3‰ for $\delta^{18}O$ (Dimitrakopoulus & Muehlenbachs, 1987). Previous studies used isotopic compositions of calcite cements in the NAFB and proved their potential to understand diagenetic processes relevant during gas generation (Mátyás, 1998; Schulz et al. 2009). In addition, stable isotope ratios may also be used to infer inorganic reactions and reaction rates (Hoefs, 2009).

In Fig. 48 a cross-plot of $\delta^{13}C$ versus $\delta^{18}O$ of samples from the present study is illustrated. Samples from both, Puchkirchen Group and Hall Formation, show a $\delta^{13}C$ of about ±0‰ and a $\delta^{18}O$ ratio between -8 and -2‰, similar to those of sea water. Cements from the transition zone (Cc III) differ from cements in the water- and gas-bearing zones (Cc I and Cc II) by a slight negative shift in carbon ($\delta^{13}C$: -1.5‰) and oxygen isotope ratios ($\delta^{18}O$: -2.5‰) (Fig. 49). A similar anomaly in isotopic composition was observed in sandstones from the Swiss part of the NAFB by Mátyás (1998). This author attributed the shift to meteoric flush. In the case of the studied Oligocene-Miocene sandstones, hydrochemical data prove a connate, rather than a meteoric origin of the formation waters (Andrews et al., 1987). The simultaneous decrease of stable carbon and oxygen isotopes could be explained by rapid cementation at the GWC. Fast reaction rates result in kinetic isotope fractionation (Hoefs, 2015) where the lighter isotope will be quicker incorporated during mineral precipitation and the mineral will then be enriched in the lighter isotope. Following the approach of Kim & O'Neil (1997), temperature calculations give an average formation temperature of ~50°C of these light isotopes from the transition zone. These estimations agree well with present-day temperatures (40 - 70°C) and it is suggested that these late diagenetic calcites are in equilibrium with the recent reservoir conditions. Biogenic degradation pathways can be easily identified by $\delta^{13}C$ in carbonates if the system is geochemically closed (e.g. no fluid transport) (Dimitrakopoulus & Muehlenbachs, 1987). For example, aerobic degradation results in a depletion of $\delta^{13}C$ up to -20.6‰. In contrast, carbonate phases, which grow during secondary microbial gas generation show enrichment in ^{13}C ($\delta^{13}C$ up to +14.3‰). Neither the first nor the second process can be identified. This indicates an either well mixed system or the absence of these processes during formation of the cements.

4.1.7. Conclusions for Oligocene-Miocene rocks

The study of Oligocene-Miocene reservoir rocks in the Puchkirchen Group and the Hall Formation, hosting primary microbial gas and a small amount of thermogenic gas, contributes significantly to the understanding of the relation between hydrocarbon accumulation and pore space evolution. The diagenetic history is summarized in Fig. 50:

- Only minor differences exist between the diagenetic evolution and reservoir quality of sandstones in the Puchkirchen Group and Hall Formation. In contrast, reservoir quality strongly depends on the paleo-geographic position within the varying detrital input and transport distances.
- During eogenesis microbial gas was generated by organic matter metabolism in intercalating calcareous shales. Bacterial activity, amongst others, stimulated alkaline conditions, which favored carbonate precipitation (Cc I - Cc III). Early cementation retarded further compaction.
- The produced CO_2 was incorporated into the cements. Calcite from water- and gas-bearing zones show $\delta^{13}C$ and $\delta^{18}O$ between +1‰ and -5‰ [VPDB], respectively, which correspond to a marine setting during calcite precipitation.
- Finally, Ca^{2+} ions of dissolved carbonate minerals, which were corroded during methanogenesis (Rodriguez et al., 2000; Meister et al., 2011), reacted with dissolved CO_2 of the formation water. Blocky calcite (Cc III) precipitated intensively and formed strongly cemented low permeable zones near the GWC. In comparison this horizon is slightly depleted in ^{18}O ($\delta^{18}O$: -8‰), which could be caused by fast cementation process.
- The presence of microbial gas, and the low formation water salinity consistently suggest a decomposition of gas hydrates and the release of gas and freshwater to the system (see also Schulz et al., 2009).
- Carbonate precipitation at the GWC may have a significant influence on hydrocarbon production.

4.2. Upper Eocene

In this section, the mineralogy, as well as the isotopic signature of authigenic carbonate cements is described separately for investigated rocks from each Eocene stratigraphic unit, with respect to diagenetic features caused by different pore fluids. An overview of investigated core intervals is given in Fig. 51.

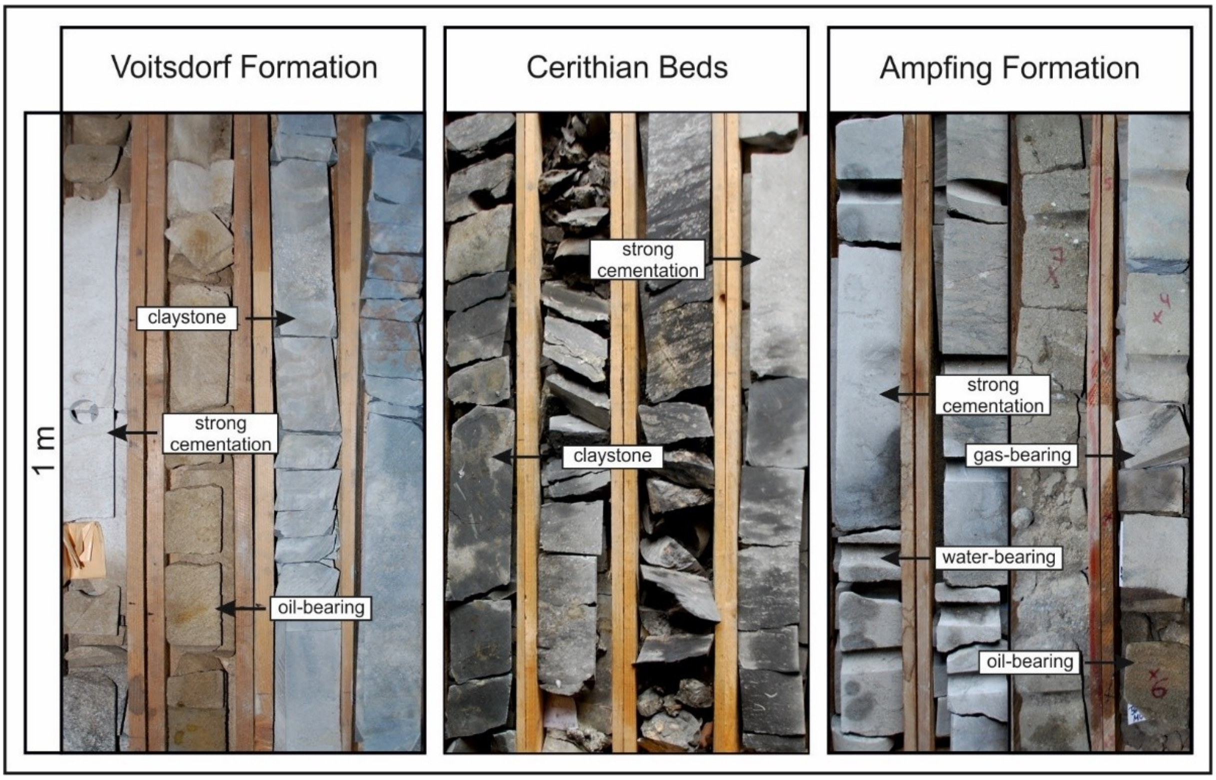

Fig. 51 Overview of core boxes: The bottom of the core boxes is left, the top in the right upper corner. Left: Voitsdorf Formation with strongly cemented and oil-bearing coarse-grained sandstones embedded within varicolored mudstones (ca. 1810 m below ground level). Centre: Cerithian Beds with strongly cemented, coarse-grained sandstone in dark-grey, fossiliferous mudstones (ca. 1870 m). Right: Ampfing Formation with water-bearing and strongly cemented medium-grained sandstones (left) (ca. 1660 m) and oil- and gas-bearing sandstones (right) (ca. 1580 m).

4.2.1. Sedimentary petrology

Voitsdorf Formation

The Voitsdorf Formation comprises non-marine mudstones and sandstones. Sandstones of the studied core intervals are typically about 2 m thick and are medium-grained and locally carbonate-cemented (Fig. 52a). They are interbedded with dark-grey mudstone horizons, which occasionally host dispersed and coarse-grained quartz grains (Fig. 51).

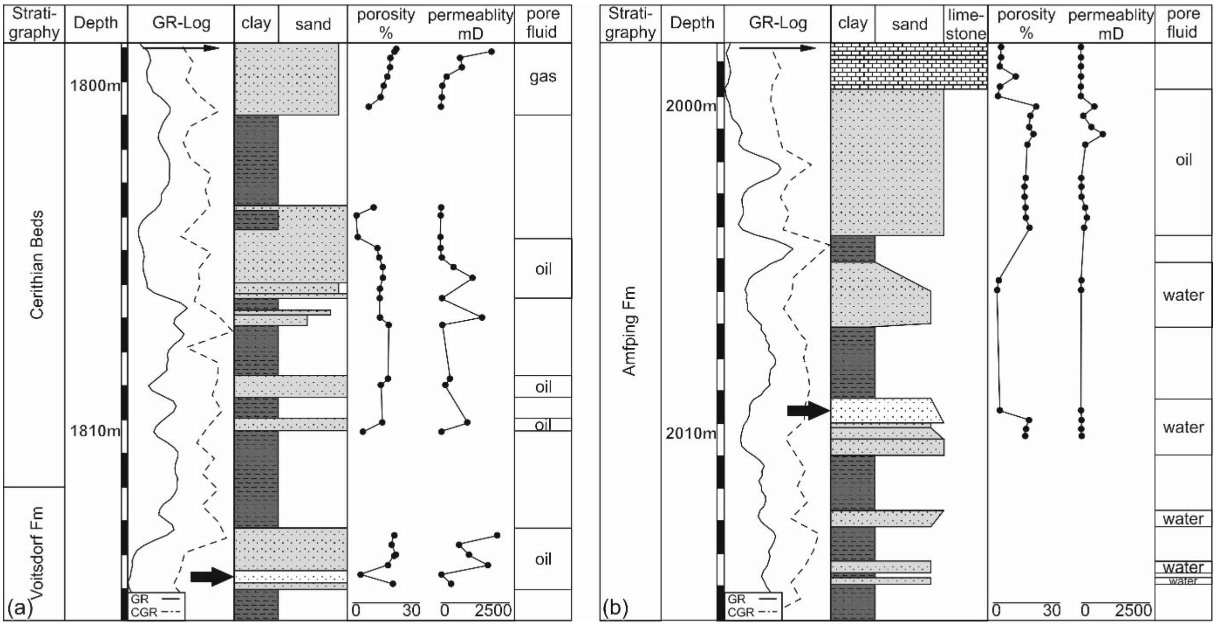

Fig. 52 Lithological profiles of investigated cores from a) Voitsdorf Formation and Cerithian Beds and b) Ampfing Formation plotted together with porosity, permeability, and pore fluid content. Sandstones with reduced porosity due to strong carbonate cementation are colored in white and marked with a black arrow. GR: gamma ray log; CGR: measured core gamma ray.

Detrital grains are angular, poorly sorted, grain supported, and show a low sphericity. The main components are quartz (40% of all minerals and porosity) and feldspar (18%). Quartz occurs as monocrystalline (28%) and minor polycrystalline (12%) grains. Alkali feldspar (17%) dominates over plagioclase (1%), further the amount of albite is higher than that of anorthite. Detrital muscovite, biotite (5%) and some lithic fragments (7%) occur in minor amounts. The lithic fragments are predominantly of metamorphic origin (e.g. mica schists). Sandstones of the Voitsdorf Formation are classified as lithic arkoses, according to Folk´s classification (Folk, 1974) (Fig. 53). The mean clay mineral content (kaolinite, illite, and chlorite) is 10%, carbonate cements amount 5% in few samples. The porosity and permeability average 15% and 400 mD, respectively.

Sandstones of Cerithian Beds

The studied reservoir rocks of the Cerithian Beds are in average 4 m thick and consist of coarse-grained sandstones interlayered with fossil-rich dark-grey mudstones (Figs. 51, 52a). Grains are typically angular, grain supported, show a high sphericity, and moderate to poor sorting. Quartz (41%) and feldspar (21%) are the main components. Monocrystalline quartz (26%) prevails over polycrystalline quartz (15%), whereas alkali feldspar (19%) is more common than plagioclase (2%, mainly albite). These sandstones have 10% lithic fragments whereas pyrite, iron oxides, clay minerals and mica are present in amounts of up to 6%. Consequently, the sandstones are classified as lithic arkoses after Folk (1974) (Fig. 53). Sandstones of the Cerithian Beds show a mean porosity of 15% (17 - 20%) and permeability of 1350 mD (790 - 1900 mD).

Ampfing Formation

Investigated sandstones of the Ampfing Formation are medium-grained and up to 6 m thick (Figs. 51, 52b). The moderately sorted grains are angular, grain supported and exhibit high sphericity. The main mineral phases are quartz (42% total; 27% monocrystalline; 15% polycrystalline) and feldspar (15% total; 12% alkali feldspar; 3% plagioclase). Lithic fragments (11%) are mainly of metamorphic origin. Partly increased contents of muscovite and biotite (7%) likely result from the disintegration of mica schists. Clay minerals and carbonate cement are present in considerable amounts (8% and 5l%, respectively). Foraminifera are rare, but their presence supports the marine depositional environment. Ampfing sandstones plot into the field of lithic arkoses (Folk, 1974) (Fig. 54). Samples, which are located in the northern part of the NAFB, can be classified as feldspatic litharenites, minor subarkoses and sublitharenites (Fig. 53). Porosity of these sandstones averages 12% (7 - 17%), while the mean permeability is 140 mD (3 - 570 mD).

Sandstones of the Ampfing Formation show a higher compositional maturity than the underlying sandstones of Cerithian Beds and Voitsdorf Formation. The textural maturity of sandstones from the Ampfing Formation and Cerithian Beds is comparable, whereas sandstones of the Voitsdorf Formation are poorly sorted.

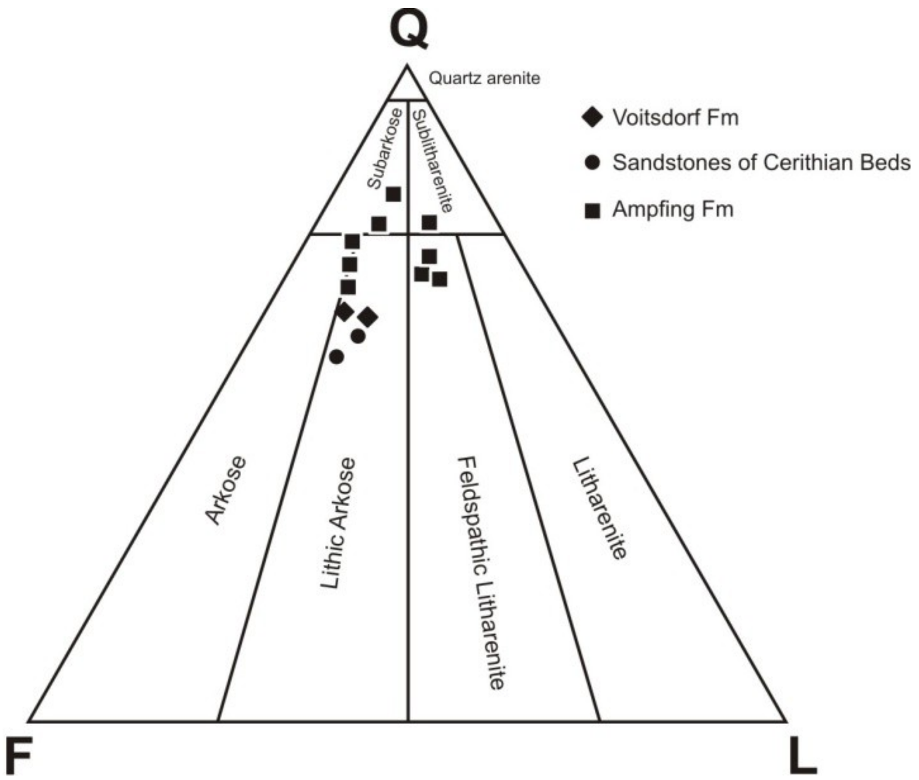

Fig. 53 Ternary classification plot for clastic rocks after Folk (1974), showing non-cemented samples from the investigated stratigraphic units.

XRD analysis

Eocene sandstone samples of the NAFB are differentiated into three stratigraphic units:

- **Voitsdorf Formation**

Most sandstone samples in water- and hydrocarbon-bearing zones have high porosities (15%). However, strongly cemented intervals with less than 3% porosity also occur in both, the oil- and the water-bearing zone. These strongly cemented sandstones will be discussed separately at the end of this section. X-ray diffraction patterns from each fluid zone, representative for the Ampfing Formation, the Cerithian Beds and the Voitsdorf Formation, are presented in Figs. 54, 55 and 56.

The mineralogical composition of the Voitsdorf Formation is illustrated by X-ray diffraction patterns in Fig. 54. It compares a cemented and an oil-bearing sandstone. The amount of calcite is higher in the cemented sample zone than in the underlying oil-bearing horizon.

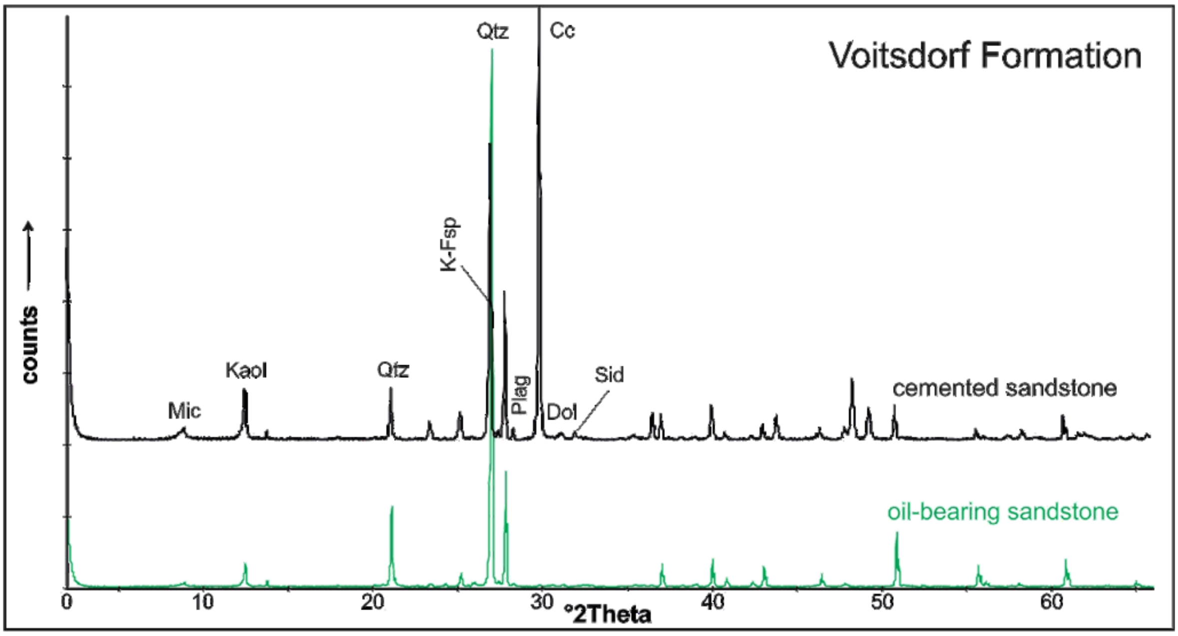

Fig. 54 Representative X-ray diffraction patterns from the Voitsdorf Formation of a cemented sandstone and an oil-bearing sandstone (Mic=mica; Kaol=kaolinite, Qtz=quartz, K-Fsp=K-feldspar, Plag=plagioclase, Cc=calcite, Dol=dolomite, Sid=siderite).

- **Cerithian Beds**

Samples of the Cerithian Beds belong to the gas-, oil-, and strongly cemented zone (Fig. 55). The cemented sandstone from the strongly cemented zone depicts the highest calcite content.

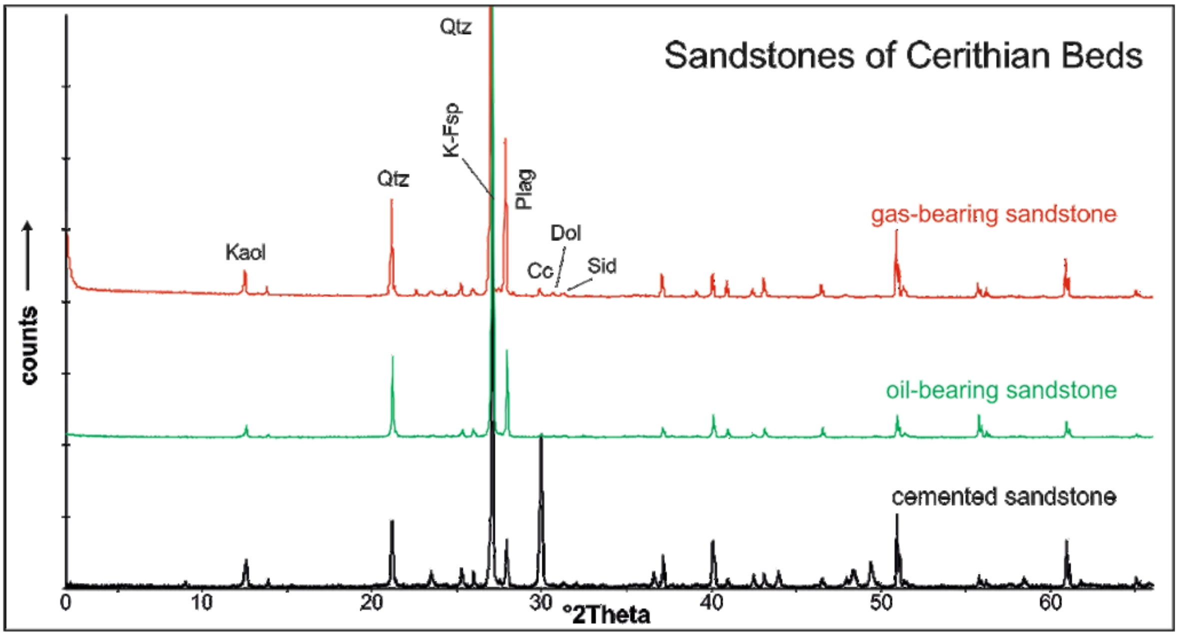

Fig. 55 Representative X-ray diffraction patterns from the Cerithian Beds of a cemented sandstone and an oil- and gas-bearing sandstone (Kaol=kaolinite, Qtz=quartz, K-Fsp=K-feldspar, Plag=plagioclase, Cc=calcite, Dol=dolomite, Sid=siderite).

- **Ampfing Formation**

In Fig. 56 characteristic X-ray diffraction patterns are presented for water-, oil-, and gas-bearing as well as for cemented sandstones of the Ampfing Formation. It is visible that the cemented sandstone exhibits the highest calcite content. In addition, also the presence of dolomite in this horizon is evident. By comparison, gas-bearing sandstones bear the highest kaolinite content.

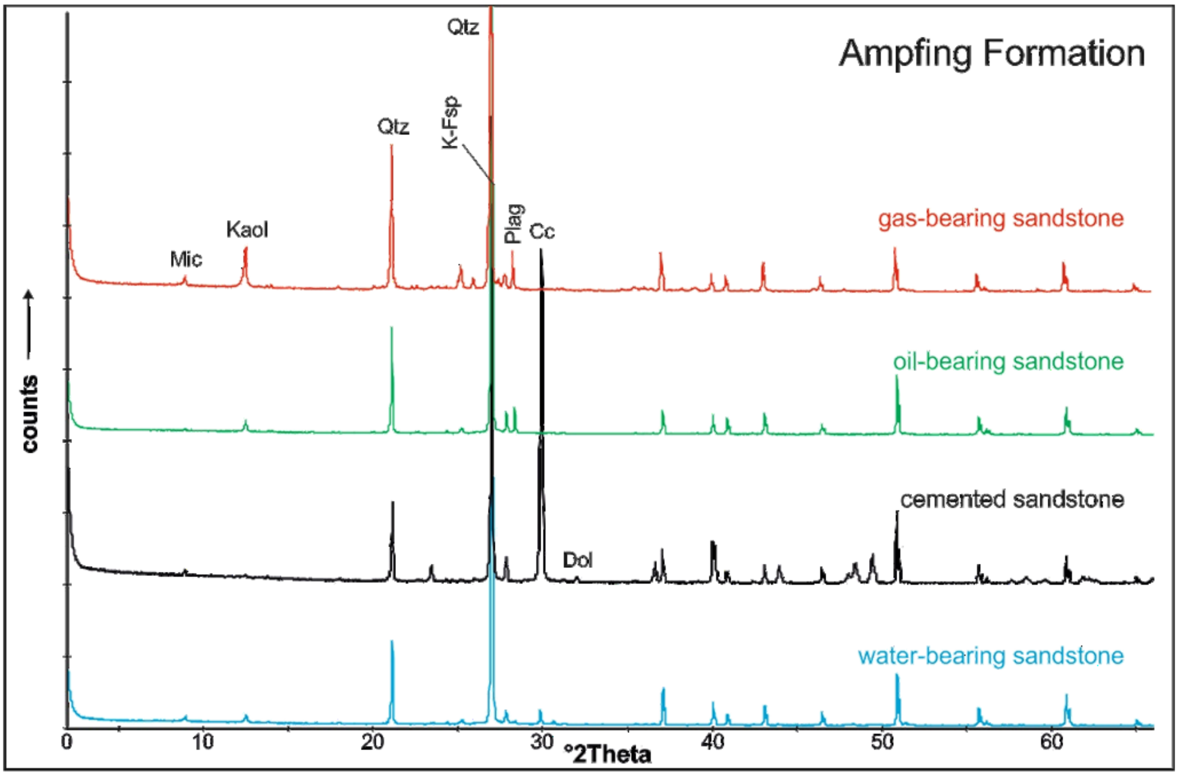

Fig. 56 Representative X-ray diffraction patterns from the Ampfing Formation of a water-bearing sandstone, a cemented sandstone, and a gas- and an oil-bearing-sandstone (Mic=mica, Kaol=kaolinite, Qtz=quartz, K-Fsp=K-feldspar, Plag=plagioclase, Cc=calcite, Dol=dolomite).

According to their stratigraphic age, the porous and non-porous (cemented) sandstones were summarized based on the sedimentpetrographic investigations (mineralogy, porosity), demonstrated in Fig. 57. Additionally, the depth range of the samples below subsurface are imaged.

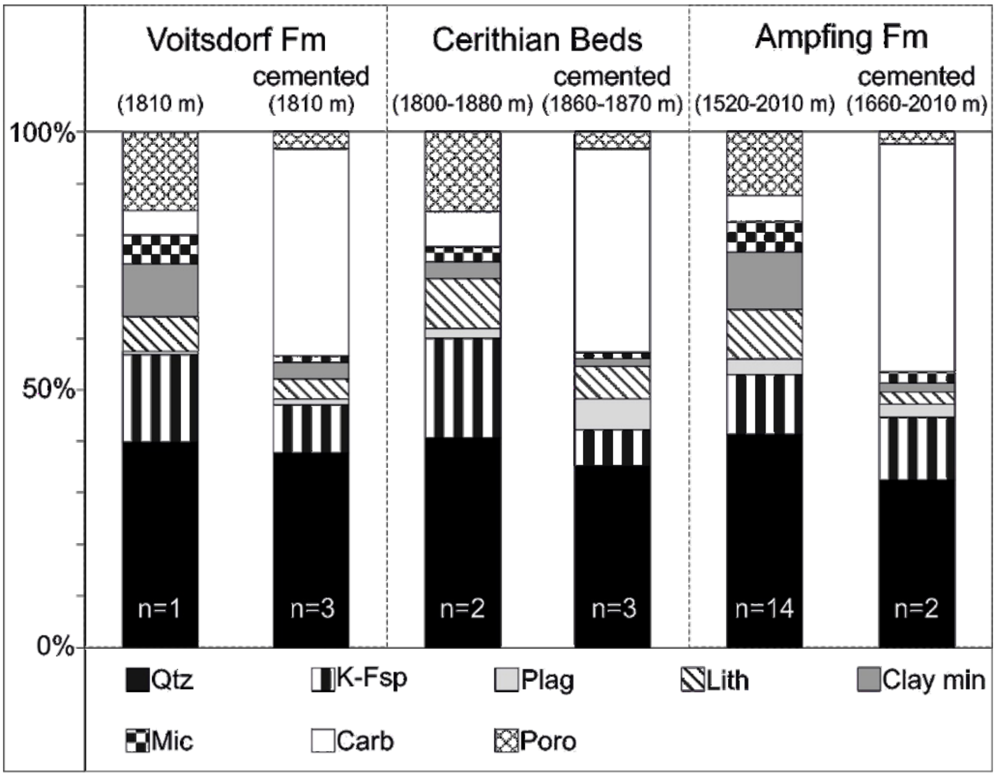

Fig. 57 Mineralogical composition and porosity (%) determined by point counting and semi-quantitative XRD analysis of samples from Voitsdorf Formation, sandstones of Cerithian Beds and Ampfing Formation. Reservoir sandstones (left column) and strongly cemented sandstones (right column) are plotted separately. (Qtz=quartz, K-Fsp=K-feldspar, Plag=plagioclase, Lith=Lithic fragments, Carb=carbonate, Poro=porosity; n=number of samples).

4.2.2. Diagenetic features

Carbonate-cemented sandstones within the water- and oil-bearing zones

Strongly carbonate-cemented sandstones, between 0.1 and 0.5 m thick, occur either (i) within the water-bearing zone (Ampfing Formation) or (ii) within the oil-bearing horizon (Voitsdorf Formation, Cerithian Beds) (Fig. 52), but were not observed in the gas-bearing zone. Detrital grains from strongly cemented sandstones of the Voitsdorf Formation exhibit more compaction than those from the younger formations (Cerithian Beds, Ampfing Formation). The investigated samples from the cemented zone originate from a depth of 1660 - 2010 m below ground level.

The mean percentage of carbonate minerals is 42% in carbonate cemented sandstones, which are dominated by calcite (40%; Cc III; minor Cc II, Cc IV, seldom Cc I). Dolomite, ankerite and siderite account each for ~1%. Quartz represents 35%, feldspar 13% and lithic fragments 3%. Clay minerals (kaolinite, illite; 2%), mica (2%), and subordinately glauconite, pyrite, detrital carbonate grains and fossils appear also. Their porosity was measured in the lab and is only 3%.

a. Thin section microscopy

- Voitsdorf Formation

Detrital particles in the Voitsdorf Formation comprise mainly quartz and feldspar (Figs. 58a,b). Some kaolinite minerals form in the vicinity to mica, especially muscovite, and restrict the porosity locally. Additionally, some biotite mineral flakes are visible in sediments of the Voitsdorf Formation (Fig. 58c). These minerals are completely encased by carbonate cement.

The percentage of carbonate cement in these samples reaches 45% (on a whole rock basis). Calcite is the only carbonate cement phase in the Voitsdorf Formation (Figs. 58a,b), and displays different morphologies: Microcrystalline cement (Cc II) occurs locally around detrital grains, especially in areas with poor grain sorting. The most prominent cement type is the blocky/homogenous Cc III, with a uniform extinction direction. In some areas the blocky/homogenous cement grades into poikilitic cement Cc IV (Figs. 58d,e).

In all strongly cemented horizons feldspar is largely replaced by calcite cement and quartz is strongly corroded and (Figs. 58f-h). Thereby, albite is most affected; alkali feldspar displays strongly altered rims.

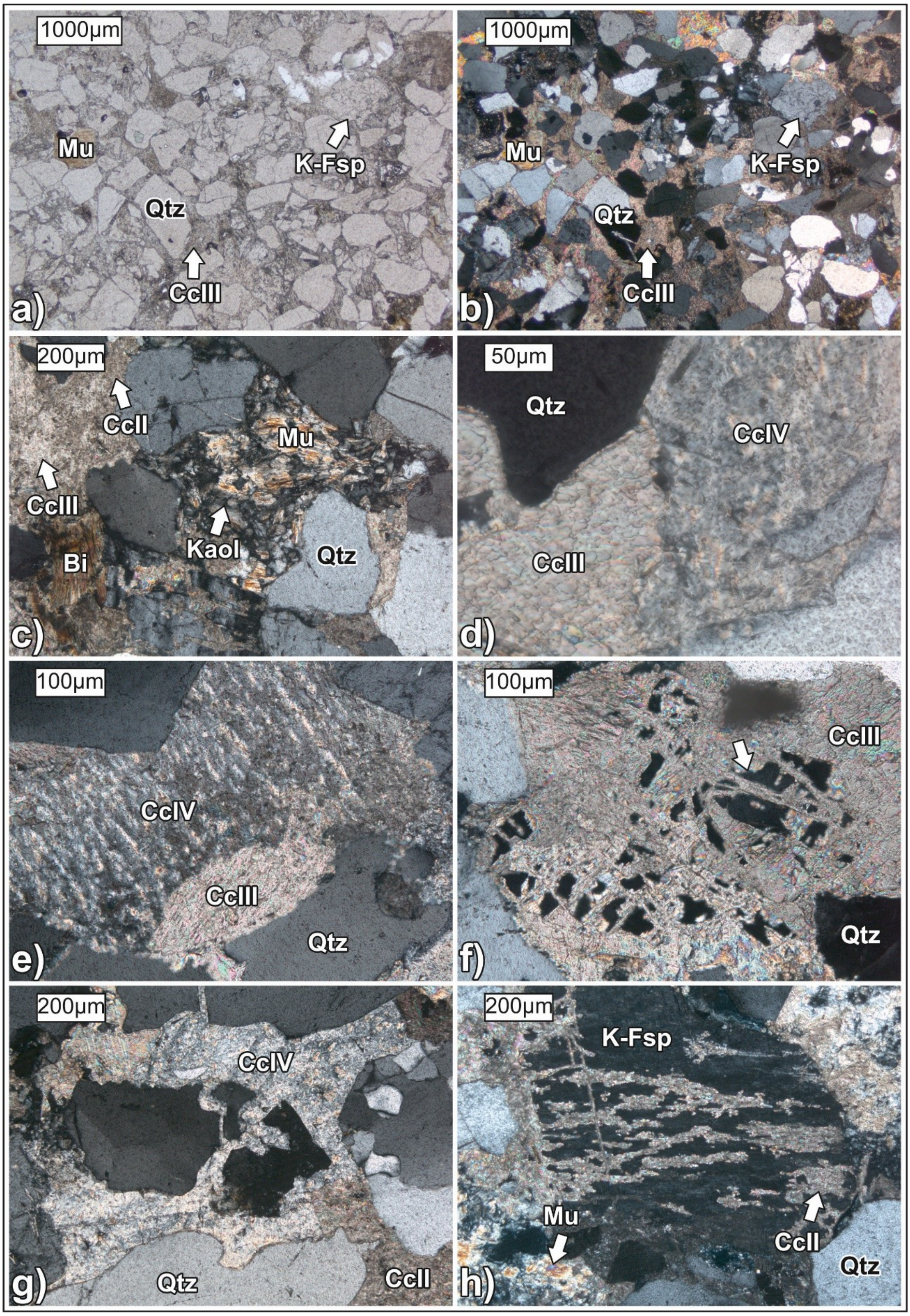

Fig. 58 Thin section photographs of cemented sandstones of the Voitsdorf Formation: a,b) overview of the texture in plane- and cross-polarized light; c) detrital grains, mica and kaolinite surrounded by Cc II and Cc III; d,e) prevailing carbonate cement generations (Cc III and Cc IV); f-h) strong corrosion and partial replacement of siliciclastic grains by calcite cement.

- Sandstones of Cerithian Beds

The strongly cemented sandstones of the Cerithian Beds show poor sorting (Figs. 59a,b). Besides quartz, some K-feldspar grains are present as primary components as well. Besides, also some biotite mineral flakes are visible in sediments of the Cerithian Beds.

Their pore space is completely filled with carbonate cement, which reveals different morphologies: microcrystalline Cc II and blocky/homogenous Cc III; similar to the cemented sandstones of the Voitsdorf Formation. The paragenetic relationship of this two cement generations, Cc II and Cc III is visible in Fig. 59c. Apart from the common grain-supported texture, local cement-supported texture of the detrital grains is recognizable from Figs. 59c,d. Occasionally, dolomite appears as fine crystal grains, encased in blocky/homogenous Cc III (e.g. Fig. 59e). In addition, foraminifera are preserved and filled with blocky/homogenous Cc III (Fig. 59f).

The K-feldspar grains show strong corroded margins, where they are at contact with carbonate cement (Fig. 59g). Siliciclastic grains are partial dissolution at contact with cement. Thereby feldspar grains are affected the most, because they demonstrate stronger corrosion marks than quartz grains (Fig. 59h).

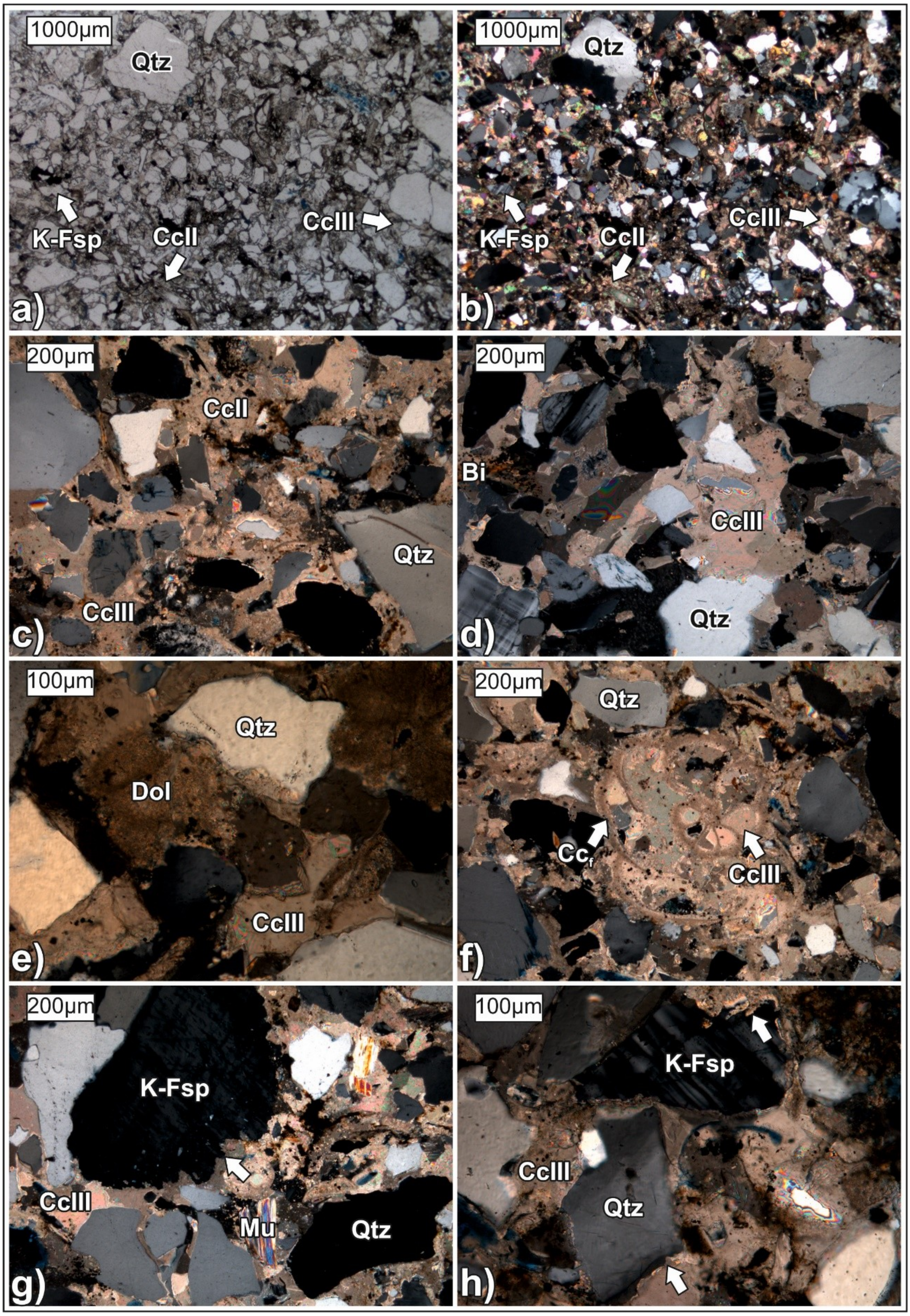

Fig. 59 Thin section photographs of cemented sandstones of the Cerithian Beds: a,b) overview of the texture in plane- and cross-polarized light; c,d) prevailing carbonate cement generations (Cc II and Cc III), grains are partially cement-supported; e) dolomite phase within calcite cement. f) foraminifer embedded in calcite cement; g,h) corrosion marks at K-feldspar and quartz at contact with calcite cement.

- Ampfing Formation

Detrital particles are mainly composed of quartz, feldspar (K-feldspar) and mica (muscovite).

The percentage of carbonate cement in strongly cemented samples reaches 49% (on a whole rock basis). Calcite is the only carbonate cement phase in the Ampfing Formation (Figs. 60a,b).

Locally microcrystalline cement (Cc II) occurs around detrital grains, especially in areas with poor grain sorting. However, a pervasive blocky/homogenous calcite (Cc III) with a uniform extinction predominates (Fig. 60c). In some areas the blocky/homogenous cement (Cc III) grades into poikilitic cement (Cc IV) (Fig. 60d), which is also pervasive and fills the pores completely. The paragenetic relationships of the pervasive cements Cc III and Cc IV are visible more in detail in Figs. 60e,f, where it is visible that Cc III is surrounded by Cc IV.

Siliciclastic minerals (quartz and feldspar) are considerably disintegrated, when they are at contact with both pervasive cement types (Cc III, Cc IV). Strong partial dissolution and replacement by calcite is apparent (Figs. 60c,g,h). Also some glauconite grains are strongly corroded at contact with carbonate cement.

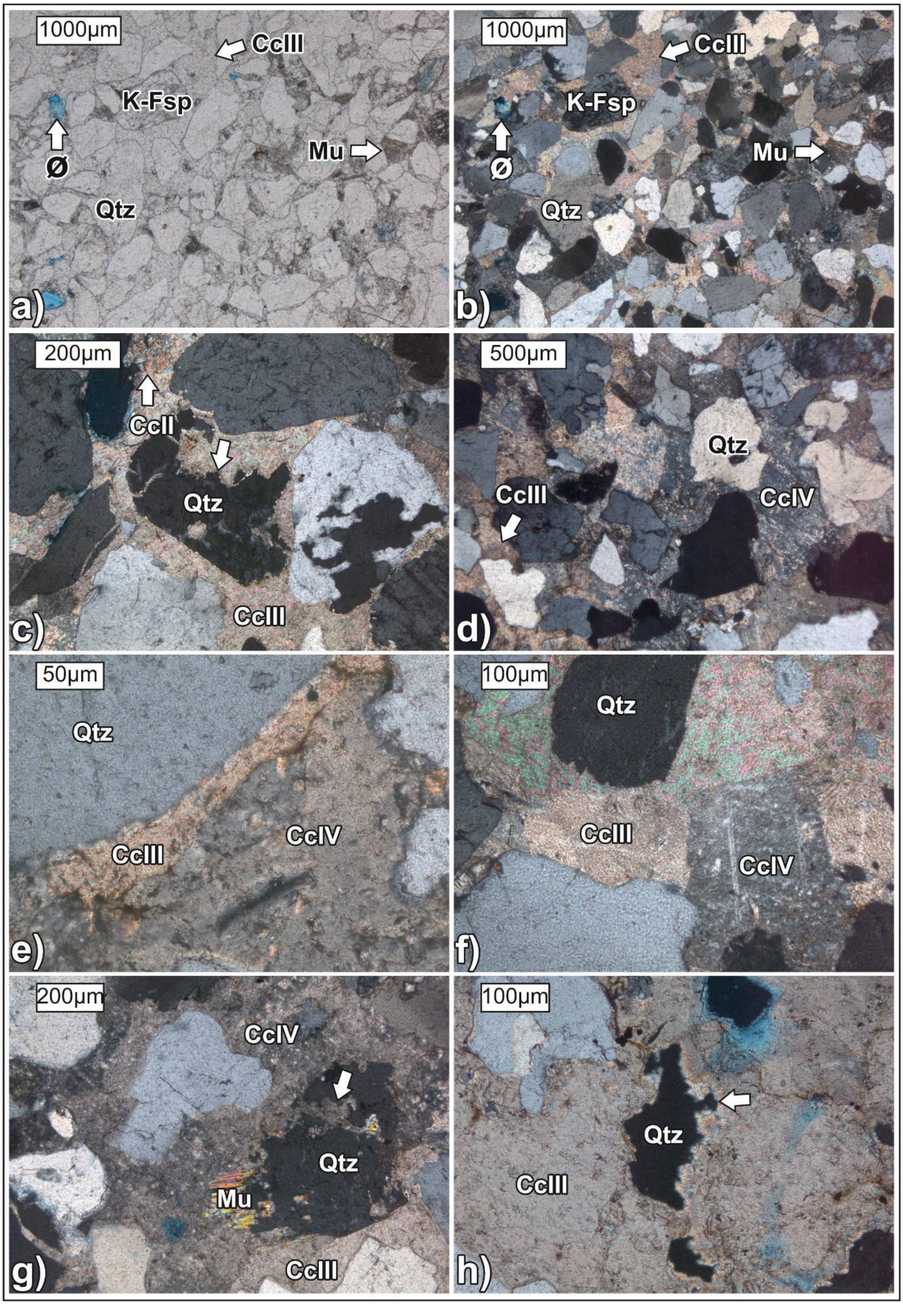

Fig. 60 Thin section photographs of cemented sandstones of the Ampfing Formation: a,b) overview of the texture in plane- and cross-polarized light; c) prevailing carbonate cement generation Cc III with some microcrystalline Cc II; d,e,f) blocky/homogenous Cc III grades into poikilitic Cc IV; g,h) strong partial disintegration and replacement of quartz grains by calcite Cc III and Cc IV.

b. Electron microprobe microscopy

- Voitsdorf Formation

Electron microscope images of strongly cemented sandstone of the Voitsdorf Formation are provided in the following figures:

Besides the dominant detrital quartz, also feldspar grains (mainly K-feldspar) are present (Figs. 61a-d, 62). These grains exhibit comparably more compaction than similar samples from the Cerithian Beds and Ampfing Formation. In addition, siderite-biotite intergrowth is typical for sandstones of the Voitsdorf Formation (Fig. 61c), whereas it is less common or missing in sandstones of the Cerithian Beds.

Eogenetic kaolinite clusters are encased completely by blocky/homogenous cement (Cc III) (Figs. 61b,e). This cement is composed of calcite, as visible in the Ca-map in Figs. 62a,b. The WDX element maps also show slightly elevated Fe contents in Cc III.

The corrosion and partial replacement of siliciclastic grains is noticeable (e.g. Fig. 61d). The detrital particles display different stages of stability (Fig. 62a): The feldspars show stronger corrosion, with albite the most affected (e.g. Fig. 61b). Quartz minerals exhibit etched rims. The fracturing of some quartz grains favors dismembering and replacement by calcite (Figs. 61c,d).

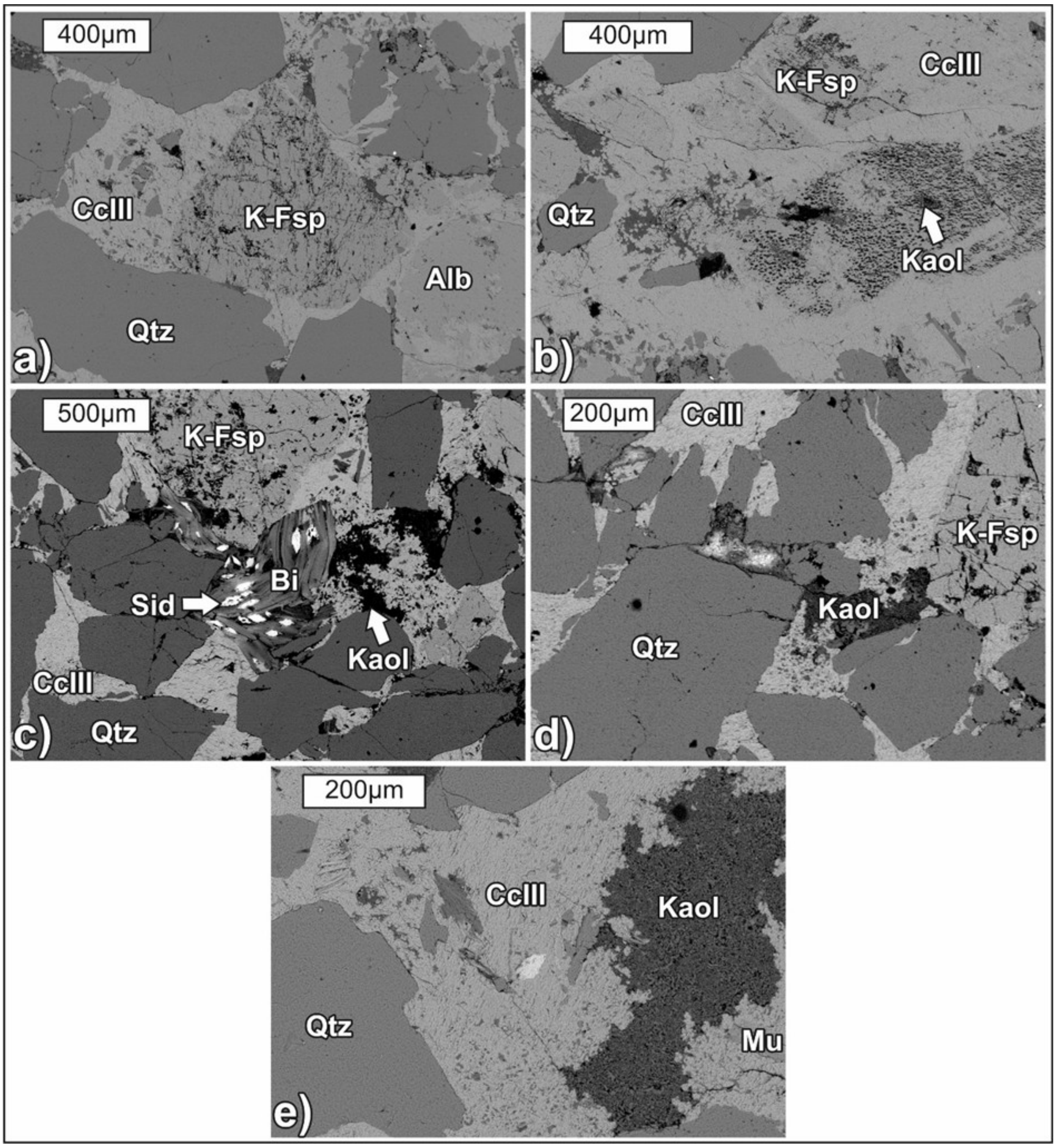

Fig. 61 BSE-images of cemented sandstones of the Voitsdorf Formation: a) overview of the texture with pore filling carbonate cement, to note are the corrosion marks on quartz grains and albite; b) kaolinite cluster encased in calcite cement Cc III; K-feldspar is partly disintegrated and replaced; c) siderite-biotite mineral assemblage, typical for the Voitsdorf Formation; d) corrosion and partial replacement of detrital grains and kaolinite by Cc III; e) relictic kaolinite in the interstices of detrital grains is surrounded by calcite cement.

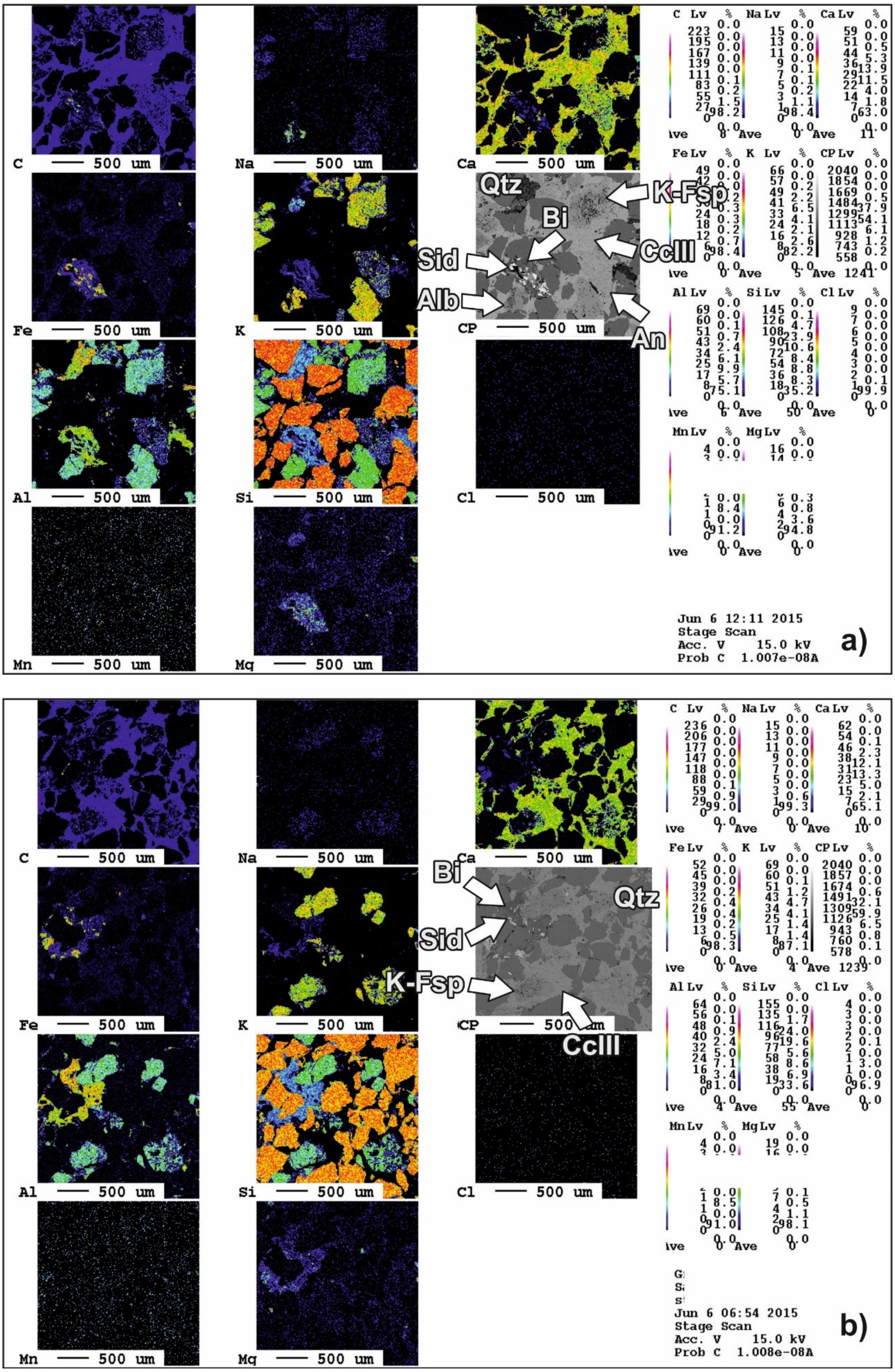

Fig. 62 a,b) Wave length dispersive (WDX) element maps of cemented sandstone of the Voitsdorf Formation (CP=BSE image).

- Sandstones of Cerithian Beds

The texture of a representative sample from the strongly cemented horizon of the Cerithian Beds is shown in Fig. 63a. Aside from quartz grains and subordinately feldspar (K-feldspar) grains also mica (muscovite and biotite) occur. Single layers are enriched by a variety of fossils (Figs. 63b,c, 64a). The shells and foraminifera are well preserved.

The detrital particles are surrounded by calcite cement (Figs. 63a-f, 64a,b). The two common generations of cements are visible: microcrystalline Cc II and blocky Cc III. The pervasive character of Cc III is apparent. The pervasive cement Cc III is composed of calcite, with slightly elevated Mg contents (Figs. 64a,b). Besides the general grain-supported character of the grains, they are locally cement-supported (Figs. 62a-e). Although the fossils are embedded within the calcite cement, they do not show any replacement phenomenon (Figs. 63b,c).

Partial dissolution and replacement of siliciclastic grains occur (Figs. 63a-f, 64a,b): Especially the disintegration of anorthite (Si, Al, Ca) and is replacement by calcite (Ca) along fractures is apparent (e.g. Fig. 63f). In comparison, K-feldspar (Si, Al, K) are not that strong affected (e.g. Figs. 63e, 64a,b). Quartz (Si) grains exhibit corroded margins and partial replacement by calcite along fractures (Figs. 63a,b,d, 64a,b).

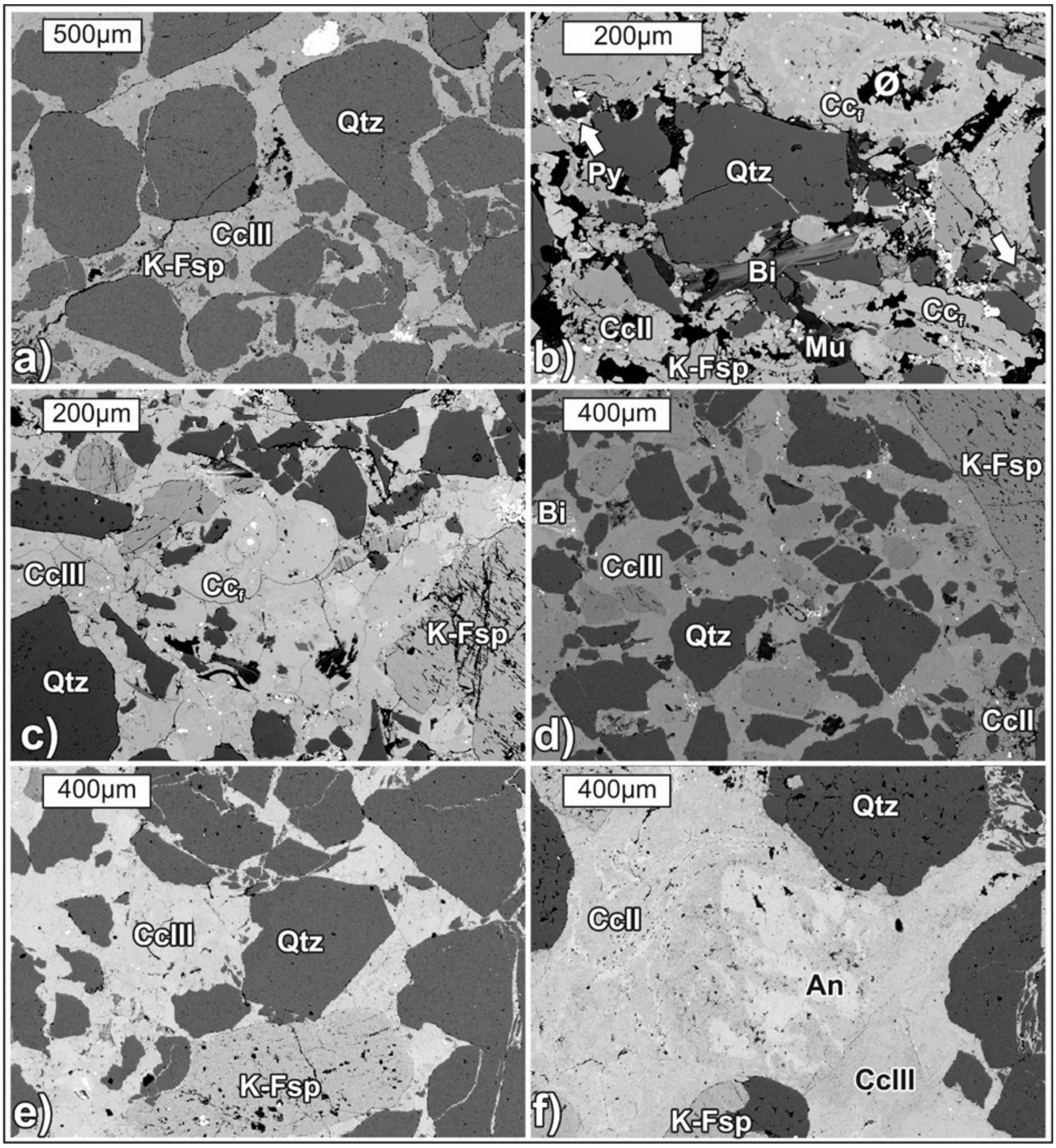

Fig. 63 BSE-images of cemented sandstones of the Cerithian Beds: a) overview of the texture with pore filling carbonate cement, to note are the corrosion marks on quartz grains and K-feldspar; b,c) abundant fossils, typical for the sandstones of the Cerithian Beds; d,e) local cement-supported texture of quartz grains, which show apparent corroded margins; f) anorthite grain is partial disintegrated and replaced by calcite cement (Cc II and Cc III).

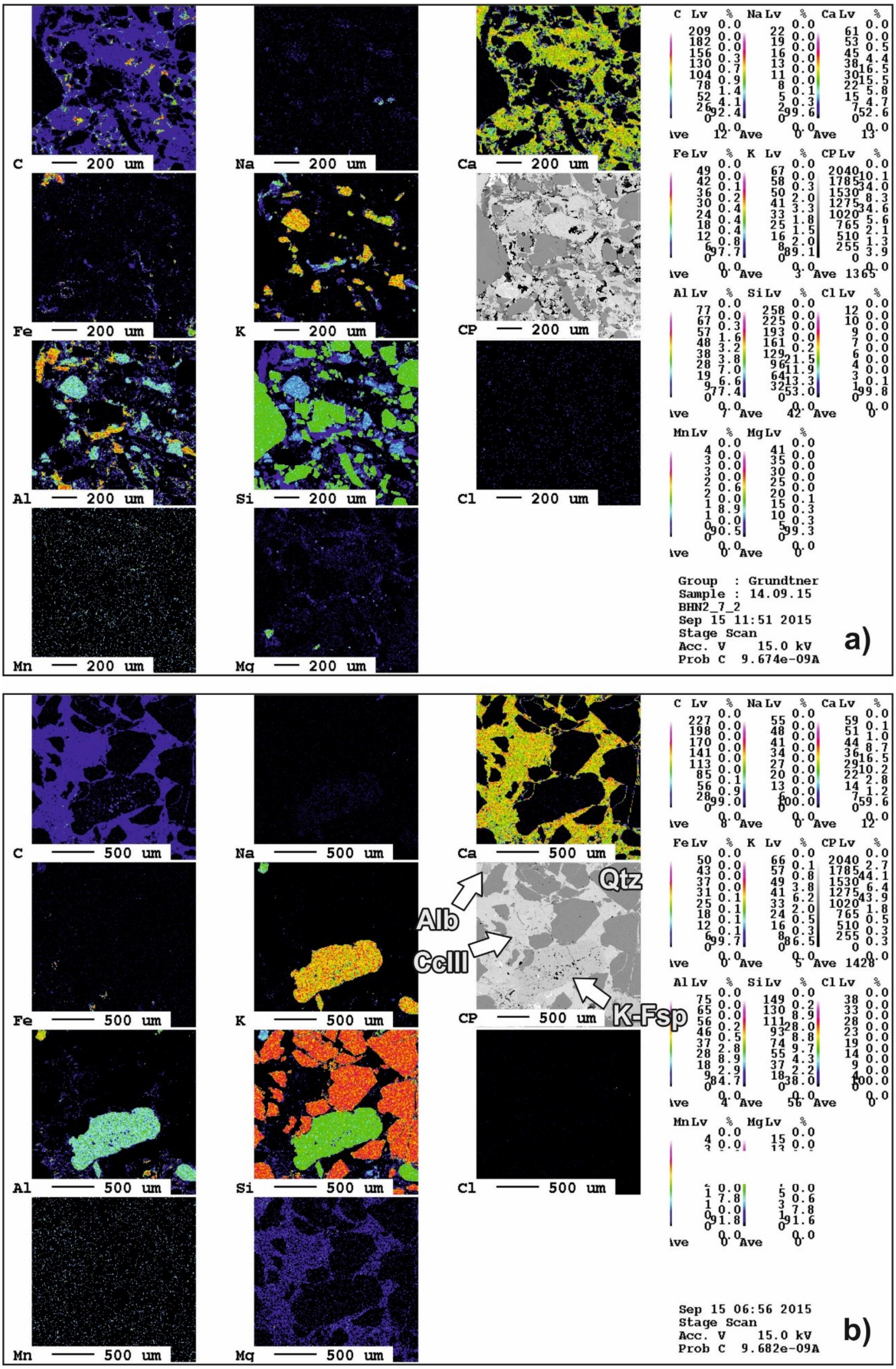

Fig. 64 Wave length dispersive (WDX) element maps of cemented sandstone of sandstones of the Cerithian Beds (CP=BSE image).

Intervals of strongly cemented sandstones are common between bitumen-impregnated horizons within the well BHN2 (see also Sachsenhofer et al., 2006): The top of the investigated core is prominent, where the strong carbonate cemented sandstones put a ceiling on the reservoir sandstones, which are filled with solid bitumen. The contact zone of these two different pore fillings (carbonate and bitumen) was investigated sedimentpetrographically in detail (Figs. 65a,b): Obviously, a cemented (Ca) zone is situated in the upper part of the pictures and the bitumen-impregnated (C) in the lower (Fig. 65c). The upper part of the Ca-map is dominated by a bright color, suggesting calcite (Ca) as the dominant pore filling. A slight enrichment in Mg is evident within these carbonate cements, an evidence for "Cc III-a" within this sample. In these intervals carbonate cementation caused a distinct reduction in porosity. The calcite depicts two morphologies: a microcrystalline (Cc II) and a blocky/homogenous (Cc III) one (Figs. 65a,b). Cc II is located near the oil-impregnated zone. It is corroded and partially dissolved at the contact with the bitumen. Thus, the cement may be recrystallized in the contact zone with the hydrocarbons. In comparison, Cc III is the dominant cement type in the upper part. The K-feldspar grains are disintegrated partially and the fractures filled with oil at the lower part. Further, quartz grains display etched margins.

The bitumen-impregnated zone hardly ever shows an indication for any carbonate minerals (Fig. 65c). In this region silica is prevailing with quartz (Si) minerals. Some K-feldspars (Si, Al, K) are present as well. Obviously, the distribution of hydrocarbon is visible in the C-map. Inverse to the Ca-map, an enrichment in the lower part is visible, which could be a sign of the distribution of the oil. C is distributed in the open pores, which is black in the CP (BSE)-map. It is located mostly along grain contacts.

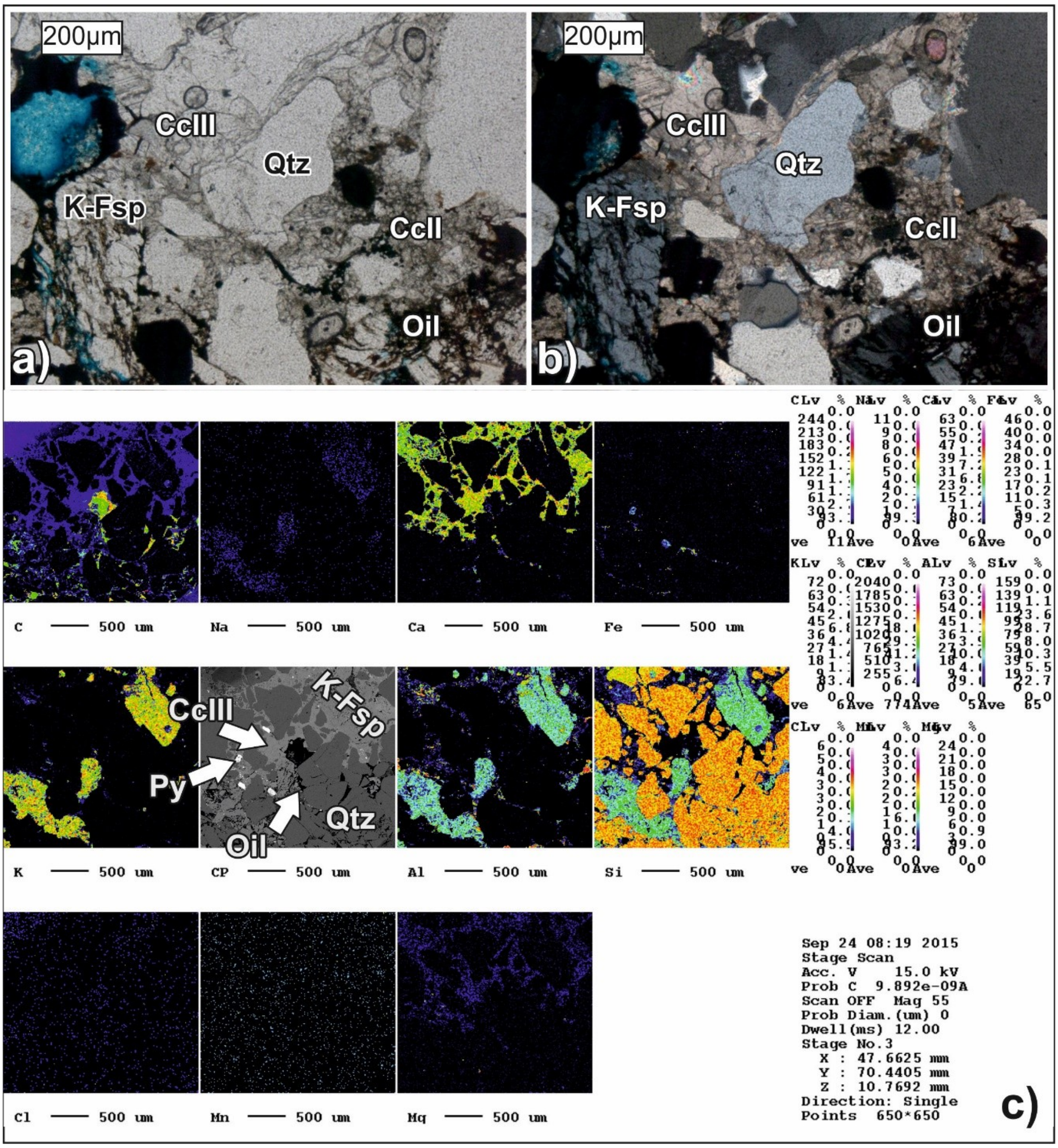

Fig. 65 Thin section photographs of cemented sandstones within the oil-bearing zone: a,b) overview of the texture in plane- and cross-polarized light of Eocene sandstones; c) Wave length dispersive (WDX) element maps of cemented sandstone (CP=BSE image).

- Ampfing Formation

WDX element maps support calcite (Ca) to be the only carbonate cement type for the strongly cemented samples of the Ampfing Formation (Figs. 66a,b). Slightly increased Mg contents in the pervasive calcite cements (“Cc III-a”) of strongly cemented sandstones are obvious.

In addition, the different stabilities of the detrital siliciclastic materials are visible in Figs. 66a,b. The quartz (Si) minerals are comparably stable; they show corroded margins only. In comparison, the feldspars albite (Si, Al, Na) and K-feldspar (Si, Al, K) are partial dissolved and replaced by calcite cement. Thereby, K-feldspar is replaced along its cleavage planes primarily, whereas albite is nearly completely replaced by the carbonate cement, as observable in the Ca-map. Only feldspar remnants are left.

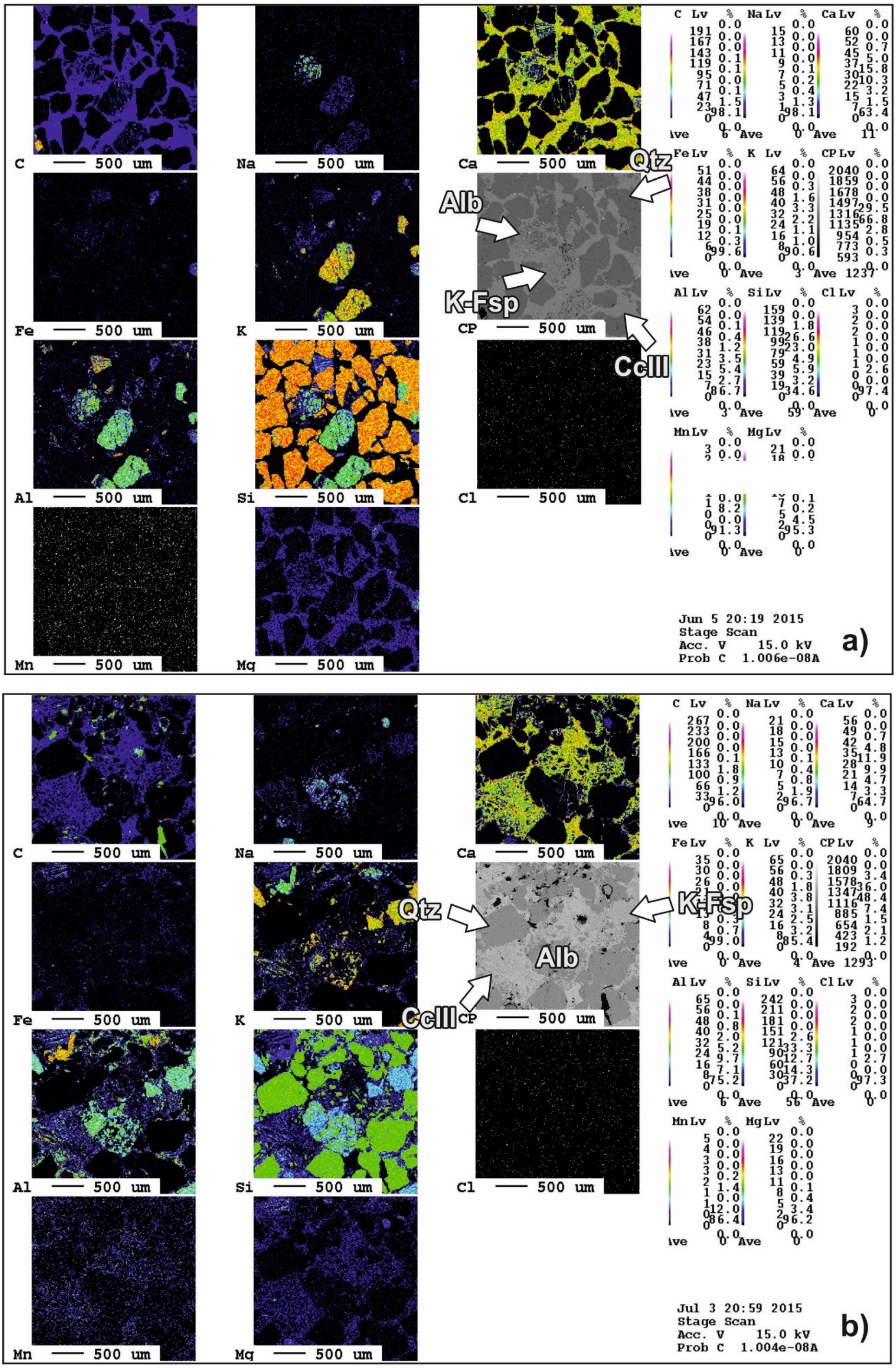

Fig. 66 Wave length dispersive (WDX) element maps of cemented sandstones of the Ampfing Formation (CP=BSE image).

c. Scanning Electron Microscopy

- Voitsdorf Formation

SEM images of the strongly cemented horizons of the Voitsdorf Formation display the impact of carbonate cementation:

Detrital quartz grains are directly overgrown by the authigenic calcite cement (Fig. 67a).

The blocky morphology of the pervasive calcite cement is visible in Fig. 67b. This calcite displaying in Figs. 67c fills porosity extensively.

Feldspar grains are altered and resorbed (Fig. 67d).

Kaolinite booklets (Figs. 67b,e) and fine needles of illite (Fig. 67f) grow on resorbed feldspar (Figs. 67e,f) and calcite cement (Fig. 67b), and therefore, are considered as late stage cement generation.

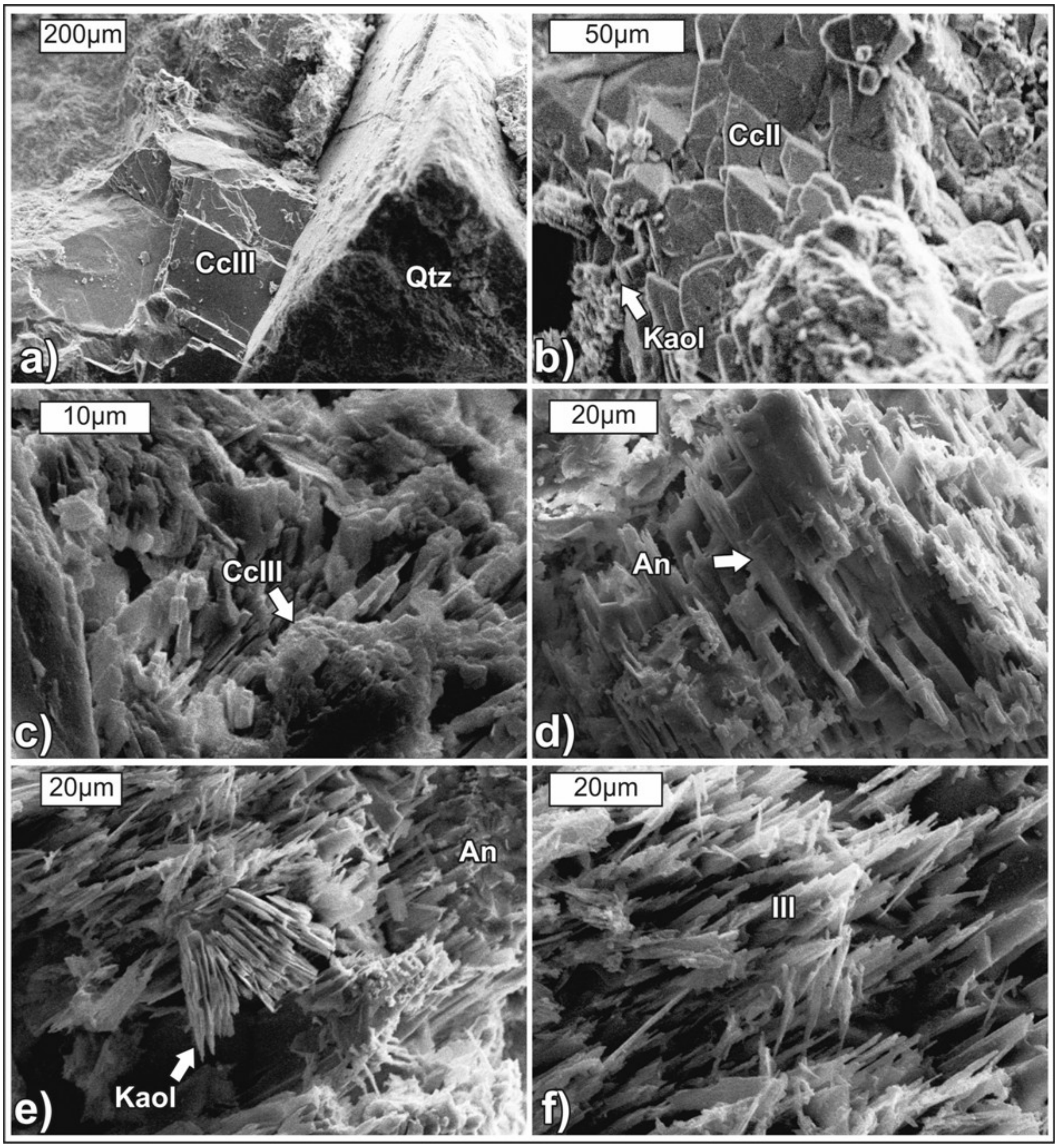

Fig. 67 SEM-images of cemented sandstones of the Voitsdorf Formation: a) contact of detrital quartz grain with pervasive calcite cement; b) blocky growth morphology of carbonate cement with kaolinite overgrowth; c) calcite cement; d) alterated feldspar grains; e) kaolinite booklets; f) illite needles.

- Ampfing Formation

Cemented sandstone SEM images of the Ampfing Formation are shown in Fig. 68:

Quartz minerals, which are the prevailing detrital components, are covered by a thin coating of calcite. Therefore the single detrital grains are not well visible (Fig. 68a-e). Occasionally also some dolomite is present in the carbonate coatings (Fig. 68f).

The feldspar grains are resorbed and have corroded surfaces (Figs. 68g,h).

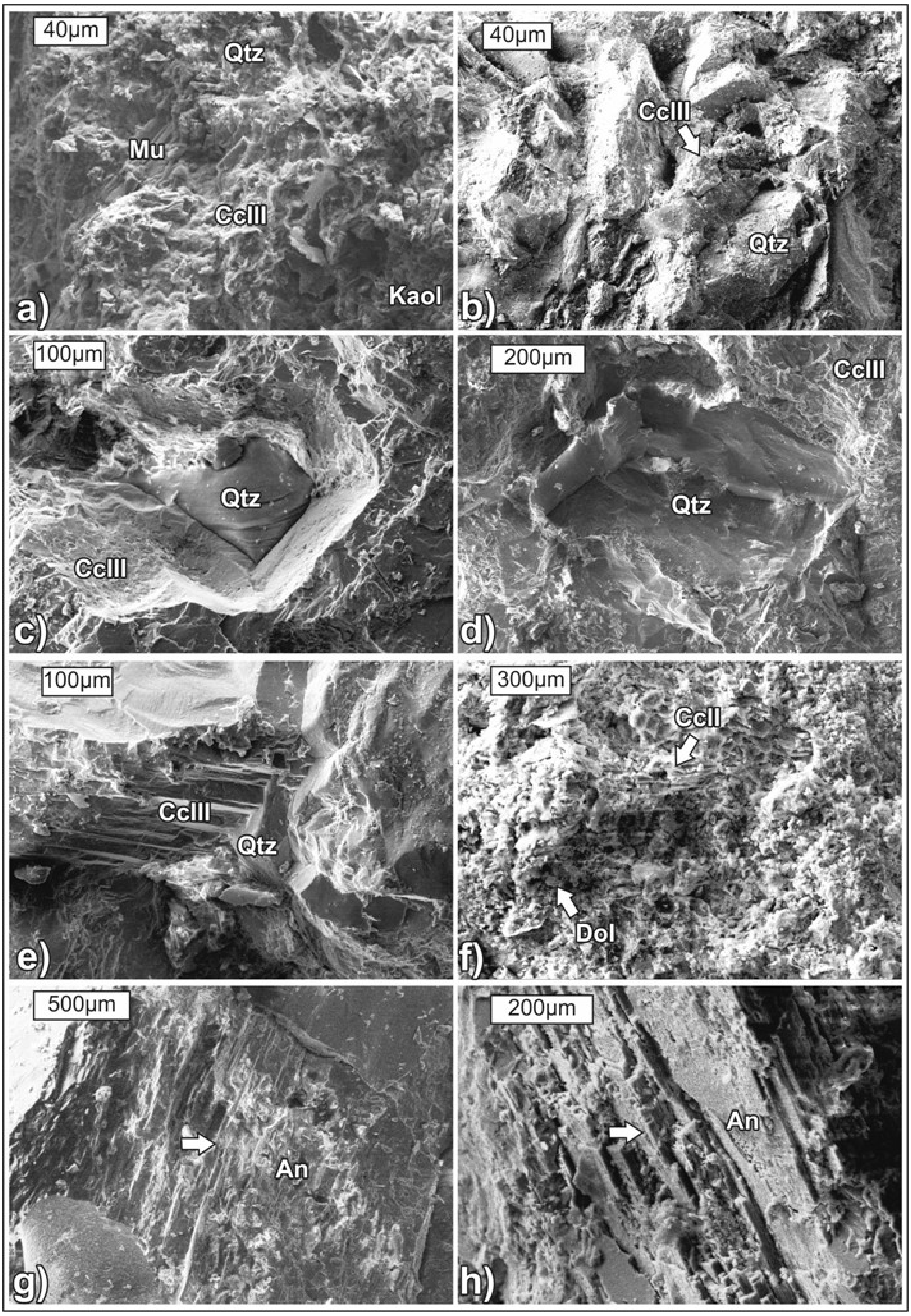

Fig. 68 SEM-images of cemented sandstones of the Ampfing Formation: a-e) overview of the texture of the cemented zone, detrital quartz grains surrounded by pore filling Cc III; f) besides calcite, locally also dolomite mineral phases are present; g,h) resorbed feldspar grains.

Water-bearing sandstone

Water-bearing sandstones were available only from the Ampfing Formation. These samples originate from a depth of 1660 - 2020 m below ground level.

Carbonate cement minerals are present within water-bearing sandstones with about 6% consisting mainly of calcite (Cc II and Cc III, seldom Cc I; 5%), and traces of ankerite (1%). The mean percentage of quartz, feldspar and lithic fragments is 38, 16 and 11%, respectively. Clay minerals, such as illite, smectite, kaolinite, and minor chlorite were identified, which amount in total to 11%. Mica is rare (5%). Accessorily, glauconite, hematite, pyrite, detrital carbonate grains and fossils occur. The mean porosity of water-bearing sandstone measured in the lab is 13%.

a. Thin section microscopy

Locally, detrital grains are surrounded by diagenetic clay mineral rims or carbonate cements (Figs. 69a,b). Based on their paragenetic relationship, it is evident that clay minerals were formed first, followed by carbonate cements. The relative high porosity values are a result of interparticle porosity. A brownish-colored mixture of clay minerals (illite with some smectite), iron oxides or mud (undifferentiated fine-grained matrix), formed at the pore throats (Figs. 69c,d).

Two calcite generations, older microcrystalline Cc II and younger blocky/homogenous Cc III were identified. Calcite cement (Cc II) is often strongly corroded, if it is at contact with authigenic illite respectively kaolinite (Figs. 69e,f). The blocky/homogenous cement generation (Cc III) appears as coarse aggregates in mm-size, showing a granular morphology. Within the water-bearing sandstones Cc III is the prevailing calcite phase.

Some quartz and K-feldspar grains show corroded margins and are covered by a microcrystalline cement generation (Cc II), which is partially replaced by the prevailing blocky/homogenous one (Cc III) (Figs. 69c,g). Furthermore, partial dissolution of feldspar and replacement by clay minerals, involving kaolinite and illite, is evident.

Kaolinite forms booklets growing into open pores (Figs. 69d,h), which marks the last diagenetic stage within the water-bearing sandstones according to SEM (Fig. 71, see below).

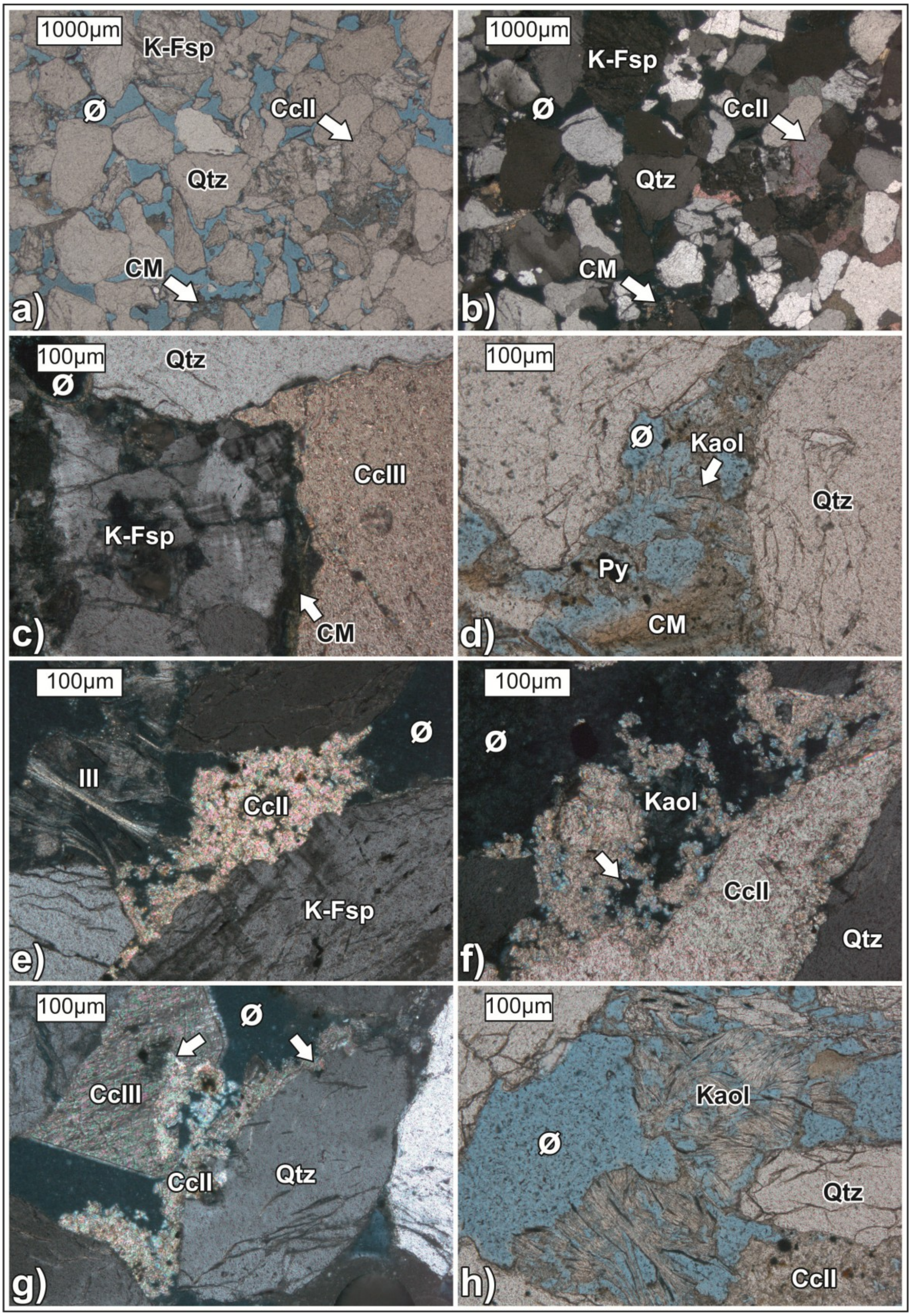

Fig. 69 Thin section photographs of water-bearing sandstones from the Ampfing Formation: a,b) overview of the texture in plane- and cross-polarized light; c,d) brownish-colored rims of clay minerals and iron oxides around detrital grains; e,f) Cc II strongly corroded at contact with illite respectively kaolinite; g) Cc II corrodes quartz grains and Cc III replaces Cc II partially; h) kaolinite fans grow into the open pores.

b. Electron microprobe microscopy

Electron microscope images of the water-bearing samples from the Ampfing Formation are shown in Fig. 70:

Quartz grains are the main mineral phase; subordinately K-feldspar and lithic fragments are present as well. This sandstone achieves a high porosity (Fig. 70a).

Glauconite represents an eogenetic (authigenic) phase in the water-bearing samples. The alteration of glauconite is considerable (Fig. 70d). Several muscovite flakes and pyrite are enclosed by clay minerals. These clay minerals consist mainly of illite and smectite and fill the interstices of the grains locally (Figs. 70b,c).

Furthermore, also carbonate cement (Cc II and Cc III) is present. Both cement types show relictic character in the form of distinct dissolution features.

Apart from carbonates, also quartz, feldspar and lithic fragments show distinct partial disintegration. Lithic fragments are fractured, feldspar is partly dissolved and quartz has corroded margins (Figs. 70a-e).

Locally the porosity is decreased by kaolinite fans, which grow into the open pores. The relictic calcite cement is strongly decomposed and partially replaced by kaolinite (Fig. 70e).

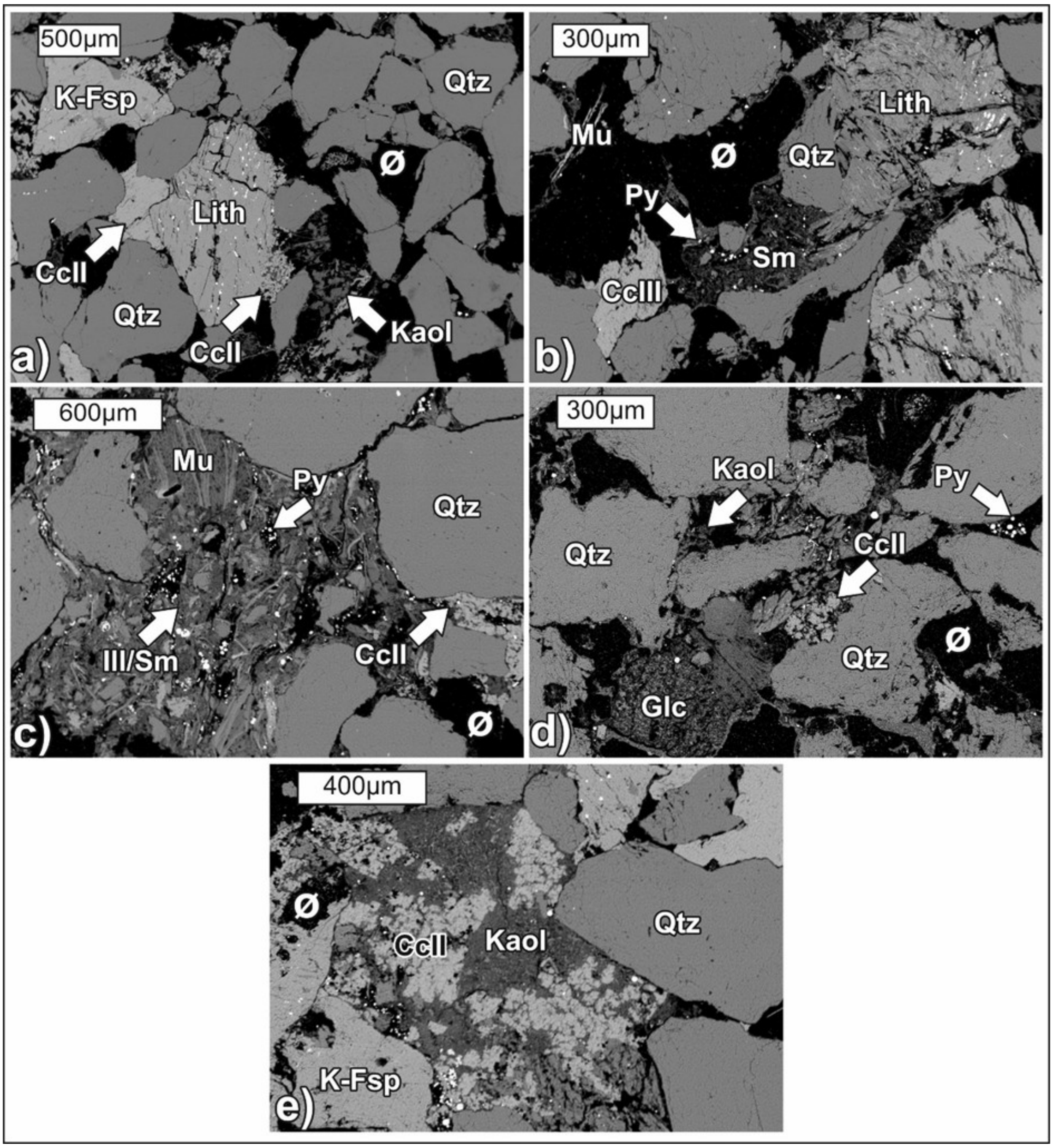

Fig. 70 BSE-images of water-bearing sandstones from the Ampfing Formation: a) overview of the texture with relictic carbonate cement and kaolinite as pore filling; b,c) smectite minerals formed at the margins of grains; calcite and lithic fragments are strong corroded; d) etched quartz and glauconite margins with some kaolinite and calcite fillings at the interstices of grains; e) partial replacement of calcite cement by kaolinite.

c. Scanning Electron Microscopy

Fig. 71 provides an overview about the texture of the water-bearing sandstones of the Ampfing Formation in SEM images.

Detrital quartz and K-feldspar grains are surrounded by some kaolinite fans (e.g. Fig. 71a).

Although minor calcite is present within these water-bearing sandstones, an area with a local high calcite content was investigated. Figs. 71b-d were taken within such a strongly cemented area of the Ampfing Formation. It shows that detrital grains, like quartz grains (Figs. 71b,c) and muscovite flakes (Figs. 71c,d), are encased by calcite. The cement has fine granular crystals and is therefore interpreted as microcrystalline Cc II. Grains, which are surrounded by this early calcite Cc II are not corroded (Fig. 71c). Moreover, on the surface of this siliciclastic mineral are some small quartz crystals.

Compared to the relative stable quartz mineral, K-feldspar shows disintegration (Fig. 71a). Nevertheless some quartz grains may be heavily corroded. This is evidenced by the rough, corroded surface of a quartz grain, which is not covered by carbonate cement (Fig. 71e).

Prominent kaolinite booklets (Figs. 71f,g) grow on different mineral surfaces and are interpreted as last authigenic phase. Apart from kaolinite, some chlorite overgrowths on detrital mineral grains are also present (Fig. 71h). The chlorite is characterized by individual platelets, which are single euhedral crystals. The increased content in Fe typically for chlorite was confirmed by EDX measurements.

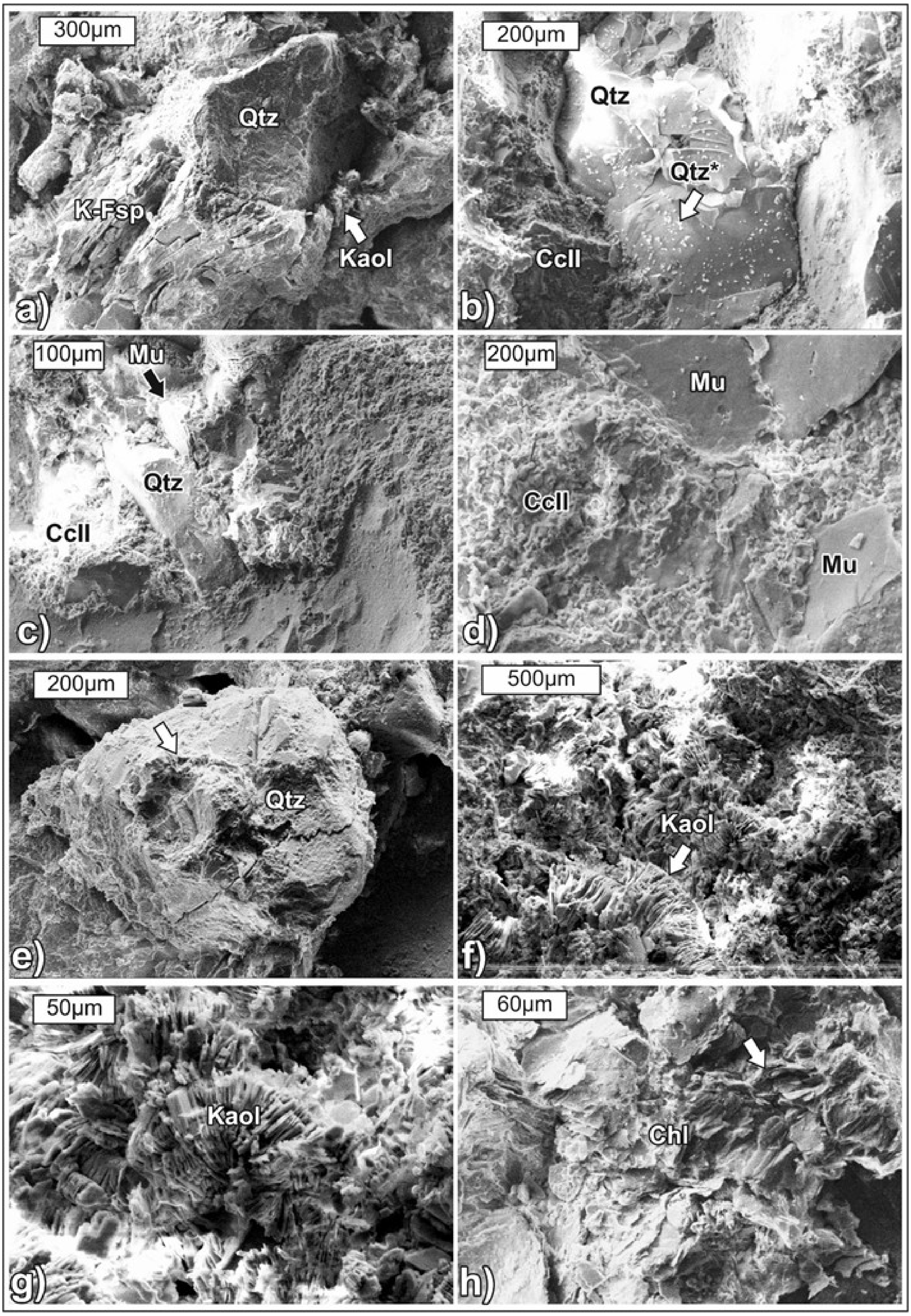

Fig. 71 SEM-images of water-bearing sandstones from the Ampfing Formation: a) detrital quartz and K-feldspar grain, contact zone filled with kaolinite; local high calcite content: b-d) detrital components surrounded by calcite cement Cc III; e) detrital quartz grain with corrosion marks; f,g) kaolinite booklets growing into open pores, h) chlorite sheets.

Oil-bearing sandstone

The investigated samples from the oil-bearing zone originate from a depth of 1580 - 2000 m below ground level.

Carbonate cement is present in minor amounts (6%). The cement mainly consists of calcite (Cc II and Cc III, seldom Cc I) and ankerite (each ~2%). Dolomite and siderite (each ~1%) are subordinate. The percentage of quartz, feldspar and lithic fragments is 44, 14 and 7%, respectively. Clay minerals (10%) consist of illite, smectite, kaolinite and subordinate chlorite. Mica is present with 5%. Traces of glauconite, hematite, pyrite, detrital carbonate grains and fossils were also identified. A mean porosity of 14% was determined in the lab for all investigated oil-bearing sandstones.

a. Thin section microscopy

- Voitsdorf Formation

An overview of the oil-bearing sandstone from the Voitsdorf Formation is presented in Figs. 72a,b.

Detrital minerals include quartz and feldspar and minor muscovite and biotite, which often occur in clusters (Figs. 72c,d). Subordinately clay minerals are present (Fig. 72d). Partial dissolution of alkali feldspar causes authigenic clay mineral formation (Fig. 72d). EDX analysis proved that the clay mineral shown in Fig. 72d is kaolinite. The partial disintegration also generates secondary porosity. Growth of siderite within biotite is a characteristic diagenetic feature of the Voitsdorf Formation. Occasionally, the siderite forms well defined rhombs (Figs. 72e,f).

Similar to water-bearing and strongly cemented sandstones, two calcite cement types (Cc II and Cc III) are present in the hydrocarbon-bearing sandstones. The microcrystalline cement is again locally replaced by the sparitic one. Cc II and Cc III are recrystallized and show dissolution features, where they appear near illite (Figs. 72g,h). Therefore, the carbonate cements are interpreted as relictic.

In all porous sandstones, feldspar and, to some extent, quartz show dissolution fabrics (Figs. 72d,g,h).

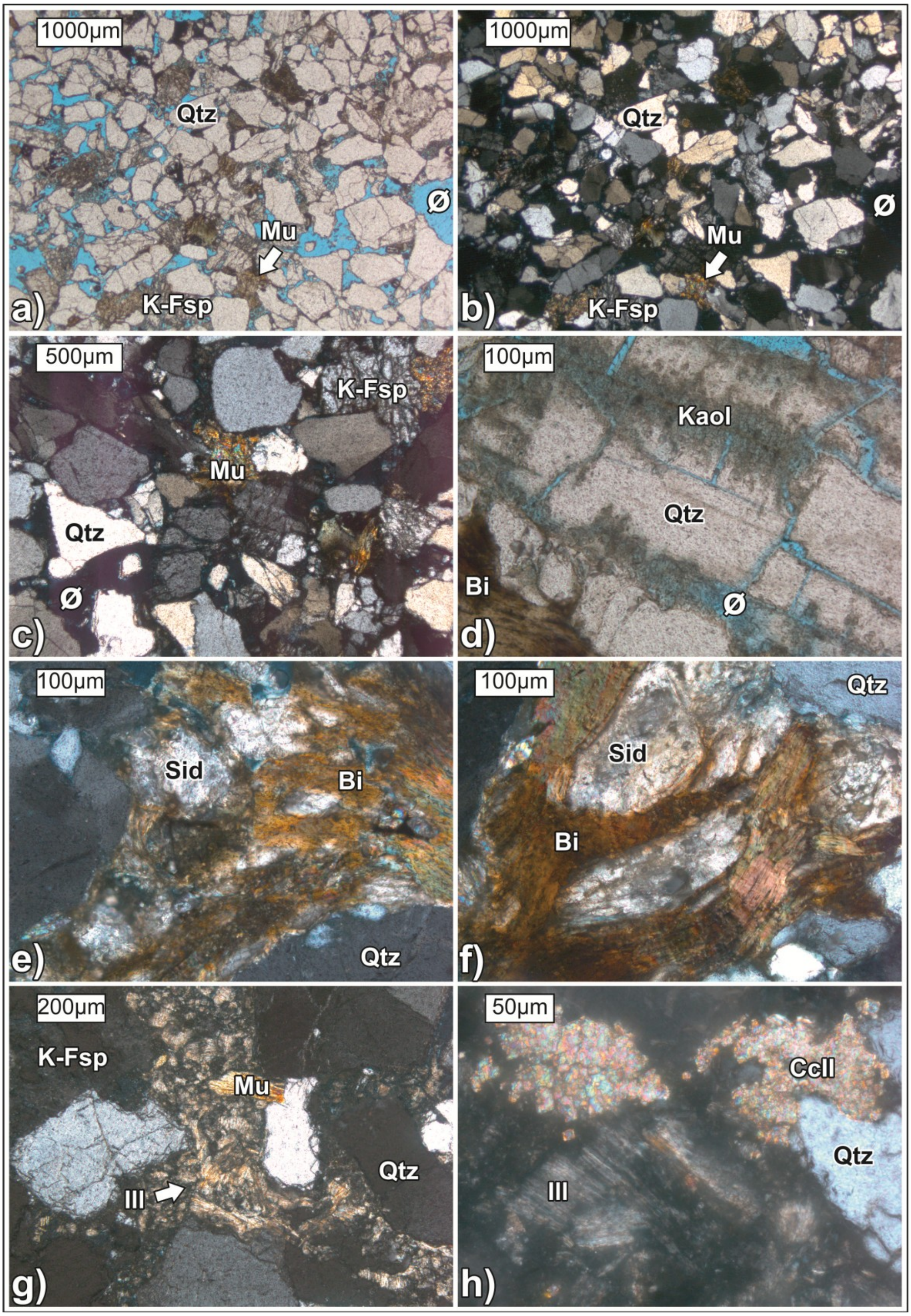

Fig. 72 Thin section photographs of oil-bearing sandstones from the Voitsdorf Formation: a,b) overview of the texture in plane- and cross-polarized light; c) pores filled with muscovite sheets locally; d) disintegrating K-feldspar and kaolinite growth; e,f) siderite-biotite mineral assemblage, typical for the Voitsdorf Formation; g,h) carbonate fragments near illite show dissolution features.

- Sandstones of Cerithian Beds

The overview images of an oil-bearing sandstone from Cerithian Formation (Figs. 73a,b) reveals poor sorting of the mineral grains.

In the Cerithian Beds, calcite cement margins are specked with iron oxides (hematite) and pyrites (Figs. 73c,d).

Between the detrital particles carbonate minerals are represented by microcrystalline Cc II and blocky/homogenous Cc III (Figs. 73d-g).

The formation of carbonate cements is accompanied by the corrosion of detrital siliciclastic minerals, like quartz (Figs. 73c,f). The feldspar is replaced by Cc II locally and its disintegration produces secondary porosity (Fig. 73h).

Secondary porosity is also generated by the partial dissolution of carbonate cements (Fig. 73g). Calcite generations show distinct corrosion marks by etched margins. Note that the quartz grain in the center of Fig. 73f appears to be cement-supported.

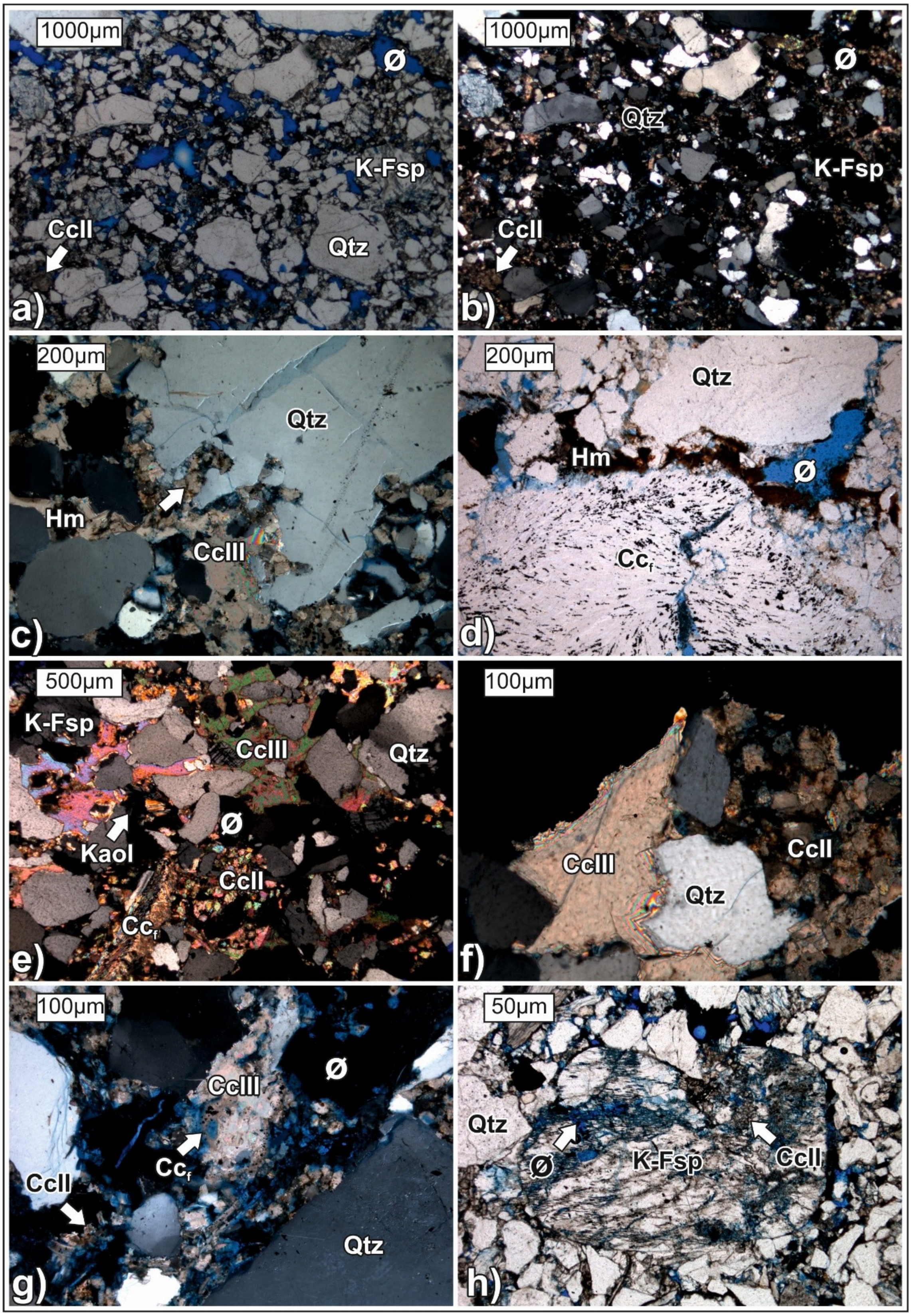

Fig. 73 Thin section photographs of oil-bearing sandstones of the Cerithian Beds: a,b) overview of the texture in plane- and cross-polarized light; c,d) hematite rims around detrital components; e) cement generations corrode quartz grains, which are cement-supported; f) different calcite cement types (Cc II, Cc III), quartz corrosion at contact to carbonate; g) generation of secondary porosity by partial carbonate dissolution; h) feldspar disintegration generates secondary porosity.

- Ampfing Formation

Thin section photographs of the oil-bearing Ampfing Formation are presented in Fig. 74:

Sandstones of the Ampfing Formation contain mainly quartz, K-feldspar and mica. In addition, they comprise also glauconite minerals (Fig. 74a,b). The glauconite has peloidal morphology (Fig. 74c). Its brown color indicates some alteration. Eogenetic glauconite and its alteration products are restricted to the Ampfing Formation. Occasionally pores are filled with clay minerals. Thereby different generations of clay minerals are evident (Figs. 74d-h):

(i) Typically, a brownish-colored mixture of clay minerals, iron oxides and mud (undifferentiated fine-grained matrix) developed along the margins of the open pores during eogenesis (Figs. 74d-g).

(ii) Big fans of muscovite and illite fill the pores and indicate some alteration (Fig. 74e,h). This result is supported by element map of K contents (Fig. 78, see below).

(iii) Kaolinite booklets are the most characteristic authigenic and diagenetically last mineral phase for hydrocarbon-bearing Eocene sandstones. It preferably grows on clay mineral rims and is present at the interstices of detrital grains (Fig. 74e). They decrease porosity locally.

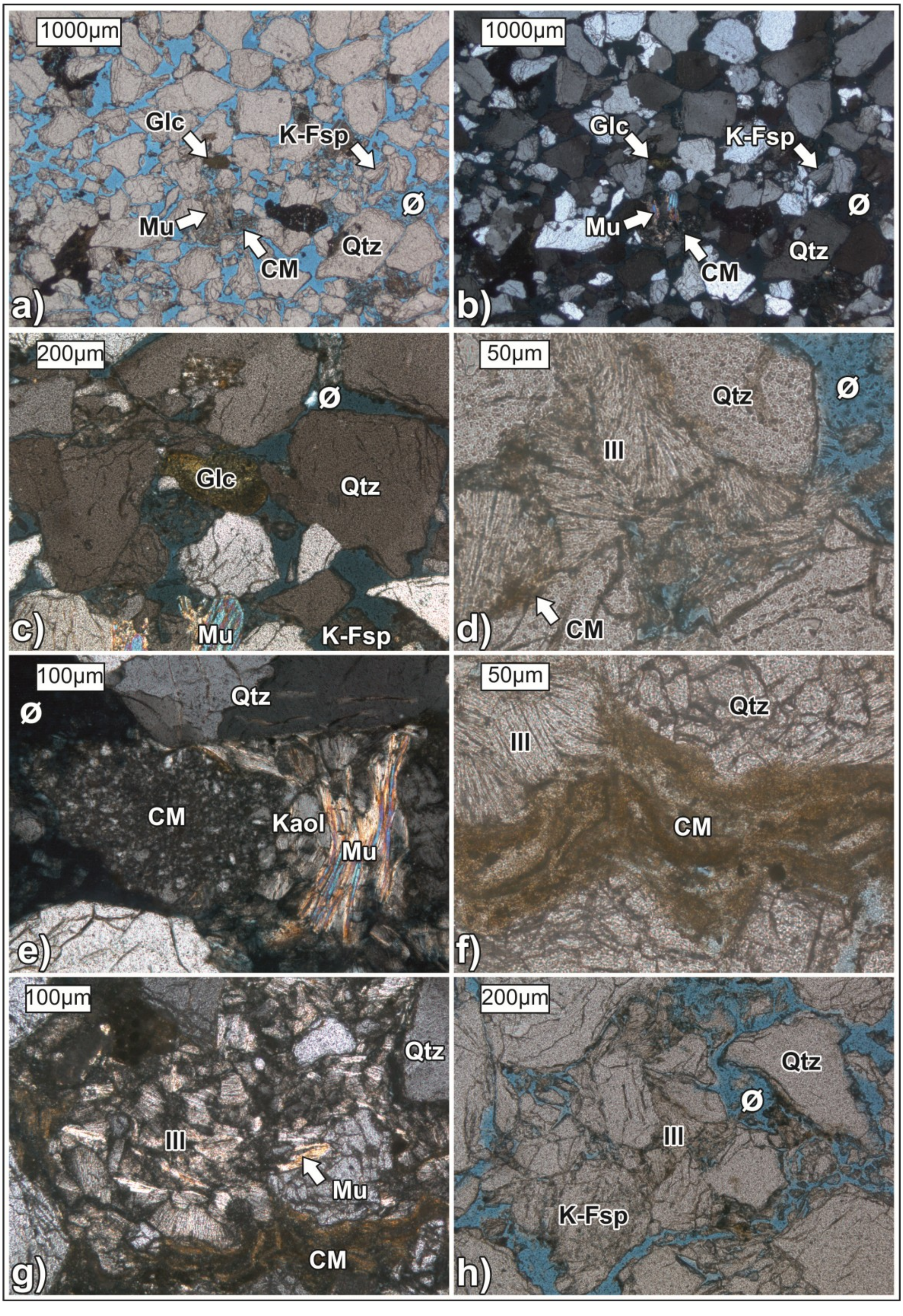

Fig. 74 Thin section photographs of oil-bearing sandstones of the Ampfing Formation: a,b) overview of the texture in plane- and cross-polarized light; c) alterated glauconite pellet; d-f) accumulation of muscovite, clay minerals and kaolinite at the interstices; g) paragenetic relationship of clay mineral rim (outside) and pore filling illite (inside); h) illite booklets at the interstices.

b. Electron microprobe microscopy

- Voitsdorf Formation

An overview of electron microscope images is shown for oil-bearing samples from the Voitsdorf Formation in Fig. 75:

Quartz and minor K-feldspar are the main components. Clay minerals, and rarely pyrite, border the margins of these grains, (Fig. 75a). Clay minerals have an illite and smectite signature by the EDX analysis (Figs. 75b,c). Subordinately, inside this clay filling, some muscovite and calcite particles have been observed as well (Fig. 75c). It frequently occurs as siderite crystals in assemblage with biotite flakes (Figs. 75a,c-f). Occasionally, siderite minerals appear which are not associated with biotite (Figs. 75g,h). They often show well defined rhombs (e.g. Fig. 75f). Siderite displays also some corroded margins (Fig. 75g). In addition, the disintegration of K-feldspar causes the formation of the clay mineral kaolinite (Fig. 75f). A relative high amount of siderite is present.

Quartz, feldspar and carbonate minerals are disintegrating and exhibit etched margins (Figs. 75a-h).

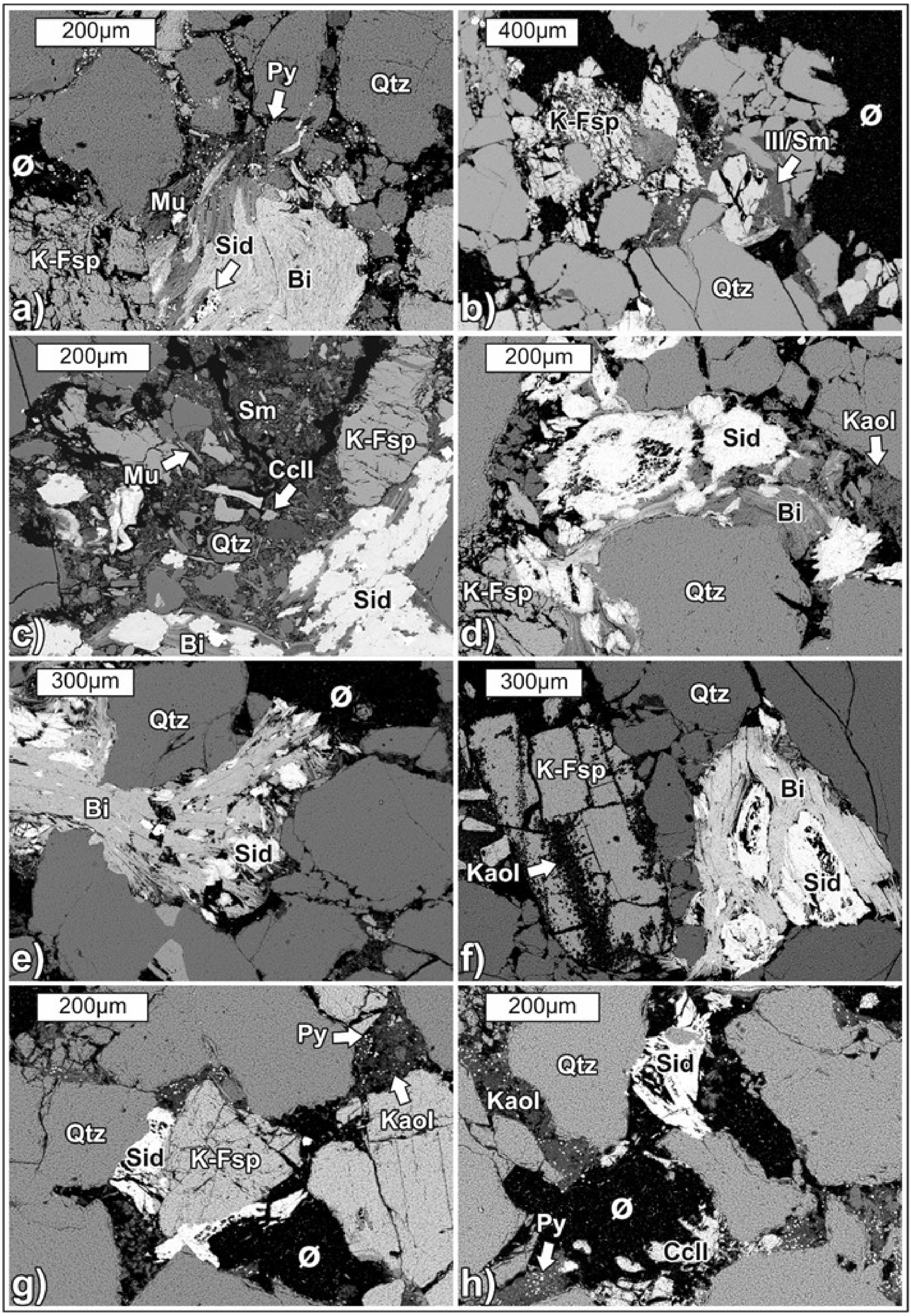

Fig. 75 BSE-images of oil-bearing sandstones from the Voitsdorf Formation: a) overview of the texture with minor pyrite and partial K-feldspar dissolution; b) some clay minerals as pore filling (illite, smectite) and disintegrating K-feldspar; c-e) biotite flakes with siderite, kaolinite and partial dissolved calcite as local pore filling; f) disintegrating K-feldspar and kaolinite growth, biotite encompass siderite rhombs; g,h) siderite without biotite between grains; d) e) big siderite crystals within biotite.

- Sandstones of Cerithian Beds

An overview of the texture of the oil-bearing sandstones of the Cerithian Beds is provided in Fig. 76:

Based on microprobe analysis, quartz and some feldspar, largely K-feldspar, were identified. Besides, some fossils are present, which is typical for this formation (Figs. 76a,b). Along the grain contacts, some pyrites are also present (Fig. 76b).

The space between the detrital grains is partially filled with carbonate minerals, which show different morphologies (Cc II and Cc III) (Fig. 76c). An area with increased calcite (Ca) cementation is shown in Figs. 76d and 77. The microcrystalline Cc II is partially dissolved, which causes secondary porosity. The homogenous Cc III fills the complete space between grains locally, and encloses dolomite and pyrite minerals (Fig. 76e).

Further, the stabilities of the siliciclastic minerals are evident (Figs. 76a-h, 77): Quartz (Si) grains exhibit etched margins. In comparison, K-feldspar (Si, Al, K) is partially disintegrated and albite (Si, Al, Na) is affected the strongest by dissolution.

The relictic character of the carbonate cement resulted in the generation of secondary porosity (Figs. 76f,g). In turn, the secondary porosity is reduced by kaolinite (Fig. 76h). The replacement of calcite (Ca) by Si- and Al-rich kaolinite is apparent (Fig. 77).

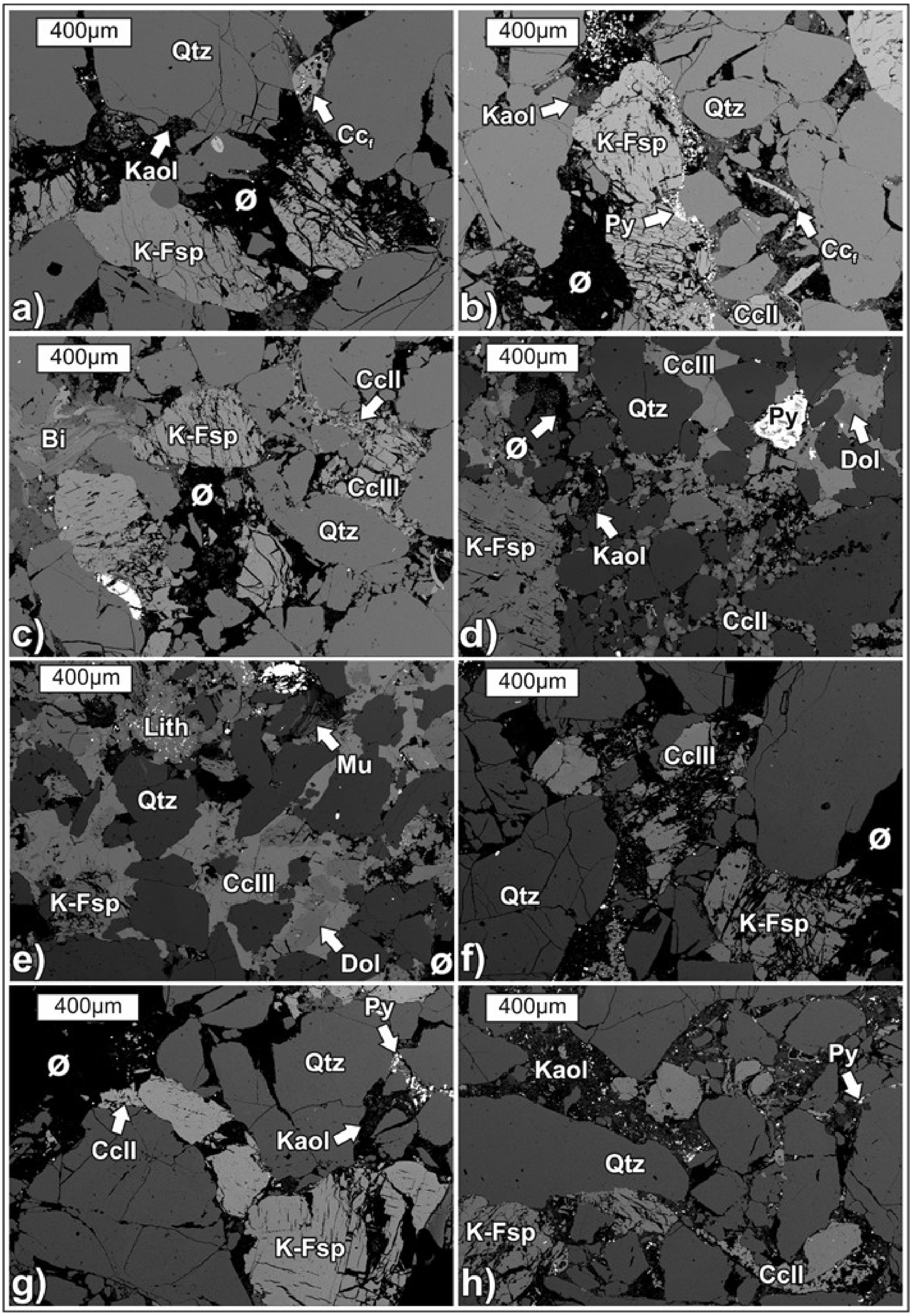

Fig. 76 BSE-images of oil-bearing sandstones from the Cerithian Beds: a,b) fossils and partial disintegrating K-feldspar with pyrite seams; c) two carbonate generations: Cc II and Cc III) d,e) area of increased cementation, some dolomite is also present; f-h) relictic calcite cement and disintegrating K-feldspar grains generating secondary porosity, which is locally decreased by kaolinite.

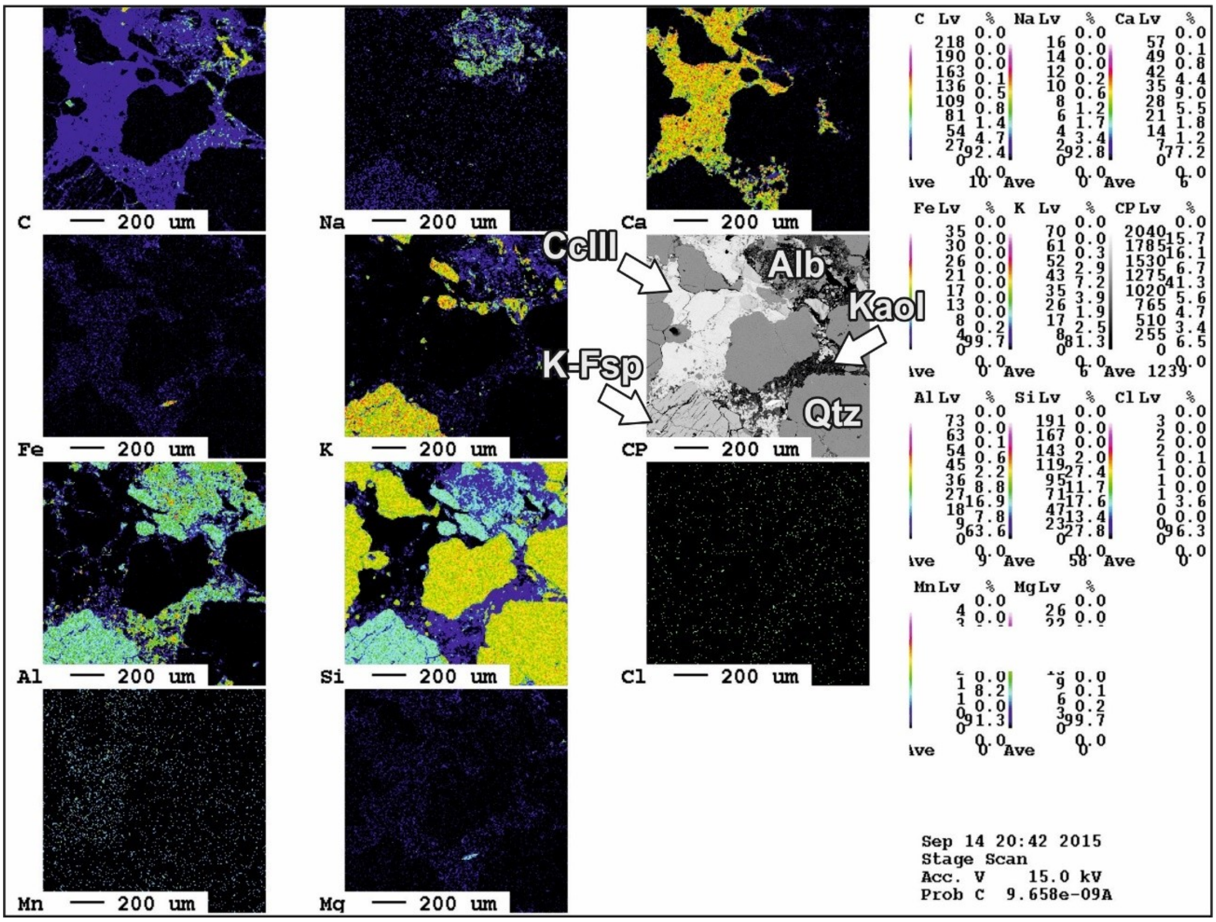

Fig. 77 Wave length dispersive (WDX) element maps of oil-bearing sandstone zone of the Cerithian Beds (CP=BSE image).

- Ampfing Formation

The grains are mainly composed of quartz (Si) (Figs. 78a,b). Subordinately K-feldspar (Si, Al, K) and albite (Si, Al, Na) grains are present. The disintegration of albite is clearly observable in the (Na-), K- Al- and Si-map. The pores in the central part of the map is filled with clay minerals, the elemental composition of Si, Al, K is typical for illite. On the K-map it is visible that the margins of the clay mineral accumulation show the highest K-content (illite). Moreover, this clay mineral is slightly enriched in Mg and Fe.

Theses samples show a low Ca content, which proves the absence of carbonate minerals in Figs. 78a,b.

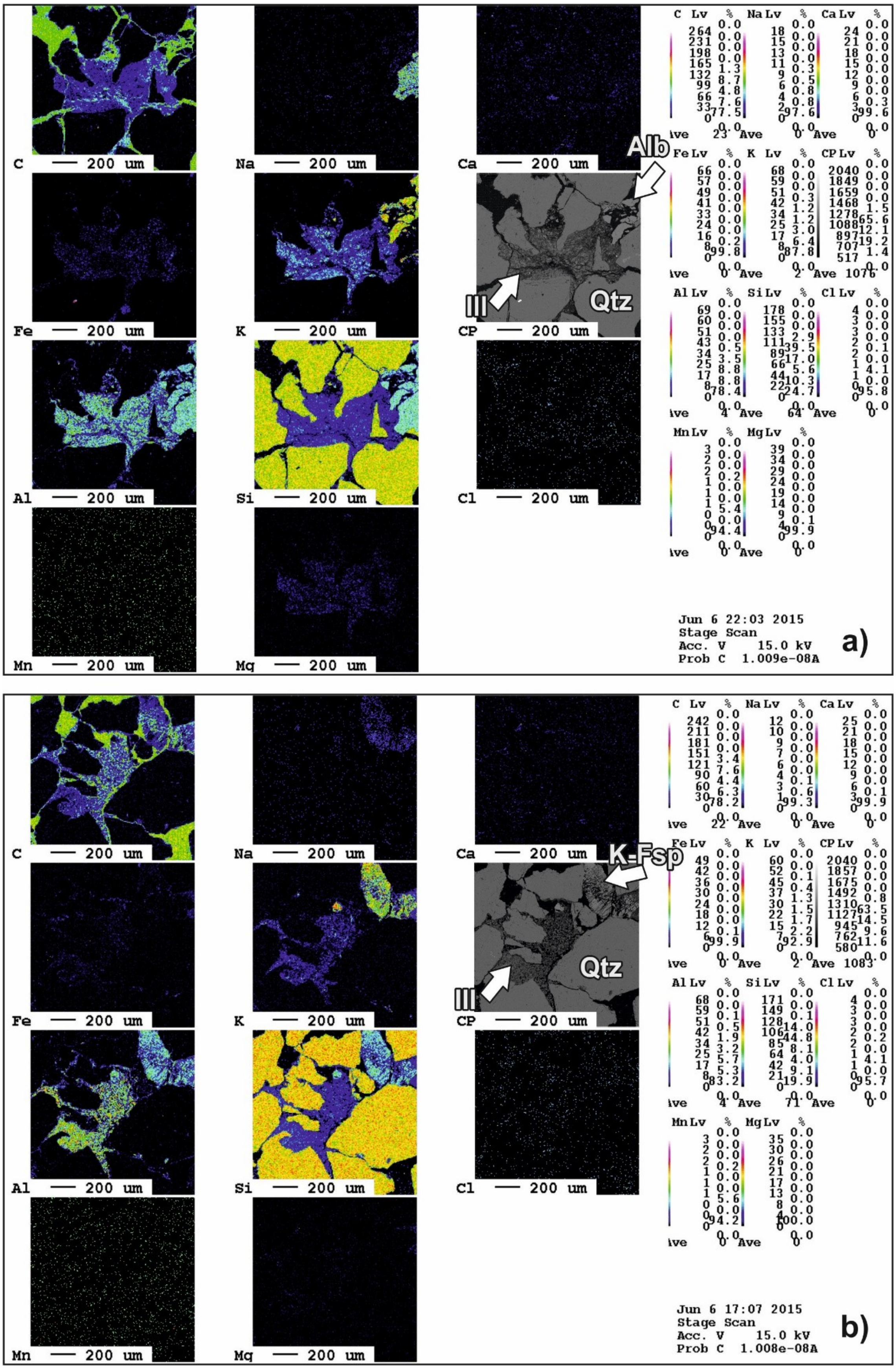

Fig. 78 Wave length dispersive (WDX) element maps of oil-bearing sandstone of the Ampfing Formation (CP=BSE image).

c. Scanning Electron Microscopy

- Ampfing Formation

The morphology and arrangement of mineral grains in oil-bearing sandstones of the Ampfing Formation is shown in Fig. 79:

Pyrite grows typically on detrital grains and has two morphologies: (i) framboidal (Fig. 79a) and (ii) polyhedral aggregate crystals (Fig. 79b).

Detrital grains feature etching marks. The surface of albite grains is roughened by corrosion (Fig. 79c). Quartz minerals have corroded surfaces (Fig. 79d).

Kaolinite booklets grow on the corroded grains within the open pores. On the top of this clay mineral, a sphere formed, which has been identified as chlorite by its typical EDX spectrum (Fig. 79e).

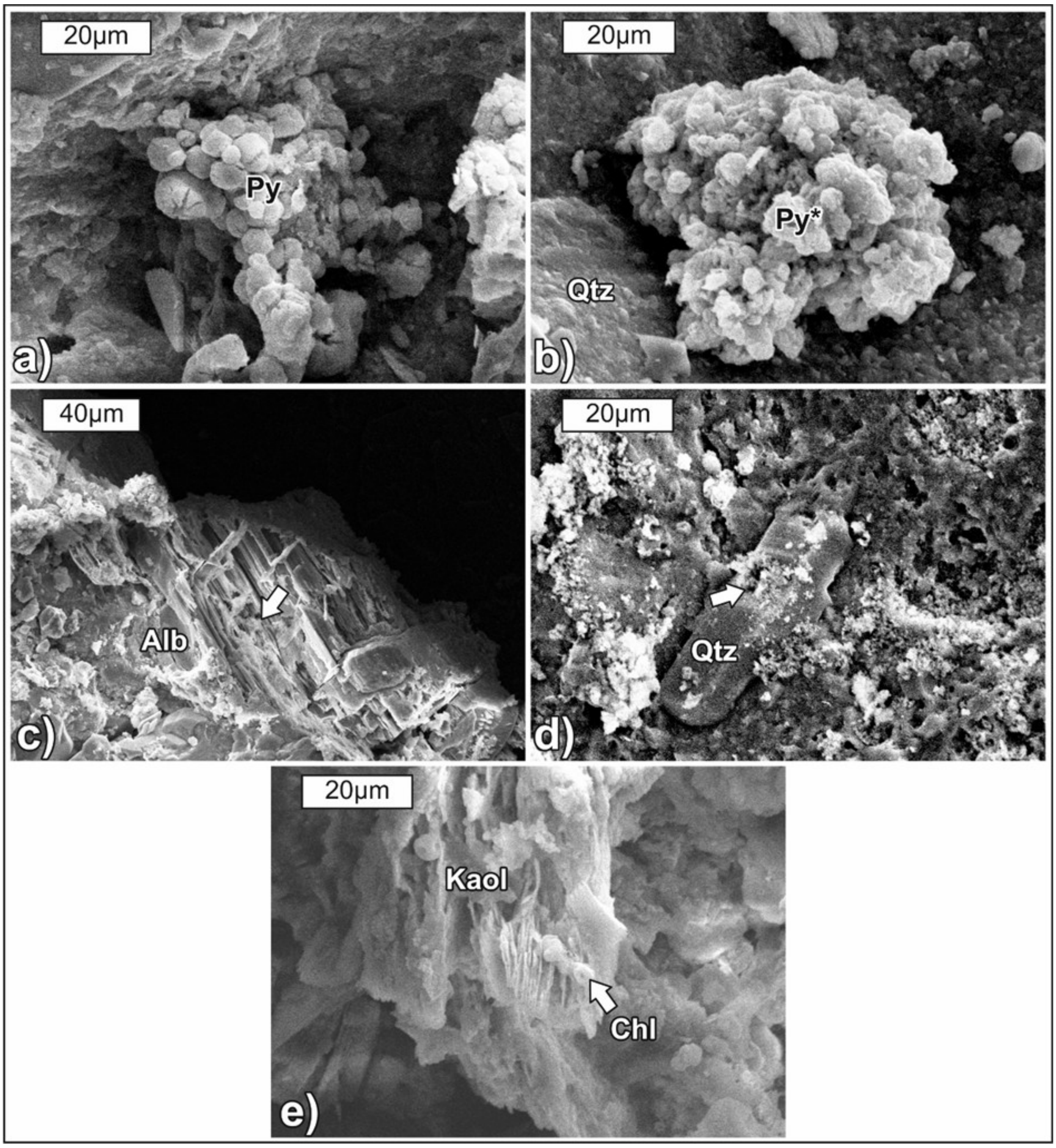

Fig. 79 SEM-images of oil-bearing sandstones of the Ampfing Formation: a) framboidal pyrite; b) polyhedral pyrite bunch grown on quartz surface; c) albite grain with etched surface; d) quartz crystal with etched surface; e) kaolinite booklets with chlorite encrustation.

Gas-bearing sandstone

The investigated samples from the gas-bearing zone in the Cerithian Beds and the Ampfing Formation originate from a depth of 1520 - 1800 m and from a depth of 1520 - 1800 m below ground level, respectively.

A mean content of about 4% carbonate was determined. Calcite (Cc II and Cc III, seldom Cc I) is the prevailing cement mineral with 2%, whereas dolomite, ankerite and siderite occur each with ~1%. The average contents of quartz content, feldspar and lithic fragments are 47, 14 and 7%, respectively. The amount of mica (10%) exceeds the amount of clay minerals (3%). Clay minerals were identified as illite, smectite, kaolinite and minor chlorite. Glauconite, hematite, pyrite, detrital carbonate grains and fossils occur accessorily. Gas-bearing sandstones have a mean porosity of 15%, measured in the lab.

a. Thin section microscopy

- Sandstones of Cerithian Beds

Quartz and minor amount of K-feldspar grains are present (Figs. 80a,b). Hematite rims formed around those grains at the contact to the calcite phase (Figs. 80c,d). Big open pores are evident in gas-bearing sandstones of the Cerithian Beds.

The carbonate minerals occur locally between grains and display a relictic character, (e.g. Figs. 80e-g). The calcite generations were identified as rare eogenetic columnar Cc I (Fig. 80c), which grows on the surfaces of detrital grains. This calcite type is surrounded by the microcrystalline cement Cc II (Figs. 80d-g).

The dissolution of Cc II generates secondary porosity. The contact of calcite and kaolinite is characterized by the partial recrystallization and dissolution of calcite Cc II by kaolinite (Figs. 80f,g). Kaolinite booklets in the open pores are characteristic as last diagenetic phase (Fig. 80h).

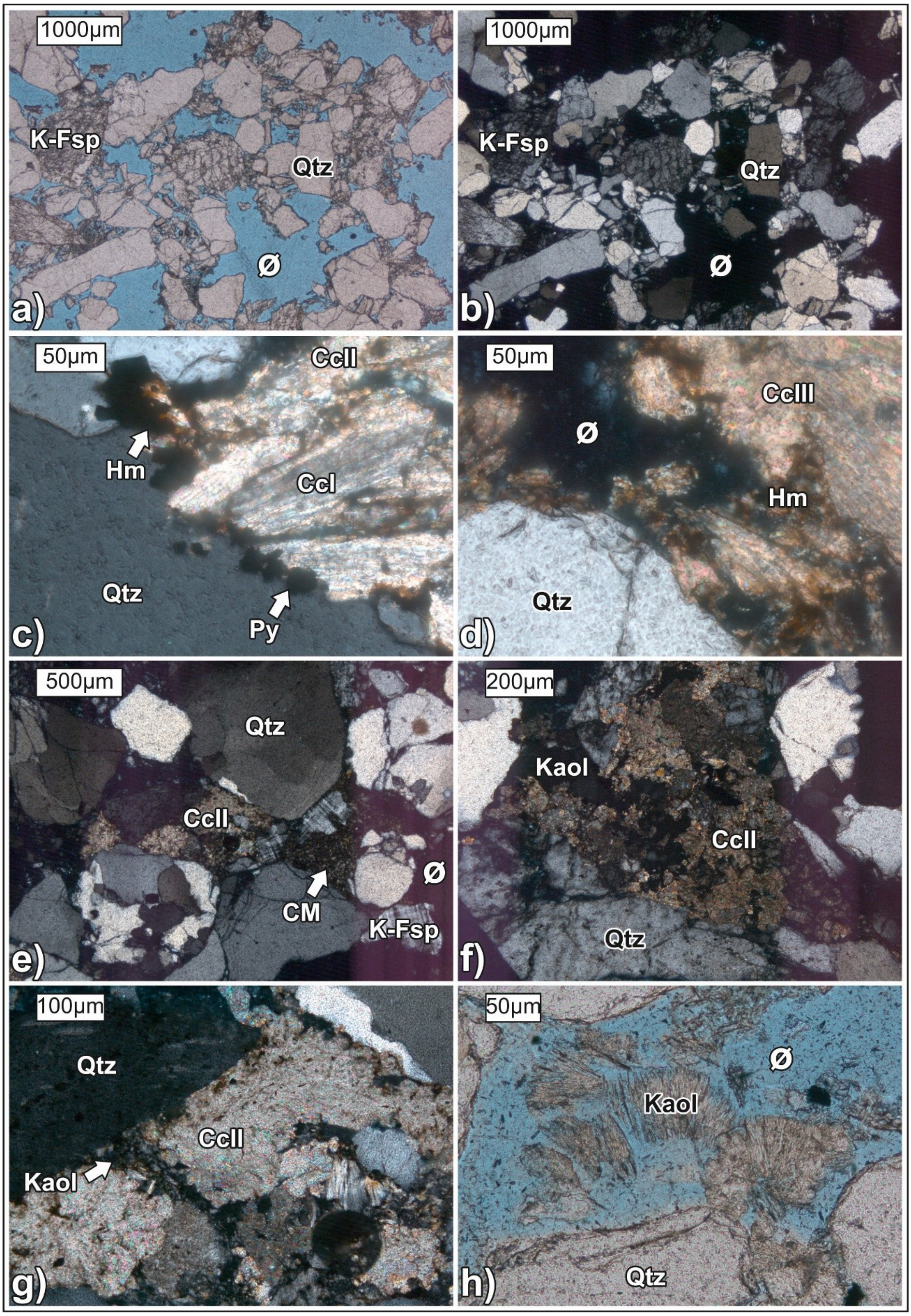

Fig. 80 Thin section photographs of gas-bearing sandstones of the Cerithian Beds: a,b) overview of the texture in plane- and cross-polarized light; c) columnar Cc I surrounded by microcrystalline Cc II; hematite seams along mineral contacts; d) hematite as rim at crystal margins; e) relictic calcite cement (microcrystalline Cc II) at interstices; f,g) partial replacement of calcite cement by kaolinite; h) kaolinite fans grow into open pores.

- Ampfing Formation

Gas-bearing samples from the Ampfing Formation are outstanding by the abundance of kaolinite. In this sample the pore space is strongly decreased (Figs. 81a,b).

The presence of different generations of clay minerals within the hydrocarbon-bearing sandstones is evident:

(i) Brownish clay minerals form rims within open pores. Moreover, at least two generations of kaolinite exist (Figs. 81c-d). Eogenetic kaolinite is represented by fine grained aggregations.
(ii) Large mica booklets (~100 µm) appear within the samples of the Ampfing Formation (e.g. Figs. 69d,e,h; 74g; 81a,b,e,f,h).
(iii) The telogenetic kaolinite booklets are characteristic for all hydrocarbon-bearing sandstones of all horizons (Figs. 81c-g). Commonly they achieve a size of ~50 µm in the reservoir units.

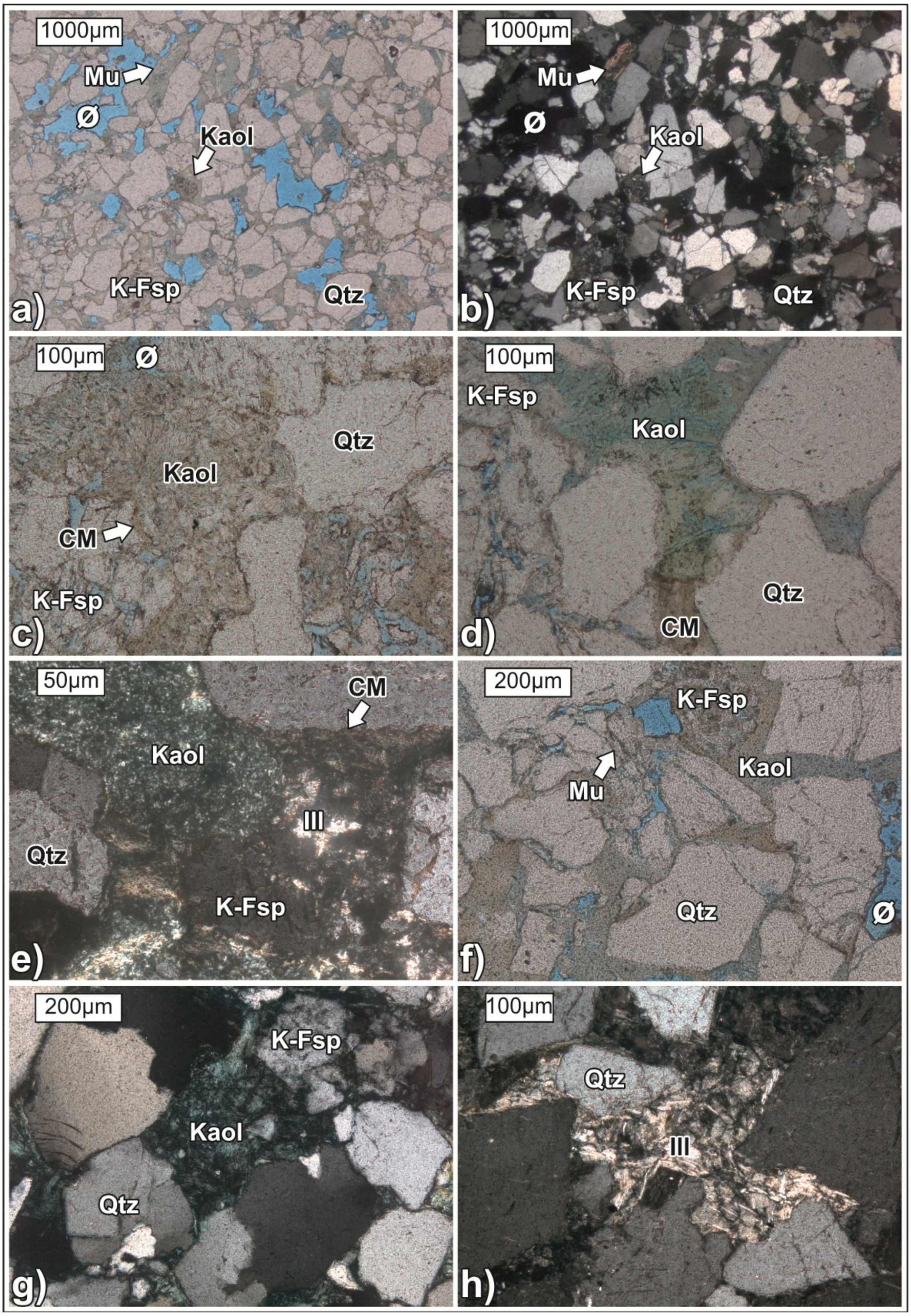

Fig. 81 Thin section photographs of gas-bearing sandstones of the Ampfing Formation: a,b) overview of the texture in plane- and cross-polarized light; c,d) brownish clay minerals rims and kaolinite; e-h) kaolinite booklets decrease pore network.

b. Electron microprobe microscopy

- Sandstones of Cerithian Beds

Electron microscope images of the gas-bearing samples from the Cerithian Beds are presented in Fig. 82:

Quartz grains are grain supported and the prevailing mineral phase. Subordinately, feldspar minerals, involving K-feldspar and low amounts of albite, are present (Fig. 82a). The matrix is composed of illite and smectite minerals. Fossils, like shells and foraminifera are abundant, which is typical for sandstones of the Cerithian Beds.

Relictic calcite Cc II is present in the interstices of grains (Figs. 82b,c). In addition, within the relictic cement, a dolomite core is evident (Fig. 82d).

The disintegration of K-feldspar and the generation of secondary porosity are apparent in Fig. 82b. Additionally, partial disintegration affected also albite grains (Figs. 82a,b,e). Further, the quartz grains display etched rims (Figs. 82a-f).

Relictic recrystallized calcite cement phases with strong corrosion marks in the contact to kaolinite minerals are characteristic (Fig. 82e). Some of them are even replacement by this clay mineral (Figs. 82d,f).

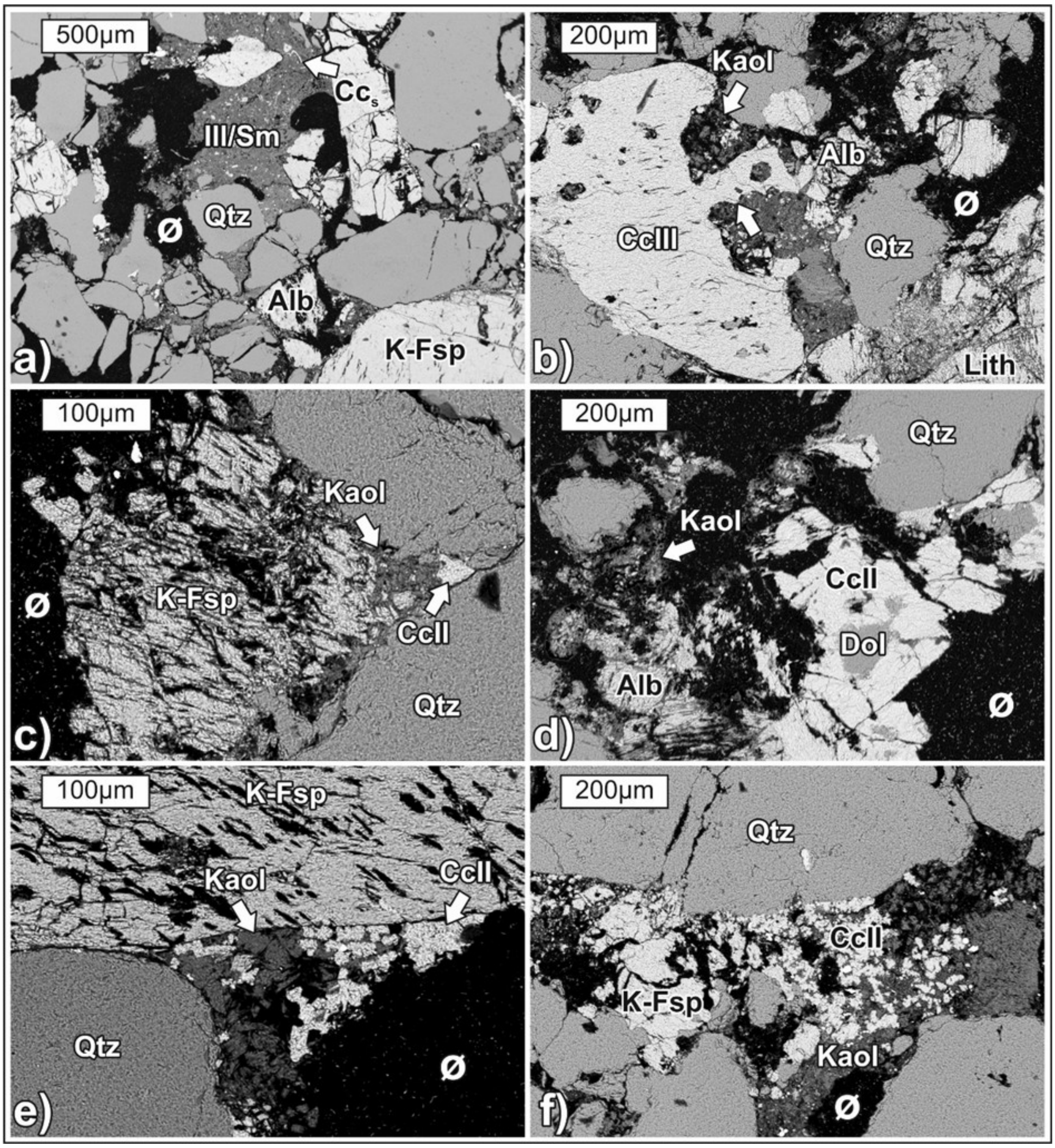

Fig. 82 BSE-images of gas-bearing sandstones from the Cerithian Beds: a) overview of the texture with some clay minerals as pore filling; b) strong corroded and relictic calcite cement; the holes are partially filled with kaolinite; c) disintegrating K-feldspar; in the interstice of K-feldspar and quartz grains are calcite and kaolinite present; d) dolomite surrounded by relictic and partially dissolved calcite cement; albite show advanced disintegration; e) kaolinite and calcite in the interstice of quartz and weak K-feldspar; f) partial replacement of calcite cement by kaolinite.

- Ampfing Formation

The electron microscope images of the gas-bearing Ampfing Formation (Fig. 83) are similar to their thin section images (Fig. 81):

Especially feldspar grains exhibit disintegration. Commonly albite exhibits the strongest corrosion. It is porous respectively perforated (Fig. 83a). K-feldspar grains are corroded and fractured (Figs. 83b-e). Not only feldspar, but also quartz grains are affected and show etched, even fringed, margins (Figs. 83a-e).

Abundant kaolinite filling is present between the grains and reduces the porosity (Figs. 83a-e).

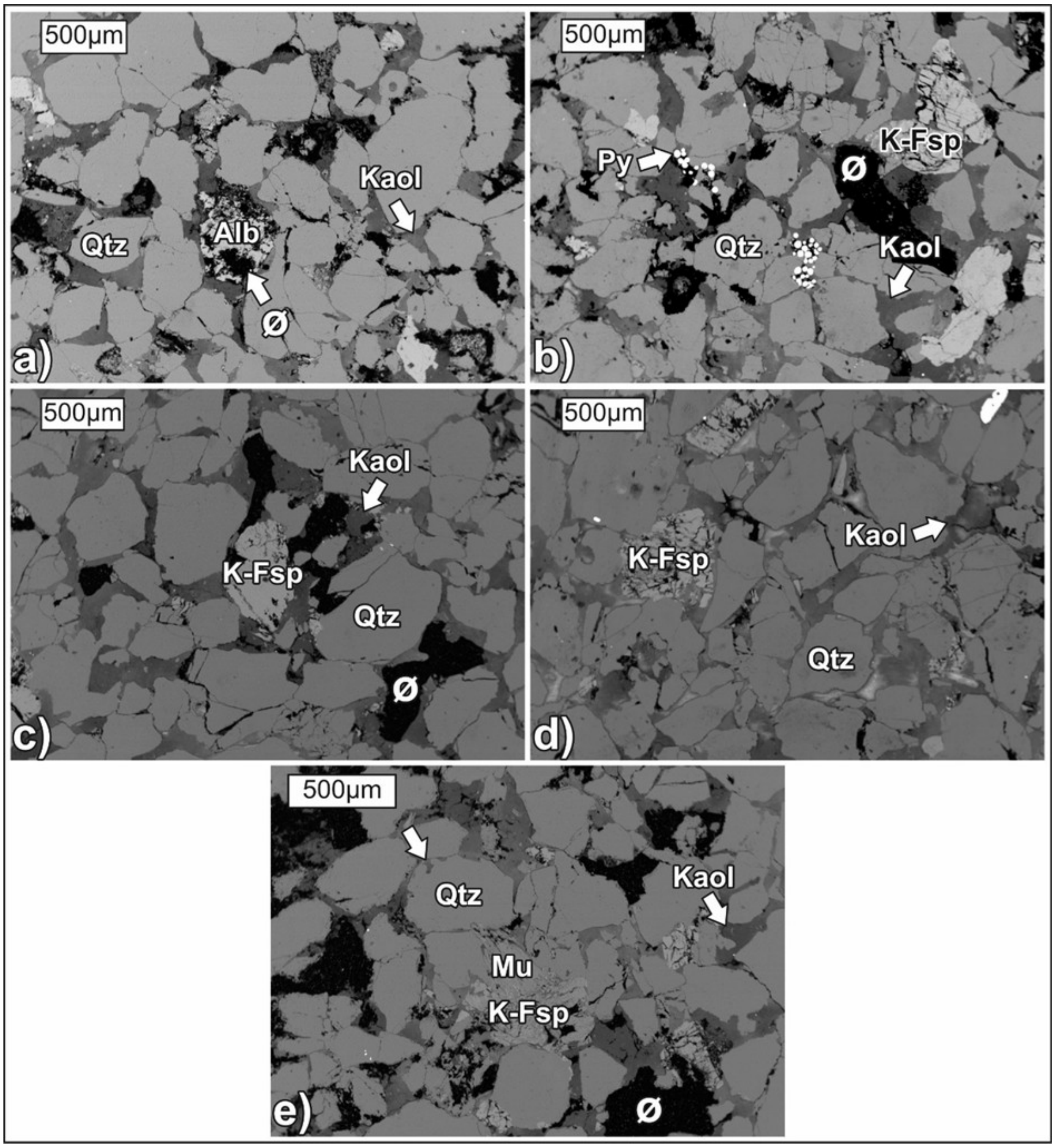

Fig. 83 BSE-images of gas-bearing sandstones from the Ampfing Formation: a) disintegration albite grain, generating secondary porosity; etched margins of the quartz grains; b-e) overview of the texture with kaolinite as pore filling, which decreases porosity, to note are the corroded margins and fractures of quartz and feldspar grains.

c. Scanning electron microscopy

- Sandstones of Cerithian Beds

The relationship of detrital grain and authigenic filling of gas-bearing sandstones of the Cerithian Beds is exemplified by SEM images in Fig. 84.

Kaolinite booklets grow independent of the mineral type into the open pores and reduce porosity locally:

(i) Quartz grains are covered by kaolinite (Fig. 84a).

(ii) On the surface of a K-feldspar some kaolinite booklets formed. The surface of this grain is considerably corroded (Fig. 84b).

(iii) Detrital muscovite flakes are present as well and partly overgrown by authigenic kaolinite (Fig. 84c).

(iv) Also on authigenic calcite minerals, finely dispersed kaolinite booklets grow on the surface, which shows some etched marks (Fig. 84d).

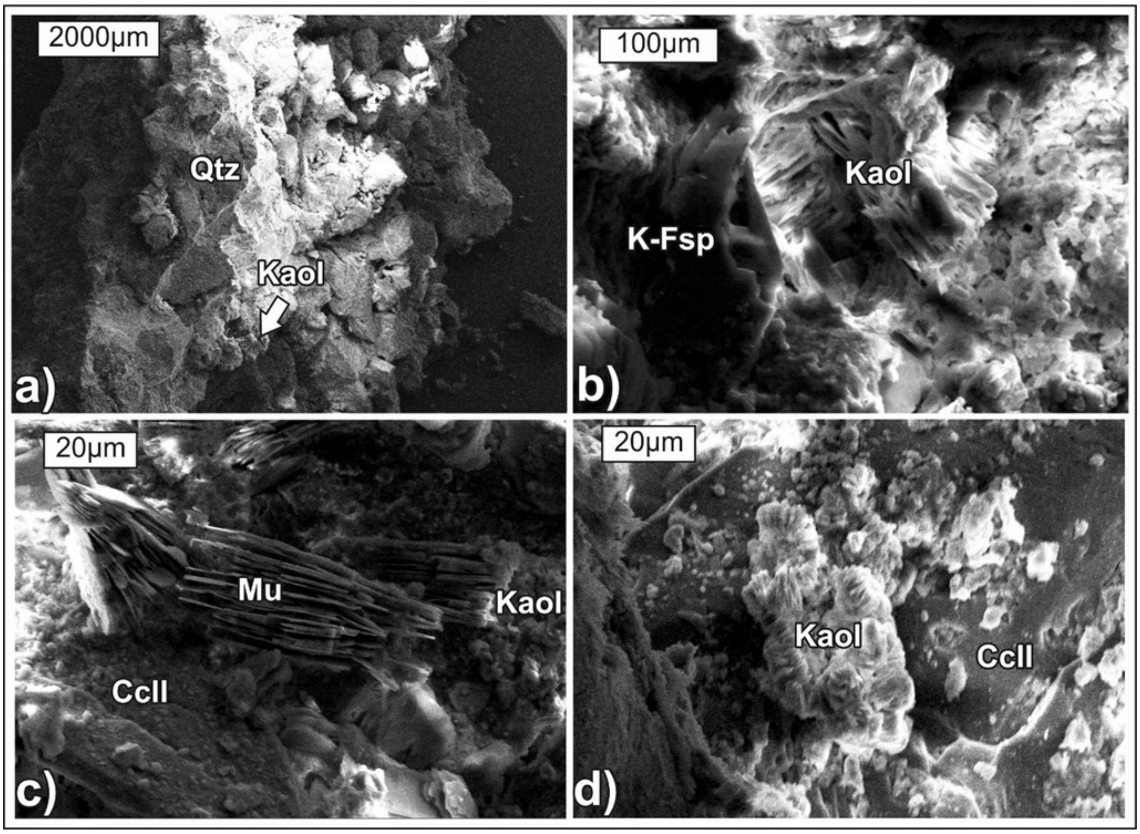

Fig. 84 SEM-images of gas-bearing sandstones of the Cerithian Beds: a) detrital quartz grains show kaolinite overgrowths; b) kaolinite overgrowths on disintegrated K-feldspar; c) muscovite flakes encased by Cc II and kaolinite; d) kaolinite booklets grow on calcite cement.

- Ampfing Formation

The grain morphology and their relationship to the pore filling of gas-bearing sandstones of the Ampfing Formation are illustrated by SEM images (Fig. 85).

Detrital components comprise mainly quartz and feldspar grains, whereas lithic fragments are rare. The typical step like morphology of K-feldspar is visible in Fig. 85a.

Together with quartz grains, these detrital minerals are covered by authigenic calcite and clay minerals (Figs. 85a-f):

(i) On the surface of a quartz grain, small calcite crystals are present in Fig. 85b. Locally detrital grains are surrounded by carbonate cement (Fig. 85b). They show etched marks on mineral surfaces in the contact to this authigenic phase (Fig 85c).

(ii) Thin illite overgrowths formed on the carbonate cement itself (Fig. 85c). Further, illite and chlorite occurs rarely in the interstices of detrital grains (Figs. 85d,e).

(iii) The grains and eogenetic cements are often covered by kaolinite (Figs. 85a,f). The thick layers of kaolinite, like in Fig. 85f, are fine grained and do not show the typical kaolinite booklet structures.

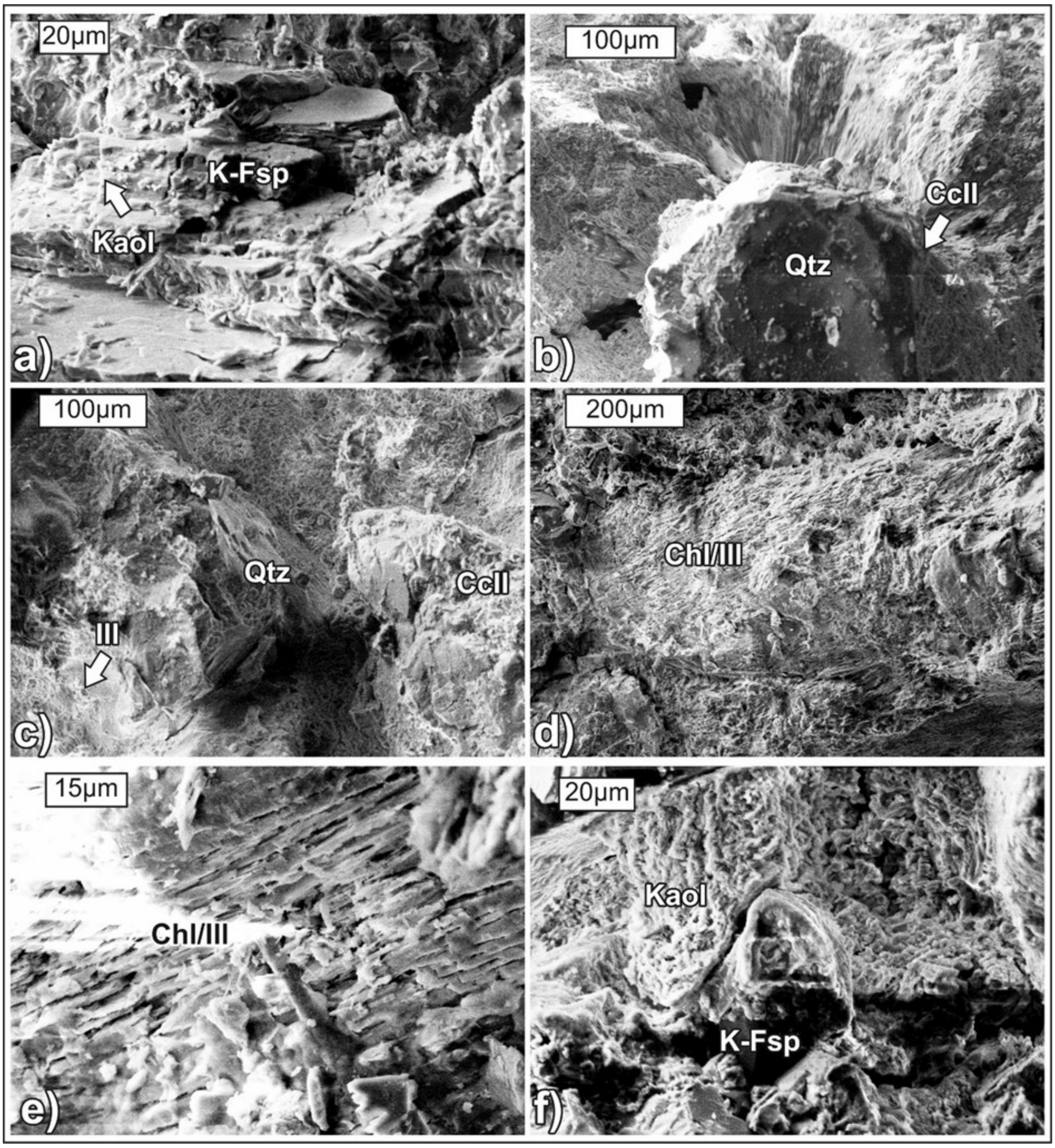

Fig. 85 SEM-images of gas-bearing sandstones of the Ampfing Formation: a) K-feldspar grain covered with kaolinite; b) etched mineral surface of a quartz grain with some calcite crystals on it; c) local pore filling with calcite and illite; e,f) chlorite/illite agglomerations; f) kaolinite covers detrital grains.

4.2.3. Effect on pore space parameters

To examine the influence of the stratigraphic position and the fluid type on porosity and permeability first, these parameters are cross plotted in Figs. 86, 87.

Porosity versus permeability

The porosity and permeability values from different stratigraphic units representing different facies zones are cross plotted in Fig. 86. Additionally, they were differentiated whether they are porous (filled data points in Fig. 86) or cemented (unfilled data points in Fig. 86). The porous sample from the Voitsdorf Formation has porosity and permeability of 18% and 400 mD, respectively. Reservoir sandstones from the Cerithian Beds exhibit porosities of 17 to 20% (mean: 18) and permeabilities of 790 to 1900 mD (mean: 1350 mD). Thus theses samples achieve the best reservoir properties. Porous samples from the Ampfing Formation show a wider variation with porosity values ranging from 12 to 21% (mean: 15%). Permeability values range from 5 to 570 mD (mean: 180 mD). Samples from the Cerithian Beds and a single sample from the Voitsdorf Formation are quite similar, whereas sandstones of the Ampfing Formation show lower values. Strongly cemented sandstones from all Eocene units plot in the low porosity (mean: 3%) and permeability (mean: 0 mD) area.

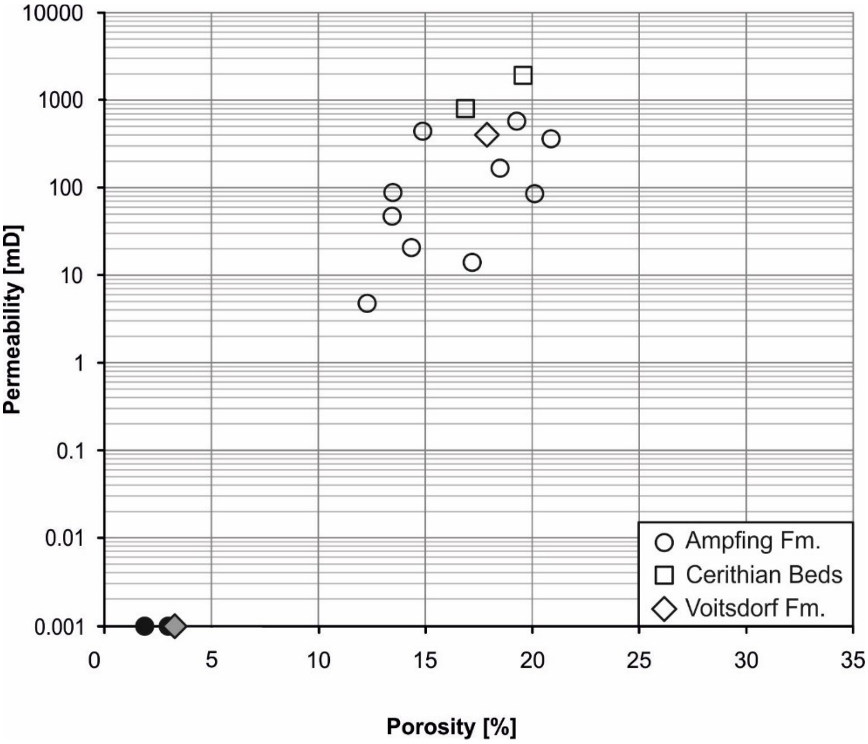

Fig. 86 Semilog plot of permeability versus porosity from samples, differentiated according to their stratigraphic age respectively facies (porous (filled) and cemented (unfilled) sandstone samples).

The influence of the specific fluid zones on porosity and permeability is exemplified in Fig. 87. Gas-bearing sandstones exhibit values from 12 to 20% (mean 16%) for porosity and 5 to 1900 mD (mean 780 mD) for permeability. The single gas-bearing sample with comparably lower porosity and permeability values reveals enhanced kaolinite cementation. Oil-bearing samples show a range between 18 and 21% porosity and 166 and 400 mD permeability. A mean of 19% porosity and 310 mD permeability is characteristic. The strongly cemented sandstones have porosities from 2 to 3% and permeabilities of 0 mD. Fluid-bearing (water/oil/gas) sandstones show comparable pore space parameter values in the range of 5 to 12% and 20 to 1900 mD. Most notably, gas-bearing samples show the highest permeability values. Porosity and permeability of the gas-bearing sample with the high percentage of kaolinite are significantly decreased (circle).

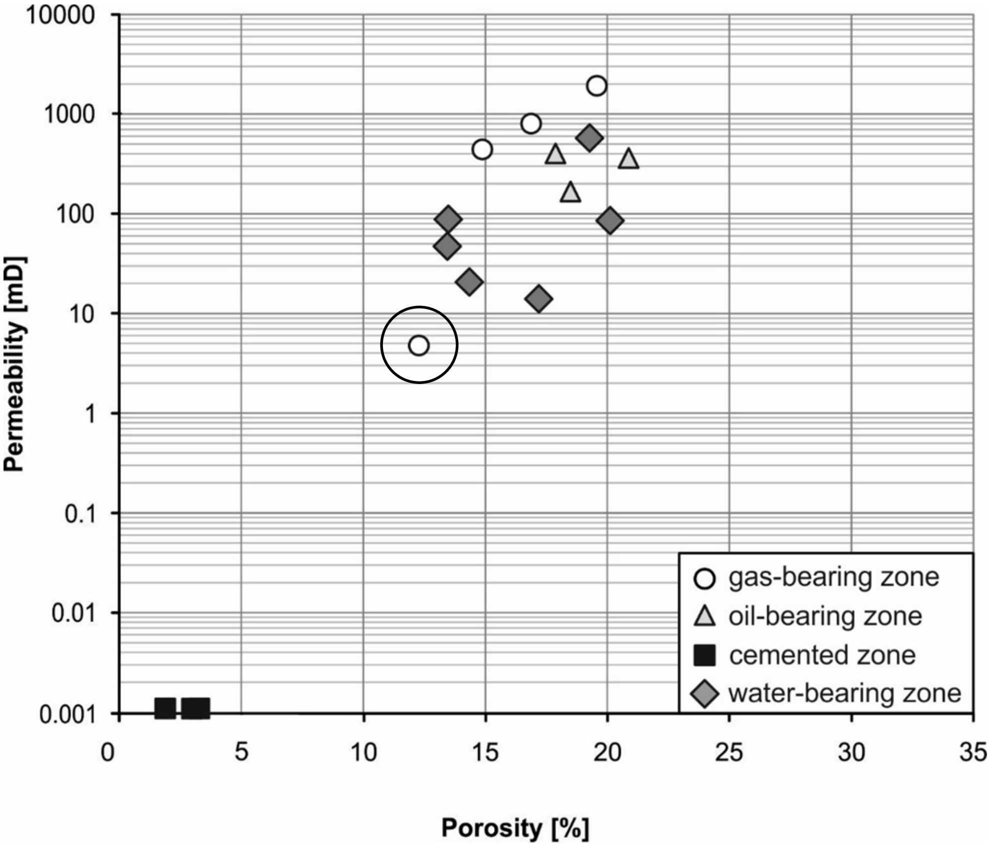

Fig. 87 Semilog plot of permeability versus porosity from samples, differentiated according to their fluid content (water/oil/gas/cemented).

Influence of carbonate cementation on pore space quality

In response to the question to what extent carbonate cementation effects pore space, the amount of calcite cement is plotted versus porosity and permeability in Figs. 88 and 89. Further the samples are subdivided according to their fluid fill: water/oil/gas/cemented, for a better discrimination of the influence of the different pore content on the pore space quality. The calcite contents are mean values evaluated from semi-quantitative XRD-analysis and point-counting.

The calcite content is plotted versus porosity in Fig. 88. The strongly cemented samples differ considerably from the other samples. They reveal low porosities of 2 to 3% with a calcite content of up to 50%. Lower carbonate values are present in water-, oil-, and gas-bearing sandstones (1 - 10%), with a mean of 6%. The water-bearing sample with higher calcite content (20%) is located near the contact zone to the strongly cemented horizon.

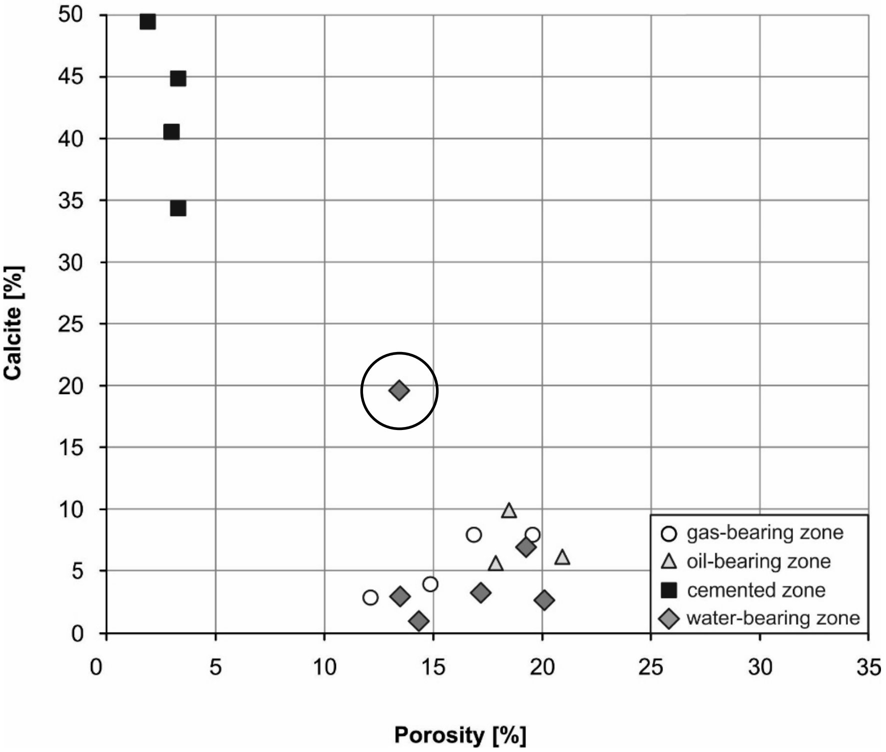

Fig. 88 Plot of calcite content versus porosity, differentiated according to their fluid content (water/oil/gas/cemented).

Calcite content is plotted versus permeability in Fig. 89. As expected, the strongly cemented sandstone samples with calcite contents varying from 35 to 50% show permeability values of 0 mD. By comparison, the water-, oil-, and gas-bearing sandstones range in permeability between 3 and 1900 mD with varying calcite content (1 - 10%). Also in this plot, the water-bearing sample near the strongly cemented horizons stands out by its higher calcite content. However, its permeability is similar to the other water-bearing samples.

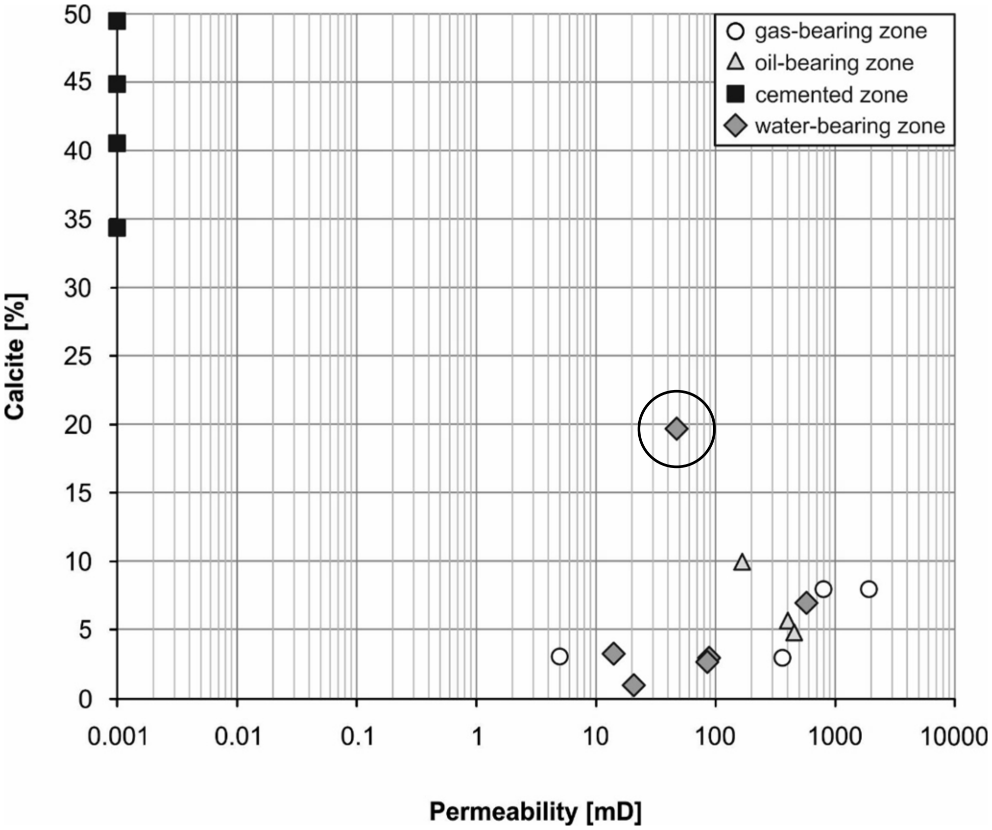

Fig. 89 Semilog plot of calcite content versus permeability, differentiated according to their fluid content (water/oil/gas/cemented).

Despite of the low number of samples, there is evidence of a trend. The sample marked with a circle in Figs. 88 and 89, which does not follow the trend, is enriched in calcite. The sample with higher calcite contents (circle) is located near the strongly cemented zone within the water-bearing zone of Ampfing Formation.

4.2.4. Isotopic composition

The stable carbon ($\delta^{13}C$) and oxygen ($\delta^{18}O$) isotopic composition of carbonate fractions from bulk rock samples was determined. The approach implies the problem that the measured values are mixed signals from different authigenic carbonate generations and in the case of the sandstones from the Cerithian Beds also from fossils. $\delta^{18}O$ was cross-plotted with $\delta^{13}C$, and samples were grouped according to their pore filling (gas/oil/water/cement) and stratigraphic unit. Four clusters (carbonate isotope groups 1-4; see Fig. 90) were identified:

Porous sandstones plot into the carbonate isotope groups 1 and 4. Sandstones of the Voitsdorf Formation and the Cerithian Beds show a range in $\delta^{13}C$ from -5.9 to +2.2‰ and in $\delta^{18}O$ from -8.3 to -4.3‰. The $\delta^{13}C$ ratios are similar to those of marine carbonates, whereas $\delta^{18}O$ ratios exhibit a slight negative shift (carbonate isotope group 1). In comparison, the reservoir rocks of the Ampfing Formation (carbonate isotope group 4) are more negative. The difference is not controlled by diagenetic features visible under the microscope. Within each group a trend of $\delta^{13}C$ and the prevailing cement type (Cc II and Cc III, respectively) was observed in gas- oil- and water-bearing sandstones. An increasing amount of Cc III in comparison to Cc II is accompanied by lighter $\delta^{13}C$.

Strongly cemented sandstones with up to 45% calcite (Cc III-a and Cc III-b) plot into carbonate isotope groups 2 and 3, and show opposing behavior (Fig. 90). The calcite cement of the strongly cemented sandstones of the Ampfing Formation and Cerithian Beds is designated "Cc III-a" and the calcite cements of the strongly cemented Voitsdorf sandstones as "Cc III-b" based on their paragenetic relationship:

Cc III-a – The pervasive calcite cement Cc III within the mentioned horizons is characterized by a small increased Mg-content, based on microprobe analysis (Fig. 64). Moreover, the grains from these strongly cemented sediments exhibit a minor grade of compaction (e.g. Figs. 59a,b, 60a,b). Cc III-a is related to a lighter $\delta^{13}C$ (carbonate isotope group 2). Comparable isotope values were measured for strongly cemented sandstones associated with bitumen (oil) from the Cerithian Beds ($\delta^{13}C$: -27.3 to +1.9‰, $\delta^{18}O$: -8.6 to -0.1‰). Their values are presented in Fig. 89, whereat the bitumen-bearing samples from the Cerithian Beds plot in the carbonate isotope group 1 and the cemented sandstones in carbonate isotope group 2 (Fig. 90). The associated well (BHN2) is already described petrologically by Sachsenhofer et al. (2006).

Cc III-b – This calcite differs to Cc III-a by slightly elevated Fe contents (Fig. 62). Furthermore, a higher degree of grain compaction was observed at Cc III-b sandstones (e.g. Figs. 58a,b). Cc III-b is associated to heavier $\delta^{13}C$ (carbonate isotope group 3).

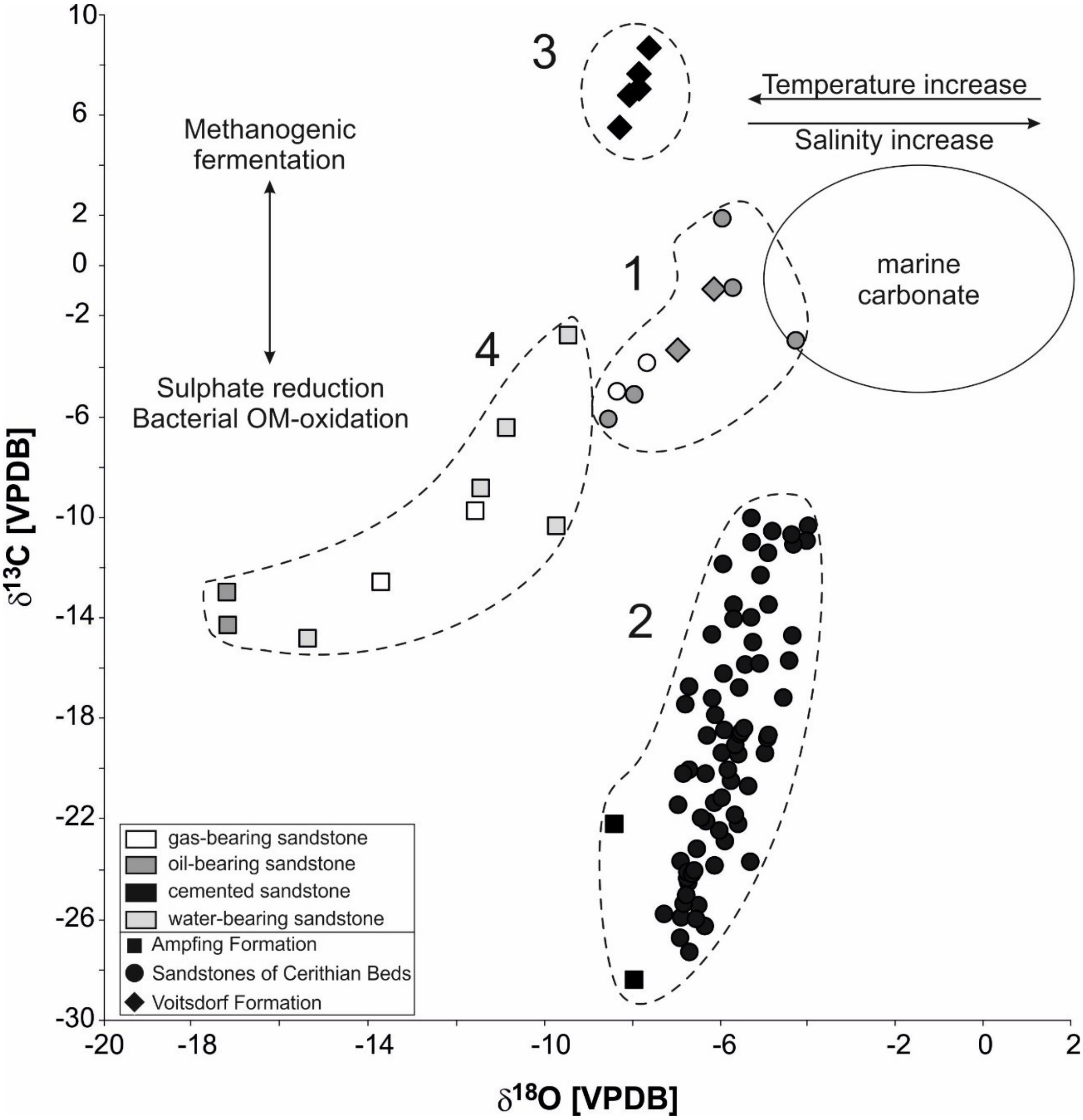

Fig. 90 Plot of carbon and oxygen stable isotopic composition of bulk carbonates from Eocene sandstones. Typical values for marine carbonates (after Dimitrakopoulus & Muehlenbachs, 1987) are shown for comparison. Influence of salinity and temperature, as well as methanogenic fermentation and bacterial sulfate reduction after Allan & Wiggins (1993). (OM=organic matter)

4.2.5. Discussion

Influence of depositional environment on sedimentary petrology

The studied Upper Eocene rocks have been deposited during a transgressive event and comprise from bottom to top (i) fluviatile to deltaic (Voitsdorf Formation), (ii) tidal (Cerithian Beds) and (iii) shallow marine sandstones (Ampfing Formation) (Malzer et. al., 1993; Wagner, 1998; Rasser & Piller, 2004). Sandstones of the non- to marginal marine Voitsdorf Formation and Cerithian Beds occur as channel-shaped reservoir bodies embedded in non-reservoir rocks. In contrast, the overlying shallow marine sandstone of the Ampfing Formation developed as laterally continuous layers (Nachtmann, 1989).

The higher (initial) compositional maturity observed for the (southern) shallow-marine Ampfing Formation reflects the comparably higher transport distance from the hinterland and continuous reworking by wave action, compared to fluviatile/deltaic Voitsdorf Formation and brackish Cerithian Beds. Furthermore, the occurrence of glauconite and (rare) foraminifera results from the marine depositional environment in the Ampfing Formation. In contrast, Voitsdorf Formation and Cerithian Beds are less mature (see Figs. 53, 54). Mineralogical composition and intensity of the weathering of the hinterland, and the depositional environment have a great influence on the abundance of chemically unstable silicate minerals (e.g. detrital clay, mica, feldspar). Especially in the Voitsdorf Formation, deposited in a proximal, non-marine setting, chemically unstable minerals are abundant, reflecting the short transport distance from a crystalline hinterland (Bohemian Massif).

Paragenetic relationships

Silicate minerals - Partial disintegration of feldspar and phyllosilicates and replacement by clay minerals are evident. In case of the marine Ampfing Formation, glauconite pellets formed at the sediment-water interface in the shallow-marine realm (Porrenga, 1967). In all reservoir units feldspar and, to some extent, quartz show dissolution features. Hydrogeochemical modelling of siliciclastic reservoir rocks (e.g. Van Berk et al., 2009) showed that anorthite dissolves first and K-feldspar later. Authigenic clay minerals with some iron hydroxides or organic material formed as overgrowths on detrital grains or locally as alteration product in-situ.

Illite formed as most prominent clay mineral. The disintegration of albite minerals supplied Na for smectite growth. Chlorite is restricted to the Ampfing Formation and developed due to the corrosion of Fe-, and Mg-rich lithic fragments and glauconite. Eogenetic kaolinite formed by feldspar disintegration in absence of K^+. Quartz-overgrowths have not been observed. Probably this is because extensive eogenetic carbonate precipitation impeded silicate cementation. During burial diagenesis, these eogenetic clay minerals altered into more stable clay minerals, like illite.

A second kaolinite generation is present in hydrocarbon-bearing sandstones of the Ampfing Formation. The kaolinite booklets reach a size of approximately 100 µm and, thus, they have a larger size than to kaolinite flakes in older stratigraphic units. Kaolinite formed by leaching of detrital aluminosilicate minerals, mainly feldspar and mica/illite. It often grows on older clay minerals (illite, smectite). A replacement of corroded calcite by the second kaolinite generation is evident. Furthermore, this kaolinite grows into the remaining open pores and, hence, represents the last authigenic formation.

Carbonate minerals - The first carbonate generation (Cc I) is represented by columnar calcite, which grows on the surface of mineral grains. Afterwards microcrystalline calcite (Cc II) formed. The blocky/homogenous cement (Cc III) partly recrystallized the microcrystalline one. Within the strongly cemented zones of the Cerithian Beds and the Ampfing Formation, the blocky/homogenous calcite cements are slightly enriched in Mg and have light $\delta^{13}C$ (Cc III-a). In comparison, the texture of the strongly cemented Voitsdorf Formation shows more compaction, than strongly cemented sandstones in the overlying units. Moreover, these calcites are enriched in Fe and have heavy $\delta^{13}C$ (Cc III-b). Therefore it is suggested, that the Cc III-a formed earlier and Cc III-b later during diagenesis. Only within the strongly cemented sandstone the blocky/homogenous cements grades into poikilitic cement (Cc IV) locally. The porosity was reduced due to these early carbonate cementation phases (Cc II, Cc III). With increasing distance to the carbonate sources (fossils or detrital limestone), the magnitude of carbonate cementation decreases. Carbonate precipitation was accompanied by partial dissolution of siliciclastic minerals.

Diagenetic processes

Diagenetic processes are controlled by microbial degradation of organic matter for energy extraction. Especially carbonate precipitation is governed by metabolization, because of the allocation of reagents and the control on pore water conditions (Eh and pH). Organic matter metabolization commences during sedimentation and results in the generation of gas (CH_4 and CO_2). Isotopic composition of some gases associated with oils from Eocene reservoirs indicate a mixture of thermogenic and primary microbial gas derived from these early stages of organic matter metabolization (Pytlak et al., 2016).

The observed diagenetic features are used as basis for the following interpreted post-depositional processes (Fig. 91).

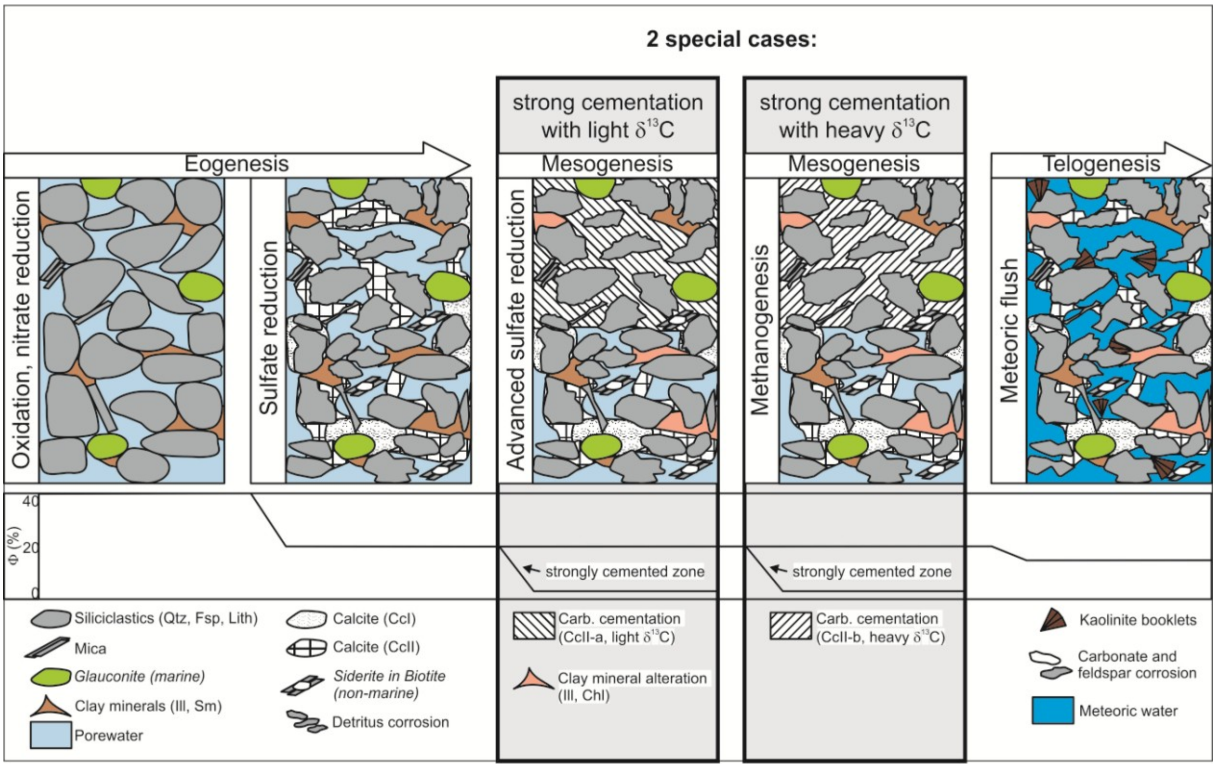

Fig. 91 Conceptual model of the diagenetic history of Eocene sandstones, which bear water oil and gas. The two described special cases of the strong carbonate cementation at water- and oil-bearing zones are highlighted in the framed boxes.

a. Eogenesis

Diagenetic processes start immediately after deposition. The generation of microbial gas controls the pH and Eh via changes of the solubility product during the degradation of organic matter (Schulz et al., 2009; Schulz & Van Berk, 2009). This may trigger dissolution of primary minerals and precipitation of cements. The organic substance is also a source of ions. Two extreme endmembers and any combination of them for organic matter degradation exist: (i) in anoxic conditions organic matter $C^{(0)}H_2O$ degrades into $C^{(IV-)}H_4$ and thus result in a consumption of H^+ (increase in pH) and (ii) when free oxygen or oxidizing agents such as iron or manganese oxides are present $C^{(0)}H_2O$ reacts to $C^{(IV+)}O_2$. This results in the release of $4H^+$ per mole CH_2O and thus in pH decrease (Schulz et al., 2009; Schulz & Van Berk, 2009). Synsedimentary oxygen reduction and later nitrate reduction initiate oxygen depleted settings (Froelich et al. 1979; Einsele, 2000; Schulz et al., 2009). The nitrate reduction is accompanied by manganese and subsequently iron reduction. The electrochemical potential moves from positive to negative and enables the solution of Mn- and Fe-oxides and hydroxides by reduction. In that way, electron acceptors are formed to support nitrate oxidation (Froelich et al., 1979).

The presence of iron oxides (i.e. hematite) (e.g. Fig. 72c,d) and pyrite (e.g. Figs. 63b, 76c,d, 79a,b) is most frequent in the sandstones of Cerithian Beds. These mineral formations indicate the presence of dissolved free Fe^{2+} ions within the pore water at the moment of precipitation. The common Fe^{2+} concentration of the Eocene sea water might be increased additionally with the delivery from the crystalline hinterland. Slightly soluble Fe^{3+} was transported in the form of $Fe(OH)_3$ colloids together with organic material, or incorporated into or adhered to clay minerals (e.g. Ryan & Gschwend, 1992; Chilingarian & Wolf, 1994). During a very early stage of diagenesis these compounds disintegrated and Fe^{3+} was reduced to Fe^{2+}, which passed into solution. Subsequently iron (Fe^{3+}) minerals precipitated (Ryan & Gschwend, 1992). Typically hematite and pyrite formed very fast within the Eocene sandstones, depending on the attendance of other terminal electron acceptors (TEA): Hematite is an indicator for an oxic milieu: (i) on the one hand, hematite is of detrital origin and was deposited together with the fine grained sediment, which caused the brownish coloring of the eogenetic clay mineral rims around grains (e.g. Figs. 69c,d) characteristic for the Ampfing sandstones and (ii) on the other hand diagenetic hematites formed synsedimentarily via oxidation of soluble Fe^{2+} under alkaline conditions (see also Chan et al., 2000).

Typically this diagenetic hematite forms coatings around grains in the sandstones of the Cerithian Beds (e.g. Fig. 79c,d). (iii) Pyrite precipitated already in the water column of the sea water, with high S^{2-} concentrations, in an oxygen depleted setting (e.g. Berner, 1981). The intercalating organic matter-rich shale layers of the Cerithian Beds provide excellent microzones, which enabled the pyrite formation. A rapid turnover from an oxic into an oxygen depleted environment is suggested for this tidal facies, which enabled the formation of hematite at first under oxic conditions and afterwards pyrite mineralization under reduced conditions (Berner, 1981; Chan et al., 2000). In contrast, the fluviatile/deltaic Voitsdorf and the shallow-marine Ampfing Formation contain low amounts of pyrite (≤ 1%), which support the low sulphide concentration of the pore water. Eogenetic processes in Eocene sandstones comprise also the formation of glauconite in the Ampfing Formation (Fig. 74c). In comparison to the oxic hematite and anoxic pyrite, this iron potassium phyllosilicate is a typical mineral in suboxic, shallow marine setting (e.g. Porrenga, 1967; Füchtbauer, 1988). This formation requires the availability of K^+ and Fe^{2+}. K^+ and Fe^{2+} were delivered by the seawater (see also Meunier & El Ablani, 2007) and the disintegration of feldspar and phyllosilicates.

Subsequently clay minerals were generated in this early stage of diagenesis (Figs. 74d,f,g). The formation of illite, the most prominent clay mineral type within the early clay mineral aggregations, is caused by the disintegrations of detrital feldspar and phyllosilicates particles. Especially the dissolution of the instable feldspar type anorthite is suggested to start the first, because of its higher CO_2 buffering capacity (Van Berk et al., 2009). Thereby, Si^{4+}, Al^{3+}, and Ca^{2+} ions were released and became available for further reactions. Within the Eocene samples, only a low amount of anorthite minerals were observed and are suggested to be dissolved during the early stages of diagenesis largely. The dissolution of anorthite stabilizes the pH of pore water on a high level (Van Berk et al., 2009; 2013; Fu, 2014). Therefore the feldspars albite and K-feldspar do not show this strong dissolution features as anorthite (e.g. Fig. 62a). Albite and K-feldspar are disintegrating and partly dissolved within the Eocene sandstones. It is assumed that corrosion of albite and K-feldspar commenced only when anorthite was almost totally consumed. K-feldspar grains are more stable than albite (e.g. Fig. 66a). This is because of the higher buffering capacity of albite compared to K-feldspar (Van Berk et al., 2009). Albite dissolution released the elements Si^{4+}, Al^{3+}, and Na^{2+}, whereas partial K-feldspar dissolution allocated Si^{4+}, Al^{3+} and K^+ ions. The processes of feldspar dissolution proceeded during the entire diagenetic history of Eocene reservoir rocks and was an essential ion source for further authigenic mineral formations.

The dissolution of feldspar is frequently concomitant with the precipitation of clay minerals, as it is exemplified in Fig 72d. The released ions, dissolved within the pore water, were incorporated into authigenic hydrous aluminum phyllosilicates. But also the partial dissolution of the metamorphic lithic fragments and mica enabled the liberation of ions, such as $Mg^{2+,}$ Mn^{2+} and Fe^{2+}. Eogenetic clay minerals of Eocene sandstones comprise smectite, illite (e.g. Figs. 70b,c, 82a), and minor amounts of kaolinite and chlorite. The formation of the particular clay mineral type depends on the availability of the cations and of the pH of the solution. Pore water can be either (i) diluted by fresh meteoric water, which is less concentrated in ions and thus acidic, or (ii) derived from sea-water, which is higher concentrated and alkaline (Hurst & Irwin, 1982). According to the constant high pH, which is buffered by feldspar dissolution, and the concentration of cations dissolved in the pore water during the eogenesis of Eocene sandstones, the formation of 2:1 clay types smectite and illite was favored (e.g. Kerr, 1952; Hurst & Irwin, 1982; Wilson et al., 2014). Accordingly, smectite and illite are the most prominent eogenetic clay minerals in the shallow marine Ampfing Formation.

When O and NO_3^- are consumed, SO_4^{2-} reduction commences. Sulfate reduction and methanogenesis are the predominating processes during advanced diagenesis (Froelich et al., 1979; Einsele, 2000). Continuous microbial activity and reduction of Fe^{3+} increase pore water alkalinity (Machel & Mountjoy, 1986; Curtis, 1978). In addition, the partial feldspar dissolution, as described above, was important for the eogenetic microbial activity. Since this process holds the pH of the pore water constant via buffering, carbonate precipitation was favored (Van Berk et al., 2009). The free Ca^{2+} from anorthite was a possible supplementary substitute for carbonate formation (Van Berk et al., 2009), next to the common Ca-sources as sea water, fossils or detrital limestone. In the bicarbonate buffer system, carbonate species were produced by the buffering effect of feldspar dissolution (Van Berk et al., 2009). The bicarbonate buffer system comprises the carbonate species: carbonic acid (CO_3^{2-}), bicarbonate ion (HCO_3^-), and carbon dioxide (CO_2). The presence of the prevailing species is dependent on the pH of the pore water. Under alkaline conditions ($pH > 7$) bicarbonate and carbonic acid are predominant. With increasing pH ($pH > 10.3$) the CO_3^{2-} occupies the dominant position (e.g. Appelo & Postma, 2005). In the case of the Eocene sandstones, microbial produced carbon (C^{4+}) build chemical compounds, such as carbonate species in the pore water. The microbial stimulated alkaline conditions result in the presence of HCO_3^- and later CO_3^{2-}. The generation of these carbonate species might result in the oversaturation with regard to calcite (Fu, 2014), leading to carbonate precipitation (Curtis et al., 1977). The initial $\delta^{13}C$ pool ($\delta^{13}C$: ±0‰ [VPDB]), the carbon source for Eocene carbonate cements, was gradually depleted in

^{13}C due to microbial metabolization of organic matter during diagenesis (Hesse & Schacht, 2011). The eogenetic zone of bacterial oxidation has a low impact on the isotope fractionation, whereas sulfate reduction results in the progressive lowering of the δ^{13}C values (see Fig. 89). Based on carbonate isotopy an eogenetic stage of sulfate reduction (δ^{13}C: 0 to -15‰) and an advanced stage of sulfate reduction (δ^{13}C: > -25‰) can be distinguished (e.g. Claypool & Kaplan, 1974; Irwin et al., 1977; Curtis, 1978; Gluyas, 1983, 1984; Allan & Wiggins, 1993; see Fig. 9).

The first carbonate generation is represented by columnar calcite (Cc I) (e.g. Fig. 80d). This calcite type occurs rarely as incrustation between detrital grains, and is extensively replaced by younger calcite cements. In fluviatile (Voitsdorf Formation), and subordinately in tidal (Cerithian Beds) settings, siderite formed within biotite flakes, which provided the necessary Fe^{2+} (e.g. Figs. 72e,f, 75a,c-f). The formation of siderite requires suboxic to reducing environments with low S^{2-} concentrations (Hammer et al., 2010). The open pores were significantly reduced due to the early microcrystalline calcite cement (Cc II). Later, sparitic cement (Cc III) partly replaced the microcrystalline calcite (e.g. Fig. 69g). Less cemented porous sandstones of the Voitsdorf Formation and the Cerithian Beds belong to the carbonate isotope group 1 and show a δ^{13}C ratio between -5.9 to +2.2‰ and a δ^{18}O ratio between -8.3 to -4.3‰ (Fig. 90). δ^{13}C (> -5.9) are similar to sea water carbonates and indicates that these cement generations (Cc II, Cc III) are associated with the eogenetic stage of sulfate reduction. Although the isotopic composition of Cc II and Cc III cannot be differentiated separately, the samples showed an increasing amount of Cc III accompanied by lighter δ^{13}C anyway. This confirms that Cc II represents an older cement phase δ^{13}C similar to the initial isotope pool (marine) and that the δ^{13}C values of the Cc III indicate that they were already affected by fractionation presuming a younger phase. δ^{18}O ratios exhibit a slight negative shift reflecting the primary fluviatile to brackish depositional setting and thus, provided additional evidence for the eogenetic formation of the cements in these sediments.

The precipitation of carbonate cements is accompanied by the partial dissolution of siliciclastic minerals (feldspar, quartz). The importance of this dissolution for the bicarbonate buffering system was already discussed above. Quartz has corroded margins within the Eocene sediments. Especially the strongly cemented sandstones include strongly etched quartz grains, which are even partially dissolved (e.g. Figs. 58f,g). Knauss & Wolery (1988) and Davis et al. (2011) observed intense corrosion marks on the quartz surface in the test of stronger alkaline solutions (pH > 8), because of higher dissolution rates. Kashik (1965) and Friedman & Sanders (1978) suggested a dissolution of quartz at a pH > 9. The release of silica (SiO_2) supported the formation of authigenic silicate minerals, such as clay mineral, and subordinately microcrystalline quartz.

b. Mesogenesis

The "advanced stage" of bacterial sulfate reduction is recorded by strongly cemented sandstone samples within the Ampfing Formation (e.g. Figs. 60a,b) and the Cerithian Beds (Figs. 59a,b). The sparitic cement (Cc III-a) shows local recrystallization patterns into poikilitic cement (Cc IV) (e.g. Figs. 58d,e,g). The texture indicates a comparably early stabilization of the grains by cementation. A slight Mg enrichment in these pervasive Cc III-a is interpreted as indicator for gradual organic matter conversion (Schulz et al., 2009; Schulz & Van Berk, 2009) in a suboxic setting (Einsele, 2000). These carbonate cements show very light $\delta^{13}C$ values (-28.4 to -22.2‰) and moderately light $\delta^{18}O$ ratios (-8.4 to -7.9 ‰) and belong to the carbonate isotope group 2. The ratios are similar to those observed in strongly cemented sandstone samples from Cerithian Beds ($\delta^{13}C$: -27.3 to -10.1‰; $\delta^{18}O$: -7.3 to -4.0‰), which occur together with an asphaltene rich solid bitumen (Sachsenhofer et al., 2006). Commonly, such light $\delta^{13}C$ values ($\delta^{13}C > -25‰$) are described to derive at the "advanced" stage of sulfate reduction zone due to progressive organic matter metabolization (Chien et al., 2012; Watson et al., 1995). In Fig. 90 a trend of the $\delta^{13}C$ ratios from porous (oil-bearing) to strongly cemented horizons from the Cerithian Beds (well BHN2) from +1.9 to -27.3‰ is apparent. This isotope distribution reflects the gradual depletion of the initial (sea water) carbon isotope pool in ^{13}C during sulfate reduction by organic matter metabolization. Porous sandstones exhibit heavier isotopes and belong to the carbonate isotope group 1 (Fig. 90). They have minor amounts in carbonate cement (Cc II, minor Cc III) and more compacted. Moreover, some of these grains are even broken. By comparison, strongly cemented sandstones are depleted in ^{13}C, contain abundant carbonate cement (Cc III, minor Cc II) and are less compacted. These features indicate precipitation of

Cc II and Cc III during the early stages of diagenesis, both within the porous and strongly cemented Cerithian Beds. Grains from porous sandstones with low amounts of carbonate cement were compressed during burial. With increasing cementation by Cc III, light $\delta^{13}C$ was incorporated and the fabric was protected from further compaction. The influence of fossils with marine isotopic composition, especially within the fossil-rich Cerithian Beds, is negligible, because all these Eocene samples comprise shells and foraminifera. Therefore, there is no revision of the general statement on the biochemical zonation within the investigated samples needed. Based on their $\delta^{13}C$ the strongly cemented sandstones from the Cerithian Beds formed during the biochemical zone of "advanced stage" of bacterial sulfate reduction.

Sulfate reduction leads into methanogenesis, when sulfate is depleted. This defines the onset of mesogenesis. Organic matter is metabolized by microbial fermentation and carbonate reduction becomes the dominant process during mesogenesis (Whiticar, 1999; Einsele, 2000; Campbell, 2008). The carbonate cement, which precipitates in this zone, incorporates the C originating from reduced CO_2. Inagaki et al. (2015) observed microbial methanogenesis in a depth of 1700 to 2000 m below sea floor, but timing and depth of mesogenesis are difficult to define.

The zone of methanogenesis is indicated by positive $\delta^{13}C$ ratios. Heavy ^{13}C is derived from fermentation (Irwin et al., 1977; Watson et al., 1995; Einsele, 2000) and carbonate reduction (Whiticar, 1999) during microbial methanogenesis (Carvalho et al., 1995; Einsele, 2000; Schulz & Van Berk, 2009). The initial presence of free Fe^{2+} in the pore waters enables the incorporation of the reduced (ferrous) form of Fe into carbonate minerals (Figs. 61a). Carbonates with such characteristics have been observed exclusively within strongly cemented sandstones of the oil-bearing zone (Cc III-b) in the Voitsdorf Formation. Samples from this section show positive $\delta^{13}C$ (+5.5 to +8.7 ‰) and moderately light $\delta^{18}O$ (-8.3 to -7.6 ‰) ratios (carbonate isotope group 3; Fig. 90). In addition, the comparably tighter texture of the strongly cemented sandstone in the oil-bearing zone of the Voitsdorf Formation suggests advanced compaction and a later diagenetic formation of the carbonate minerals compared to the cements from Cc III-a. The sparitic cements (Cc III-b) grade locally into poikilitic cement (Cc IV). Cc IV was observed within the isotopically light Cc III-a and heavy Cc III-b and therefore it is suggested that this recrystallization does not cause a shift in isotopic composition.

Carbonate cement minerals of group 3 may be connected to a paleo-oil-water contact (OWC), where bacterial activity may trigger alkaline conditions and carbonate precipitation (Machel & Mountjoy, 1986; Watson et al., 1995). Some glauconite pellets altered within hydrocarbon-bearing sandstones at the shallow-marine Ampfing Formation. Fu et al. (2015) related glauconite alteration in reservoir rocks to oil biodegradation. However, oil within the studied Ampfing reservoir shows no sign of biodegradation (Gratzer et al., 2011; Pytlak et al., in press). Today the samples are located above the OWC. Changing OWCs may be explained by continuing oil charge or by the Karpatian/Badenian westward tilting of the NAFB (Gusterhuber, 2012).

In samples from all formations, eogenetic clay minerals are partly altered into more stable clay minerals, involving illite or more chlorite. Depending on the availability of ions (K^{+}, Al^{2+}, Na^{2+}, Ca^{2+}, Mg^{2+}, Fe^{3+}, Si^{4+}, OH^{-}), which were released from the partial dissolution of minerals (especially aluminosilicates) during mesogenesis, particular clay mineral types form. The alteration of kaolinite and smectite in illite or chlorite depends on the availability of Fe^{3+} and Mg^{2+} cations. Hower et al. (1976) and Hoffman & Hower (1979) suggested a temperature of 60 - 100°C for the alteration of smectite into illite. Smectite may also be altered transformed into chlorite. In addition, early diagenetic Eogenetic kaolinite and smectite serve as ion source (e.g. K^{+}, Al^{2+}, Na^{2+}, Si^{4+}) and can be recrystallized transformed into illite and chlorite by the aid of Fe^{3+} originating from the corrosion of iron oxides (Velde, 1984), Fe-, and Mg-rich lithic fragments and glauconite in the Ampfing Formation. Some of the big booklets (< 100 µm) within the gas-bearing sandstones of the Ampfing Formation show interference colors similar to muscovite (e.g. 74g) and are probably alterated muscovite into illite. Illite formed as the most common mineral within investigated Eocene sandstones. Based on its predominance in the clay mineral fraction in the Eocene sandstones, it can be assumed that a certain proportion of detrital muscovite, eogenetic smectite and kaolinite were alterated into the more stable illite.

c. Telogenesis

The telogenetic stage affected the Eocene reservoir rocks by kaolinite precipitation and mineral destabilization (Figs. 69e, 81b-f). These processes indicate a lowering in pH of the fluid phase, which suggests a meteoric flush (e.g. Hurst & Irwin, 1982; Bjørlykke & Brendsdal, 1986; Bjørlykke et al., 1989; Bjørkum et al., 1990). Kaolinite formed by leaching of Al-rich silicate minerals, mainly feldspar and illite, in the form of small booklets (~50 µm). It often grows on older clay mineral accumulations (illite, smectite). Lanson et al. (2002) and Hammer et al. (2010) emphasized that meteoric flush removes ions, amongst others K^+, from the system and, hence, promotes kaolinite rather than illite precipitation. Quartz- or feldspar overgrowths have not been observed, therefore it is assumed, that Si^{4+} was removed or diluted, respectively. Kaolinite formation strongly reduced the porosity. Independent support for dilution by meteoric water in Eocene reservoir sandstones is provided by hydrochemical data, which prove a late Pleistocene meteoric origin of some formation waters (Andrews et al., 1987).

Carbonate cements (Cc II and Cc III) from the porous sandstones of the Ampfing Formation (carbonate isotope group 4; Fig. 90) are characterized by a trend towards lighter isotope ratios independent of their fluid content (gas/oil/water). The depletion of ^{18}O relative to a marine setting might be another indication of meteoric flush (Dimitrakopoulus & Muehlenbachs, 1987; Watson et al., 1995). The lighter $\delta^{13}C$ ratios are attributed to proceeding sulfate reduction. Petrographically, cements of carbonate isotope group 4 (Cc II and Cc III) resemble that of group 1 (e.g. Figs. 69, 72, 73, 80). But isotope group 1 belongs to a non-marine (fresh-/brackish water) and isotope group 4 to a marine (sea water) setting. However, the $\delta^{18}O$ of carbonate isotope group 4 indicates a decrease of the pore water salinity relative to the sea water although the facies would suggest a shallow marine milieu. Therefore, it is presumed that the isotopic composition of the porous sandstones of the Ampfing Formation, associated to carbonate isotope group 4, were overprinted by telogenetic meteoric flush. The isotopic signal within this horizon is significant, since the meteoric flush influenced the laterally continuous Ampfing Formation stronger than the underlying Voitsdorf Formation and Cerithian Beds.

4.2.6. Conclusion for Eocene rocks

The present study contributes to the understanding of the relation between hydrocarbon accumulation and pore space evolution in Eocene reservoir units (Voitsdorf Formation, Cerithian Beds and Ampfing Formation) from the NAFB. A summary of the most important diagenetic processes is provided in Fig. 91.

- The reservoir quality is strongly controlled by varying detrital input and transport distance from the hinterland, and, hence, the paleo-geographic position. Low compositional maturity is associated to high feldspar and as an alteration product high clay mineral content, which restricts fluid flow. Sandstones from the Ampfing Formation show the highest maturity.
- These eogenetic clay minerals comprise mainly illite and smectite, and subordinately kaolinite. Commonly they are mixed with iron oxides and fine grained organic material, and appear as coatings around detrital grains or clusters between grains.
- Metabolism of organic matter within surrounding clayey marls provided microbial gas. Eogenetic carbonate precipitation (Cc I - Cc III) was promoted by bacterially stimulated alkaline conditions. This early cementation decreased the initial porosity and prevented further compaction. Isotopic composition of gases from some oil reservoirs (e.g. well Bad Hall) support the presence of primary microbial gas, which later became mixed with thermogenic hydrocarbons.
- The carbonate precipitation is accompanied by a partial dissolution of siliciclastic grains (feldspar, quartz).
- Calcite cements in the porous Voitsdorf Formation and the Cerithian Beds show $\delta^{13}C$- and $\delta^{18}O$-values between -5.9 to +2.2‰ and -8.3 to -4.3‰ [VPDB] (carbonate isotope group 1), respectively, which supports pore water with reduced salinity during calcite precipitation.
- Strongly cemented sandstones from the Cerithian Beds and Ampfing Formation encompass mainly the calcite generations (Cc III-a and Cc IV). The texture of these sediments indicates less compaction and thus early cementation. In addition, the calcites are slightly enriched in Mg and show $\delta^{13}C$ ratios of (-28.4 to -22.2‰; carbonate isotope group 2). It is suggested that these light ratios are formed in the “advanced stage” of sulfate reduction.

- Strongly cemented sandstones within the oil-bearing zone exhibit isotopically heavy carbonate cements (carbonate isotope group 3: $\delta^{13}C$ under +8.7‰). Positive isotope values and Fe-enrichment in carbonate cements (Cc III-b and Cc IV) are likely associated with fermentation (methanogenesis). Further, the texture displays more compaction, than sandstones from the Cerithian Beds and Ampfing Formation.
- Telogenesis is characterized by mineral destabilization (e.g. strong carbonate and feldspar corrosion, minor corrosion of quartz) and kaolinite precipitation.
- A dilution of formation water (meteoric flush) is indicated by light $\delta^{18}O$ ratios (carbonate isotope group 4: -17.2 to -9.4‰) of the carbonate cements from the shallow-marine Ampfing Formation during telogenesis.

4.3. Upper Cretaceous

The main focus of this thesis is put on Oligocene and Eocene reservoir sandstones. For completeness, study results of Upper Cretaceous (Cenomanian) reservoir sandstones are briefly reviewed below (see Grundtner et al., 2016).

Based on lithology and log characteristics, Nachtmann (1995b) subdivided the Cenomanian green-sandstones into three units (CE1 - CE2) (Fig. 91). CE1 corresponds to the Bad Abbach Member of Niebuhr et al. (2009), whereas CE2 and CE3 correspond to the underlying Saal Member.

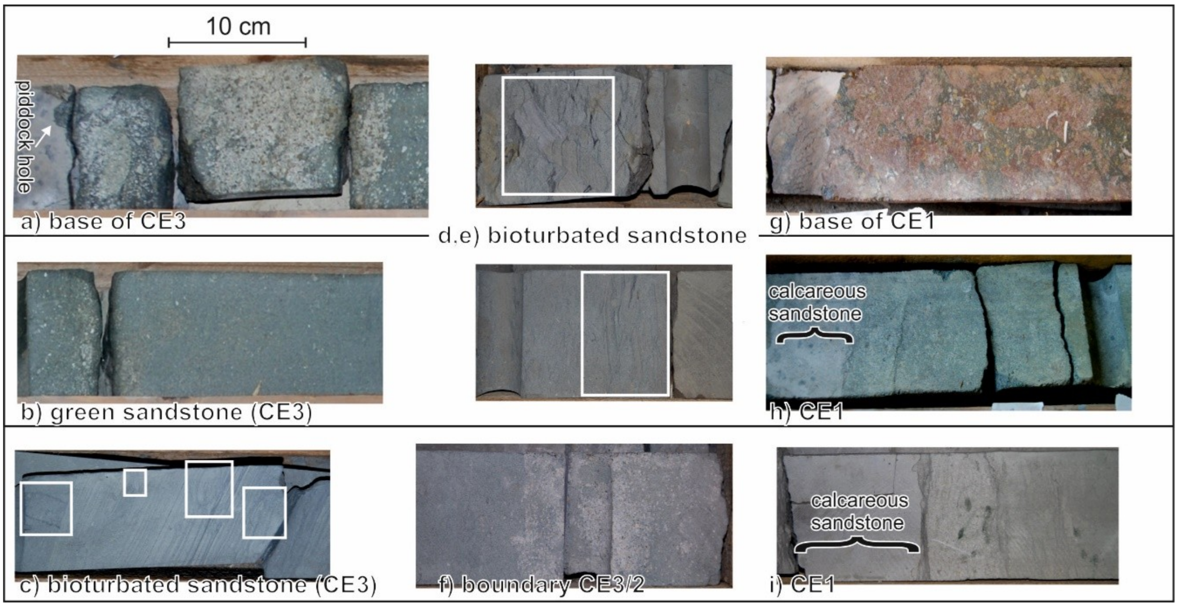

Fig. 92 Core photographs from the Trattnach Oil Field with Cenomanian reservoir rocks (at a depth of 1110 - 1150 m below ground level): a) Base of CE3 with underlying carbonates (Malm). CE3: b) typical green sandstone and c) weak bioturbation (white boxes). Typical bioturbation features of CE3 and CE3: d) vertical and horizontal burrows, e) cross bedding, f) bimodal grain size distribution. g) Base of CE1 (“marker bed” sensu Nachtmann, 1995). Cemented layers: h) green sandstone and i) hardground (after Groß et al., 2015b).

4.3.1. Sedimentary petrology

The upper unit (Bad Abbach Member sensu Niebuhr et al., 2009), is fossil-rich, bioturbated and frequently cemented. Sandstones and conglomerates from the upper unit consist mainly of quartz, glauconite and calcite, besides low amounts of dolomite, berthierine and clay minerals. They show a bimodal grain size distribution. Coarser grains originated from storm events. Calcareous sandstone layers are characterized by a high percentage of bioclasts and limy mud. A red "marker bed" defines the base of the upper unit (Fig. 92).

The two lower units (Saal Member sensu Niebuhr et al., 2009) comprise green fine-grained sand- and siltstone layers, and medium- to coarse-grained sandstones. Their greenish color derives from glauconite, signifying shallow marine facies. Glauconite occurs as pellets in different states of alteration. Locally, glauconite also forms cement. The sandstones from the lower units are defined as subarkoses (Fig. 93). They are compositional less mature than those from the upper unit. Bioturbation obliterated primary sedimentary structures (Fig. 92).

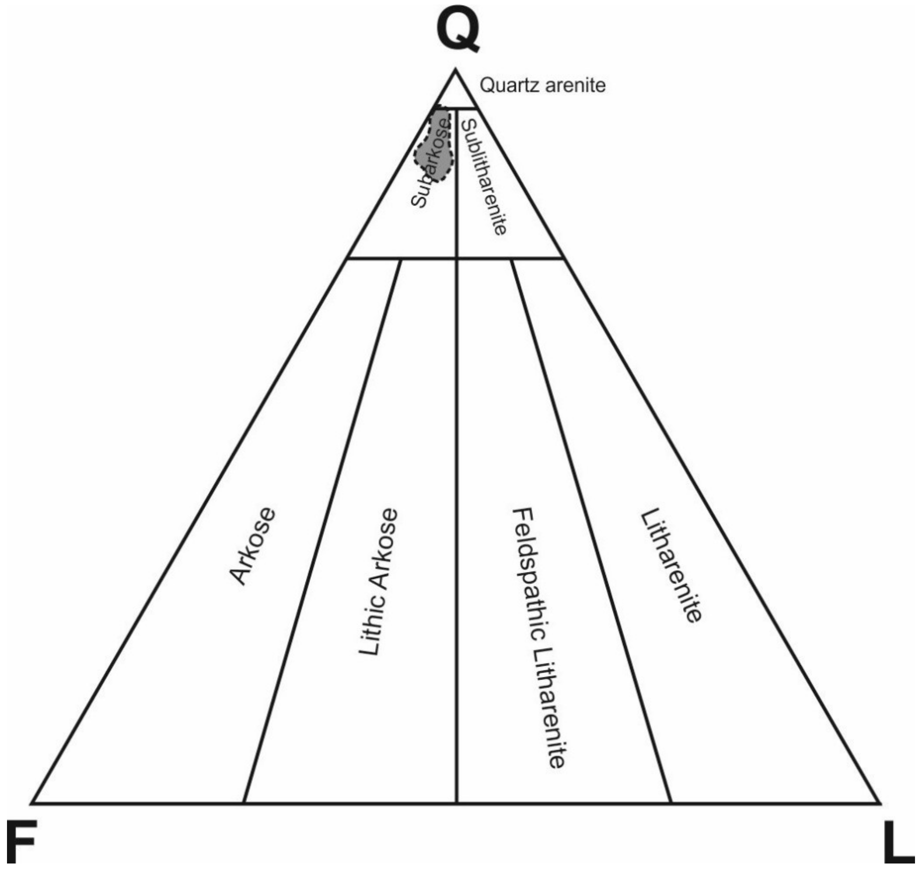

Fig. 93 Sandstone classification after Folk (1974) (after Groß et al., 2015).

4.3.2. Diagenetic features

The diagenetic history is strongly dependent on facies and the primary mineralogy. Pure calcite cement prevails in the upper unit. Two carbonate cement generations can be differentiated by their morphology: an earlier microcrystalline (Cc II) and a later blocky (Cc III) one. High amounts of carbonate cement, which reduce porosity remarkably, have been observed in samples with calcic bioclasts (Fig. 94a). The carbonate precipitation is accompanied by a corrosion of siliciclastic grains. Locally, the cement is recrystallized into idiomorphic rhombs of authigenic dolomite. In general, the upper unit is poor in clay minerals and glauconite pellets. Only in some areas, Al contents initially measurements denote a mixture of clay and carbonate minerals (see also Groß et al., 2015a). Occasionally these clay minerals, mainly illite, occur as coatings around detrital grains and are covered by carbonate cement. Therefore, they are interpreted as primary matrix or a very early cement phase. These clay minerals were locally replaced by authigenic blocky calcite cement (Cc III). Booklet structures formed initially by kaolinite are visible in the SEM images of several samples (e.g. Fig. 94b). EDX investigations indicate partial chloritization of kaolinite.

Sandstones from the lower units are typically poorly cemented (Fig. 94c). Clay minerals identified as illite, kaolinite and mixed layers, are the dominant pore filling. Some micrite is encountered within intervals rich in calcitic bioclasts and fossils. In addition, euhedral quartz overgrowths also occur on older cements (Fig. 94d). Typically, porosity of fine grained sandstones is reduced by a clayey primary matrix. Clay minerals from this matrix are often re-crystallized into chlorite. Although minor cementation results in high porosity values, the presence of clay minerals reduces the permeability.

Within the Cenomanian oil-bearing sandstones, intervals of strongly cemented horizons are visible (Figs. 94e,f). In these intervals carbonate cementation caused a distinct reduction in porosity. Calcite (Cc III) displays a blocky/homogenous morphology and fills the whole pores. The overlying zone shows pores which bear oil stains. In addition to the conventional typical olive green glauconite pellets, some glauconite grains show a brown color and are altered. The boundary of strongly cemented and poor cemented layers is sharp.

In addition, a dolomitization of the earlier carbonate pore filling is evident in one well in of the study area (Figs. 94g,h). Here, well defined and comparably large dolomite rhombs are present.

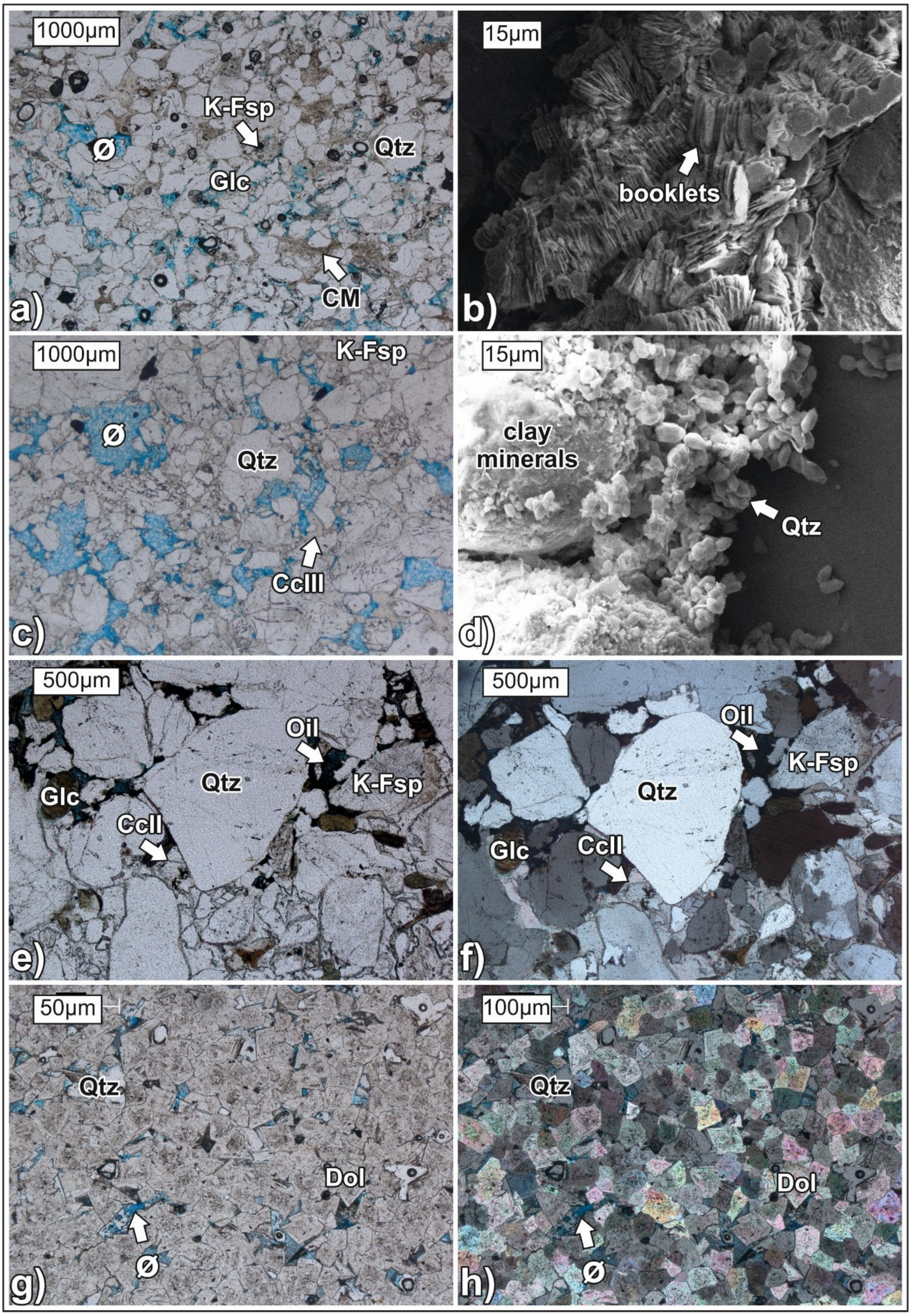

Fig. 94 Cenomanian sandstones: a) thin section overview of the texture in plane-polarized light from lower units; b) SEM-image of chlorite (altered kaolinite); c) thin section overview of the texture in plane-polarized light from upper unit; d) SEM-image of euhedral quartz overgrowth on clay mineral-covered grains; e,f) strongly cemented sandstone at contact with oil-bearing zone in plane- and cross-polarized light; g,h) thin section overview in plane- and crossed polarized light of dolomitization.

4.3.3. Effect on pore space quality

The degree of open pore space is strongly controlled by carbonate cement, whereas permeability is mainly controlled by clay minerals. Regarding porosity and permeability (Fig. 95), which were measured in the lab, Cenomanian reservoir rocks can be grouped in four rock types (RT1 - 4; established by RAG). The sequence of RT1 to RT4 represents the decrease of the reservoir quality from good reservoir (RT1) to non-reservoir (RT4) properties of these sandstones. Investigations from Groß et al. (2015b) on Cenomanian sandstones from Trattnach Field (depth range: 1110 - 1140 m below subsurface) reveal that the upper of the coarse-grained CE3 sandstones has the highest permeability values and thus the highest reservoir quality (RT1: matrix- and cement-free). RT 2 and 3 comprise sandstones with (minor) carbonate cement and clay matrix/cement. Thereby the CE1 and the lower section of CE3 are composed of fine sand and belong to RT3. Samples with clay mineral matrix/cement and minor carbonate cement have the lowest permeabilities (< 10 mD). In general, two types of Cenomanian sandstones are differentiated:

- Minor carbonate cemented sandstones, with a low amount of clay mineral matrix are characterized by intergranular porosity. Their porosity and permeability amount 15 to 25% and ~100 mD, respectively. It is assumed that the majority of the primary clay minerals were removed during eogenesis. Further, the absence of a calcareous source, like fossils, is responsible for the minor carbonate cement.
- Sandstones in vicinity to calcareous layers are enriched in carbonate cement. Siliciclastic minerals, such as K-feldspar, quartz and clay minerals are often replaced. Porosity values of 10 to 15% and permeability of < 10 mD are characteristic. The degree of carbonate precipitation and decrease in porosity is related to the fluid flow from over- and underlying calcareous, low permeable layers.

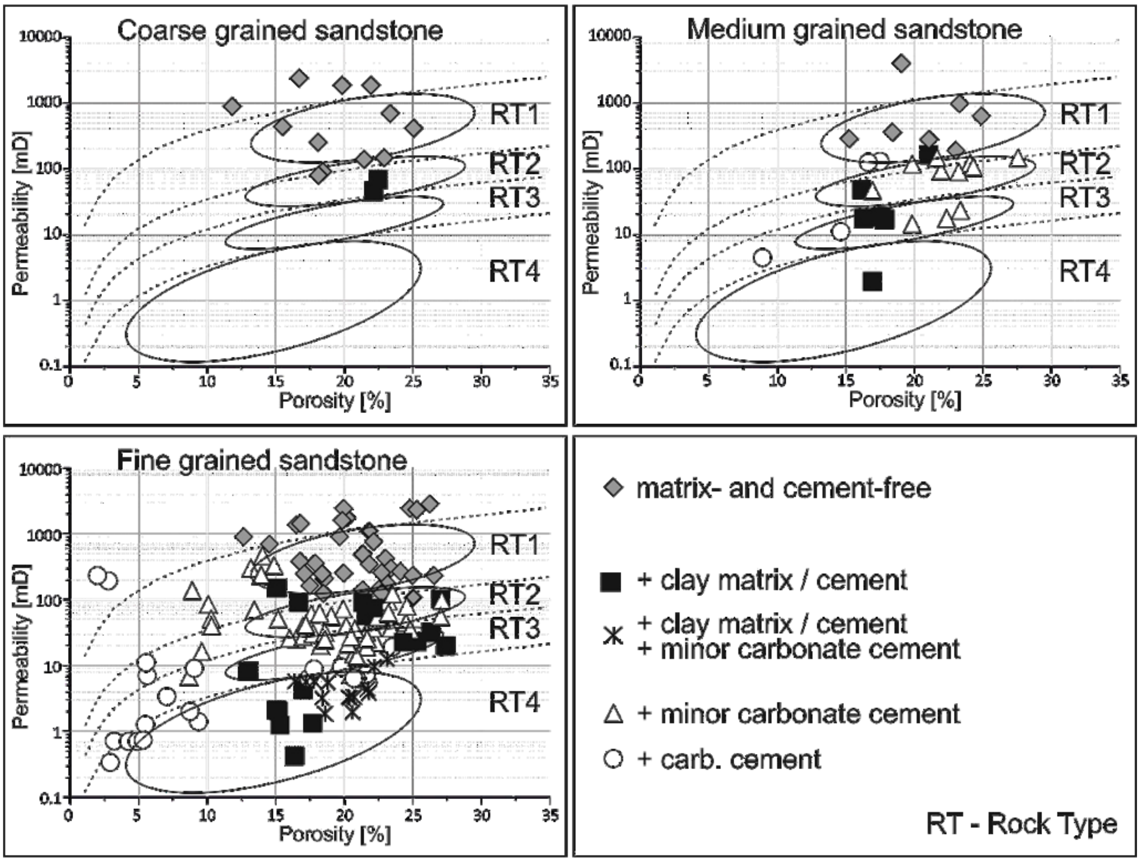

Fig. 95 Semilog plot of permeability versus porosity from samples of coarse- to fine-grained sandstones, differentiated according to their pore filling (modified after Groß et al., 2015b).

4.3.4. Carbonate isotopy

$\delta^{13}C$ and $\delta^{18}O$ of authigenic carbonate phases can be used to trace their formation conditions and, hence, the diagenetic history. The initial isotope composition gets altered by diagenetic processes, such as microbial processes ($\delta^{13}C$) and changes in formation water and temperature ($\delta^{18}O$).

The carbonate cements of Cenomanian reservoir sandstones range between -13.6 and +3.3‰ in $\delta^{13}C$ and between -23.9 and -4.2‰ in $\delta^{18}O$ (Fig. 96). These values exhibit a trend towards lighter isotope ratios relative to sea water carbonates ($\delta^{13}C$ of -5 to +4‰, $\delta^{18}O$ of -5 to +3‰; Dimitrakopoulus & Muehlenbachs, 1987).

Very light $\delta^{13}C$ ratios (-32.7 to -16.6‰) were observed in a strongly cemented horizon within the oil-bearing zone in one well (open circles in Fig. 96). They represent a strongly cemented horizon within the oil-bearing zones.

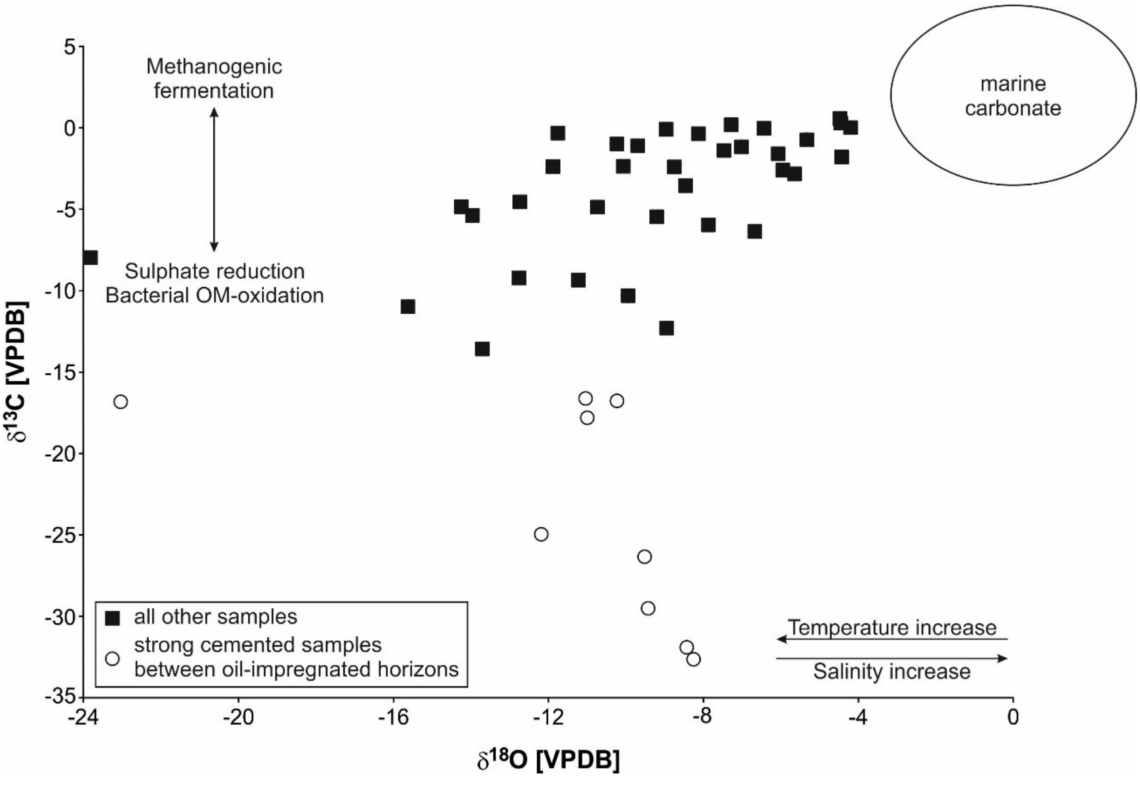

Fig. 96 Plot of carbon and oxygen stable isotopic composition of bulk carbonate cements from investigated sandstones. Effects of diagenetic (OM=organic matter) processes on stable isotope trends are given (after Allan & Wiggins, 1993). In comparison, marine carbonates vary in their $\delta^{13}C$ from +4 to -5‰ and $\delta^{18}O$ from -5 to +3‰ (Dimitrakopoulus & Muehlenbachs, 1987).

4.3.5. Discussion

Influence of depositional environment on sedimentary petrology

The Cenomanian sandstones developed at the northern margin of the Neotethys. A shallow marine facies is indicated by horizons rich in glauconite, fossils and bioturbation. The primary mineralogical input varies horizontally and vertically: (i) The upper unit has high carbonate contents (e.g. fossils, bioclasts, limy mud). (ii) The two lower units contain less carbonate and more clay minerals. The sandstone composition of all units is also controlled by a southward increase in transport distance and a change from a granite- to a carbonate-dominated hinterland from east to west (Grundtner et al., 2016).

Diagenetic history

The diagenesis is strongly controlled by the primary mineralogical input, which affects the authigenic mineral formation.

The disintegration of mica enabled glauconite precipitation in a reduced setting. Other clay minerals (mainly illite; chlorite, smectite and kaolinite) formed by the release of ions (Fe^{2+}, K^{+}, etc.) due to dissolution and alteration (e.g. Fig. 94a,c,d).

Two carbonate generations, an older microcrystalline Cc II and a younger blocky carbonate Cc III, formed during eogenesis (Groß et al., 2015b). Enhanced carbonate precipitation, stimulated by bacterial oxidation of organic matter (Hesse & Schacht, 2011), decreased the porosity. Carbonate cements, which formed under shallow marine conditions exhibit stable isotope values of about -6.7 to +3.3‰ for $\delta^{13}C$ and -10.2 to -4.3‰ for $\delta^{18}O$ (Fig. 96). Carbonate cementation is accompanied by the partial disintegration and replacement of feldspar, phyllosilicates and minor quartz.

Advanced carbonate reduction during burial leads to a depletion of heavy carbon isotopes. Thus the strongly cemented horizons with very light $\delta^{13}C$ (> -32.7‰; Figs. 94e,f; 96) indicate a formation under “advanced” sulfate reduction during deeper burial (Irwin et al., 1977). Sandstones with this light $\delta^{13}C$ show a comparably higher compaction, suggesting a later diagenetic formation of the carbonate cement.

The formation of some euhedral quartz overgrowths on older cements (Fig. 94d), which were not observed in Eocene and Oligocene-Miocene reservoir rocks, and the chloritization of kaolinite (Fig. 94b) indicate higher formation temperatures. For quartz overgrowths temperatures of at least 60 to 80°C are necessary. Typically quartz overgrowths form at 90 to 165°C (Bjørlykke & Egeberg, 1993; Walderhaug, 1994; 2000). According to Worden & Morad (2003), Boles & Frank (1979) and Ehrenberg et al. (1993), chloritization of kaolinite in the presence of Fe- and Mg-ions commences at temperatures of about 100°C.

The depletion of ^{18}O (> -23.9‰) relative to a marine setting might be due to meteoric flush (Dimitrakopoulus & Muehlenbachs, 1987). Interestingly samples with coarse grain size, and not necessarily samples with high permeability, are affected by the meteoric flush, particularly.

4.3.6. Conclusion for Upper Cretaceous rocks

The diagenesis of Cenomanian reservoir rocks shows the following characteristics:

- Diagenesis is strongly dependent on facies. Primary mineralogical input is controlled by the paleo-geographic position in relation to the particular hinterland and transport distance.
- During eogenesis, several cement generations in the studied samples formed. Clay mineral cement often consists of illite, kaolinite and chlorite. Carbonate cement is present in the form of micrite (Cc II) or blocky (Cc III) calcite.
- In some samples, euhedral quartz overgrowths and chloritization of kaolinite occur indicating relative high temperatures ($\geq 100°C$).
- Light $\delta^{18}O$ ratios of the carbonate cements from coarser-grained sandstones reflect dilution of the formation water (meteoric flush). Strongly cemented sandstones, which show $\delta^{13}C$ as low as -32.7‰, are suggested to form by biodegradation of organic matter or hydrocarbons.
- The reservoir quality of Cenomanian sandstones is affected by carbonate cementation, which is controlled by the availability of carbonate sources. Weakly cemented sandstones with higher permeability and strongly cemented sandstones in the vicinity of calcareous rocks can be differentiated.

5. Final conclusions

The study of the diagenetic evolution of siliciclastic reservoir rocks in the Austrian part of the NAFB provided important new insights on rock-fluid interactions.

The study reveals a strong relationship between carbonate precipitation and microbial gas generation in the reservoir rocks of the NAFB. Important insights into the relation of hydrocarbon generation and their alteration products are provided by $\delta^{13}C$ of authigenic carbonate minerals. Based on the observed diagenetic features, paragenetic sequence can be interpreted (Fig. 97). The events of strong carbonate cementation are highlighted and the different stratigraphic horizons (Upper Cretaceous, Eocene, Oligocene-Miocene) are color-coded.

The primary microbial gas generation has the biggest influence on the growth of carbonate cements. During eogenesis, microbial CH_4 and CO_2 were generated by organic matter metabolism in intercalating calcareous shales. Bacterial activity stimulated alkaline conditions and triggered carbonate precipitation. The produced CO_2 was incorporated into the carbonate cement. The carbon isotopy of this incorporated CO_2 provides information on the alteration of the carbon pool within the system during diagenesis. The primary signal gets progressively modified by the oxidation of metabolizable organic matter. The individual stages of degradation can be distinguished by characteristic isotopic composition of the carbonates and specific mineral growth.

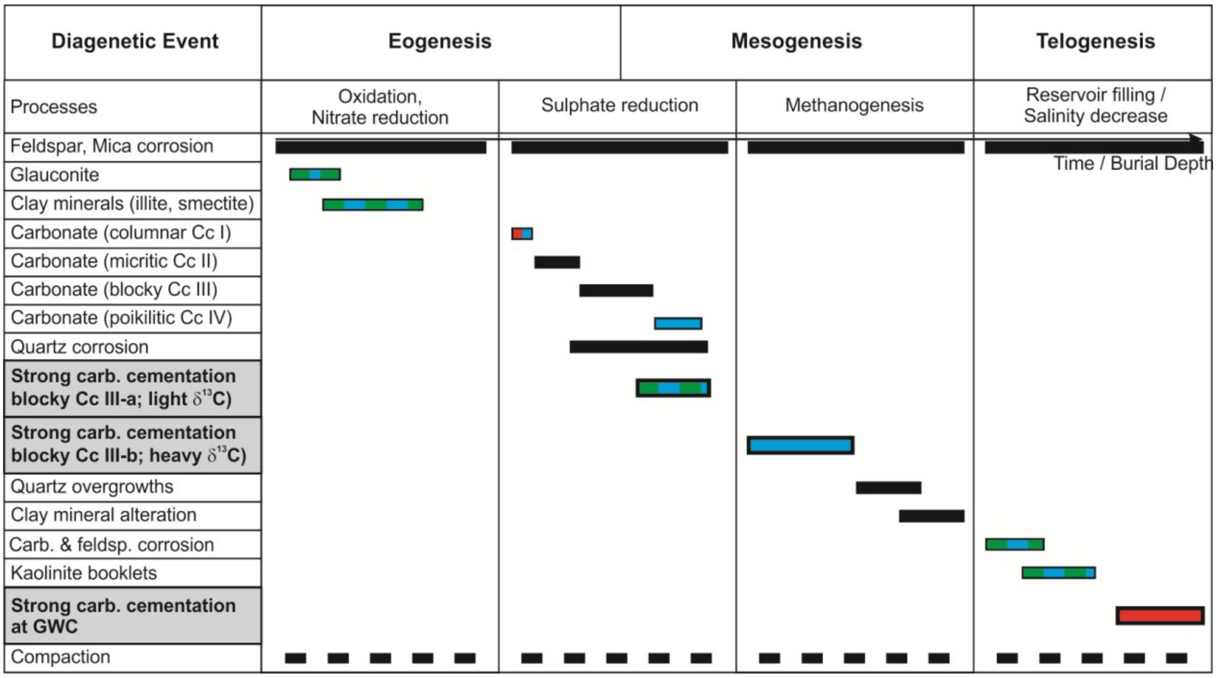

Fig. 97 Paragenetic sequence for Cenomanian (green), Eocene (blue) and Oligocene-Miocene (red) sandstones, general processes are black.

5.1. Sedimentary petrology and diagenesis of Upper Cretaceous sandstones

The Cenomanian reservoir rocks are subarkoses and represent a shallow-marine facies. They can be subdivided into two lower units that consist of green (glauconitic) sandstones, which are compositional less mature than those from the upper unit. The upper unit consists of fossil-rich, bioturbated and frequently cemented fine to medium-grained sandstones. Calcareous sandstones include bioclasts and limy mud. The sandstone composition of all units is also controlled by a southward increase in transport distance and a change from a crystalline- to a carbonate-dominated hinterland from east to west.

The eogenetic processes were strongly controlled by the primary mineralogical input and the depositional environment. Especially the formation of glauconite is characteristic for these shallow marine sandstones (Fig. 97). Cenomanian sandstones encompass mainly authigenic clay mineral growth, related to feldspar and mica disintegration (Fig. 97). Low compositional maturity was associated with high feldspar content and related high clay mineral content (smectite, illite, kaolinite and chlorite), which decreased the pore network.

After the consumption of oxygen and nitrogen due to bacterial oxidation of organic substances, sulfate is the oxidizing agent for metabolization. The primary isotope pool of the system is equalized to marine carbonates. On the basis of organic matter degradation it gets fractionated. The carbonate isotopes get successively depleted in heavy ^{13}C, and thus a negative ratio is indicative for advanced burial diagenesis. In general, the zone of sulfate reduction is characterized by intensified carbonate (calcite and dolomite) precipitation.

Besides clay minerals, Upper Cretaceous sandstones comprise also a minor amount of eogenetic calcite (microcrystalline Cc II and blocky/homogenous Cc III) as cement phase (Fig. 97). The formation of these carbonates was stimulated by the metabolization of organic matter, which led to the formation of microbial gas (CH_4 and CO_2). Surrounding organic matter-rich shales served as substance for the energy extraction. The carbonate cementation was accompanied by a partly dissolution of siliciclastic components (quartz, feldspar) (Fig. 97).

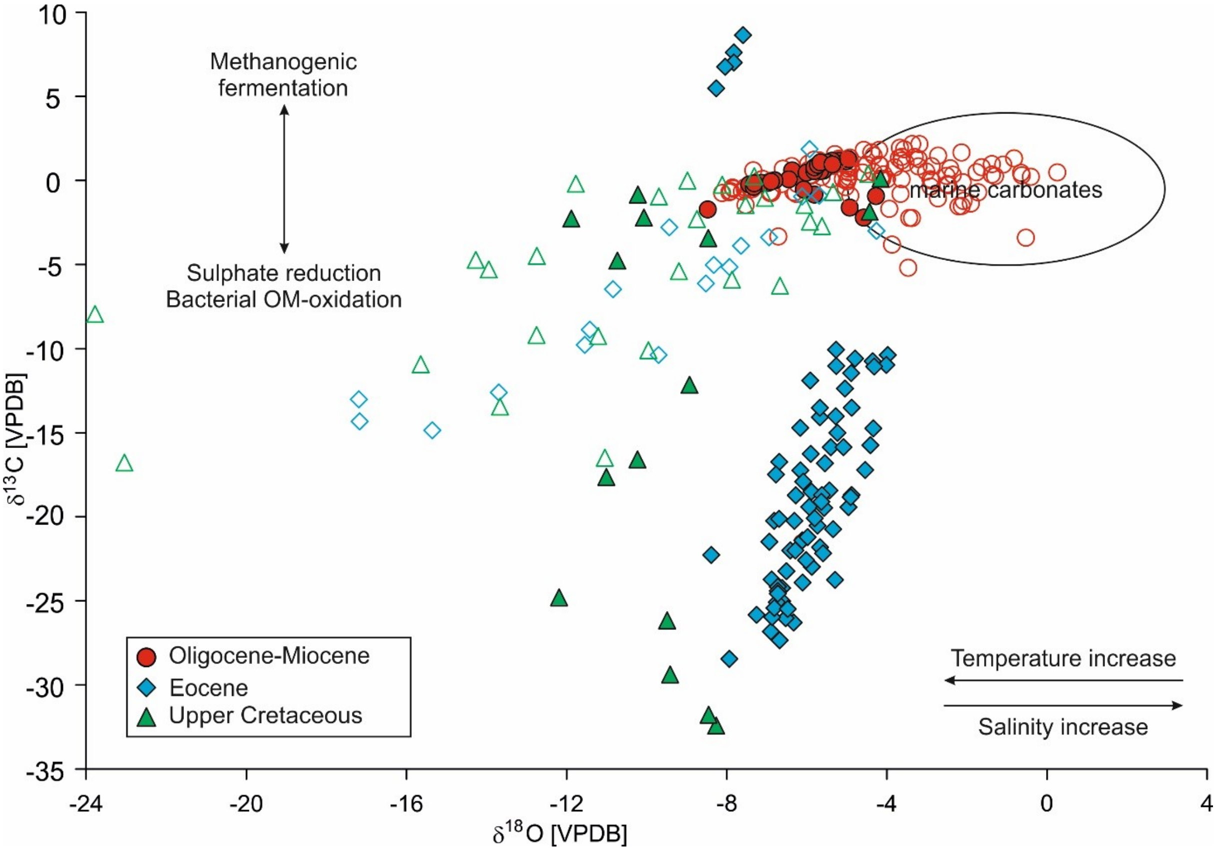

Fig. 98 Stable oxygen and carbon isotopy of bulk carbonate cements from Upper Cretaceous (green triangle), Eocene (blue diamond) and Oligocene-Miocene (red circle) sandstones. Carbonate cemented sandstone samples are filled and porous samples are unfilled. The field for initial marine carbonate is shown after Dimitrakopoulus & Muehlenbachs (1987). The isotopic fractionation trends are after Allan & Wiggins (1993) (OM=organic matter).

Carbonate cementation is dependent on the availability of carbonate sources, like fossils and limestone. Thus, three rock types can be differentiated:

(i) Weakly cemented sandstones with high permeability ($\delta^{13}C$: -12.3 to +3.3‰, $\delta^{18}O$: -10.2 to -4.5‰; green unfilled triangles in Fig. 98),

(ii) Strongly cemented sandstones, which occur in the vicinity of calcareous rocks, or are rich in bioclasts and fossils ($\delta^{13}C$: -32.7 to -16.6‰, $\delta^{18}O$: -12.2 to -8.3‰; green filled triangles in Fig. 98), and

(iii) Strongly cemented sandstones (mainly Cc III-a, minor Cc II) with $\delta^{13}C$ lower than -25‰ (thick green-blue bar in Fig. 97; $\delta^{13}C$: -4.8 to 0‰, $\delta^{18}O$: -11.9 to -4.2‰; green filled triangles in Fig. 98). This indicates an input of light carbon isotopes in the "advanced stage" of sulfate reduction.

The formation of some euhedral quartz overgrowths on clay minerals, and the chloritization of kaolinite indicate higher formation temperatures (≥ 100°C) during progressive burial (Fig. 97).

The coarse grained porous sandstones of Upper Cretaceous tend to more negative $\delta^{18}O$-values (> -23.9‰) compared to marine carbonates (green unfilled triangles in Fig. 98). Mineral destabilization (e.g. carbonate, feldspar corrosion) and advanced kaolinite precipitation indicate the system's disequilibrium (Fig. 97). The overprint of the isotopic composition of eogenetic Cc II and Cc III and the mineral disintegration can be explained by a telogenetic meteoric flush. Additional support for dilution of the pore water by meteoric water in Upper Cretaceous (and Eocene) reservoir sandstones is provided by the low salinity of their formation waters.

5.2. Sedimentary petrology and diagenesis of Eocene sandstones

The Eocene sandstones are lithic arkoses (to feldspatic litharenites) and were deposited in fluviatile, tidal to shallow-marine environments. Reservoir quality is related to the paleo-geographic position in relation to the crystalline hinterland, which determines the detrital input by the transport distance additionally.

Eogenesis comprises mainly authigenic clay mineral growth, which is associated to feldspar and mica disintegration (Fig. 97). Illite, smectite, and minor kaolinite, are the dominating clay minerals. Low compositional maturity is associated with high feldspar content and related high clay mineral content, which decrease the pore network. Besides, within the shallow marine Ampfing Formation also glauconite pellets formed (Fig. 97).

Syn- and post-sedimentary organic matter metabolization of dark clayey marls generated gas. This microbial activity stimulated eogenetic carbonate formation, represented by the carbonate cements Cc I - Cc IV (Fig. 97). They decreased the primary porosity and stabilized the texture during compaction. Additionally, siliciclastic grains were partially dissolved due to an increase in pH (Fig. 97).

Sulfate reduction and carbonate reduction were the dominating processes during burial diagenesis (Figs. 97, 98). This clearly appears from the cement:

(i) Porous sandstones (Cc I - Cc III) vary in δ^{13}C between -5.9 to +2.2‰ and in δ^{18}O between -8.3 to -4.3‰ (blue unfilled diamonds in Fig. 98). The lighter δ^{18}O ratios of Eocene fluviatile to tidal sandstones reflect the non-marine setting during eogenetic calcite precipitation. The lighter carbonate isotopes indicate a fractionation by organic matter metabolization.

(ii) Calcite cements (Cc III-a, minor Cc IV) in strongly cemented sandstones formed during the "advanced stage" of sulfate reduction. Typically they show δ^{13}C values ranging from -28.4 to -22.2‰ and are slightly enriched in Mg contents. Further, their texture indicates light compaction (thick green-blue bar in Fig. 97; filled blue diamonds in Fig. 98).

(iii) Strongly cemented sandstones (Cc III-b, minor Cc IV) exhibit $\delta^{13}C < +8$ (filled blue diamonds in Fig. 98) and are enriched in Fe. Comparable more compaction is indicated by their texture, which leads to the conclusion of a diagenetically later formation at the stage of methanogenesis (thick blue bar in Fig. 97).

Kaolinite booklets represent the last authigenic formation within Eocene reservoir sandstones (Fig. 97). The mineral growth is accompanied by the partial dissolution of detrital feldspar and eogenetic carbonates (Fig. 97). The telogenetic hydrogeochemical imbalance and associated mineral precipitation is linked to the meteoric flush. Dilution of formation water is supplemented by light $\delta^{18}O$ ratios (-17.2 to -9.4‰) of porous sandstones (unfilled blue diamonds in Fig. 98).

5.3. Sedimentary petrology and diagenesis of Oligocene-Miocene sandstones

Oligocene-Miocene sandstones mainly host microbial methane. In general, the reservoir quality strongly depends on the paleo-geographic position within the varying detrital sources and transport distances. Sedimentpetrographic investigations indicate that reservoir rocks of the Oligocene-Miocene can be differentiated into three depositional settings: northern slope, channel belt and southern slope. The main reservoir rocks were deposited along the submarine Puchkirchen channel. Sandstones with higher matrix content were deposited outside the channel. They are classified as lithic arkoses to litharenites. The prevailing pore fillings are calcite and dolomite. They show distinct corrosion and occur as „relictic cement”.

Microbial gas (CH_4 and CO_2) was generated by organic matter metabolism in intercalating calcareous shales. Bacterial activity contemporaneously stimulated alkaline conditions and favored authigenic carbonate precipitation of columnar (Cc I), microcrystalline (Cc II) and blocky/homogenous calcite (Cc III) cements (Fig. 97). Advanced compaction was hindered by this early cementation. In addition, siliciclastics were corroded and partial replaced by the carbonate cement (Fig. 97). These deep-marine sediments exhibit eogenetic carbonate cements with mean $\delta^{13}C$ of +1.1‰ and $\delta^{18}O$ of -5.3 (unfilled red circles in Fig. 98).

Finally, a distinct and low permeable zone formed at the GWC within these reservoir sandstones (thick red bar in Fig. 97). The whole pores are filled with carbonate cement, which is composed primarily of calcite. Especially in this zone, the siliciclastic grains are partially dissolved and replaced. In comparison to the eogenetic formed cements, the carbonates in this area are slightly depleted in ^{18}O ($\delta^{18}O$: -8‰; filled red circles in Fig. 98), which could be caused by a fast cementation process. For the formation of this zone, it is suggested that Ca^{2+} ions of dissolved carbonate minerals, which were corroded during methanogenesis, reacted with dissolved CO_2 of the formation water. Homogeneous/blocky calcite (Cc III) precipitated and formed strongly cemented low permeable zones near the GWC.

6. References

Aberer, F. (1958): Die Molassezone im westlichen Oberösterreich und in Salzburg. Mitteilungen der Geologischen Gesellschaft in Wien, 50, 23-93.

Aharon, P. (2000): Microbial processes and products fueled by hydrocarbons at submarine seeps. In: Riding, R.E., Awramik, S.M. (Eds.) Microbial Sediments. Springer, Berlin, 270-281.

Ali, S.A., Clark, W.J., Moore, W.R, Dribus, J.R. (2010): Diagenesis and Reservoir Quality. Oilfield Review, 22, 2, 14-27.

Allan, J.R., Wiggins, W.D. (1993): Dolomite reservoirs: Geochemical Techniques for Evaluating Origin and Distribution. AAPG Continuing Education Course Note Series, 36, 170p.

Amieux, P. (1982): La cathodoluminescence: methode d´etude sedimentologique des carbonates. Bulletin des Centres de Recherche Exploration-Production Elf-Aquitaine, Pau, 6, 2, 437-483.

Andrews, J. N., Goldbrunner, J. E., Darling, W. G. & Youngman, M. J. (1987): The Geochemistry of Formation Waters in the Molasse basin of Upper Austria. - Environmental Geological Water Sciences, 10, 43-57.

Appelo, C.A.J., Postma, D. (2005): Geochemistry, Groundwater and Pollution. Balkema Publisher, Amsterdam, 2nd edition, 668p.

Bachmann, G., Müller, M., Weggen, K. (1987): Evolution of the Molasse Basin (Germany, Switzerland). Tectonophysics, 137, 77-92.

Bahlburg, H., Breitkreuz, C. (2004): Grundlagen der Geologie. Spektrum Akademischer Verlag; Auflage: 2. Auflage, 403p.

Bechtel, A., Gratzer, R., Linzer, H.-G., Sachsenhofer, R.F. (2013): Influence of migration distance, maturity and facies on the stable isotopic composition of alkanes and on carbazole distributions in oils and source rocks of the Alpine Foreland Basin of Austria: Organic Geochemistry, 62, 74-85.

Belaed, S. (2007): Charakterisierung potenzieller Muttergesteine für biogenes Erdgas in der österreichischen Molassezone. Diploma thesis, Technical University of Clausthal, Germany, 96p.

Bernard, B.B., Brooks, J.M. Sackett, W.M. (1976): Natural gas seepage in the Gulf of Mexico. Earth and Planetary Letters, 31, 48-54.

Bernard, B.B., Brooks, J.M., Sackett, W.M. (1978): Light hydrocarbons in recent Texas continental shelf and slope sediments: Journal of Geophysical Research, 83, 4053-4061.

Berner, R.A. (1981): A new geochemical classification of sedimentary environments. Journal of Sedimentary Petrology, 51, 359-365.

Bjørkum, P.A., Walderhaug, O. (1990): Geometrical arrangement of calcite-cemented layer within shallow marine sandstones. Earth Sciences Reviews, 29, 145-161.

Bjørkum, P.A., Mjøs, R., Walderhaug, O, Hurst, A. (1990): The role of the late Cimmerian unconformity for the distribution of kaolinite in the Gullfaks Field, northern North Sea. Sedimentology 37, 396-406.

Bjørkum, P.A., Walderhaug, O., 1990. Geometrical arrangement of calcite-cemented layer within shallow marine sandstones. Earth Sciences Reviews, 29, 145-161.

Bjørlykke, K. (1983): Diagenetic reactions in sandstones. In: Parker, A., Sellwood, B.W. (Eds.) Sediment Diagenesis. Reidel Publishing Company, NATO ASI Series, 169-213.

Bjørlykke, K. (2014): Relationships between depositional environments, burial history and rock properties. Some Principal aspects of diagenetic processes in sedimentary basins. Sedimentary Geology, 301, 1-14.

Bjørlykke, K., Brendsdal, A. (1986): Diagenesis in the Brent sandstone in the Statfiord field, North Sea. In: Gautier, D. (Ed.), Roles of Organic Matter in Sediment Diagenesis, SEPM Special Publication, 38, 157-167.

Bjørlykke, K., Egenberg, P.K. (1993): Quartz Cementation in Sedimentary Basins. AAPG Bulletin, 77, 1538-1548.

Bjørlykke, K., Ramm, M., Saigal, G.C. (1989): Sandstone diagenesis and porosity modification during basin evolution. Geologische Rundschau, 78, 1, 243-268.

Blatt, H., Middelton, G., Murray, R. (1980): Origin of Sedimentary Rocks. Prentice Hall, Englewood Cliffs, 2nd edition, 782p.

Boles. J.R., Franks, S.G. (1979): Clay diagenesis in Wilcox sandstones of southwest Texas; implications of smectite diagenesis on sandstone diagenesis. Journal of Sedimentary Research, 49, 55-70.

Borowski, K. (2006): Lithofacies and depositional environment of the Upper Hall Formation, Alpine Molasse basin, Upper Austria: Diploma thesis, Technical University Bergakademie Freiberg, Germany, 126p.

Bottig, M. (2008): Diagenetische Umwandlungen in Sandsteinen der gasgesättigten, der sekundär verwässerten, der Wasser-, und der Übergangszone des Erdgas – Speichers Haidach in der Molasse Zone, Österreich. Diploma thesis, University of Vienna, Austria, 80p.

Bottig, M., Gier, S., Jilg, W. (2016): Artificially induced clay mineral authigenesis in an underground gas storage field, North Alpine Foreland Basin, Austria. AAPG Bulletin.

Braumüller, E. (1961): Die paläogeographische Entwicklung des Molassebeckens in Oberösterreich und Salzburg. Erdöl-Erdgas Zeitschrift, 77, 509-521.

Brenner, R.L., Ludvigson, G.A., Scal, R., Dogan, A.U. (1991): Diagenetic modeling of siliciclastic systems: Status report. Kansas Geological Survey, Bulletin, 233, 123-137.

Brindley, G.W. (1980): Quantitative X-ray mineral analysis of clays. In: Brindley, G.W., Brown, G. (Eds.) Crystal Structures of Clay Minerals and their X-ray Identification, Mineralogical Society, London, 411-438.

Brix, F., Schultz, O. (1993): Erdöl und Erdgas in Österreich. Veröffentlichungen aus dem Naturhistorischen Museum Wien, 2nd edition, Vienna, 19, 24, 688 p.

Campbell, K.A., Francis, D.A., Collins, M., Gregory, M.R., Nelson, C.S., Greinert, J., Aharon, P. (2008): Hydrocarbon seep-carbonates of a Miocene forearc (East Coast Basin), North Island, New Zealand. Sedimentary Geology, 204, 3-4, 83-105.

Carvalho, M.V., De Ros, L.F., Gomes, N.S. (1995): Carbonate cementation patterns and diagenetic reservoir facies in the Campos Basin Cretaceous turbidites, offshore eastern Brazil. Marine and Petroleum Geology, 12, 741-758.

Chan, M.A., Parry, W.T., Bowman, J.R. (2000): Diagenetic Hematite and Manganese Oxides and Fault-Related Fluid Flow in Jurassic Sandstones, Southeastern Utah. AAPG Bulletin, 84, 9, 1281-1310.

Chien, C.W., Huang, C.Y., Chen, Z., Lee, H.C., Harris, R. (2012): Miocene shallow-marine cold seep carbonate on fold-and thrust Western Foothills, SW Taiwan. Journal of Asian Earth Sciences, 56, 200-211.

Chilingarian, G.V., Wolf, K.H. (1994): Diagenesis, IV (Developments in Sedimentology). Elsevier Science Ltd, 1st edition, 546p.

Cicha, I., Rögl, F., Rupp, C., Ctyroká, J. (1998): Oligocene-Miocene foraminifera of the Central Paratethys. Abhandlungen der Senckenbergischen Naturforschenden Gesellschaft 549, 137-153.

Circone, S., Stern, L.A., Kirby, S.H., Durham, W.B., Chakoumakos, B.C., Rawn, C.J., Rondinone, A.J., Ishii, Y. (2003): CO2 Hydrate: Synthesis, Composition, Structure, Dissociation Behavior, and a Comparison to Structure I CH4 Hydrate. The Journal of Physical Chemistry, B 107, 5529-5539.

Claypool, G.E., Kaplan, I.R. (1974): The origin and distribution of methane in marine sediments. In: Kaplan, I. R. (Ed.) Natural Gases in Marine Sediments. Marine Sciences, 3, 99-140.

Claypool, G.E., Threlkeld, C.N. (1983): Anoxic diagenesis and methane generation in sediments of the Blake Outer Ridge, Deep Sea Drilling Project Site 533, Leg 76, in: Sheridan, R.E., Gradstein, F.M., et al. (Eds.), Initial Reports of the Deep Sea Drilling Project. U.S. Govt. Printing Office, Washington, 76, 391-402.

Coleman, D.D. (1976): Isotopic characterization of Illinois natural gas. PhD thesis, University Illinois, Urban-Champaign.

Choquette, P.W., Pray, L. (1970): Geologic nomenclature and classification of porosity in sedimentary carbonates. AAPG Bulletin, 54, 207-250.

Covault, J.A., Hubbard, S.M., Graham, S.A., Hinsch, R., Linzer, H.G.. (2009): Turbidite-reservoir architecture in complex wedge-top depocenters, Tertiary Molasse foreland basin. Marine and Petroleum Geology, 26, 379-396.

Curtis, C.D. (1978): Possible links between sandstone diagenesis and depth related geochemical relations occurring in enclosing mudstones. Journal Geological Society London, 135, 107-117.

Curtis, C.D., Petrowski, C., Oertl, G. (1972): Stable carbon isotope ratios within carbonate concretions: a clue to place and time of formation. Nature, 235, 98-100.

Curtis, C.D., Burns, R.G., Smith, J.V. (1977): Sedimentary geochemistry: environments and processes dominated by involvement of an aqueous phase (and discussion). Philosophical Transactions of the Royal Society of London, Series A, Mathematical and Physical Sciences, 286, 353-372.

Davis, M.C., Wesolowski, D.J., Rosenqvist, J., Brantley, S.L., Mueller, K.T. (2011): Solubility and near-equilibrium dissolution rates of quartz in dilute NaCl solutions at 398–473 K under alkaline conditions. Geochimica et Cosmochimica Acta, 75, 401-415.

De Ruig, M.J., (2003): Austria: New Insights from 3D Seismic Data: Deep marine sedimentation and gas reservoir distribution in Upper Austria. Oil Gas European Magazine, 29, 64-73.

De Ruig, M.J., Hubbard, S.M. (2006): Seismic facies and reservoir characteristics of a deep - marine channel belt in the Molasse foreland basin, Puchkirchen Formation, Austria. American Association Petroleum Geologists Bulletin, 90, 735-752.

Devol, A.H. (1978): Bacterial oxygen uptake kinetics as related to biological processes in oxygen-deficient zones of the oceans. Deep-Sea Research, 25, 137–146.

Dimitrakopoulus, R., Muehlenbachs, K. (1987): Biodegradation of petroleum as a source of 13C-enriched carbon dioxide in the formation of carbonate cement. Chemical Geology, 65, 283-291.

Doose, P.R., Sandstrom, M.W., Jodele, R.Z., Kaplan I.R. (2007): 28. Interstitial Gas Analysis of Sediment Samples from Site 368 and Hole 369A, in: Gardner, J., Herring, J. (Eds.), Deep Sea Drilling Project Reports and Publications, 41, 861-863.

Doveton, J.H. (1994): Geologic log interpretation. SEPM Short Course, 29, 1-169.

Ehrenberg, S.N. (1993): Preservation of anomalously high porosity in deeply buried sandstones by grain-coating chlorite: Examples form the Norwegian continental shelf. AAPG Bulletin, 77, 1260-1286.

Einsele, G. (2000): Sedimentary Basins: Evolution, Facies, and Sediment Budget. Springer, 792p.

Flügel, E. (1978): Mikrofazielle Untersuchungsmethoden von Kalken, Springer, Berlin.

Flügel, E. (2010): Microfacies of Carbonate Rocks – Analysis, Interpretation and Application. Springer-Verlag Berlin Heidelberg, 984p.

Folk, R. L. (1974): Petrology of sedimentary rocks. Hemphill, Austin, 107p.

Fralick, P.W., Barrett, T J. (1995): Depositional controls on iron formation associations in Canada: Special Publications of the International Association of Sedimentologists, 22, 137-156.

Friedman, I., O´Neil, J.R. (1977): Compilation of stable isotope fractionation factors of geochemical interest. In: Fleischer, M. (Ed.) Data of Geochemistry, US Geological Survey Professional Paper, 440-KK.

Friedman, G.M., Sanders, J.E. (1978): Principles in Sedimentology. Wiley, 792p.

Froelich, P.N., Klinkhammer, G.P., Bender, M.L., Luedtke, N.A., Heath, G.R., Cullen, D., Dauphin, P., Hammond, D., Hartman, B., Maynard, V. (1979): Early oxidation of organic matter in pelagic sediments of the eastern equatorial Atlantic: suboxic diagenesis. Geochimica et Cosmochimica Acta, 43, 1075-1090.

Fu, Y. (2014): Development and Application of Numerical Modeling for Evaluating and Predicting Hydrogeochemical Processes Temporally and Spatially Evolving in Petroleum Reservoirs: Case Studies: Miller Oilfield (UK North Sea) and Siri Oilfield (Danish North Sea). Ph.D. thesis, Clausthal University of Technology, Germany, 213p.

Fu, Y., Van Berk, W., Schulz, H.M., Mu, N. (2015): Beritherine formation in reservoir rocks from the Siri oilfield (Danish North Sea) as result of fluid-rock interactions: Part II. Deciphering organic-inorganic processes by hydrogeochemical modeling. Marine and Petroleum Geology, 65, 317-326.

Füchtbauer, H. (1988): Sediment-Petrologie. Teil. II: Sedimente und Sedimentgesteine. Schweizerbart, Stuttgart, 1141p.

Gautier, D.L., Claypool, G.E. (1984): Interpretation of methanic diagenesis in ancient sediments by analogy with processes in modern diagenetic environments. AAPG Memoir, 37, 111-123.

Gier, S. (1999): Diagenese pelitischer Sedimente in der Molassezone Oberösterreichs. Mitteilungen der Österreichischen Mineralogsichen Gesellschaft, 144, 45-68.

Gier, S. (2000): Clay mineral and organic diagenesis of the Lower Oligocene Schöneck Fishshale, western Austrian Molasse Basin. Clay minerals, 35, 709-717.

Gier, S., Ottner, F., Johns, W.D. (1998): Layer-charge heterogeneity in smectites of I/S phases in pelitic sediments from the Molasse Basin, Austria. Clays and Clay Minerals, 46, 670-678.

Gluyas, J.G. (1983): The genesis and diagenesis of shale nodular limestone sequences. PhD. Thesis, University of Liverpool.

Gluyas, J.G. (1984): Early carbonate diagenesis within phanerozoic shales and sandstones the NW European shelf. Clay Minerals, 19, 309-321.

Gorenc, M.A., Chan, M.A. (2015): Hydrocarbon induced diagenetic alteration of the Permian White Rim Sandstone, Elaterite Basin, southeast Utah. American Association of Petroleum Geologists Bulletin, 99, 5, 807-829.

Gratzer, R., Bechtel, A., Sachsenhofer, R.F., Linzer, H.G., Reischenbacher, D., Schulz, H.M. (2011): Oil-oil and oil-source correlations in the Alpine Foreland Basin of Austria: Insights from biomarker and stable carbon isotope studies. Marine and Petroleum Geology, 28, 1171-1186.

Grosos, R. (2010): Sedimentology and Stratigraphy of deep-water Miocene deposits in the Molasse Basin, Upper Austria. Geological Society of America Annual Meeting, Meeting abstract, 42, 636.

Groß, D., Grundtner, M.L., Misch, D., Riedl, M., Sachsenhofer, R.F., Scheucher, L. (2015a): Diagenetic Evolution and Reservoir Quality of Sandstones in the North Alpine Foreland Basin: A Microscale Approach. Microscopy and Microanalysis, 21, 1123-1137.

Groß, D., Sachsenhofer, R.F., Rech, A., Sageder, St., Geissler, M., Schnitzer, St., Troiss, W. (2015b): The Trattnach Oil Field in the North Alpine Foreland Basin (Austria). Austrian Journal of Earth Sciences, 108, 2, 151-171.

Grundtner, M.L., Gross, D., Samsu, A.S., Linzer, H.G., Misch, D., Sachsenhofer, R.F., Scheucher, L., Schnitzer, S. (2016): Diagenesis in Cenomanian Clastic Reservoir Rocks of the Alpine Foreland Basin (Austria). 78th EAGE Conference and Exhibition 2016, Extended abstract, 31th May 2016, Vienna, Austria, Abstract.

Grunert, P., Harzhauser, M., Rögl, F., Sachsenhofer, R., Gratzer, R., Soliman A., Piller, W.E. (2010): Oceanographic conditions as a trigger for the formation of an Early Miocene (Aquitanian) Konservat-Lagerstätte in the central Paratethys Sea. Palaeogeography, Palaeoclimatology, Palaeoecology, 292, 425-442.

Grunert P., Soliman A., Ćorić, S., Roetzel R., Harzhauser M., Piller W.E. (2012): Facies development along the tide-influenced shelf of the Burdigalian Seaway: An example from the Ottnangian stratotype (Early Miocene, middle Burdigalian). Marine Micropaleontology, 84-85, 14-36.

Grunert, P., Hinsch, R., Sachsenhofer, R.F., Bechtel, A., Ćorić, S., Harzhauser, M., Piller, W.E., Sperl, H. (2013): Early Burdigalian infill of the Puchkirchen Trough (North Alpine Foreland Basin, Central Paratethys): facies development and sequence stratigraphy. Marine and Petroleum Geology, 39, 164-186.

Grunert, P., Auer, G., Harzhauser, M., Piller, W.E. (2015): Stratigraphic constraints for the Upper Oligocene to Lower Miocene Puchkirchen Group (North Alpine Foreland Basin, Central Paratethys). Newsletters on Stratigraphy, 48, 1, 111-133.

Gusterhuber, J., Dunkl, I., Hisch, R., Linzer, H.G., Sachsenhofer, R.F. (2012): Neogene uplift and erosion in the Alpine Foreland Basin (Upper Austria and Salzburg). Geologica Carpathica, 63, 295-305.

Gusterhuber, J., Hinsch, R., Linzer, H.G., Sachsenhofer, R.F. (2013): Hydrocarbon generation and migration from sub-thrust source rocks to foreland reservoirs. The Austrian Molasse Basin. Austrian Journal of Earth Sciences, 106, 115-136.

Gusterhuber, J., Hinsch, R., Sachsenhofer, R.F. (2014): Evaluation of hydrocarbon generation and migration in the Molasse fold and thrust belt (Central Eastern Alps, Austria) using structural and thermal basin models. American Association of Petroleum Geologists Bulletin, 98, 253-277.

Hammer, E., Mørk, M.B.E., Næss, A. (2010). Facies controls on the distribution of diagenesis and compaction in fluvial-deltaic deposits. Marine and Petroleum Geology, 27, 1737–1751.

Hesse R. (1986): Eogenesis pore-water/sediment interaction: modern offshore basins. Geosciences Canada, 13, 3, 165-196.

Hesse, R., (2003): Pore water anomalies of submarine gas-hydrate zones as tool to assess hydrate abundance and distribution in the subsurface: What have we learned in the past decade? Earth-Science Reviews, 61, 149-179.

Hesse, R. Schacht, U. (2011): Early Diagenesis of Deep-Sea Sediments. In: Hüneke, H., Mulder, Th. (Eds.): Developments in Sedimentology, 63, 557-713.

Hesse, R., Shah, J., Islam, S. (2004): Physical and chemical growth conditions of Ordovician organogenic deep-water dolomite concretions: implications for the d18O of Early Palaeozoic sea water. Sedimentology, 51, 601-625.

Hinsch, R. (2008): New Insights into the Oligocene to Miocene Geological Evolution of the Molasse Basin of Austria. Oil Gas European Magazin, 34, 138-143.

Hinsch, R. (2013): Laterally varying structure and kinematics of the Molasse fold and thrust belt of the Central Eastern Alps: Implications for exploration: AAPG Bulletin, 97, 1805-1831.

Hinsch, R. Hubbard, S., Kofler, N. (2007): Stratigraphic Trap Exploration in a Mature Basin: Examples for New Concepts from the Austrian Molasse Basin: OIL GAS European Magazine, 33 , 172–176.

Hoefs, J. (2009): Stable Isotope Geochemistry. Springer, 6th edition, Berlin Heidelberg, 286p.

Hoefs, J. (2015): Stable Isotope Geochemistry. Springer, 7th edition, Berlin Heidelberg, 389p.

Hoffman, J., Hower, J. (1979): Clay mineral assemblages as low grade metamorphic geothermometers: Application to the thrust faulted disturbed belt of Montana. In: Scholle, P.A., Schluger, P.S. (Eds.) Aspects of Diagenesis, Society for Sedimentary Geology, Special Publication, 26, 55-79.

Hower, J., Eslinger, E.V., Hower, M.E., Perry, E.A. (1976): Mechanism of burial metamorphism in argillaceous sediment: 1. Mineralogical and chemical evidence. American Geological Society Bulletin, 87, 725-737.

Hubbard, S.M., De Ruig, M.J., Graham, S.A. (2005): Utilizing outcrop analogs to improve subsurface mapping of natural gas-bearing strata in the Puchkirchen Formation, Molasse Basin, Upper Austria. Austrian Journal of Earth Sciences, 98, 52–66.

Hubbard, S.M., Graham, S.G., Weislogel, A., De Ruig, M.J., Wooden, J.L., (2006): Detrital zircon ages from the Molasse basin of Upper Austria: Insights into deep-water sedimentation in the Oligocene-Miocene Puchkirchen Formation. GSA Annual Meeting Abstracts with Programs, 38, 370p.

Hubbard, S.M., Romans, B.W., Graham, S.A. (2008): Deep-water foreland basin deposits of the Cerro Toro Formation, Magallanes basin, Chile: Architectural elements of a sinuous basin axial channel belt. Sedimentology, 55, 5, 1333–1359.

Hubbard, S.M., De Ruig, M.J., Graham, S.A. (2009): Confined channel-levee complex development in an elongate depo-center: Deepwater Tertiary strata of the Austrian Molasse Basin. Marine and Petroleum Geology 26, 85-112.

Hudson, J.D. (1982): Pyrite in ammonite-bearing shales from the Jurassic of England and Germany. Sedimentology, 29, 639-667.

Hurst, A., Irwin, H. (1982): Geological modelling of clay diagenesis in sandstones. Clay Mineralogy, 17, 5-22.

Inagaki, F., Hinrichs, K.-U., Kubo, Y., Bowles, M.W.,Heuer, V. B., Hong, W.-L., Hoshino, T., Ijiri, A., Imachi, H., Ito, M., Kaneko, M., Lever, M.A., Lin, Y.-S., Methé, B.A., Morita, S., Morono, Y., Tanikawa, W., Bihan, M., Bowden, S.A., Elvert, M., Glombitza, C., Gross, D., Harrington, G. J., Hori, T., Li, K., Limmer, D., Liu, C.-H., Murayama, M., Ohkouchi, N., Ono, S., Park, Y.-S., Phillips, S.C., Prieto-Mollar, X., Purkey, M., Riedinger, N., Sanada, Y., Sauvage, J., Snyder, G., Susilawati, R., Takano, Y., Tasumi, E., Terada, T., Tomaru, H., Trembath-Reichert, E., Wang, D. T., Yamada, Y. (2015): Exploring deep microbial life in coal-bearing sediment down to~2.5 km below the ocean floor. Science, 349, 420-424.

Irwin, H., Curtis, C.D., Coleman, M. (1977): Isotopic evidence for source of diagenetic carbonates formed during burial of organic-rich sediments. Nature, 269, 209-213.

Irwin, H., Hurst, A. (1983): Applications of geochemistry to sandstone reservoir studies. In: Brooks, J. (Ed.) Petroleum Geochemistry and Exploration of Europe. Geological Society Special Publication, 12, Blackwell, Oxford, 127-146.

JCPDS table (1974): Joint Committee for the Powder Diffraction Standards: Selected Powder Diffraction Data for Minerals. JCPDS, Pennsylvania. USA.

Janoschek, R.H. (1959): Oil Exploration in the Molasse Basin of Western Austria. Proceedings of the Fifth World Petroleum Congress, Sect. I, New York, 849-864.

Janoschek, R.H. (1966): Erdöl und Erdgas in Oberösterreich. Schätze aus Österreichs Boden, 70-72.

Jones, D.M., Head, I.M., Gray, N.D., Adams, J.J., Rowan, A.K., Aitken, C.M., Bennett, B., Hung, H., Brown, A., Bowler, B.F.J., Oldenburg, T., Erdmann, M., Larter, S.R. (2008):. Crude-oil biodegradation via methanogenesis in subsurface petroleum reservoirs. Nature, 451, 176-181.

Jørgensen, B.B., Kasten, S. (2006): Sulfur cycling and methane oxidation. In: Schulz H.D., Zabel, M. (Eds.), Marine Geochemistry, 271-310.

Kashik, S.A. (1965): Replacement of quartz by calcite in sedimentary rocks. Geochemistry International, 2, 133-138.

Kastner, M., Elderfield, H., Martin, J.B., Suess, E., Kvenvolden, K.A., Garrison, R.E. (1990): Diagenesis and interstitial water chemistry at the Peruvian continental margin-major constituents and strontium isotopes. In: Suess, E., Von Huene, R., et al. (Eds.), Peru Continental Margin Proceedings of the Ocean Drilling Program. Scientific Results, 112, 413-440.

Kerr, P.F. (1952): Formation and Occurrence of Clay Minerals. Clays and Clay Minerals, 1, 1, 19-32.

Kim, S.T., O'Neil, J.R. (1997): Equilibrium and nonequilibrium oxygen isotope effects in synthetic carbonates, Geochimica et Cosmochimica Acta, 61, 3461-3475.

Kollmann, K. (1977): Die Öl- und Gasexploration in der Molassezone Oberösterreichs und Salzburgs aus regionalgeologischer Sicht. Erdöl-Erdgas Zeitschrift, 93, 36-49.

Knauss, K.G., Wolery T.J. (1988): The dissolution kinetics of quartz as a function of pH and time at 70 C. Geochimica et Cosmochimica Acta, 52, 43-53.

Kraishan, G.M. (1997): Controls On Sandstone Reservoir Quality: Permian To Early Cretaceous Sequeneces, Barrow Sub-Basin, North West Shelf, Western Australia. Ph.D. thesis, University of Adelaide, Australia, 311p.

Kröll, A., Wagner, L., Wessely, G. and Zych, D. (2005): Molassezone Salzburg-Oberösterreich. Strukturkarte der Molassebasis 1:200 000. Geologische Bundesanstalt, Vienna.

Krumbein, W.C., Garrels, R.M. (1952): Origin and classification of chemical elements in terms of pH and oxidation-reduction potentials. Journal of Geology, 60, 1-33.

Kuhlemann, J., Kempf, O. (2002): Post-Eocene evolution of the North Alpine Foreland Basin and its response to Alpine tectonics. Sedimentary Geology 152, 45-78.

Landis, E.N., Keane, D.T. (2010): X-ray Microtomography. Materials Characterization, 61, 12, 1305-1316.

Lanson, B., Beaufort, D., Berger, G., Bauer, A., Cassagnabère, A., Meunier, A. (2002): Authigenic kaolin and illitic minerals during burial diagenesis of sandstones: a review. Clay Minerals, 37, 1-22.

Linzer, H.-G. (2001): Cyclic channel systems in the Molasse foreland basin of the Eastern Alps - The effects of late Oligocene foreland thrusting and early Miocene lateral escape (abs.). AAPG Bulletin, 85, 118.

Linzer, H.-G. (2002): Structural and stratigraphic traps in channel systems and intraslope basins of the deep-water Molasse foreland basin of the Alps: AAPG 2002 Annual Convention Abstracts, AAPG Search and Discovery article 90007.

Linzer, H.-G. (2009): Gas in imbricated channel systems of the foreland basin of the Eastern Alps (Austria): AAPG 2008 Annual Convention and Exhibition, San Antonio, Texas.

Linzer, H.G., Decker, K., Peresson, H., Dell'Mour, R., Frisch, W. (2002): Balancing lateral orogenic float of the eastern Alps. Tectonophysics, 354, 211-237.

Lonergan, M. & Derksen, R. (2007): South Slope Project Review. Unpublished internal proprietary report RAG, 51p.

Lundegard, P.D., Kharaka, Y.K., Rosenbauer, R.J. (1992): Petroleum as a potential diagenetic agent: Experimental evidence. In: Kharaka, Y.K., Maest, A.S. (Eds.) Proceedings of the 7th international symposium on water-rock interaction, 1, Low temperature environments, 7, 329-335.

Machel, H.G., Mountjoy, E.W. (1986): Chemistry and environments of dolomitisation-a reappraisal. Earth Science Review, 23, 175-222.

MacInnis, I.N., Brantley, S.L. (1992): The role of dislocations and surface morphology in calcite dissolution, Geochimica Cosmochimica Acta, 56, 1113–1126.

Maclean, L.C., Tyliszczak, T., Gilbert, P.U., Zhou, D., Pray, T.J., Onstott, T.C., Southam, G. (2008): A high-resolution chemical and structural study of framboidal pyrite formed within a low-temperature bacterial biofilm. Geobiology, 6, 471-480.

Malzer, O. (1981): Geologische Charakteristik der wichtigsten Erdöl- und Erdgasträger der oberösterreichischen Molasse: Teil 2: Die Konglomerate und Sandsteine des Oligozäns. Erdöl-Erdgas Zeitschrift, 97, 20-28.

Malzer, O. (1993): Molasse westlich und südwestlich der Böhmischen Masse, Oberösterreich. In: Brix, F. und Schulz O. (Eds.) Erdöl und Erdgas in Österreich. Veröffentlichungen naturhistorisches Museum Wien, 302-315.

Malzer, O, Rögl, F., Seifert, P., Wagner, L., Wessely, G., Brix, F. (1993): Die Molassezone und deren Untergrund. In: Brix, F. und Schulz O. (Eds.) Erdöl und Erdgas in Österreich. Veröffentlichungen naturhistorisches Museum Wien, 297-298.

Marshall, D.J. (1988): Cathodoluminescence of geological materials, Unwin Hyman, London, 146p.

Masalimova, L.U., Lowe, D.R, McHargue, T. Derksen, R. (2015): Interplay between an axial channel belt, slope gullies and overbank deposition in the Puchkirchen Formation in the Molasse Basin, Austria. Sedimentology, 62, 1717-1748.

Matter, A., Ramseyer, K. (1985): Cathodoluminescence petrography as a tool for provenance studies of sandstones. In: Zuffa, G.G. (Ed.) Provenance of Arenites, NATO ASI Series, 148, 191-211.

Mátyás, J. (1998): Carbonate Cements in the Tertiary Sandstones of the Swiss Molasse Basin: Relevance to Palaeohydrodynamic Reconstruction. In: Morad, S. (Ed.) Carbonate Cementation in Sandstones: Distribution Patterns and Geochemical Evolution. Special Publications international Association of Sedimentologists, 26, 141-162.

Mazurenko, L.L., Matveeva, T.V., Prasolov, E.M., Shoji, H., Obzhirov, A.I., Jin, Y.K., Poort, J., Logvina, E.A., Minami, H., Sakagami, H., Hachikubo, A., Salomatin, A.S., Salyuk, A.N., Prilepskiy, E.B., CHAOS 2003 Scientific Team (2009): Gas hydrate forming fluids on the NE Sakhalin slope, Sea of Okhotsk. Geological Society London Special Publications, 319, 51-72.

Meister, P., Gutjahr, M., Frank, M., Bernasconi, S.M., Vasconcelos, C., McKenzie, J.A., (2011): Dolomite formation within the methanogenetic zone induced by tectonically driven fluids in the Peru accretionary prism. Geology, 39, 563-566.

Meunier, A., El Albani, A. (2007): The glauconite-Fe-illite-Fe-smectite problem: a critical review. Terra Nova, 19, 95-104.

Milkov, A.V. (2011): Worldwide distribution and significance of secondary microbial methane formed during petroleum biodegradation in conventional reservoirs. Organic Geochemistry, 36, 299-310.

Moore, D.M., Reynolds, R.C., Jr. (1997): X-Ray Diffraction and the Identification and Analysis of Clay Minerals, Oxford University Press, New York, 2nd edition, 378p.

Morse J.W., Wang, Q. (1997): Pyrite formation under conditions approximating those in anoxic sediments: II. Influence of precursor iron minerals and organic matter. Marine Chemistry, 57, 187-193.

Nachtmann, W. (1989): Lagerstättengeologisches Modell des Obereozäns im Raum Sattledt (Oberösterreichische Molasse). Geologische Paläontologische Mitteilungen Innsbruck, 16, 213-227.

Nachtmann, W. (1995a): Bruchstrukturen und ihre Bedeutung für die Bildung von Kohlenwasserstoff-Fallen in der oberösterreichischen Molasse. Geol. Paläont. Mitt. Innsbruck, 20, 221-230.

Nachtmann, W. (1995b): Das Cenoman im Untergrund der oberösterreichischen Molasse – eine lagerstättengeologische Betrachtung. Zentralblatt für Paläontologie, I, 1, 2, 271-281.

Nachtmann, W., Wagner, L., (1987): Mesozoic and Early Tertiary evolution of the Alpine foreland in Upper Austria and Salzburg, Austria. Tectonophysics, 137, 61-76.

Nichols, G. (2009): Sedimentology and stratigraphy. Wiley-Blackwell 2nd edition, 432p.

Niebuhr, B., Hiss, M., Kaplan, U., Tröger, K.A., Voigt, S., Voigt, T., Wiese, F., Wilmsen, M. (2007): Lithostratigraphie der norddeutschen Oberkreide. Schriftreihe der Deutschen Gesellschaft für Geowissenschaften, 55, 1-136.

Niebuhr, B., Pürner, T., and Wilmsen, M. (2009): Lithostratigraphie der außeralpinen Kreide Bayerns. Schriftenreihe der Deutschen Gesellschaft für Geowissenschaften, 65, 7-58.

Nordstrom, D.K., Plummer, L.N., Wigley, T.M.L., Wolery, T.J., Ball, J.W., Jenne, E.A., Bassett, R.L., Crerar, D.A., Florence, T.M., Fritz, B., Hoffman, M., Holdren, G.R. Jr, Lafon, G.M., Mattigod, S.V., McDuff, R.E., Morel, F., Reddy, M.M., Sposito, G., Thrailkill, J. (1979): A comparison of computerized chemical models for equilibrium calculations in aqueous systems, in: Jenne, E.A. (Ed.), Chemical Modeling in Aqueous Systems, Speciation, Sorption, Solubility, and Kinetics. American Chemical Society 93, 857-892.

Pettijohn, F.J., Potter, P.E., Siever, R. (1987): Sand and sandstone, Springer, New York, 2nd edition, 553p.

Polesny, H. (1983): Verteilung der Öl- und Gasvorkommen in der oberösterreichischen Molasse. Erdöl-Erdgas-Zeitschrift, 99, 90-102.

Porrenga, D. H. (1967): Glauconite and chamosite as depth indicators in the marine environment. Marine Geology, 5, 495-501.

Prochnow, E.A., Remus, M.V.D., Ketzer J.M. (2006): Organic - inorganic interactions in oilfield sandstones: Examples from turbidite reservoirs in the Campos Basin, offshore eastern Brazil. Journal of Petroleum Geology, 29, 4, 361-380.

Pytlak, L., Gross, D., Sachsenhofer, R.F., Bechtel, A., Gratzer, R., Linzer, H.-G. (2016): Generation, mixing and alteration of thermogenic and microbial gas in oil deposits: The case of the Alpine Foreland Basin (Austria). Marine and Petroleum Geology.

Pytlak, L., Gross, D., Sachsenhofer, R.F., Bechtel, A., Gratzer, R., Linzer, H.-G. (in press): Gas accumulations in Oligocene-Miocene reservoirs in the Alpine Foreland Basin (Austria): Evidence for gas mixing and gas degradation. Journal of Earth Sciences.

Rasser, M.W. (2000): Coralline red algal limestones of the late Eocene Alpine Foreland basin in Upper Austria: component analysis, Facies and Palecology. Facies, 42, 59-92.

Rasser, M.W. & Piller, W.E. (2004): Crustose algal frameworks from the Eocene Alpine Foreland. Paleogeography, Paleoclimatology, Paleoecology, 206, 21–39.

Rech, A. (2011): Log-facies and log-correlation of Upper Cretaceous sediments in the Molasse Basin (Upper Austria). Diploma thesis, University of Leoben, Austria, 124p.

Reischenbacher, D., Sachsenhofer, R.F. (2011): Entstehung von Erdgas in der oberösterreichischen Molassezone: Daten und offene Fragen. Berg- und Hüttenmännische Monatshefte, 156, 455-460.

Rhoads, D.C, Morse, J.W. (1971): Evolutionary and ecologic significance of oxygen-deficient marine basins, Lethaia, 4, 413-428.

Rickard, D., Schoonen, M.A.A., Luther III, GW. (1995): Chemistry of iron sulfides in sedimentary environments. In: Vairavamurthy, M.A., Schoonen, M.A.A. (Eds.) Geochemical Transformations of Sedimentary Sulfur. American Chemical Society Symposium Series, 612, 168-193.

Rickard, D. (1997): Kinetics of pyrite formation by the H2S oxidation of iron (II) monosulfide in aqueous solutions between 25 and 125 °C: the rate equation. Geochimica et Cosmochimica Acta, 61, 115-134.

Robinson, D., Zimmer, W. (1989): Seismicstratigraphy of late Oligocene Puchkirchen Formation of Upper Austria. Geologische Rundschau, 78, 49-79.

Rodriguez, N.M., Paull, C.K., Borowski, W.S. (2000): Zonation of authigenic carbonates within gas hydrate-bearing sedimentary sections on the Blake Ridge: Offshore southeastern North America, in: Paull, C.K., Matsumoto, R., Wallace, P.J., Dillon, W.P. (Eds.), Proceedings of the Ocean Drilling Program. Scientific Results, 164, 301-312.

Röder, D., Bachmann, G. (1996): Evolution, structure and petroleum geology of the German Molasse Basin. In: Ziegler, P., Horvath, F. (Eds.) Peri-Tethys Memoir 2, Structure and Prospects of Alpine Basins and Forelands. Mèmoire du Museum National d´Histoire naturelle, 170, 263-284.

Rögl, F., Hochuli, P., Muller, C. (1979): Oligocene-Early Miocene stratigraphic correlations in the Molasse Basin of Austria. Annales Geologiques des Pays Helleniques, Tome hors series, 1045-1050.

Rosenfeld, W.M., Silverman, S.R. (1959): Carbon isotope fractionation in the bacterial production of methane. Science, 130, 1658-1659.

Ryan, J.N., Gschwend, P.M. (1992): Effect of iron diagenesis on the transport of clay colloids in an unconfined sand aquifer. Geochimica et Cosmochimica Acta, 56, 1507-1522.

Sachsenhofer, R.F., Gratzer, R., Tschelaut, W., Bechtel, A. (2006): Characterization of non-producible oil in Eocene reservoir sandstones (Bad Hall Nord field, Alpine Foreland Basin, Austria). Marine and Petroleum Geology, 23, 1, 1-15.

Sachsenhofer, R.F., Schulz, H.M. (2006): Architecture of Lower Oligocene source rocks in the Alpine Foreland Basin: a model for syn- and post-depositional source-rock features in the Paratethyan realm. Petroleum Geoscience, 12, 363-377.

Sachsenhofer, R.F., Leitner, B., Linzer, H.G., Bechtel, A., Coric, S., Gratzer, R., Reischenbacher, D., Soliman, A. (2010): Deposition, erosion and hydrocarbon source potential of the Oligocene Eggerding Formation (Molasse Basin, Austria). Austrian Journal of Earth Sciences, 103, 1, 76-99.

Samsu, A. (2015): Final report Cenomanian. Unpublished internal proprietary report RAG, 18p.

Scheucher, L.E.A., Vortisch, W., Sachsenhofer, R.F. (2012): Petrographie und Diagenese rupelischer Siliziklastika der Bohrungen Mühlreith 3b, Mühlreith 3c und Weissenkirchen 1. Unpublished internal proprietary report RAG, 27p.

Schmidt, F., Erdogan, L.T. (1996): Palaeohydrodynamics in exploration. In: Wessely G., Liebl W. (Eds.) Oil and gas in Alpidic thrust belts and basins of central and eastern Europe. European Association of Geoscientists and Engineers Special Publication, 5, 255-265.

Schnitzer, St. (2013): Sedimentary environment, diagenesis and reservoir properties of the Cenomanian greensandstones of the Molasse zone in Upper Austria. Unpublished internal proprietary report RAG, 377p.

Schnitzer, St., Bieg, U., Sachsenhofer, R.F. (2012): The Regensburg Formation (Cenomanian) in the Molasse Basin in Upper Austria. 29th IAS Meeting of Sedimentology: Sedimentology in the Heart of the Alps: 10th - 13th September 2012 Schladming, Austria: Third Circular, Programme, 379.

Schoell, M. (1977): Die Erdgase der süddeutschen Molasse – Anwendung von D/H- und 13C/12C-Isotopenanalysen zur Klärung ihrer Entstehung. Erdöl, Erdgas Zeitung, 93, 311-322.

Schoonen, M.A.A. (2004): Mechanisms of sedimentary pyrite formation. Geological Society of America, Special Papers, 379, 117-134.

Schultz, L. G. (1964): Quantitative interpretation of mineralogical composition from X-ray and chemical data for the Pierre shale. US Geol. Survey Prof Paper 391-C. Washington.

Schulz, H.M. (2003): Die westliche Zentral-Paratethys an der Wende Eozän/Oligozän - Ozeanographie eines Randmeeres und Bildung von Erdölmuttergesteinen. Habilitation thesis, Clausthal University of Technology, Germany.

Schulz, H.M., Sachsenhofer, R.F., Bechtel, A., Polesny, H., Wagner, L. (2002): The origin of hydrocarbon source rocks in the Austrian Molasse Basin (Eocene-Oligocene transition). Marine and Petroleum Geology, 19, 683-709.

Schulz, H.M., Bechtel, A., Rainer, T., Sachsenhofer, R.F., Struck, U. (2004): Paleoceanography of the western Central Paratethys during Early Oligocene nannoplankton Zone NP23 in the Austian Molasse Basin. Geologica Carpathica, 55, 311-323.

Schulz, H.M., Bechtel, A., Sachsenhofer, R.F. (2005): The birth of the Paratethys during the Early Oligocene: From Tethys to an ancient Black Sea analogue? Global and Planetary Change, 49, 163-176.

Schulz, H.M., Van Berk, W., Bechtel, A., Struck, U., Faber, E. (2009): Bacterial methane in the Atzbach-Schwanenstadt gas field (Upper Austrian Molasse Basin), Part I: Geology. Marine and Petroleum Geology, 26, 1163-1179.

Schulz, H.M., Van Berk, W. (2009): Bacterial methane in the Atzbach-Schwanenstadt gas field (upper Austrian Molasse Basin), Part II: Retracing gas generation and filling history by mass balancing of organic carbon conversion applying hydrogeochemical modelling. Marine and Petroleum Geology, 26, 1180-1189.

Selley, R.C. (1998): Elements of Petroleum Geology. Gulf Professional Publishing, 2nd edition, 470p.

Selley, R.C. (2000): Applied Sedimentology. Academic Press, 2nd edition, 523p.

Senes, J., Marinescu, F. (1974): Cartes paléogéographiques du Neogene de la Paratethys centrale. Mémoire de Bureau de Recherches Géologiques et Minières, 78, 785-792.

Sissingh, W. (1997): Tectonostratigraphy of the North Alpine Foreland Basin: correlation of Tertiary depositional cycles and orogenic phases. Tectonophysics, 282, 223-256.

Slatt, R.M. (2006): Stratigraphic reservoir characterization for petroleum geologists, geophysicists, and engineers, Elsevier Publication Company, 2nd edition, 492p.

Sommer, S.E. (1972): Cathodoluminescence of carbonates. I. Characterization of cathodoluminescence from carbonate solid solutions. Chemical Geology, 9, 257-273.

Stahl, W. (1975). Kohlenstoff-Isotopenverhältnisse von Erdgasen – Reifekennzeichen ihrer Muttersubstanzen. Erdöl und Kohle, Erdgas, Petrochemie, 28, 188-191.

Stosch, H.G. (1999): Einführung in die Isotopengeochemie. Vorlesungsskript, 226p.

Strauss, C. (2008): Lithofacies, Depositional Environment, Stratigraphic Architecture and Hydrocarbon Prospectivity of the Hall Formation within the NW-Austrian Molasse Trough. Unpublished internal proprietary report RAG, 72p.

Stright, L. & Bernhard, A. (2007): Validating lithofacies in well logs and seismic data using core from Puchkirchen deep-water channel belt deposits in the Molasse Basin. Upper Austria. Stanford Project on Deep-water Depositional Systems(SPODDS), 15 (proprietary report).

Süss, M.P., Strauss, C., Hinsch, R. (2008): Sequence Stratigraphy and depositional dynamics of the Puchkirchen basin (Upper Austria). Unpublished internal proprietary report RAG, 28p.

Surdam, R.C., Crossey, L.J., Hagen, E.S., Heasler, H.P. (1989): Organic-inorganic interactions and sandstone diagenesis. AAPG Bulletin, 73, 1-23.

Swart, P.K., Wortmann, U.G., Mitterer, R.M., Malone, M.J., Smart, P.L., Feary, D.A., Hine, A.C. (2000): Hydrogen-sulfide rich hydrates and saline fluids in the continental margin of South Australia. Geology, 28, 1039-1042.

Tucker, M.E. (1985): Einführung in die Sedimentpetrologie. Ferdinand Enke Verlag, Stuttgart, 265p.

Tucker, M.E. (1996): Methoden der Sedimentologie. Ferdinand Enke Verlag, Stuttgart, 366p.

Tukey, J.W., 1977. Exploratory Data Analysis, Addison-Wesley, Boston.

Ulmer-Scholle, D.S., Scholle, P.A, Schieber, J. Raine, R.J. (2014): A color guide to the Petrography of Sandstones, Siltstones, Shales and Associated Rocks. AAPG Memoir, 109, 526p.

Van Berk, W., Schulz, H.M., Fu, Y. (2009): Hydrogeochemical modelling of CO2 equilibria and mass transfer induced by organic–inorganic interactions in siliciclastic petroleum reservoirs. Geofluids, 9, 253-262.

Van Berk, W., Schulz, H.M., Fu, Y. (2013): Controls on CO2 fate and behavior in the Gullfaks oilfield (Norway): how hydrogeochemical modeling can help decipher organic-inorganic interactions. AAPG Bulletin, 97, 2233-2255.

Van Berk, W., Schulz, H.M. (2015): B1-02 Rock and Fluids Properties and Interactions in Hydrocarbon Systems. GeoBerlin, Annual Meeting of DGGV and DMG, 4-7 October 2015, Berlin.

Velde, B. (1984): Transformation of clay minerals. In: Duran, B. (Ed.) Thermal phenomena in sedimentary basins. International Collequim Bordeaux, June 7-10 1983, 11-116.Veron, J. (2005): The Alpine Molasse Basin – Review of Petroleum Geology and Remaining Potential. Bulletin für angewandte Geologie, 10, 1, 75-86.

Veron, J. (2005): The Alpine Molasse Basin – Review of Petroleum Geology and Remaining Potential. Bulletin angewandte Geologie , 10, 1, 75-86.

Wagner, L.R. (1980): Geologische Charakteristik der wichtigsten Erdöl- und Erdgasträger der oberösterreichischen Molasse, Teil I: Die Sandsteine des Obereozän. Erdoel-Erdgas-Zeitschrift, 96, 338-346.

Wagner, L.R. (1996): Stratigraphy and hydrocarbons in the Upper Austrian Molasse Foredeep (active margin). In: Wessely G., Liebl W. (Eds.) Oil and gas in Alpidic thrust belts and basins of central and eastern Europe. European Association of Geoscientists and Engineers Special Publication, 5, 217-235.

Wagner, L.R. (1998): Tectono-stratigraphy and hydrocarbons in the Molasse Foredeep of Salzburg, Upper and Lower Austria. In: Mascle, A., Puifdefábregas, C., Luterbacher, H.P., Fernández, M. (Eds.) Cenozoic Foreland Basins of Western Europe. Geological Society Special Publications, 134, 339-369.

Walderhaug, O. (1994): Precipitation rates for quartz cement in sandstones determined by fluid-inclusion microthermometry and temperature-history modeling: Journal of Sedimentary Research, 64, 324–333.

Walderhaug, O. (2000): Modeling quartz cementation and porosity in Middle Jurassic Brent Group sandstones of the Kvitebjørn field, northern North Sea: American Association of Petroleum Geologists, Bulletin, 84, 1325–1339.

Walderhaug, O., Bjørkum, P.A. (1998): Calcite cement in shallow marine sandstones: growth mechanisms and geometry, in: Morad, S. (Ed.), Carbonate Cementation in Sandstones: Distribution Patterns and Geochemical Evolution. International Association of Sedimentologists, Special Publication, 26, 179-192.

Wallmann, K., Aloisi, G., Haeckl, M., Tishcenko, P., Pavlova, G., Greinert, J., Kutterolf, S., Eisenhauer, A. (2008): Silicate weathering in anoxic marine sediments. Geochimica et Cosmochimica Acta, 72, 3067-3090.

Watson, R.S., Trewin, N.H, Fallick, A.E. (1995): The formation of carbonate cements in the Forth and Balmoral Fields, northern North Sea: a case for biodegradation, carbonate cementation and oil leakage during early burial. Geological Society, London, Special Publications, 94, 177-200.

Weibel, R., Friis, H. (2004): Opaque minerals as keys for distinguishing oxidizing and reducing diagenetic conditions in the Lower Triassic Bunter Sandstone, North German Basin. Sedimentary Geology 169, 129-149.

Wessely, G., Schreiber, O.St., Fuchs, R. (1981): Lithofazies und Mikrostratigraphie der Mittel- und Oberkreide des Molasseuntergrundes im östlichen Oberösterreich. Jahrbuch der Geologischen Bundesanstalt, 124, 175-281.

Whiticar, M.J. (1993): Stable isotopes and global budgets. In: Khalil, M.A.K. (Ed.) Atmospheric Methane: Sources, Sinks, and Role in Global Change, NATO ASI Series I, Global Environmental Change, 13, 8, 138-67.

Whiticar, M.J. (1999): Carbon and hydrogen isotope systematics of bacterial formation and oxidation of methane. Chemical Geology, 161, 291–314.

Whiticar, M.J., Faber, E., Scheoll, M. (1986): Microbial methane formation in marine and freshwater environments: carbon dioxide reduction vs. acetate fermentation – isotope evidence: Geochimica et Cosmochimica Acta, 50, 693-709.

Wilkin, R.T., Barnes, H.L. (1997): Formation processes of framboidal pyrite. Geochimica et Cosmochimica Acta, 61, 323-339.

Wilson, M.J., Wilson, L., Patey, I. (2014): The influence of individual clay minerals on formation damage of reservoir sandstones: a critical review with some new insights. Clay Minerals, 49, 2, 147-164.

Worden, R.H., Burley, S.D. (2003): Sandstone Diagenesis: The Evolution of Sand to Stone. In: Burley S.D., Worden R.H. (Eds.) Sandstone Diagenesis: Recent and Ancient, International Association of Sedimentologists, 3-44.

Worden, R.H., Morad, S. (2003): Clay minerals in sandstones: controls on formation, distribution and evolution. Clay mineral cements in sandstones, 1-41.

Zeikus, J.G., Wolfe, R.S. (1972): Methanobacterium thermoautotrophicum sp. n., an anaerobic, autotrophic, extreme thermophile. Journal Bacteriological, 109, 707–713.

Zinkernagel, U. (1978): Cathodoluminescence of quartz and its application to sandstone petrography. Contributions Sedimentology, 8, 69p.

Zweigel, J. (1998): Eustatic versus tectonic control on foreland basin fill: Sequence stratigraphy, subsidence analysis, stratigraphic modelling and reservoir modelling applied to the German Molasse basin. Contribution to Sedimentary Geology, 20, 137-140.

Zymela, S. (1996): Carbon, Oxygen and Strontium isotopic composition of diagenetic calcite and siderite from the upper Cretaceous formation of Western Alberta, PhD thesis, McMaster University, Canada.

7. List of figures

8. Abbreviations

GWC = gas-water contact

OWC = oil-water contact

Eh = redox potential (pe)

TOC = total organic carbon

HI = hydrogen index

Ma = Million years

ka = thousand years

CE1 = Cenomanian 1 (equivalent to Bad Abbach Member)

CE 2 = Cenomanian 2 (equivalent to upper part of Saal Member

CE 3 = Cenomanian 3 (equivalent to lower part of Saal Member)

CL = cathodoluminescence

XRD = X-ray diffractometry

SEM = scanning electron microscopy

EMP = electron microscopy

BSE = back-scatter

CP = BSE image

WDX = wave-length dispersive

µCT = micro-computed tomography

Alb = albite

An = anorthite

Ank = ankerite

Bi = biotite

Cc = calcite

Cc I to Cc IV = calcite generations: Cc I oldest and Cc IV youngest

Cc_f = Calcite from fossil

Chl = chlorite

Dol = dolomite

Fsp = feldspar

Glc = glauconite

Grt = garnet

Hm = hematite

Ill = illite

K-Fsp = K-feldspar

Lith = lithic fragments

Mu = muscovite

Py = pyrite framboidal

Py* = pyrite idiomorphic

Qtz = quartz

Sid = siderite

Ø = porosity

9. Appendix

9.1. Representative pictures form investigated cores

Hall Formation (Lower Miocene)

Upper Puchkirchen Formation (Lower Miocene)

Upper Puchkirchen Formation at southern slope (Lower Miocene)

Lower Puchkirchen Formation (Upper Oligocene – Lower Miocene)

Ampfing Formation (Eocene)

Cerithian Beds (Eocene)

Voitsdorf Formation (Eocene)

9.2. Semi-quantitative analysis from point counting

Hall Formation (Lower Miocene)

Sample	Zone	Qtz_{mono}	Qtz_{poly}	Fsp	Lith	Clay min	Mica	Carb	Poro
A.2	gas-bearing	26.3	4.5	10.64	9.3	4.7	3.4	41.2	28.9
A.3	gas-bearing	27.2	4.3	9.82	4.9	6.8	4.1	42.9	18.9
B.1	gas-bearing	34.0	6.4	9.0	6.1	5.0	5.8	33.8	5.0
B.2	gas-bearing	34.1	7.1	7.9	10.0	3.7	5.1	32.2	6.7
B.3	gas-bearing	34.0	6.3	9.0	6.1	5.7	7.8	30.8	7.3
B.4	gas-bearing	27.7	10.2	8.0	9.1	0.7	1.3	43.0	3.8
C.2	gas-bearing	28.2	9.6	7.6	5.7	7.9	2.3	38.7	25.3
C.3	gas-bearing	32.6	12.0	6.9	9.8	4.2	4.0	30.6	18.0
C.4	gas-bearing	38.3	7.8	4.4	8.7	9.6	5.2	26.1	25.8
D.1	gas-bearing	27.0	10.1	8.2	11.2	8.2	11.2	26.1	3.6
D.3	gas-bearing	27.1	7.2	11.1	5.3	9.6	11.8	28.0	26.4
D.4	gas-bearing	30.8	3.0	5.6	5.6	9.9	14.9	30.3	10.1
D.5	gas-bearing	21.9	6.8	5.9	11.2	10.3	13.2	30.7	16.3
D.6	gas-bearing	25.8	10.3	6.5	9.7	9.7	13.9	24.3	23.1
E.1	gas-bearing	33.3	6.4	10.6	11.9	7.5	2.6	27.8	28.4
E.10	gas-bearing	27.0	10.0	12.1	13.9	9.1	5.7	22.4	29.0
E.2	gas-bearing	30.9	15.0	10.2	13.3	2.0	3.1	25.5	27.1
E.3	gas-bearing	28.1	9.1	9.3	12.4	2.2	3.5	35.4	27.5
E.4	gas-bearing	31.5	7.9	14.0	11.3	3.2	1.3	30.8	26.6
E.7	water-bearing	22.3	3.7	12.1	16.8	6.9	3.0	27.6	29.9
E.8	cemented	19.5	3.8	9.8	5.7	7.3	2.1	48.5	3.3
E.9	gas-bearing	24.9	6.8	15.2	13.0	13.3	1.9	25.0	28.9
F.1	cemented	25.0	5.3	4.1	5.3	5.9	4.2	49.9	6.4
F.2	gas-bearing	24.1	12.0	7.5	12.3	3.5	4.4	36.1	26.9
G.1	gas-bearing	21.3	2.6	6.69	3.9	12.7	4.6	48.3	5.3
H.3	water-bearing	32.3	2.6	14.54	4.4	3.7	4.7	37.8	1.7
H.4	water-bearing	28.5	5.7	10.36	7.3	5.7	4.3	38.2	0.3

Upper Puchkirchen Formation (Lower Miocene)

Sample	Zone	Qtz_{mono}	Qtz_{poly}	Fsp	Lith	Clay min	Mica	Carb	Poro
A.1	water-bearing	18.5	5.4	18.7	21.5	7.3	4.2	24.5	26.1
A.2	water-bearing	16.2	15.0	11.1	17.9	5.8	8.1	25.9	21.4
A.3	water-bearing	22.0	3.9	13.2	14.8	10.2	7.5	28.5	18.1
A.4	water-bearing	33.6	1.2	11.7	17.9	5.4	6.5	23.9	25.7
A.5	cemented	25.9	4.5	12.0	7.7	7.3	11.7	30.9	0.0
A.6	gas-bearing	28.6	11.0	9.0	14.9	11.9	9.0	15.7	20.7
A.7	gas-bearing	25.5	14.5	10.6	17.7	4.6	7.1	20.0	20.3
A.8	gas-bearing	24.4	7.9	6.0	10.8	8.0	7.1	35.9	24.8
A.9	gas-bearing	18.5	17.3	6.1	15.3	7.1	5.5	30.2	8.3
B.1	water-bearing	33.4	1.5	6.1	22.6	3.8	7.6	25.0	17.9
B.3	water-bearing	29.5	16.8	8.6	15.4	5.9	6.8	17.1	25.5
B.4	water-bearing	29.9	10.4	7.4	19.1	5.2	4.4	23.7	18.1
B.5	water-bearing	29.6	7.4	10.5	12.9	3.1	6.5	30.0	7.6
B.6	cemented	23.2	2.2	7.0	3.7	0.3	4.7	58.9	0.3
B.7	gas-bearing	17.9	10.8	6.8	9.8	9.4	12.8	32.5	2.1
B.8	gas-bearing	20.0	13.7	10.4	17.4	8.7	12.4	17.4	7.1
B.9	gas-bearing	13.2	19.5	12.6	20.4	10.9	4.6	18.9	5.6
C.4	gas-bearing	32.0	8.2	8.5	16.8	5.5	5.5	23.6	15.4
C.6	gas-bearing	35.4	10.2	9.0	12.0	5.9	4.6	23.1	25.0
C.7	gas-bearing	30.8	9.8	9.0	7.3	6.2	6.9	30.1	24.2
D.1	water-bearing	33.9	1.9	9.2	15.7	4.0	5.2	30.1	17.7
D.2	water-bearing	26.4	13.7	8.2	20.5	5.8	5.7	19.7	24.0
D.3	cemented	28.3	5.2	10.6	13.4	5.5	6.2	30.8	19.7
D.4	cemented	24.9	10.8	8.3	19.1	2.6	4.5	29.9	21.9
D.5	gas-bearing	34.0	5.0	8.6	9.6	7.7	9.8	25.0	3.1
D.6	gas-bearing	17.9	8.0	6.0	21.0	5.7	5.6	35.9	2.1
E.1	gas-bearing	29.7	7.5	9.3	7.0	6.8	6.0	12.9	20.8
F.2	gas-bearing	30.7	0	11.1	2.0	5.4	4.7	46.1	1.0

Upper Puchkirchen Formation at southern slope (Lower Miocene)

Sample	Zone	Qtz_{mono}	Qtz_{poly}	Fsp	Lith	Clay min	Mica	Carb	Poro
A.1	water-bearing	33.0	7.8	6.0	16.3	11.4	9.2	16.3	0.5
A.2	water-bearing	27.0	13.2	10.9	20.1	9.8	12.1	6.9	2.8
A.3	cemented	26.0	9.3	15.2	12.2	7.9	8.6	20.3	7.3
A.5	gas-bearing	32.6	7.6	7.2	18.8	17.1	13.7	2.9	17.1
A.6	gas-bearing	40.0	5.8	9.5	19.1	7.6	8.5	9.6	8.9
A.8	gas-bearing	15.9	15.9	3.6	25.4	10.9	7.3	21.0	11.5
B.1	/	14.2	6.2	3.7	41.0	12.6	11.2	11.1	0.0
B.2	/	15.2	6.5	7.3	42.7	5.6	5.3	17.5	0.0
B.3	water-bearing	10.0	4.9	9.6	51.7	11.0	12.1	0.8	22.8
B.5	cemented	10.0	1.1	0.4	40.6	9.9	18.7	19.3	0.0
B.6	cemented	11.6	0.0	3.4	49.2	7.7	11.1	17.0	23.3
B.7	cemented	20.4	5.2	4.8	49.3	4.0	4.3	12.1	0.6
B.9	cemented	12.1	1.0	3.1	53.5	8.1	7.4	14.9	20.8
B.10	/	11.6	8.3	6.8	44.1	9.2	10.2	9.8	14.6
C.a	water-bearing	18.2	12.2	7.6	47.9	5.6	2.0	6.5	19.3
C.b	water-bearing	15.7	12.0	9.0	39.9	13.3	5.0	5.0	18.9
C.c	water-bearing	9.3	8.2	7.0	50.9	15.5	4.9	4.2	17.8
C.d	water-bearing	12.3	9.6	0.7	47.4	12.5	0.7	16.8	7.0
C.e	water-bearing	20.1	13.0	13.8	33.9	10.2	3.8	5.3	11.7
C.f	cemented	9.1	0.3	2.5	57.8	6.3	3.8	20.8	8.0
C.h	gas-bearing	19.5	8.6	2.4	45.8	1.4	5.1	17.3	19.5
C.i	/	6.9	6.0	3.1	53.7	10.5	8.0	11.7	21.1
C.j	/	10.2	14.7	9.4	45.4	7.8	0.3	12.1	9.9
C.k	/	13.7	6.6	4.9	48.8	8.7	5.5	12.9	17.4
C.l	/	8.0	1.9	3.7	65.2	3.7	1.2	16.2	19.4
C.m	/	18.0	10.6	13.4	45.9	7.7	3.7	0.7	8.4
C.n	/	19.3	9.3	7.9	50.1	4.6	3.5	5.4	20.8
C.1	water-bearing	17.9	2.7	6.4	44.0	10.6	7.8	10.6	17.5
C.2	water-bearing	16.2	12.0	4.3	49.1	4.3	1.8	12.3	19.5
C.3	water-bearing	8.5	6.2	2.6	57.3	10.5	4.5	10.6	20.6
C.4	water-bearing	13.2	11.6	2.6	58.0	6.4	7.0	1.3	20.9

C.5	water-bearing	7.0	2.9	2.3	72.0	7.6	7.6	0.8	7.6
C.6	gas-bearing	7.3	8.2	4.1	57.4	9.5	3.4	10.1	16.9
C.7	gas-bearing	8.6	3.7	6.5	65.7	7.8	7.0	0.7	0.0

Lower Puchkirchen Formation (Upper Oligocene – Lower Miocene)

Sample	Zone	$\mathrm{Qtz}_{\mathrm{mono}}$	$\mathrm{Qtz}_{\mathrm{poly}}$	Fsp	Lith	Clay min	Mica	Carb	Poro
A.1	water-bearing	30.0	1.4	10.5	7.7	7.0	8.0	35.4	1.3
A.2	water-bearing	35.3	3.2	12.5	6.1	6.0	6.0	30.9	1.3
A.3	water-bearing	28.3	4.1	9.4	7.3	7.3	8.0	35.5	0.0

Ampfing Formation (Eocene)

Sample	Zone	$\mathrm{Qtz}_{\mathrm{mono}}$	$\mathrm{Qtz}_{\mathrm{poly}}$	Fsp	Lith	Clay min	Mica	Carb	Poro
A.1	oil-bearing	38.1	19.1	7.1	11.4	4.5	3.6	5.3	11.0
A.2	gas-bearing	39.2	17.4	8.5	5.8	1.7	7.7	2.5	17.3
B.1	gas-bearing	31.3	17.4	10.4	5.5	2.6	16.3	3.5	13.0
C.1	water-bearing	26.9	10.9	20.4	8.4	4.4	7.0	5.9	16.2
C.2	cemented	20.6	13.3	9.8	2.9	0.3	2.5	48.7	1.9
D.1	water-bearing	27.1	16.9	7.5	11.0	3.5	4.7	17.4	11.9
D.2	water-bearing	28.5	18.4	8.6	14.5	4.4	8.0	2.8	14.7
D.3	water-bearing	30.2	17.2	10.0	12.6	3.3	7.7	2.2	16.8
E.1	water-bearing	15.1	7.1	30.1	14.2	8.1	4.4	9.7	11.4
E.2	water-bearing	17.4	9.0	17.6	17.6	17.6	4.4	4.4	12.0
E.3	water-bearing	19.3	12.5	18.7	9.4	24.3	4.7	4.7	6.5
F.0	water-bearing	30.6	13.5	16.7	6.2	16.7	1.8	2.6	11.9
F.1	cemented	17.5	13.6	19.7	1.6	3.2	1.9	39.5	2.9
F.2	water-bearing	22.4	19.5	16.9	9.6	13.1	5.0	0.9	12.6
F.3	oil-bearing	25.9	12.1	12.7	4.2	16.9	4.2	8.4	15.6
F.4	water-bearing	20.3	16.1	19.0	5.2	34.1	2.7	1.0	1.6

Cerithian Beds (Eocene)

Sample	Zone	Qtz_{mono}	Qtz_{poly}	Fsp	Lith	Clay min	Mica	Carb	Poro
A.1	gas-bearing	28.4	12.8	19.3	10.0	2.9	3.4	6.7	16.4
A.2	gas-bearing	23.4	16.9	23.1	9.4	3.4	2.6	6.8	14.5

Voitsdorf Formation (Eocene)

Sample	Zone	Qtz_{mono}	Qtz_{poly}	Fsp	Lith	Clay min	Mica	Carb	Poro
A.1	oil-bearing	28.0	11.9	17.6	6.8	10.2	5.6	4.8	15.2
A.3	cemented	32.7	10.7	7.4	7.4	3.3	2.0	33.4	3.2
A.2	cemented	23.9	10.0	11.6	3.9	2.9	1.0	43.6	3.2
A.1Z	cemented	25.8	10.3	12.3	0.6	3.2	1.0	43.6	3.2

9.3. Semi-quantitative analysis from XRD

Hall Formation (Lower Miocene)

Sample	Zone	Qtz	Plag	KFsp	Cal	Dol	Ank	Sid	Py	Mic	Chl
A.1	gas-bearing	27.7	11.7	5.8	17.0	14.1	1.5	1.1	1.0	7.9	12.2
A.2	gas-bearing	24.2	12.0	6.9	17.2	16.3	1.6	0.7	1.0	7.5	12.6
A.3	gas-bearing	21.9	10.3	2.8	22.1	13.5	1.3	0.7	0.8	9.9	16.7
B.1	gas-bearing	31.7	6.3	3.1	30.6	7.9	0.8	0.6	0.9	9.1	8.9
B.2	gas-bearing	31.7	6.3	3.1	30.6	7.9	0.8	0.6	0.9	9.1	8.9
B.3	gas-bearing	35.5	15.5	2.4	8.7	11.5	0.8	0.9	0.9	14.4	9.4
B.4	gas-bearing	51.2	8.4	1.8	1.8	10.3	1.2	0.7	1.5	12.8	10.3
C.1	gas-bearing	36.2	7.4	4.6	9.5	10.8	7.0	0.5	0.9	10.4	12.7
C.2	gas-bearing	43.7	8.2	4.2	9.6	12.9	0.9	0.6	1.0	7.8	11.2
C.3	gas-bearing	49.2	5.8	4.2	13.4	6.2	0.9	0.7	1.0	8.1	10.4
C.4	gas-bearing	48.7	3.4	6.5	11.2	6.3	0.9	0.6	0.9	9.2	12.2
D.1	gas-bearing	17.0	9.5	2.2	13.7	21.1	0.8	3.8	0.8	17.5	13.5
D.2	gas-bearing	19.5	7.9	1.7	14.3	18.8	0.7	1.0	0.9	21.4	13.9
D.3	gas-bearing	30.2	7.5	1.0	7.2	12.4	1.1	1.0	0.9	22.8	16.0
D.4	gas-bearing	25.2	12.6	0.9	7.6	24.1	1.2	0.8	0.9	26.8	0.0
D.5	gas-bearing	24.3	5.0	2.3	17.1	8.8	0.5	1.3	1.3	22.9	16.4
D.6	gas-bearing	37.0	12.3	0.8	11.2	0.7	0.9	1.1	1.0	21.0	14.0
E.1	gas-bearing	44.2	8.1	3.3	11.9	11.8	0.8	0.9	0.8	8.0	10.3
E.2	gas-bearing	39.5	7.3	6.0	15.1	12.4	0.7	0.7	0.9	7.6	9.8
E.3	gas-bearing	41.1	7.6	4.8	14.1	13.5	1.0	0.5	0.8	7.2	9.4
E.4	gas-bearing	40.3	4.9	4.5	10.6	13.5	0.9	0.5	0.8	10.8	13.2
E.7	water-bearing	40.4	5.6	6.1	11.5	15.3	1.0	0.4	0.8	8.6	10.1
E.8	cemented	24.2	4.6	3.6	41.6	9.3	0.5	0.4	0.8	6.5	8.4
E.9	gas-bearing	31.7	10.4	4.8	9.8	14.2	1.2	1.9	0.9	10.7	14.3
E.10	gas-bearing	43.3	7.6	4.3	8.7	12.1	1.0	0.5	1.0	10.2	11.3
F.1	cemented	23.1	4.8	1.9	25.1	8.4	0.8	0.0	0.9	13.7	21.3
F.2	gas-bearing	32.5	10.2	4.2	14.3	11.8	1.2	0.7	0.8	12.1	12.1
G.1	gas-bearing	33.9	7.0	3.0	15.6	20.1	0.9	0.9	0.1	10.3	8.2

H.1	water-bearing	28.2	30.9	1.0	11.8	11.9	1.0	0.9	0.1	4.6	9.8
H.2	water-bearing	34.0	16.9	6.6	13.8	12.1	1.7	0.4	0.1	4.7	9.6
H.3	water-bearing	28.4	16.1	7.1	19.3	10.6	1.1	0.8	0.1	5.4	11.3
H.4	water-bearing	21.3	14.0	5.3	28.0	4.1	1.1	1.3	0.1	8.7	16.1

Upper Puchkirchen Formation (Lower Miocene)

Sample	Zone	Qtz	Plag	KFsp	Cal	Dol	Ank	Sid	Py	Mic	Chl
A.1	water-bearing	15.5	25.0	4.2	6.9	32.3	0.5	0.5	0.5	9.2	5.4
A.2	water-bearing	23.9	17.2	5.8	5.2	25.5	0.6	0.6	0.7	12.3	8.2
A.3	water-bearing	12.7	40.3	6.7	6.9	23.9	0.7	0.3	0.4	5.1	3.0
A.4	water-bearing	23.4	19.0	3.5	22.0	13.4	0.8	0.9	0.6	9.3	7.1
A.51	cemented	30.4	8.4	3.3	13.3	21.6	1.7	0.9	1.0	10.6	8.7
A.52	cemented	30.3	4.5	0.0	25.0	10.2	1.4	1.2	1.6	12.5	13.3
A.53	cemented	33.1	12.5	4.1	9.2	13.4	1.5	1.1	1.2	12.0	12.0
A.54	cemented	31.3	18.8	2.4	7.7	10.1	1.1	1.0	1.0	10.9	15.6
A.6	gas-bearing	33.1	7.1	2.1	3.8	14.8	1.5	0.8	0.8	19.6	16.4
A.7	gas-bearing	37.2	12.9	9.4	3.4	14.8	0.7	0.5	0.8	9.7	10.4
A.8	gas-bearing	28.5	6.7	0.9	17.9	9.2	1.2	0.9	1.2	14.7	18.8
A.9	gas-bearing	30.8	8.5	2.4	19.8	10.5	0.9	0.7	1.0	12.4	13.0
B.1	water-bearing	41.9	6.2	4.1	11.7	18.4	0.9	0.7	0.9	8.1	7.1
B.2	water-bearing	43.8	6.6	0.9	6.9	18.6	1.1	0.5	0.8	9.2	11.6
B.3	water-bearing	46.4	2.5	5.4	17.1	4.1	0.8	0.6	0.1	10.1	13.1
B.4	water-bearing	33.2	7.5	10.5	12.0	18.5	1.1	0.9	0.1	10.0	6.1
B.5	cemented	35.1	11.1	12.1	5.6	4.7	0.7	0.8	1.2	12.6	16.0
B.6	cemented	28.5	7.5	2.4	25.5	21.6	3.6	0.7	0.1	7.9	2.2
B.7	cemented	27.0	8.7	2.3	5.6	15.3	1.0	0.9	1.1	19.7	18.5
B.8	gas-bearing	51.2	8.9	3.3	4.3	1.1	1.1	0.4	1.2	12.9	15.6
B.9	gas-bearing	35.1	11.1	12.1	5.6	4.7	0.7	0.8	1.2	12.6	16.0
C.1	water-bearing	28.0	6.2	2.0	8.8	16.1	1.0	0.7	1.0	18.7	17.5
C.2	cemented	19.7	7.4	3.3	21.1	15.2	1.0	0.5	0.8	9.4	21.6
C.3	gas-bearing	19.7	7.4	3.3	21.1	15.2	1.0	0.5	0.8	9.4	21.6
C.4	gas-bearing	36.7	8.3	6.5	6.0	17.3	1.4	0.8	1.0	11.5	10.6

C.5	gas-bearing	32.9	9.1	3.3	5.6	15.0	1.2	0.6	0.9	16.3	15.3
C.6	gas-bearing	44.0	12.5	7.7	4.7	7.8	1.8	0.9	0.9	9.8	9.9
C.7	gas-bearing	37.1	8.5	4.9	4.0	21.5	1.1	0.9	0.9	11.1	10.0
C.8	gas-bearing	26.7	18.5	8.8	6.5	17.7	1.2	0.4	0.7	5.8	13.8
C.9	gas-bearing	31.3	4.8	14.5	9.1	15.0	1.1	0.5	0.7	9.1	13.9
C.10	gas-bearing	18.8	3.4	6.9	11.8	17.9	1.9	2.7	1.8	18.0	16.9
D.1	water-bearing	27.5	8.0	4.2	21.2	15.6	0.8	0.4	0.7	11.9	9.7
D.2	water-bearing	35.7	10.0	6.3	2.1	14.7	1.4	0.5	0.7	15.2	13.4
D.3	cemented	25.8	10.2	2.0	31.4	14.2	0.5	0.2	0.4	8.3	6.9
D.4	cemented	26.3	12.6	4.9	5.1	28.7	0.9	0.6	0.9	11.9	8.4
D.5	gas-bearing	28.5	6.7	0.9	17.9	9.2	1.2	0.9	1.2	14.7	18.8
D.6	gas-bearing	15.7	3.6	1.5	30.8	5.6	0.3	0.3	0.4	21.1	20.6
E.1	gas-bearing	41.2	7.9	13.9	3.2	15.2	0.8	1.2	0.1	8.0	8.5
F.1	gas-bearing	41.2	7.9	13.9	3.2	15.2	0.8	1.2	0.1	8.0	8.5
F.2	gas-bearing	20.0	5.7	6.8	42.0	0.5	0.4	0.3	0.1	13.3	10.8

Upper Puchkirchen Formation at southern slope (Lower Miocene)

Sample	Zone	Qtz	Plag	KFsp	Cal	Dol	Ank	Sid	Py	Mic	Chl
A.1	water-bear.	35.3	5.7	7.9	11.7	3.0	0.9	1.8	1.1	18.8	13.7
A.2	water- bear.	33.0	24.9	11.9	0.8	6.4	0.6	0.8	0.7	12.8	8.1
A.3	cemented	28.4	19.9	8.6	9.5	4.9	0.8	0.8	0.9	15.7	10.4
A.4	cemented	55.4	9.6	6.1	2.6	1.0	1.0	0.8	0.9	10.1	12.3
A.5	gas- bear.	50.2	3.6	9.5	0.5	0.8	1.1	0.8	0.9	17.0	15.6
A.6	gas- bear.	38.2	6.0	12.4	6.7	3.0	1.2	1.1	0.9	16.5	14.0
A.7	gas- bear.	21.8	3.1	7.9	9.4	8.2	0.9	1.1	1.5	25.2	20.7
A.8	gas-bearing	39.4	7.2	6.0	15.0	1.0	1.1	0.9	1.0	13.8	14.7
B.1	/	32.1	3.0	1.6	22.0	1.3	0.7	1.0	1.2	19.7	17.4
B.2	/	35.3	2.1	20.0	23.2	2.1	0.3	0.6	0.1	8.0	8.3
B.3	water- bear.	27.9	17.7	15.8	0.6	0.6	0.6	1.0	0.8	23.4	11.5
B.4	cemented	66.1	5.9	1.1	0.8	0.7	1.0	0.7	1.0	10.4	12.2
B.5	cemented	23.2	1.5	1.4	28.1	2.5	0.8	1.4	1.7	18.6	20.9
B.6	cemented	15.1	2.7	6.9	13.3	12.3	1.0	1.0	1.2	25.9	20.5

B.7	cemented	43.9	6.5	10.0	16.3	1.6	0.3	0.5	0.1	10.3	10.5
B.9	cemented	28.5	4.8	0.6	16.6	1.5	1.0	5.5	1.3	25.4	14.8
B.10	/	31.5	13.0	2.9	6.7	4.1	0.9	4.2	0.1	17.9	18.6
B.11	/	15.1	2.7	6.9	13.3	12.3	1.0	1.0	1.2	25.9	20.5
C.a	water- bear.	49.9	3.2	14.0	13.6	0.4	0.5	1.0	0.1	8.2	9.0
C.b	water- bear.	62.1	5.0	1.4	3.7	1.6	1.1	0.9	0.1	9.2	14.7
C.c	water- bear.	57.4	12.3	8.0	0.8	1.2	1.1	0.7	0.1	7.2	11.2
C.d	water- bear.	30.0	4.5	4.5	32.4	0.5	0.4	1.9	0.1	12.6	13.0
C.e	water- bear.	53.0	20.8	11.0	1.9	0.7	0.9	0.6	0.1	5.8	5.4
C.f	cemented	44.1	4.9	0.8	20.5	0.5	0.8	7.8	0.1	9.7	10.8
C.h	gas- bear.	52.3	4.6	1.0	22.9	0.5	0.8	2.2	0.1	6.8	8.9
C.i	/	52.5	3.0	2.0	13.6	0.5	1.2	6.1	0.1	10.2	10.6
C.j	/	51.8	7.1	10.2	12.7	0.3	0.9	3.1	0.1	6.3	7.5
C.k	/	40.0	6.9	3.4	27.1	0.5	0.5	1.2	0.1	10.1	10.1
C.l	/	47.1	3.2	5.4	21.1	0.8	0.6	0.5	0.1	10.4	10.7
C.m	/	56.6	23.9	8.3	0.9	0.8	0.9	0.5	0.1	3.7	4.4
C.n	/	66.5	11.5	10.0	1.6	0.7	0.9	0.5	0.1	3.9	4.3
C.o	/	39.0	4.3	13.2	20.7	0.7	1.8	2.3	0.1	7.8	10.2
C.1	water-bear. (sec.)	53.4	3.5	8.0	14.6	0.5	0.5	1.1	0.1	8.8	9.7
C.3	water-bear. (sec.)	57.3	3.3	6.4	15.6	3.5	0.6	1.1	0.1	5.6	6.6
C.4	water-bear. (sec.)	63.8	5.7	1.5	0.8	0.7	0.6	0.9	1.0	11.5	13.5
C.5	water-bear. (sec.)	63.8	5.7	1.5	0.8	0.7	0.6	0.9	1.0	11.5	13.5
C.6	gas-bearing (sec.)	56.4	10.2	0.9	3.0	0.8	1.0	0.5	1.1	11.3	14.9
C.7	/	56.4	10.2	0.9	3.0	0.8	1.0	0.5	1.1	11.3	14.9

Lower Puchkirchen Formation (Upper Oligocene – Lower Miocene)

Sample	Zone	Qtz	Plag	KFsp	Cal	Dol	Ank	Sid	Py	Mic	Chl
A.1	water-bearing	41.1	10.8	10.8	6.1	10.3	0.9	0.6	0.1	9.4	10.0
A.2	water-bearing	44.0	7.3	1.5	15.8	7.7	0.7	0.4	0.1	11.7	10.8
A.3	water-bearing	44.0	7.4	1.5	15.8	7.7	0.7	0.4	0.1	11.7	10.8
A.4	water-bearing	35.6	13.8	4.1	3.9	21.0	1.1	0.7	0.1	11.4	8.4

Ampfing Formation (Eocene)

Sample	Zone	Qtz	Plag	KFsp	Cal	Dol	Ank	Sid	Py	Mic	Kaol
A.1	oil-bearing	80.5	8.0	6.6	0.0	0.3	0.7	0.3	0.1	0.5	3.1
A.2	gas-bearing	71.4	10.4	4.3	0.3	0.6	0.6	0.5	0.1	1.5	10.5
B.1	gas-bearing	59.4	0.8	25.9	1.6	0.5	0.7	0.8	0.1	1.9	8.5
C.1	water-bearing	86.1	1.1	4.5	5.0	0.4	0.7	0.4	0.1	0.5	1.2
C.2	cemented	37.0	0.3	4.1	55.2	0.3	0.3	0.2	0.1	0.8	1.8
D.1	water-bearing	66.8	0.3	8.5	16.7	0.2	0.4	0.3	0.5	1.7	4.6
D.2	water-bearing	73.0	1.3	2.8	0.6	0.7	0.8	1.2	1.2	3.8	14.5
D.3	water-bearing	86.0	0.5	1.8	0.3	0.2	0.6	0.6	0.8	1.8	7.4
E.1	water-bearing	44.9	3.6	34.1	5.1	0.6	0.4	0.4	0.5	2.8	7.8
E.2	water-bearing	24.7	0.0	25.7	1.5	1.0	6.5	0.6	1.0	14.3	24.7
E.3	water-bearing	49.0	0.0	36.9	0.4	0.5	2.3	0.7	0.8	1.4	8.07
F.1	water-bearing	20.4	1.8	18.8	36.2	0.3	0.4	0.6	0.1	7.6	13.9
F.2	water-bearing	61.6	11.4	18.9	0.8	1.1	0.6	0.4	0.1	1.4	3.65
F.3	water-bearing	25.6	2.3	5.7	44.6	0.3	0.4	1.0	0.1	6.2	13.8
F.4	oil-bearing	57.4	5.45	19.3	1.4	0.8	0.4	0.6	1.0	2.3	10.6

Cerithian Beds (Eocene)

Sample	Zone	Qtz	Plag	KFsp	Cal	Dol	Ank	Sid	Py	Mic	Kaol
A.1	gas-bearing	62.5	0.2	18.6	3.0	0.9	0.3	0.7	0.1	0.0	13.8
A.2	gas-bearing	53.0	0.2	34.6	1.6	0.7	0.9	0.3	0.1	0.5	8.2

Voitsdorf Formation (Eocene)

Sample	Zone	Qtz	Plag	KFsp	Cal	Dol	Ank	Sid	Py	Mic	Kaol
A.1	oil-bearing	60.1	0.8	26.2	0.5	0.5	0.7	0.8	0.1	2.8	7.7
A.1-Z	cemented	13.5	0.0	13.5	43.1	0.6	2.5	1.2	0.1	5.5	20.0
A.2	cemented	15.4	0.19	6.4	53.3	0.4	0.2	0.4	0.1	5.0	18.6
A.3A	cemented	33.8	0.0	17.5	32.8	0.5	0.6	0.3	0.1	3.4	11.0
A.3B	cemented	7.1	0.0	2.1	68.8	5.4	1.2	5.0	0.1	2.4	7.8
A.3C	cemented	34.7	0.0	12.8	26.0	0.7	0.6	0.6	0.1	5.8	18.8

9.4. $\delta^{13}C$ and $\delta^{18}O$ values

Hall Formation (Lower Miocene)

Sample	Zone	$\delta^{13}C$ [VPDB]	$\delta^{18}O$ [VPDB]
A.1	gas-bearing	0.83	-5.90
A.2	gas-bearing	0.86	-6.48
A.3	gas-bearing	0.42	-6.47
B.1	gas-bearing	0.10	-7.22
B.2	gas-bearing	-0.19	-5.96
B.3	gas-bearing	0.96	-5.93
B.4	gas-bearing	-0.69	-7.04
C.1	gas-bearing	1.33	-3.77
C.2	gas-bearing	0.95	-4.27
C.3	gas-bearing	-0.19	-6.35
C.4	gas-bearing	0.22	-5.73
D.1	gas-bearing	0.31	-5.98
D.2	gas-bearing	0.09	-5.19
D.3	gas-bearing	0.61	-6.07
D.4	gas-bearing	1.20	-5.79
D.5	gas-bearing	0.71	-6.71
D.6	gas-bearing	0.68	-5.92
E.1	gas-bearing	1.05	-3.60
E.2	gas-bearing	0.33	-6.01
E.3	gas-bearing	1.25	-5.25
E.4	gas-bearing	1.04	-5.03
E.7	water-bearing	1.68	-4.47
E.8	cemented	0.05	-6.86
E.9	gas-bearing	1.24	-5.92
E.10	gas-bearing	1.17	-5.27
F.1	cemented	-0.38	-7.74
F.2	gas-bearing	0.81	-5.92
G.1	gas-bearing	0.48	-4.69
H.1	water-bearing	0.80	-4.99

H.2	water-bearing	0.72	-5.06
H.3	water-bearing	0.65	-5.70
H.4	cemented	-0.14	-7.09

Upper Puchkirchen Formation (Lower Miocene)

Sample	Zone	$\delta^{13}C$ [VPDB]	$\delta^{18}O$ [VPDB]
A.1	water-bearing	1.41	-3.37
A.2	water-bearing	1.57	-5.39
A.3	water-bearing	1.21	-5.31
A.4	water-bearing	1.83	-4.66
A.5a	cemented	0.87	-5.77
A.5b	cemented	1.04	-5.68
A.5c	cemented	0.96	-5.55
A.5d	cemented	1.10	-5.21
A.5e	cemented	0.77	-5.90
A.5f	cemented	0.59	-5.86
A.5g	cemented	0.58	-5.76
A.5h	cemented	0.25	-6.42
A.5i	cemented	-0.01	-6.94
A.5j	cemented	-0.16	-7.43
A.5k	cemented	-0.31	-7.46
A.5l	cemented	-0.05	-7.04
A.5m	cemented	-0.33	-7.51
A.5n	cemented	-0.14	-7.25
A.5o	cemented	-0.21	-7.54
A.5p	cemented	-0.05	-7.01
A.5q	cemented	0.02	-6.92
A.5r	cemented	0.04	-6.55
A.5s	cemented	0.44	-6.10
A.5t	cemented	1.07	-5.56
A.5u	cemented	1.26	-5.10
A.5v	cemented	1.15	-5.08

A.5w	cemented	1.18	-5.46
A.6	gas-bearing	0.91	-5.43
A.7	gas-bearing	1.86	-3.64
A.8a	gas-bearing	0.55	-5.92
A.8b	gas-bearing	-0.65	-7.74
A.8c	gas-bearing	-0.46	-7.96
A.8d	gas-bearing	-0.48	-7.86
A.8e	gas-bearing	-0.74	-8.24
A.8f	gas-bearing	-0.63	-8.03
A.8g	gas-bearing	-0.69	-8.06
A.8h	gas-bearing	-0.49	-7.96
A.8i	gas-bearing	-0.44	-7.62
A.8j	gas-bearing	-0.54	-7.67
A.8k	gas-bearing	-0.51	-7.50
A.8l	gas-bearing	-0.34	-7.50
A.8m	gas-bearing	-0.02	-7.18
A.8n	gas-bearing	0.84	-5.67
A.8o	gas-bearing	0.78	-5.76
A.8p	gas-bearing	1.32	-5.02
A.9	gas-bearing	0.52	-5.08
B.1	water-bearing	1.49	-4.41
B.2	water-bearing	1.48	-2.77
B.3	water-bearing	0.84	-3.27
B.4	water-bearing	0.49	-4.40
B.5	water-bearing	0.94	-4.58
B.6	cemented	-0.53	-6.18
B.7	gas-bearing	-1.39	-1.93
B.8	gas-bearing	1.19	-3.69
B.9	gas-bearing	0.87	-4.26
C.1	water-bearing	-1.40	-7.65
C.1	water-bearing	1.08	-5.12
C.2	cemented	0.60	-6.46
C.3	gas-bearing	1.82	-4.27

C.4	gas-bearing	0.05	-5.05
C.5	gas-bearing	0.12	-4.23
C.6	gas-bearing	0.55	-7.46
C.7	gas-bearing	0.10	-4.19
C.8	gas-bearing	1.45	-2.92
C.9	gas-bearing	0.07	-5.06
C.10	gas-bearing	0.08	-3.70
D.1	water-bearing	0.87	-6.03
D.2	water-bearing	2.18	-3.43
D.3	cemented	1.35	-5.39
D.4	cemented	1.95	-3.74
D.5	gas-bearing	-0.39	-5.12
D.6	gas-bearing	-0.78	-6.99
E.1	gas-bearing	1.67	-2.18
F.1	gas-bearing	-1.68	-4.01
F.2	cemented	-1.72	-8.61

Upper Puchkirchen Formation at southern slope (Lower Miocene)

Sample	Zone	$\delta^{13}C$ [VPDB]	$\delta^{18}O$ [VPDB]
A.1	water-bearing	-1.40	-7.65
A.2	water-bearing	2.17	-3.25
A.3	cemented	-0.84	-5.91
A.4	gas-bearing	0.85	-2.94
A.5	gas-bearing	0.79	-3.87
A.6	gas-bearing	-3.33	-6.82
A.7	gas-bearing	-3.53	0.07
A.8	gas-bearing	-2.20	-3.22
B.1	/	-0.27	-2.52
B.2	/	-4.31	-3.44
B.3	water-bearing	-0.09	-2.15
B.4	water-bearing	-1.53	-2.26
B.5	water-bearing	0.79	-1.67

B.6	water-bearing	0.03	-2.95
B.7	cemented	-1.19	-4.21
B.8	cemented	-2.22	-4.65
B.9	gas-bearing	0.97	-1.73
B.10	/	0.49	-1.80
B.12	/	0.35	-2.40
C.1	water-bearing	0.52	-3.07
C.2	water-bearing	-0.09	-4.07
C.3	water-bearing	-0.79	-3.73
C.5	cemented	-0.73	-6.36
C.7	gas-bearing	0.22	-0.41
C.a	water-bearing	-1.26	-2.16
C.b	water-bearing	1.32	-0.85
C.c	water-bearing	0.36	-1.41
C.d	water-bearing	0.49	0.24
C.e	water-bearing	0.27	-1.33
C.f	water-bearing	-1.48	-2.18
C.g	water-bearing	0.95	-1.13
C.h	water-bearing	-0.70	-1.76
C.i	/	-0.21	-2.53
C.j	/	0.08	-2.97
C.k	/	-0.35	-2.97
C.l	/	-2.23	-3.44
C.m	/	-1.61	-5.01
C.n	/	0.46	-0.67
C.o	/	-3.81	-3.94
C.o-S	slickenside	-1.16	-2.78

Lower Puchkirchen Formation (Upper Oligocene – Lower Miocene)

Sample	Zone	$\delta^{13}C$ [VPDB]	$\delta^{18}O$ [VPDB]
A.1	water-bearing	0.3	-4.2
A.2	water-bearing	0.7	-2.5
A.5-J	joint	1.3	-3.3
A.6	gas-bearing	0.1	-5.5

Ampfing Formation (Eocene)

Sample	Zone	$\delta^{13}C$ [VPDB]	$\delta^{18}O$ [VPDB]
A.1	oil-bearing	-12.98	-17.21
A.2	gas-bearing	-12.57	-13.71
B.1	gas-bearing	-9.75	-11.56
C.1	water-bearing	-14.82	-15.37
C.2	cemented	-28.40	-7.95
D.1	water-bearing	-2.75	-9.45
E.1	water-bearing	-6.43	-10.85
E.3	water-bearing	-7.34	-3.51
F.0	water-bearing	-10.37	-9.72
F.1	cemented	-22.24	-8.39
F.2	water-bearing	-8.83	-11.41
F.4	oil-bearing	-14.29	-17.19

Cerithian Beds (Eocene)

Sample	Zone	$\delta^{13}C$ [VPDB]	$\delta^{18}O$ [VPDB]
A.1	gas-bearing	-3.85	-7.65
A.2	gas-bearing	-11.87	-14.34

Voitsdorf Formation (Eocene)

Sample	Zone	$\delta^{13}C$ [VPDB]	$\delta^{18}O$ [VPDB)
A.1	oil-bearing	-3.35	-6.95
A.1Z	cemented	8.675	-7.61
A.2	cemented	7.655	-7.83
A.3-A	cemented	5.51	-8.28
A.3-B	cemented	7.05	-7.84
A.3-C	cemented	6.79	-8.05

9.5. Correlation of calcite content versus porosity

Oligocene-Miocene (Correlation of calcite % vs. porosity; Fig. 46)

Pearson-Correlations		Calcite %	Porosity %
Calcite%	Correlation after Pearson	1	-0.181
	Significance (1-sided)		0.051
	N	84	83
Porosity %	Correlation after Pearson	-0.181	1
	Significance (1-sided)	0.051	
	N	83	87

Bootstrap Specifications

Method of sampling procedure	simple
Number of samples	1000
Confidence interval niveau	95.0%
Confidence interval type	percentile

Pearson-Correlations				Calcite %	Porosity %
Calcite %	Correlation after Pearson			1	-0.181
	Significance (2-sided)				0.102
	N			83	83
	Bootstrap[c]	Variance		0	0.002
		Standard error		0	0.102
		95% confidence interval	Lower value	1	-0.371
			Upper value	1	0.032
Porosity %	Correlation after Pearson			-0.181	1
	Significance (2-sided)			0.102	
	N			83	83
	Bootstrap[c]	Variance		0.002	0
		Standard error		0.102	0
		95% confidence interval	Lower value	-0.371	1
			Upper value	.032	1

Spearman-Rho-Correlations					Calcite %	Porosity %
Spearman-Rho	Calcite %	Correlation coefficient			1.000	-0.107
		Significance (2-sided)				0.337
		N			83	83
		Bootstrap[c]	Variance		0.000	-0.001
			Standard error		0.000	0.105
			95% confidence interval	Lower value	1.000	-0.312
				Upper value	1.000	0.104
	Porosity %	Correlation coefficient			-0.107	1.000
		Significance (2-sided)			0.337	
		N			83	83
		Bootstrap[c]	Variance		-0.001	0.000
			Standard error		0.105	0.000
			95% confidence interval	Lower value	-0.312	1.000
				Upper value	.104	1.000